UTS UNIVERSITY OF TECHNOLOGY SYDNEY

Heavy Haul Railroad Design Upgrading Based on Fundamental Track Dynamics

by Ameyu Temesgen Tucho

Thesis submitted in fulfilment of the requirements for the degree of

Doctor of Philosophy

under the supervision of Distinguished Professor Buddhima Indraratna and Dr.Trung Ngo

University of Technology Sydney
Faculty of Engineering and Information Technology

July 2023

CERTIFICATE OF ORIGINAL AUTHORSHIP

I, *Ameyu Temesgen Tucho* declare that this thesis is submitted in fulfilment of the requirements for the award of *Doctor of Philosophy* in the *School of Civil and Environmental Engineering, Faculty of Engineering and Information Technology* at the University of Technology Sydney.

This thesis is wholly my own work unless otherwise referenced or acknowledged. In addition, I certify that all information sources and literature used are indicated in the thesis.

This document has not been submitted for qualifications at any other academic institution.

This research is supported by the Australian Government Research Training Program.

Signature of Candidate

Production Note:
Signature removed prior to publication.

Ameyu Temesgen Tucho
Sydney, 19 July 2023

ACKNOWLEDGEMENTS

I would like to extend my deepest gratitude to my supervisor Distinguished Professor Buddhima Indraratna, for his support, constructive criticism, and continuous supervision throughout this study.

I would also like to extend my appreciation and gratitude to my co-supervisor Dr. Trung Ngo, for his insightful comments and continual encouragement.

The author would like to thank Dr. Mathew Gatson, IT officer at the Faculty of Engineering and Information Technology, for assisting in conducting the advanced simulations on the High-Performance Computing facility and access to the TRC servers during various phases of my study. I would also like to thank Professor Hadi Khabbaz and Dr. Larissa Koroleva for their encouragement, guidance, and moral support in completing this thesis.

The author would like to appreciate the financial support ARC Training Center for Advanced Technologies in Rail Track Infrastructure (ITTC-Rail) and the University Technology of Sydney (International Research Scholarship) provided.

I want to thank my late parents, Kibitu Olani and Temesgen Tucho, whom I lost during the final year of the PhD study, for giving me the courage and enthusiasm to finalize this study. This thesis is a dedication to my late parents. I would also like to extend my most profound appreciation to my siblings for their encouragement, advice, and understanding throughout my PhD study.

Last but not least, my gratitude goes to my dear friends Fresenay Gigar and Isabella Silva for their constant encouragement and moral support.

LIST OF SYMBOLS AND ABBREVIATIONS

A	Shift in the PSD curve after the test
A_e	Effective sleeper-ballast contact area
A_L	Area bounded by the loading/unloading loop
A_S	Area of the triangle
b	Width of the sleeper
b_t	Track width
B	Area between the arbitrary boundary and the final PSD curve
Bg	Marsal's breakage index
Bp	Breakage potential
c_f	Damping of the foundation
C'	Cohesion
C_e	Characteristic length
C_{Ni}	Normal damping coefficients
C_{Ti}	Tangential damping coefficients
dp	Change in mean stress
dq	Change in deviator stress
D	Damping ratio
D_{max} , D_{min}	Maximum and minimum particle size
E	Modulus of elasticity
EP	Elasto-plastic
E_r	Rail modulus of elasticity
E_s	Subgrade modulus
f	Frequency
f_p	Resonant frequency
F	Wheel load
F_{max}	Maximum axle load
F_i^J	Applied force vector
g	Acceleration due to gravity
h_e	Element size
h_s	Super elevation
H	Depth of rail track subgrade
Hw	Crosswind force
I_r	Rail moment of inertia
I_i^J	Internal force vector
k_f	Track modulus
K	Speed ratio of Rayleigh to shear wave velocity
l_e	Effective length
L_b	Total length of coupled bogie
L_e	Characteristic length
m_r	Mass of the rail
M_c	Critical state stress ratio

M_R	Resilient modulus
N	Number of cycles
p'	Mean stress
P	Vertical pressure distributed on rectangular area
Pa	Axle load
P_a	Uniform pressure on the ballast top
Pc	Vertical distance between the center of gravity of the train and centroid of the rail
P_d	Train wheel load
PSD	Particle size distribution
Pw	Distance between the center of the resultant wind force and the centre of the rail
q	Deviatoric stress
q_{cyc}	Cyclic deviator stress
$q_{cyc,max}$	Maximum cyclic deviator stress
$q_{cyc,min}$	Minimum cyclic deviator stress
q_f	Deviator stress at failure
q_{max}	Maximum deviator stress under cyclic loading
q_{peak}	Peak deviator stress
q_{ult}	Ultimate deviator stress
q_r	Rail seat load
Q_d	Dynamic load
Q_{qs}	Quasi-static load
Q_S	Wheel load
Q_T	Total vertical load
Q_w	Wind load
R	Radius of track curvature
R_b	Percentage of rubber aggregates
SAF	Stress amplification factor
S_{w-r}	Wheel-rail contact stress
T	tonne
t	time
V	Train speed
V_C	Critical speed
V_L	Limiting speed
V_P	Longitudinal wave speed
V_s	Shear wave speed
w	Deflection
W_T	Weight of train per axle
y_{max}	Maximum distance travelled my moving load
$[C]$	Damping matrix
$[F]$	Nodal force vector
$[K]$	Stiffness matrix

$[M]$	Mass matrix
$\{\ddot{U}\}$	nodal vectors of acceleration
$\{\dot{U}\}$	nodal vectors of velocity
$\{U\}$	Nodal vectors of displacement

Latin

α	Mass proportional damping coefficient
α_M	Mach cone tip angle
α_p	Ratio of train speed to compressional wave speed
α_s	Ratio of train speed to shear wave speed
α_{yz}	Angle of rotation
β	Stiffness proportional damping coefficient
γ	Unit weight
δ_{dh}	Dynamic horizontal transient deflection
δ_{dvp}	Dynamic peak vertical transient deflection
δ_{dvs}	Dynamic Peak displacement shift
δ_{DV}	Vertical transient deflection
$\delta(x - Vt)$	Dirac delta function of moving load at speed V
ε_1	Total permanent axial strain
ε_1^e	Axial recoverable strain
ε_1^p	Axial plastic strain
ε_s	Shear strain
η	Stress ratio
η_{peak}	Peak deviator stress ratio
λ	Characteristics length
λ_{min}	Minimum wavelength
υ	Poison's ratio
ρ	Material density
σ_3'	Effective confining pressure
σ'_{cyc}	Cyclic deviator stress
$\sigma'_{cyc,max}$	Maximum cyclic deviator stress
$\sigma'_{cyc,min}$	Minimum cyclic deviator stress
σ_{xx}, σ_{yy}, σ_{zz}	Normal stress along vertical, longitudinal and lateral direction, respectively
σ_{w-r}	Wheel-rail contact stress
$\tau_{xy}, \tau_{xz}, \tau_{yz}$	Shear stress in three-dimensional state
ϕ'	Friction angle
φ_{ef}	Effective friction angle
φ_m	Mobilised friction angle
φ_p	peak friction angle
χ	Number of elements required per wavelength
ψ	Angle of dilation
ω	Circular frequency

Abbreviations

ARTC	Australian Rail Track Corporation
AREMA	American Railway Engineering and Maintenance of Way Association
BBI	Ballast Breakage Index
BEM	Boundary element method
CR	Crumb Rubber
CSDZ	Compressive stable degradation zone
DAF	Dynamic amplification factor
DEM	Discrete element method
DP	Drucker-Prager
ELT	End-of-Life Tyres
FDM	Finite difference method
FE	Finite element
FEM	Finite element method
HCA	Hollow Cylindrical Apparatus
HST	High-speed trains
MC	Mohr-Coulomb
NR	Not reported
NSW	New South Wales
ODZ	Optimum degradation zone
OIZ	Optimum interlock zone
PML	Perfectly matched layer
PSR	Principal stress rotation
PSD	Particle Size Distribution
PVD	Prefabricated vertical drains
RIBS	Rubber Intermixed Ballast System
SAF	Stress amplification factor
TDA	Tyre Derived Aggregates
TfNSW	Transport for New South Wales
USP	Under Sleeper Pads
1D	One-dimensional
2D	Two-dimensional
2.5D	Two-and-half dimension
3D	Three-dimensional

TABLE OF CONTENTS

LIST OF FIGURES

LIST OF TABLES

LIST OF PUBLICATIONS

Tucho, A., Indraratna, B., & Ngo, T. (2022). Stress-deformation analysis of rail substructure under moving wheel load. Transportation Geotechnics, 36, 100805. https://doi.org/10.1016/j.trgeo.2022.100805. (Q1, IF=4.94)

Indraratna, B., Ngo, T., Ferreira, F. B., Rujikiatkamjorn, C., & **Tucho, A**. (2021). Large-scale testing facility for heavy haul track. *Transportation Geotechnics*, *28*, 100517. https://doi.org/10.1016/j.trgeo.2021.100517 . (Q1, IF=4.94)

Malisetty, R. S., Indraratna, B., **Tucho, A.** & Ngo, T., (2022). Dynamic stress response of track layers under high-speed trains. In *20th International Conference on Soil Mechanics and Geotechnical Engineering*. Australian Geomechanics Society.

Tucho, A., Indraratna, B., & Ngo, T., (2023). Dynamic stress and displacement response of ballasted railway track capturing the effect of moving load using FE analysis. *In Australia and New Zealand Conference on Geomechanics 2023*, Cairns, Australia

ABSTRACT

Railways have become one of the most preferred passenger and freight transportation modes in many countries. The past decades have witnessed a significant increase in demand for higher performance from the existing and new rail networks to retain a competitive edge against other transportation systems. This has motivated the railway industry to seek faster, heavier trains while satisfying performance requirements. High-speed and heavy axle loads pose various geodynamic and geotechnical challenges in ballasted tracks. The major challenge at elevated train speed is excessive ground vibration and stress amplification, mainly when the speed is close to the critical wave velocity of the track. Those elevated vibrations increase safety issues since large track displacement can cause a derailment, whereas stress amplification could result in excessive deformation and track instability.

In this study, a three-dimensional (3D) finite element (FE) analysis is developed to study the effect of moving load on the dynamic response of rail tracks. The FEM model is validated with two different field measurements, which are used to study the effect of train speed on the transient stress-displacement response of ballasted track. Increasing train speed amplifies vertical and lateral track displacement and alters the displacement field, especially at a critical speed. Also, the critical speed and magnitude of track deflection are observed to be influenced by subgrade modulus.

The changes attributed to dynamic stress paths and the angle of principal stress rotation are also analysed for the train speed in the range of 60-450 km/h. The conventional approach predicting track stress does not capture track response involving moving load

and associated “critical speed” effect, especially at higher speeds where significant principal stress reversal occurs. Also, the analysis shows the existence of maximum allowable train speed to prevent shear failure of the ballast layer.

After the effect of speed on track vibration and associated amplification of stress-displacement field is established through 3D FE analysis, the potential application of rubber inclusion in the ballast layer was examined. In this study, the traditional ballast layer was replaced by a Rubber-Intermixed-Ballast system (RIBS), and the response of the track under moving train loading is studied. The analysis was conducted at various train speeds to capture the distinct track response at pseudo-static, subcritical, and critical speed ranges. Finally, the practical implication of RIBS on global track response is analysed and discussed in terms of vertical stress reduction and transient displacement in the vertical and lateral directions.

.

CHAPTER 1 INTRODUCTION

1.1 Background

The rail network systems have become critical transportation infrastructure of many countries in transporting passengers and freight. However, the ongoing competition from other transportation systems pushes railway companies to seek higher performance, such as increased traffic frequency and axle loads, from existing and new networks. This has led to an exponential increase in train speed exceeding 250km/h in countries like China, the United Kingdom, and Japan (UIC, 2021). The route kilometer of High-Speed Rail has doubled in the past 30 years, with over 56,000km of high-speed rail track currently operational worldwide (BITRE, 2019). In Australia, the proposed high-speed rail with a speed of 350km/h along the Melbourne-Sydney-Brisbane corridor shown in Figure 1.1 is expected to attract 83.6 million passenger trips by 2065 (AECOM, 2011).

Figure 1.1 Proposed high-speed rail track along Melbourne-Sydney-Brisbane (AECOM, 2011)

The continuous demand for trains with elevated speed and axle load has bought a wide range of geodynamic and geotechnical challenges. The major challenge at elevated train speed is excessive ground vibration associated with Rayleigh wave propagation, mainly when the speed approaches the Rayleigh wave velocity of the substructure (Costa et al., 2015; Krylov et al., 2000), among others. For example, significant vibration was observed when the train speed approached 200km/h in the famous Ledsgard's benchmark study, which was caused by the low stiffness of the track foundation (Madshus and Kaynia, 2001). The elevated vibrations increase safety issues since the resulting large track displacements can cause derailment if the effective rail-wheel contact is lost (Connolly and Costa, 2020). Furthermore, the vibration increases the dynamic stresses in the track substructure leading to rapid degradation of the track geometry (Malisetty et al., 2022).

The track substructure is also subjected to a complex stress path and principal stress rotation associated with the effect of moving load. Accordingly, principal stress rotation due to train moving loads leads to excessive deformation of track substructure compared to monotonic and cyclic loading (Malisetty et al., 2020; Momoya et al., 2007). However, the stress paths employed in those studies are the classical 'cardioid' shape consistent with slow-moving loads, as the influence of surface wave propagation is rarely considered in laboratory testing and single-element models.

Furthermore, the demand for recycling and reuse of end-of-life tires (EOLT) is increasing to mitigate the persistent environmental, economic and social problems related to the management of waste tyres (Tasalloti et al., 2021). In Australia, the average annual waste tyre recovery is about 69% of the total 450 thousand tonnes of EOLTs produced annually (Genever et al., 2017; Randell et al., 2020). The unrecovered tires are dumped, stockpiled,

disposed of in licensed landfills, or buried on-site. Improperly stockpiled EOLTs pose substantial fire risk under extreme temperatures due to the development of exothermic reaction, which releases gases that are hazardous to human health and the environment (Randell et al., 2020). Moreover, stockpiled tyres consume a significant volume of usable land (75% void space), and their extended storage makes them an ideal habitat for rodents and other insects that transmit diseases (Sidhu et al., 2006; Torretta et al., 2015). Very often, stockpiled tires result in the leaching of metals and other harmful contaminants into waterways, groundwater, and soils. Thus, the applications of recycled rubber products in civil engineering have been proposed as one of the waste tire recovery and management approaches (Randell et al., 2020). As a part of EOLTs management, the reuse of granulated rubber in the ballast layer has been proposed as an economical and sustainable solution to enhance the performance of railway tracks (Arachchige et al., 2021; Arachchige et al., 2022; Fathali et al., 2017).

1.2 Research motivation and originality

Though the influence of train speed on the deformation amplification has been the focus of study in the past decade, the relationship between the train speed and dynamic stress paths and the associated attenuation of the stresses-displacement field in the track substructure is not well understood. Furthermore, most track dynamic analyses are primarily based on the assumption that each track geomaterial responds within the range of linear elasticity. However, with increased train speed, the shear strain in the track substructure may reach higher values, especially in the ballast layer, where the stress magnitude is more significant. Though the assumption of small-strain response is widely accepted in critical speed modelling and vibration analysis, the effect of elastoplastic models on transient displacement response and stress path is not well understood.

In addition, in conventional track analysis and design, the dynamic response of the track substructure is approximated using the DAF, which is an empirical factor employed to estimate the moving load-induced peak dynamic stress from the quasi-static response (Esveld, 2001; Van Dyk et al., 2017). The stresses are computed using analytical techniques that assume the track substructure as vertical elastic springs. These dynamic amplification factors mainly consider the rolling stock and track superstructure properties (train speed, wheel diameter, bogie spacing, and track dimensions, among others); while the quantified substructure properties are seldom incorporated (Burrow et al., 2006). However, recent studies have shown that dynamic track response is significantly affected by subgrade properties such as resilient modulus, track geometry, and subgrade stratification (Madshus et al., 2004; Nimbalkar and Indraratna, 2016). Hence, a rational analysis and prediction approach that considers complex metric geomaterial principles is required.

Over the past few decades, numerous semi-analytical and numerical approaches have been used to predict the dynamic response of tracks at elevated train speeds. In some of the semi-analytical methods, the track and foundation are modelled as a beam on spring-dashpot assemblies (Kouroussis and Verlinden, 2015; Walker and Indraratna, 2018; Zhai et al., 2009) and half-space models (Krylov, 1994; Krylov, 1999; Madshus et al., 2004), among others. While these models have been used to study a track's instantaneous response under moving load in the time and/or frequency domains, they neither capture the material nor geometric complexity of the track substructure. Over the years, several numerical methods have been employed to study track vibration, including two-and-half dimension models (2.5D) (Bian et al., 2008; Costa et al., 2012; Yang et al., 2019), three-dimensional finite element models (Banimahd et al., 2013; Connolly et al., 2013; El

Kacimi et al., 2013; Shih et al., 2017). The 2.5D models consider the track as an invariant along the direction of train movement; hence the stress transfer between discrete-spaced sleepers and ballast is not adequately represented. These computationally efficient methods are widely applied to predict ground vibration, but they are rarely applicable to study dynamic track responses involving geometric and material complexities.

Given the limitations of the aforementioned techniques, various studies have resorted to simulating moving loads using the 3D Finite Element Method (3D FEM). In the past, 3D FEM has been successfully employed to study the effect of increasing train speed on ground vibrations and instantaneous track deflection (Connolly, 2013; Sayeed, 2016; Shih et al., 2016) as well as for analysing the dynamic stress response (Banimahd et al., 2013; Li et al., 2018; Tang et al., 2019). In addition, the FEM provides promising solutions in capturing complex track geometries and implementation of advanced elastoplastic constitutive models for track substructure. Hence, the non-linear responses and long-term deformation and degradation aspects of track geomaterials can be examined using FEM (Correia and Cunha, 2014; Li et al., 2016; Varandas et al., 2020).

Hence, 3D FE modelling is implemented to study the dynamic response of railway tracks under moving train speed. The current state of practice for predicting critical speed and dynamic amplification factors does not account for track substructure response and immediate track instability at elevated train speed. Therefore, emphasis is given to studying the stress-deformation response of rail track substructure using 3D FE modelling, capturing the effect of train speed and track foundation stiffness.

1.3 Objective and scope

The main aim of this study is to evaluate the influence of increasing train speed on the dynamic response of the ballasted track using numerical analysis. The 3D FEM has been developed to simulate the moving load on ballasted track.

The specific objectives of this research can be briefly summarized as:

1. To develop 3D FE numerical capable of predicting track foundation response under moving train loading and validate against case studies.
2. To analyse the effect of increasing speed on the dynamic responses of railway track substructure.
3. To quantify the variation of intermediate stresses and associated principal stress rotation in the ballasted track subjected to moving load.
4. To study the effect of the rubber-intermixed-ballast system (RIBS) in rail track stress-deformation response.

1.4 Thesis outline

This thesis is organised into seven chapters as follows:

Chapter 1 is the thesis Introduction, where the research background, the research motivation, the objectives, and the outline of the thesis have been presented.

Chapter 2 briefly presents the literature review on the components of ballasted tracks. A detailed description of the geodynamic track response and numerical modelling techniques adopted for track analysis is presented. Furthermore, a description of ballast response under monotonic and cyclic loading is presented. Chapter 2 also summarises

pertinent studies regarding the application of tire-derived aggregates (TDA) in railway ballast.

Chapter 3 describes the numerical modelling implemented throughout the study, capturing the dynamic response of railway substructure subjected to moving train loading. The prediction is validated against analytical predictions and field measurements.

Chapter 4 presents transient vibration responses such as vertical and lateral displacements of tracks subjected to moving load. The critical speed and associated dynamic amplification factors are discussed in detail.

Chapter 5 provides a detailed analysis and prediction of the dynamic stress responses of tracks subjected to moving train loading. The results and discussion from an extensive parametric study conducted on various ranges of subgrade properties are presented. Furthermore, the relationship between train speed, dynamic stress amplification factors, and stress path is analysed.

Chapter 6 presents the transient dynamic response of the track when the ballast layer is replaced with a rubber-intermixed-ballast layer (RIBS). The influence of RIBS on track response parameters, such as dynamic displacement and stresses, is discussed in detail.

Chapter 7 summarises this study's main findings and recommendations for future studies. Finally, a list of references is presented.

CHAPTER 2 LITERATURE REVIEW

2.1 Introduction

This chapter presents the general overview of pertinent literature and provides background on geotechnical aspects of ballasted railway track dynamic response analysis, with particular reference to the influence of speed. The influence of train speed on dynamic amplification, surface wave propagation, numerical and analytical models of the railroad, and the behavior of track geomaterials under static and cyclic loading are also discussed. Finally, salient aspects of railway track design methods are presented.

2.2 Components of a ballasted railroad

The general purpose of a railway track is to provide a stable and efficient running guideway for railway vehicles, which in turn requires that the vertical and lateral track configuration is maintained throughout its service time. Stable track configuration can only be attained if each subcomponent accomplishes the desired functions under various axle loads, running speeds, and environmental and operational constraints (Indraratna et al., 2011; Li et al., 2015).

A traditional ballasted track consists of various components, which can be classified into superstructure and substructure, as shown in Figure 2.1. The superstructure usually consists of steel rails, rail pads, and sleepers, while the substructure comprises the ballast, capping, and subgrade layers (Indraratna et al., 2011). The rails are steel beams laid parallel to the direction of train movement, providing a stable surface for the circulation of wheels while ensuring support in both vertical and lateral directions. A rail pad is installed beneath the rail to provide a resilient contact interface between the rails and sleepers, which are clapped together with fasteners (Esveld, 2001). Modern rail pads can

reduce track deflection, noise, and vibration depending on their stiffness (Iwnicki, 2006). The sleepers, usually made of timber or concrete, are placed along the transversal direction to maintain track-gage and distribute stress to the ballast layer.

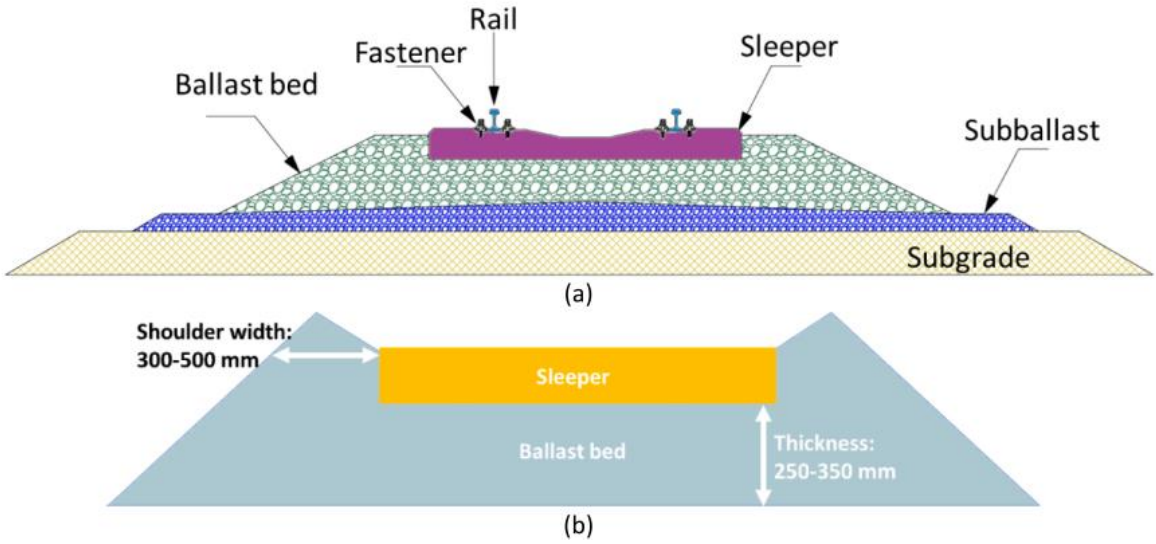

Figure 2.1 Ballasted railway track (a) track components (b) transversal cross-section of ballast (modified after Guo et al. (2022))

2.2.1 Ballast layer

Ballast is a granular and free-draining layer that provides a firm platform for the track superstructure. Ballast aggregates are usually derived from quarries by blasting and crushing good quality igneous or sedimentary rocks (Indraratna and Salim, 2005). High-quality ballast is generally characterised as uniformly graded crushed angular aggregates, that are free from interparticle cementation and fines. This granular layer is commonly 250-350 mm thick, measured from the bottom of the sleeper, whereas additional ballast material is packed around the sides of the sleeper (shoulder ballast) to ensure lateral stability (Selig and Waters, 1994).

The primary function of the ballast layer is to distribute the static and dynamic load from the train wheel to the capping and the subgrade to an acceptable level (Li et al., 2015; Selig and Waters, 1994). Some of the additional functions of the ballast layer, as documented by several researchers (Jeffs and Tew, 1991; Profillidis, 2006; Selig and Waters, 1994), are listed below:

- Provide sufficient longitudinal and lateral support to the track super-structure
- Attenuate the mechanical and acoustic vibrations generated by moving trains
- Provide adequate support for the maintenance and installation of the track and auxiliary components
- Facilitate adequate permeability for drainage purposed
- Resist breakage and degradation as well as biological and chemical weathering

Table 2.2.1 Specifications for ballast aggregates in various countries (Gaskin and Raymond, 1976; Lim, 2004; Raymond, 1985)

Ballast Property	Australia	UK	USA	Canada
Aggregate Crushing Value	<25%	<25%		
Los Angeles Abrasion	<25%	<20%	<40%	<20%
Flakiness Index	<30%			<25%
Soft and Friable Pieces		<5%	<5%	
Fines (< No. 200 sieve)		<1%	<1%	
Clay Lumps				
Bulk Density (kg/m3)	>1200kg/m3		1120kg/m3	
Particle Specific Gravity	>2.5	>2.6		

In order to fulfill the above-mentioned performance requirements and ensure track stability, the ballast should adhere to a set of specifications such as particle size, gradation, angularity, density, hardness, durability, and resistance to weathering (Li et al., 2015).

Various countries have developed a set of acceptance criteria for ballast aggregates, as summarised in Table 2.1. In addition, the requirement for railway ballast in Australia is specified in the Australian Standard AS2758.7 (2015) and Technical Specification TS3402 (2001), as given in Table 2.2.

In addition to satisfying the specification mentioned above, the ballast's thickness must be large enough to spread and attenuate the applied dynamic stress over the depth and reduce track degradation and settlement (Profillidis, 2006).

Table 2.2 Ballast particle size and gradation (AS2758.7, 2015; TS3402, 2001)

Particle size (mm)	**% passing by weight**
63	100
53	100-85
37.5	65-20
26.5	20-0
19	5-0
13.2	2-0
9.5	0

2.2.2 Capping

Capping is typically placed below the ballast layer and consists of well-graded crushed rock and sand mixtures. They must be sufficiently durable to withstand and transfer the dynamic loads from the ballast to the underlying substructure components. The thickness of the capping usually varies from 100 – 150mm to prevent penetration of ballast aggregates into the subgrade and reduce movement of fine subgrade soil into the ballast stratum (Li et al., 2015). Hence, the capping layer must satisfy the filter requirement for the ballast and subgrade, and it also serves as a drainage layer to reduce the development of excess pore water pressure during the service life of the track (Trani and Indraratna, 2010).

2.2.3 Subgrade

The subgrade is the bottom layer on which the track structure rests; and it needs sufficient stiffness and strength to support induced static and dynamic stresses (Profillidis, 2006). There are two types of subgrade: natural ground (formation) and placed soil. The natural ground usually has larger deformability (low stiffness) as compared to other railroad materials depending on the geotechnical characteristics of the soil. For instance, low subgrade stiffness results in higher track deformation, resulting in undesirable distortion of track geometry and alignment, whereas inadequate drainage can cause mud pumping (Indraratna et al., 2020; Nguyen et al., 2019). When the mechanical properties of the formation are not adequate, as in the case of soft subgrade, two approaches are recommended: soil replacement and ground improvement. Subgrade improvement approaches such as prefabricated vertical drains (PVD) or bio-engineering of native vegetation have been successfully implemented to increase the track stiffness or bearing capacity and reduce the immediate and permanent settlement of railway tracks (Fatahi et al., 2010; Indraratna et al., 2011; Indraratna et al., 2006). In some cases, a soft formation layer can be replaced by compacted fill materials (or embankments) with adequate geotechnical characteristics to withstand repeated dynamic loading (Adam et al., 2007; Arulrajah et al., 2009).

2.3 Track loading characteristics

A proper analysis, design, and maintenance plan of the rail track must consider the load transfer mechanism between the train wheel, track super-structure, and substructure. A moving load generates vertical, lateral, and longitudinal forces in the railway track

structure due to static, cyclic, and dynamic loads applied throughout its operational period.

2.3.1 Vertical forces

The vertical loads in the track structure are composed of static and dynamic loading. Esveld (2001) showed that the total vertical load (Q_T) transferred to the rail is the combination of a quasi-static load (Q_{qs}) and dynamic load (Q_d) as given in Equation 2.1. The quasi-static load is composed of the effect of the weight of the train per axle (W_T), wind load (Q_w) and the increased vertical force due to centrifugal force (Q_c) on the outer rails in the curves; and the force (Q_d) is the load is a dynamic wheel load generated by train velocity, unsprung mass, sprung mass, wheel-rail irregularity etc. The total vertical wheel load can be estimated as follows (Esveld, 2001):

$$Q_T = Q_{qs} + Q_d \tag{2.1}$$

$$Q_{qs} = Q_s + Q_w + Q_c \tag{2.2}$$

$$Q_s = \frac{W_T}{2} \tag{2.3}$$

According to Esveld (2001), the vertical track load generated by wind load and centrifugal force can be determined through the limit equilibrium analysis of the forces applied on the train, as follows:

$$Q_w + Q_c = H_w \frac{P_w}{s} + G \frac{P_c}{s^2}\left(\frac{sV^2}{gR} - h\right) \tag{2.4}$$

where, H_w is the crosswind force; P_w is the vertical distance between the resultant wind load and the rail; P_c is the vertical distance between the centre of gravity of the train and the rail; V is speed of the train; g is the gravitational acceleration; R is the radius of track curvature; h is the super elevation; s is width of the track, as given in Figure 2.2.

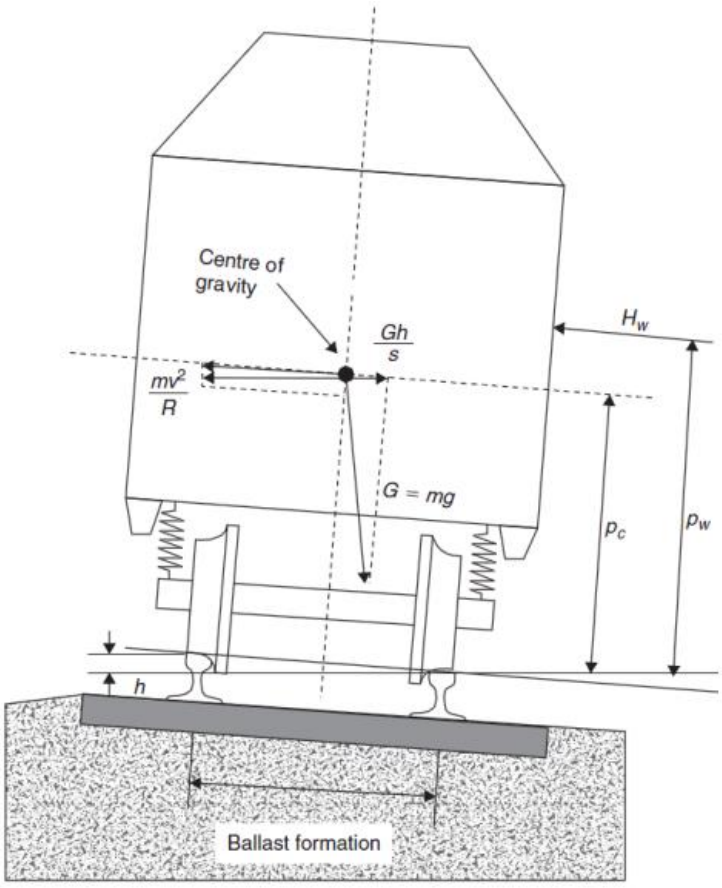

Figure 2.2 Quasi-static forces on the train traveling on curved track (modified after Esveld (2001))

The typical load transmission mechanism under train loading consists of static, cyclic and dynamic loading. The load transfer mechanism is predominantly from top to bottom, as the law of gravity governs the system, as shown schematically in Figure 2.3. The train wheel load (P_d) is transmitted from the wheel to the rail and transferred to the formation through the underlying discrete sleepers, ballast and capping layers. The interface irregularities between the wheel and rail generate dynamic stress (σ_{w-r}); and the stress

is subsequently shared between adjacent sleepers located in the vicinity of the train wheel (rail seat load q_r). Then, the load on the sleeper is further distributed to the substructure layers of the track, depending on several factors, including strength, stiffness, and damping properties of each layer.

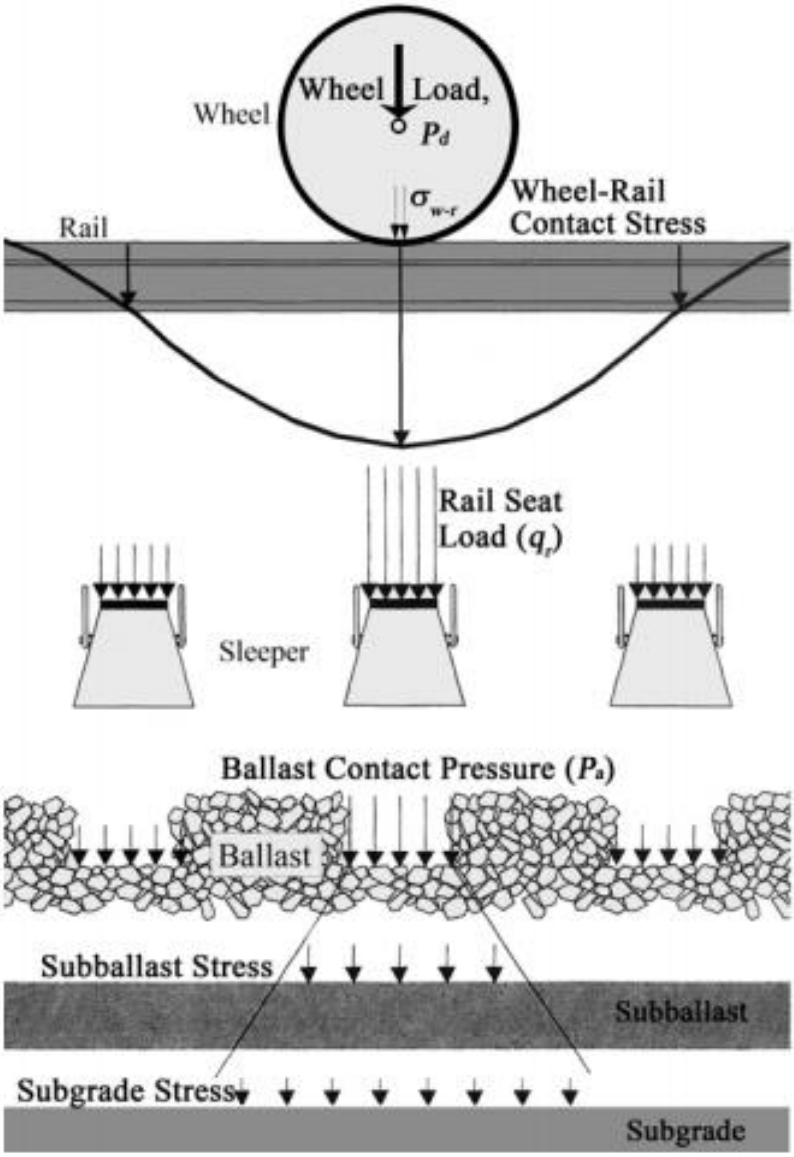

Figure 2.3 Mechanism of load distribution from train wheel to the track substructure (modified after Selig and Waters (1994))

Several equations have been recommended to compute the maximum load distributed to the sleepers based on analytical, numerical and experimental methods. However, the

methods show significant variability ranging from 31% to 60% of P_d, as summarised in Table 2.3. It is difficult to estimate the magnitude of rail seat load accurately since those relationships do not capture factors such as sleeper spacing, track stiffness, track maintenance history, subgrade properties and track degradation.

The maximum stress on the top of the ballast layers occurs when the load is directly above the sleeper. However, the magnitude of the contact stress changes with time (Nimbalkar and Indraratna, 2016) and sleeper length (Shenton, 1985), as shown in Figure 2.4. In the first few cycles of train loading, the interface stress depends on a few ballast aggregates that are in contact with the base of the sleeper (Shenton, 1985). The stress distribution changes as the void under the sleeper redistribute with the number of cycles due to particle rearrangement, densification, and breakage (Sadeghi, 2005; Zakeri and Sadeghi, 2007). Hence, the stress at the top of the ballast tends to be uniform; and it can be approximated by the pressure distribution profile shown in Figure 2.5 for design purposes.

The uniform pressure on the ballast top (P_a) can be estimated by a simplified expression (Jeffs and Tew, 1991):

$$P_a = \left(\frac{q_r}{b l_e}\right) F \qquad 2.5$$

where q_r is the rail seat load, l_e is the effective length, b is the width of the sleeper and F is a factor considering the influence of sleeper properties and track maintenance. Table 2.4 summarises the suggested effective sleeper support area for approximating contact stress. It can be noticed that those relationships result in significantly different contact stresses, and they cannot capture the track substructure properties.

Table 2.3 Maximum rail seat load estimation methods

Maximum Rail Seat Load	References and Remark
q_r=0.31P_d	Li et al. (2015) for concrete sleeper
q_r=0.42P_d	Li et al. (2015) for timber sleepers
q_r=0.31P_d	For three adjacent sleepers (Talbot, 1980)
q_r=0.43P_d	O'Rourke (1978) for timber sleepers (O'Rourke, 1978)
q_r=0.60P_d	AREMA (2015) for prestressed concrete sleeper
	ORE (1987) for prestressed concrete sleepers
q_r=0.34P_d	Li et al. (2007) considering the theory of beam on elastic foundation
q_r=0.4P_d	Profillidis (2006) considering five adjacent sleepers using FE analysis

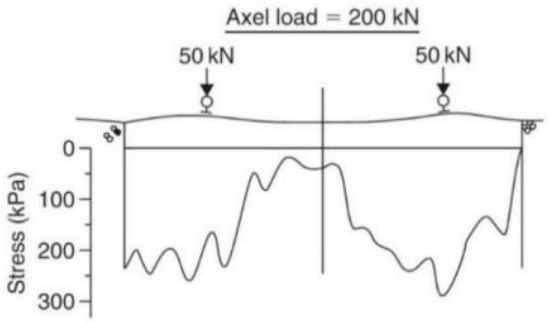

Figure 2.4 Measurement of vertical stress at the sleeper-ballast interface (Shenton, 1985)

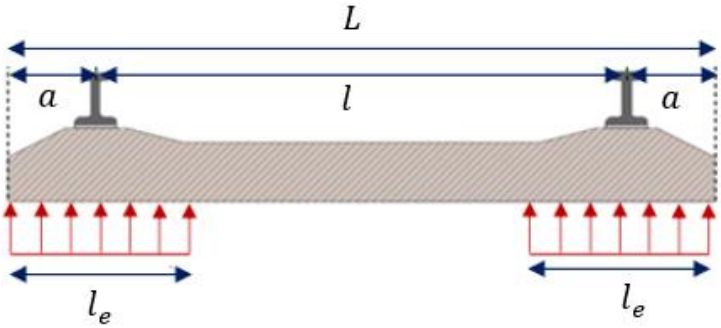

Figure 2.5 Schematic description of effective length to compute pressure at the top of the ballast layer

Table 2.4 Effective areas or length of a sleeper to compute pressure at the top of the ballast layer

Proposed approach	Effective length or area
AREMA (2015)	$A_e = \frac{2}{3}A$ where A is total contact area of at the bottom of sleeper
Atalar (2001)	$l_e = 2a$
Jeffs and Tew (1991)	$l_e = \frac{L}{3}$
Schramm (1961)	$l_e = \frac{L-l}{3}$

Once the stress amplitude is determined using Equation 2.5, the stress transmitted to the subgrade can be estimated using Boussinesq's elastic solutions (Doyle, 1980).

2.3.2 Lateral forces and longitudinal forces

Lateral forces act parallel to the long direction of the sleeper, and they are primarily caused by the buckling reaction and lateral wheel forces (Esveld, 2001). The friction between the wheel and rail and the associated reaction from the wheel flanges as the train moves causes the buckling reaction force. In addition, the high temperature-induced development of compressive stress in the rail causes the buckling reaction forces, as shown in Figure 2.6. In case of high lateral forces, the lack of lateral confinement can cause track instability, which could lead to derailment (Indraratna and Ngo, 2018).

The longitudinal forces are generated along the perpendicular direction to the sleepers; and they are influenced by the following factors (Ruge and Birk, 2007; Selig and Waters, 1994):

- The magnitude of acceleration and deceleration of the train
- Expansion and contraction of the rails caused by temperature fluctuation
- Stress wave propagation in the track

- Track creep

Figure 2.6 High temperature-induced track deformation near Speed, Victoria (Cowie, 2018)

2.3.3 Dynamic amplification factors

Several empirical relationships are proposed in conventional track design methods to predict the design vertical wheel load. In those empirical methods, the dynamic design load is expressed as a function of quasi-static load. Hence, the dynamic amplification factor (DAF) is defined as the ratio of the dynamic to the static response paramaters such as stress, displacement, or strains (Esveld, 2001). The dynamic impact factors are developed through empirical field measurement analysis and are always expressed as a function of speed. Doyle (1980) provided a summary of several amplification factors. Besides train speed, the DAF is influenced by train parameters and track parameters, such as wheel diameter, unsprung mass, wheel load track modulus, and irregularities, among others (Doyle, 1980; Esveld, 2001; Van Dyk et al., 2017). Various expressions used for estimating the DAF are described in Table 2.5.

Table 2.5 Dynamic amplification factors (modified after Doyle (1980))

Dynamic factor	**Expressions for DAF**
AREMA (2015)	$0.6 + 0.005V \ \ for\ 20 < V < 120$
ORE (1987)	$1 + \alpha + \beta + \gamma$
Sadeghi and Barati (2010)	$1.098 + 0.00129V + 2.59 \times 10^{-6}V^2$
British Railways (Doyle, 1980)	$1 + 14.136\alpha' V\sqrt{\frac{D_j P_u}{g}}$
Clarke (Doyle, 1980)	$1 + \frac{15V}{D\sqrt{U}}$
Eisenmann (Esveld, 2001)	$1 + \delta\eta t$ $\eta = 1 \ \ for\ V < 37$ $\eta = 1 + \left(\frac{V - 37}{87}\right) \ for\ 37 < V < 125$
German Railways (Schramm, 1961)	$1 + \frac{11.655V^2}{10^5} - \frac{6.252V^3}{10^7}$
Indian Railways (Srinivasan, 1969)	$1 + \left(\frac{V}{3\sqrt{U}}\right)$
South African Railways (Doyle, 1980)	$1 + 0.312\frac{V}{D}$
Talbot (Hay, 1991)	$1 + \left(\frac{33V}{100D}\right)$
Li and Selig (1998)	$1 + 0.0052\frac{V}{D}$
Esveld (2001)	$1.4\ for\ \mathrm{S} < 60$ $1 + 1.4\left[1 + \frac{\mathrm{S} - 60}{140}\right] \ for\ 60 < \ \mathrm{S} < 300$
Nimbalkar and Indraratna (2016)	$1 + \alpha\left(\frac{S}{\phi}\right)^{\beta}$
Sun et al. (2016)	$e^{0.003\mathrm{S}}$

Definition of variables:

V- Train speed
D –Diameter of the wheel
U – Track modulus
δ *and* t – Empirical parameters depend on track condition
α, β , γ – Empirical factors based on speed, track, and vehicle conditions

α' - Total rail joint tip angle
D_j – Track stiffness
P_u – Unsprung weight at one wheel
g – Gravitational acceleration
S– Train speed
ϕ- Diameter of the wheel in m
α and β – coefficients based on subgrade $\alpha = 0.0065,\ 0.0058,\ 0.0052;\ \beta$ *=(0.99-1.02); (0.89-0.92); (0.75-0.76) for Hard Rock, Concrete Bridge and Alluvial Deposit; respectively*

The expressions by German Railways Schramm (1961) and Sadeghi and Barati (2010) only consider the train speed, while the equations by Eisenmann (Esveld, 2001), Talbot Hay (1991), South African Railway (Doyle, 1980) included the effect of wheel diameter to capture the effect of wheel-rail irregularities. South African Railway (Doyle, 1980) and Talbot (Hay, 1991) are virtually similar, except the former was recommended for narrow-gauge tracks. Clarke's (Doyle, 1980) approach is an algebraic variant of Talbot's (Hay, 1991) equation. British Railways Hay (1991) focuses on train dynamics by considering irregularities at rail joints.

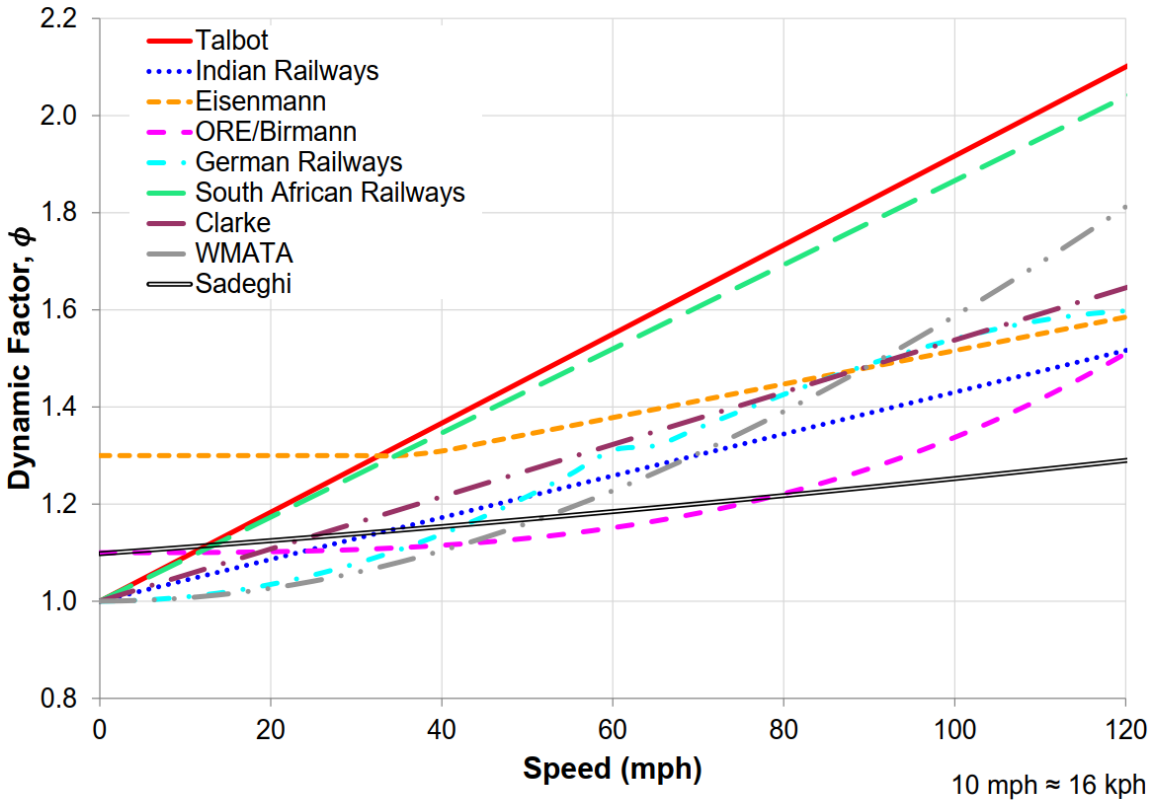

Figure 2.7 Comparison of dynamic amplification factors (Van Dyk et al., 2017)

Though overlooked in most impact factor expressions, the influence of the track is generally included as a track maintenance condition in the Eisenmann method (Esveld, 2001) and ORE (1987) methods. A notable exception is the amplification factors

recommended by Nimbalkar and Indraratna (2016), based on track stress measurement conducted at Singleton, Australia, which recommended three distinct factors based on subgrade type.

Figure 2.7 compares the dynamic amplification factors per the approaches summarised in Table 2.5. Accordingly, the amplifications are highly scattered throughout the speed range, the most conservative estimate being Talbot's (Hay, 1991) amplification factor in the medium to high speeds range.

2.4 Geodynamic aspects of moving load

2.4.1 Surface wave propagation

Railway vibrations primarily originate from the contact forces at the wheel-rail interfaces, which are generally grouped into quasi-static and dynamic excitations (Connolly et al., 2015; Knothe and Grassie, 1993; Paul de Vos, 2017). The quasi-static excitation arises from the mass of the moving train and is not affected by the traveling speed. On the other hand, dynamic excitations are affected by train speed and can be caused by parametric excitation caused by support variability, track discontinuities, rail corrugation, and wheel-rail interface excitations such as wheel irregularities, among others, as summarised in Table 2.6 (Hall, 2002; Kouroussis et al., 2014). The vibration of the train wheels is governed by the vehicle system, such as bogies springs-damping systems, as well as the weight of the train, while rail vibration is controlled by the dynamic response of track elements supporting the rail, including sleeper, ballast, capping, and subgrade (Paul de Vos, 2017). Hence, the dynamic behavior of each component depends on the interaction of the overall system (Kouroussis et al., 2014; Zhai et al., 2010).

The load generated due to dynamic excitations propagates through the track structure and ground as waves (Heelis et al., 2000; Thompson, 2008). The wave propagation mechanism depends on the material properties of the railroad and subgrade as well as track geometry. The track roughly forms a beam resting on the subgrade, with distinct natural flexural waves and associated propagation speed (Krylov et al., 2000; Madshus et al., 2004). Hence, the combination of flexural waves in the track and stress waves in the subgrade under dynamic interaction gives rise to a new natural wave whose traveling mechanism and speed are governed by the properties of the track-subgrade system. This new speed is defined as "critical speed (Gunn et al., 2015; Kaynia et al., 2000; Madshus and Kaynia, 2000). At critical speed, the wave energy is confined to the track creating significant movement (Madshus et al., 2004; Nsabimana and Jung, 2015). Hence, a new dynamic event, in addition to dynamic load generated at the wheel-rail interface, is introduced to the railroad and subgrade as the train travels at elevated train speeds approaching the critical speed.

At a speed close to the critical speed, the response generally comprises two components: quasi-static portion and dynamic(Madshus and Kaynia, 2001; Zhai et al., 2010). The quasi-static component follows the symmetrical downward bow pattern corresponding to the static mass on the train axles(Krylov, 1994; Madshus et al., 2004). On the other hand, a dynamic component introduces upward and downward oscillations below the train wheels and then gradually dissipate behind the train (El Kacimi et al., 2013; Woodward et al., 2013). This dynamic element primarily generates vibrations in the form of a ground roll, which is commonly referred to as the "Rayleigh" type (Costa et al., 2015; Madshus and Kaynia, 2001). Hence, the track response primarily depends on the weight of the train at low speed. At high-speed approaching critical speed, on the other hand, both the weight

of the train and the geodynamic behaviour of the track and subgrade, such as stress wave propagation speed, govern the track response.

The waves generated by the dynamic excitation propagate as body waves or surface waves. The body waves include the compressional (P-waves) and shear wave (S-waves), propagating through the soil beneath the ground surface. Surface waves such as Rayleigh waves and Love waves travel along the surface. Love waves are out-of-plane polarized shear waves that are predominantly observed when a surficial layer of low velocity is placed on a stiffer layer (Athanasopoulos et al., 2000). Compared to body waves, surface waves carry most of the vibration energy, significantly affecting the vibration response at the topmost part of track layers, such as ballast.

Table 2.6 Sources of track dynamic vibrations (Hall, 2002)

Stress waves induced by the track response • Axle load • Distance between train wheels • Train speed
Wheel-rail interface excitations • Unsteady riding of the vehicle • Dynamic properties of the vehicle bogie • Wheel-rail irregularities • Misalignment of motors • Acceleration and deceleration of the vehicle
Track discontinuity • Rail irregularities and distance between joints • Switches and crossings • Track forces at curves and super elevations
Support variability • Variability in the spacing and stiffness of sleepers • Stiffness variation and heterogeneity of the ballast and subgrade

Rayleigh waves travel along the surface of the track transporting about 67% of total wave energy and generating retrograde particle motion in the surficial layers, whereas Love waves have an elliptical motion in the lateral and longitudinal direction, as shown in Figure 2.8 and Figure 2.9 (Athanasopoulos et al., 2000; Richart et al., 1970). Regarding compressional waves, the particle moves along the same direction as the wave front, whereas the shear waves induce particle motion in a perpendicular direction to the wavefront. The propagation of Rayleigh waves is confined to a depth about the wavelength of the propagating waves, and its speed is slower than other types of waves, as shown in Figure 2.8.

The propagation of Rayleigh waves depends on material properties such as poison's ratio (υ), modulus of elasticity (E), and material density (ρ). The amplitude of Rayleigh waves attenuates with distance from the source due to geometric and material damping, in a manner inversely proportional to the square root of distance. Geometric damping is the loss of wave energy with the distance from the vibration source, whereas the internal sliding of soil particles causes material damping (Woods, 1968).

Although the amplitude of Rayleigh waves decreases rapidly with depth, they propagate further than the compressional and shear waves. Hence, the section immediately under the track experiences complex wave propagation phenomena involving compressional, shear, and Rayleigh waves, while locations away from the track experience Rayleigh waves only (Connolly, 2013; Woods, 1968).

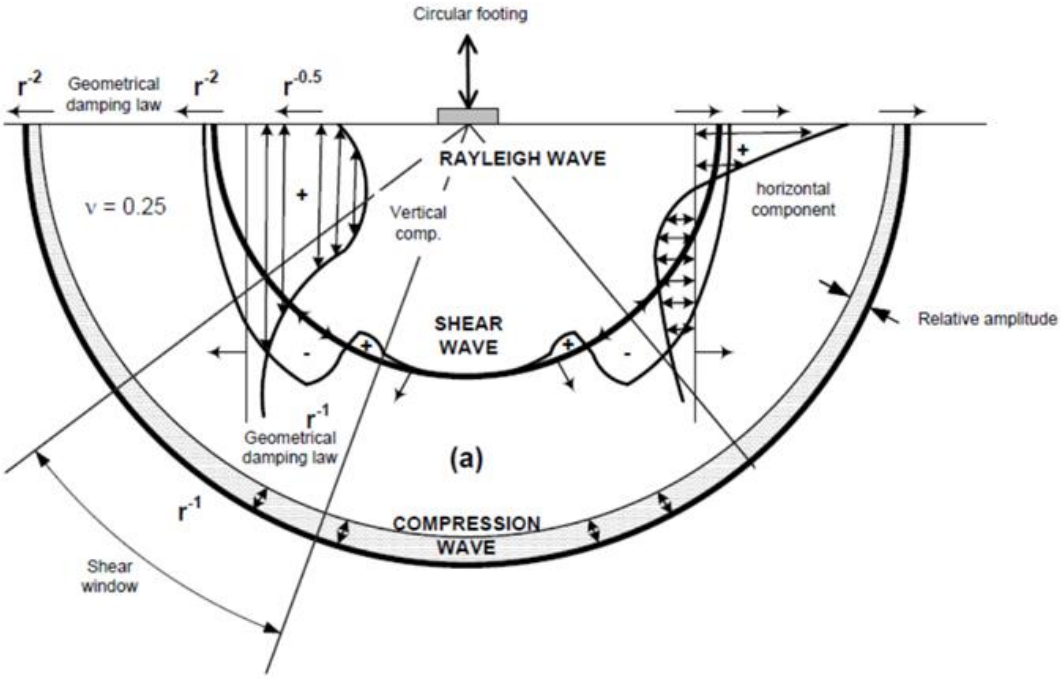

Figure 2.8 Seismic wave propagation (Woods, 1968)

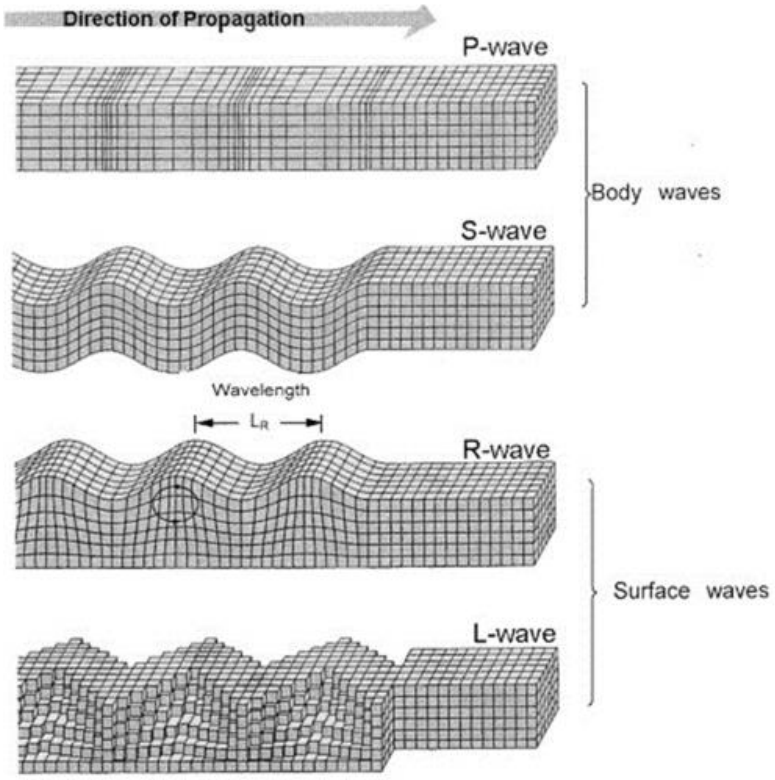

Figure 2.9 Graphical representation of seismic waves (Athanasopoulos et al., 2000)

According to the geodynamics of wave propagation in a homogeneous and isotropic medium, Rayleigh waves can be considered as combinations of the shear wave (V_s) and longitudinal wave (V_P) velocities at the surface of the half-space. The speed of the shear (V_s) and compressional (V_P) waves propagation can be calculated as (Kausel, 2006):

$$V_s = \sqrt{\frac{E}{2\rho(1+\upsilon)}} \tag{2.6}$$

$$V_P = \sqrt{\frac{E(1-\nu)}{2\rho(1+\upsilon)(1-2\nu)}} \tag{2.7}$$

where, ρ and ν are the density and Poisson's ratio, respectively.

Rayleigh waves travelling on homogeneous half-space are non-dispersive, which means the speed of propagation is independent of the vibration frequency, and the characteristics equation for wave propagation satisfying the dynamic equilibrium of propagating waves can be given as (Rahman and Barber, 1995; Richart et al., 1970):

$$K^4 - 8K^4 + \left(24 - 8\frac{1-2\nu}{1-\upsilon}\right)K^4 - \frac{8}{1-\upsilon} \tag{2.8}$$

where $K = V_R/V_s$

Several authors have recommended analytical expressions to determine the ratio K as a function of Poisson's ratio (Bergmann, 1948; Briggs et al., 2010; Malischewsky, 2005; Rahman and Barber, 1995; Rahman and Michelitsch, 2006), as shown in Figure 2.10. For the practical range of Poisson's ratio (0 to 0.5) and the purpose of railway track vibration analysis on homogeneous halfspace, Equation (2.9) shows a reasonable prediction of

Rayleigh wave speed. The ratio of Rayleigh to S-wave velocity can be approximated by (Bergmann, 1938):

$$K = \frac{0.847 + 1.117\upsilon}{1 + \upsilon} \quad 2.9$$

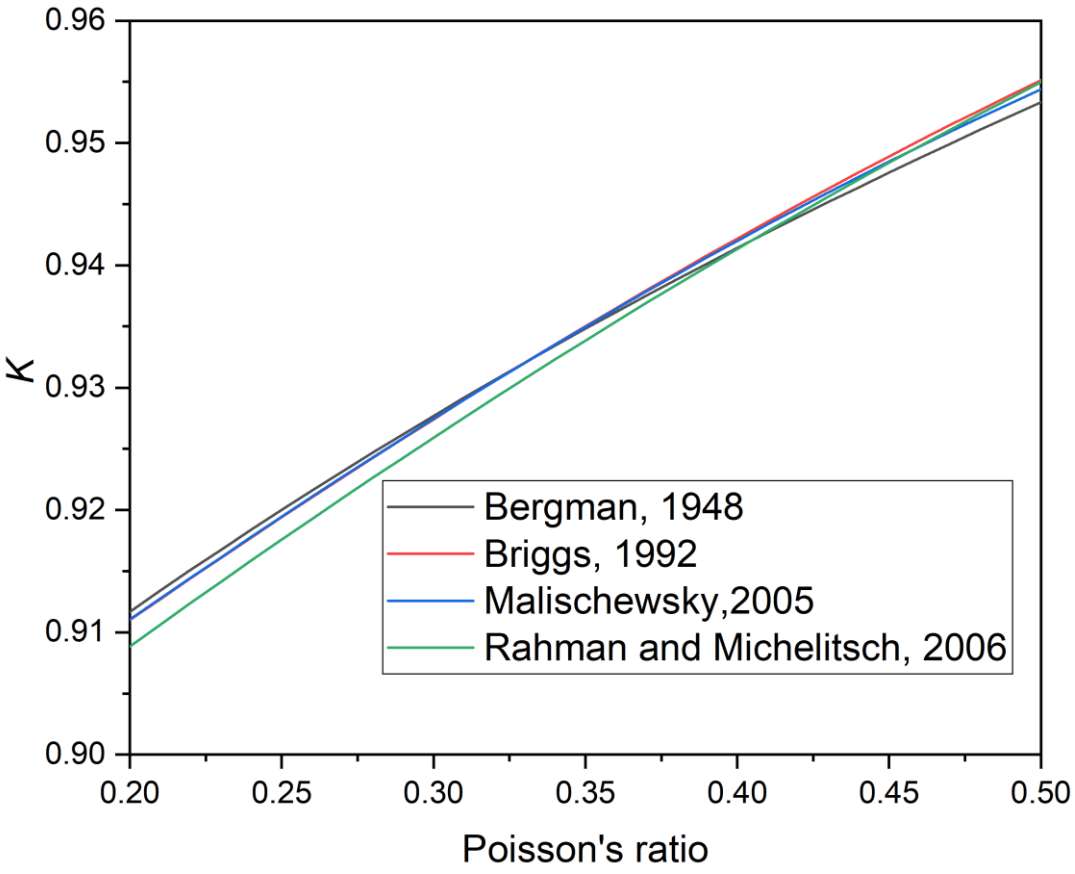

Figure 2.10 Comparison between Rayleigh wave speed approximation (modified after Connolly et al. (2013))

Rayleigh waves in a homogenous and isotropic medium are frequency-independent, as shown in Equation 2.9. However, most soil deposits are layered, and stiffness and density tend to change with depth. In such cases, the Rayleigh waves are dispersive, showing multiple Rayleigh modes (Kaynia et al., 2000; Tokimatsu et al., 1992). Stiff embankments placed on soft soil formation often make the dispersion more complicated. In this

scenario, the phase velocity of Rayleigh wave velocity depends on the train loading characteristics, such as speed and axle load configurations, in addition to elastic parameters of the layered ground (Connolly and Costa, 2020; Kausel et al., 2020).

2.4.2 Geodynamic aspects of moving load

2.4.2.1 Effect of speed on track displacements

The dynamic loading on the railway track depends on the acceleration of train components, irregularities at the wheel-rail interface, and track irregularities. However, field measurements on transient displacements and velocities show that the train speed significantly influences dynamic amplifications (Hunt, 1994; Kaynia et al., 2000; Woldright and New, 1999). At Ledsgard's benchmark study, in Sweden, significant rolling vibration of the track, embankment, and trackside was observed when the train speed was approaching 200km/h (Madshus and Kaynia, 2001). Consequently, the train speed was reduced to 60km/h shortly after the X-2000 high-speed train started operation due to the immediate threat of derailment. After several test runs at speed over various speed ranges, the peak-to-peak vertical track displacement exhibited significant amplification as the train speed increased, as depicted in Figure 2.11. The soil profile at the track site shows a soft organic clay layer at a shallow depth, with a Rayleigh wave speed range of 35-40m/s. In this case, the drastic amplification is attributed to the stress field involving the propagation of Rayleigh waves along the soft surficial layers.

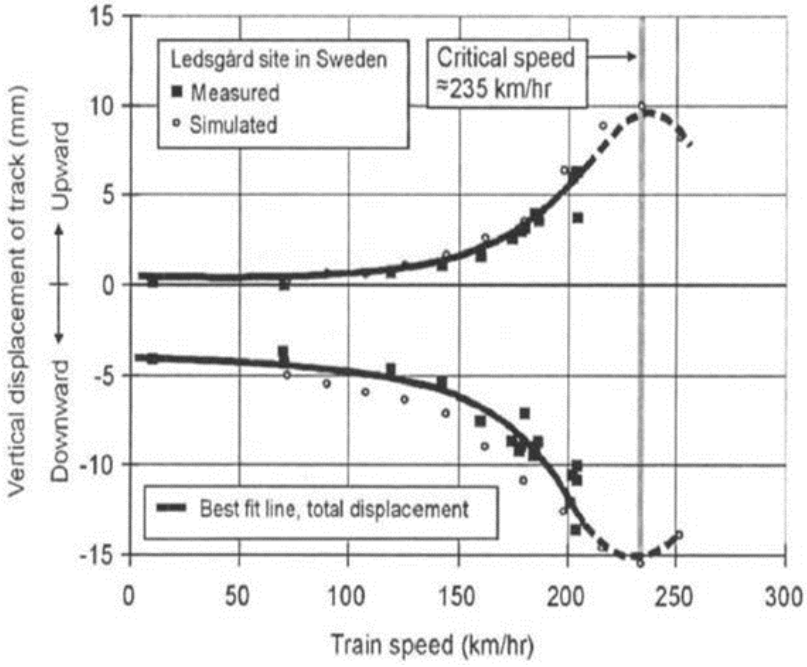

Figure 2.11 Variation of vertical displacement of rail track with speed of the train (Madshus and Kaynia, 2001)

Another notable field measurement showing high amplification was reported at railway tracks in Stilton Fen (UK) and Amsterdam-Utrech line in the Netherlands (Woldright and New, 1999). In the UK, the measured displacement showed drastic amplification of about 2.5 when the speed reached 180km/h, which was attributed to the very soft silty clay layer beneath the track embankment. In the Netherlands, the soft clay and peat at the shallow depth of 6m resulted in significant amplification of track displacement. Figure 2.12 presents the relationship between dynamic amplification and Rayleigh wave speed based on field measurement data from European sites. The normalized train speed shown on the horizontal axis is the train speed divided by the Rayleigh wave velocity the soil. The cubic polynomial function can approximate the generalised relationship, and it shows significant vibration when the train speed increases beyond 50% of Rayleigh wave velocity.

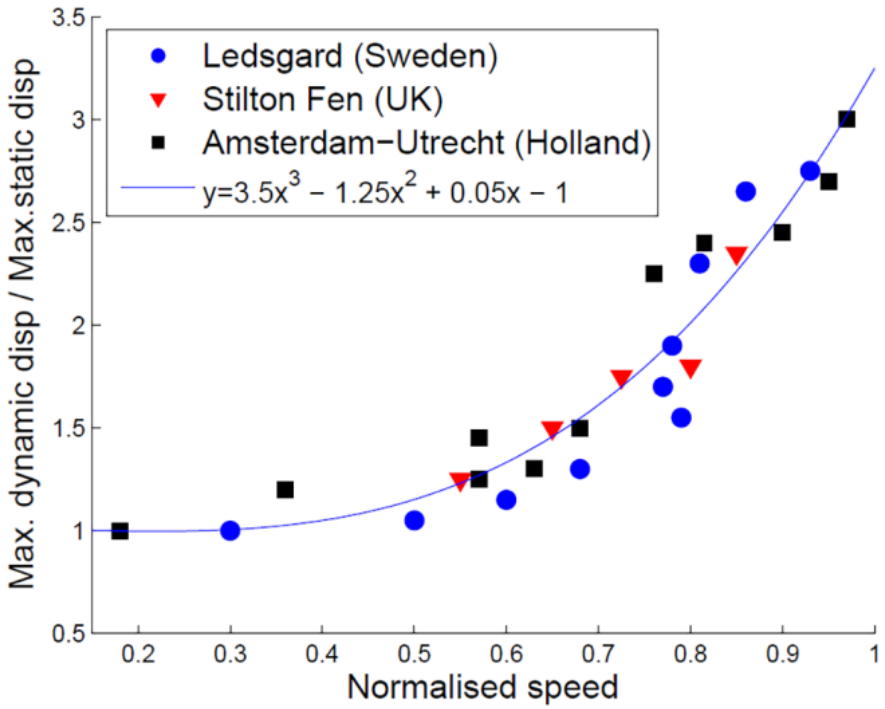

Figure 2.12 Comparison of track displacement amplification (Connolly, 2013)

When the speed of a load passes the natural wave speed of the medium through which the waves is traversing, three distinct velocity regimens are observed (Frýba, 2013; Sheng et al., 2004):

- Subcritical speed: when the load speed is below the Rayleigh wave velocity of the ground.
- Critical speed: when the load speed is equal to the Rayleigh wave speed the half-space.
- Super-critical speed regime: when load travels past the Rayleigh wave speed the ground.

Numerical and analytical studies considering moving trains have found significant track disturbance or resonance when the train speed exceeds the threshold of Rayleigh wave speed (Andersen, 2002; Krylov and Ferguson, 1994), which is accompanied by the

development of Ground Mach (Woodward et al., 2013). A moving load generates waves at each instant, and these waves propagate as a spherical wavefront in the half-space, as shown in Figure 2.13. When the speed of the moving load is less than Rayleigh wave velocity, the wavefront of all waves appears in eccentric cycles. However, as the speed approaches and passes the threshold of R-wave velocity, the Mach cone forms, as shown with the displacement contour in Figure 2.13 (b). The cone tip angle (α_M) can be estimated by (Connolly and Costa, 2020):

$$\alpha_M = \sin^{-1}\frac{V_R}{V} \qquad 2.10$$

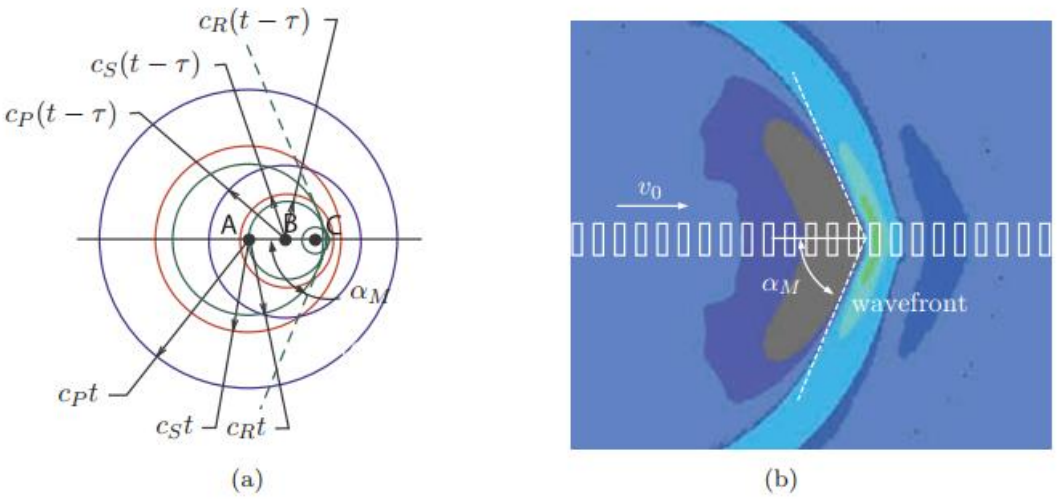

Figure 2.13 (a) Theoretical wavefront for a moving load passing Rayleigh wave speed (b) development of Mach cone (modified after Kouroussis et al. (2014))

2.4.2.2 Effect of speed on track stresses

The propagation of stress waves affects the dynamic stresses in railway tracks in addition to the amplification of transient displacements. Several field measurements on conventional railway tracks show that vertical stress in trackbed and subgrade increases

with train speed (Bian et al., 2014; Lamas-Lopez et al., 2016). Similarly, Nimbalkar and Indraratna (2016) conducted field measurements at Singleton, Australia, and observed amplification of vertical stresses within the speed range of 35 – 85km/, as shown in Figure 2.14.

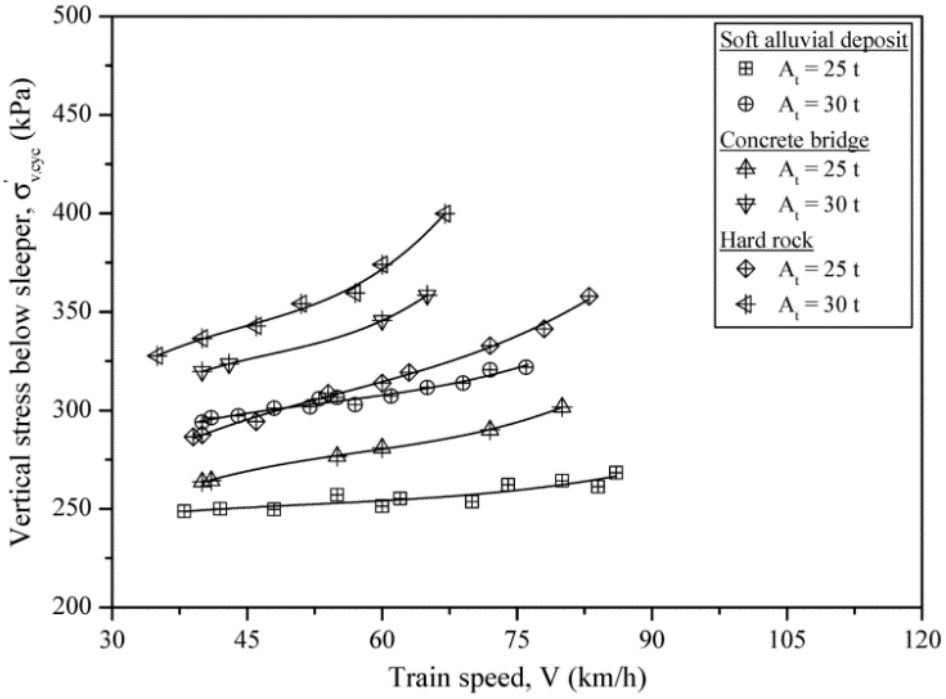

Figure 2.14 Measured dynamic stress at Singleton field trial (Nimbalkar and Indraratna, 2016)

Several researchers have concluded that vertical stresses are amplified when train speed is increased (Dong et al., 2019; Powrie et al., 2007; Sayeed and Shahin, 2016; Tang et al., 2019; Tang et al., 2019; Varandas et al., 2016; Yang et al., 2019). For instance,Yang et al. (2009) employed 2D FE analysis to predict subgrade stresses as the train speed approaches the critical speed. Their results show that the vertical and shear stresses at the critical speed are about 20% and 80% higher than the statically calculated values, respectively.

Recently, Yang et al. (2019) studied track stresses at elevated speeds, as shown in Figure 2.15, where σ_{xx} , σ_{yy}, σ_{zz} and τ_{yz} are the lateral, vertical, longitudinal and shear stresses, respectively. Consistent with the reported field measurements, the vertical stress increases with train speed. However, the shear, lateral and longitudinal stresses exhibit significant amplification as compared to the vertical normal stresses.

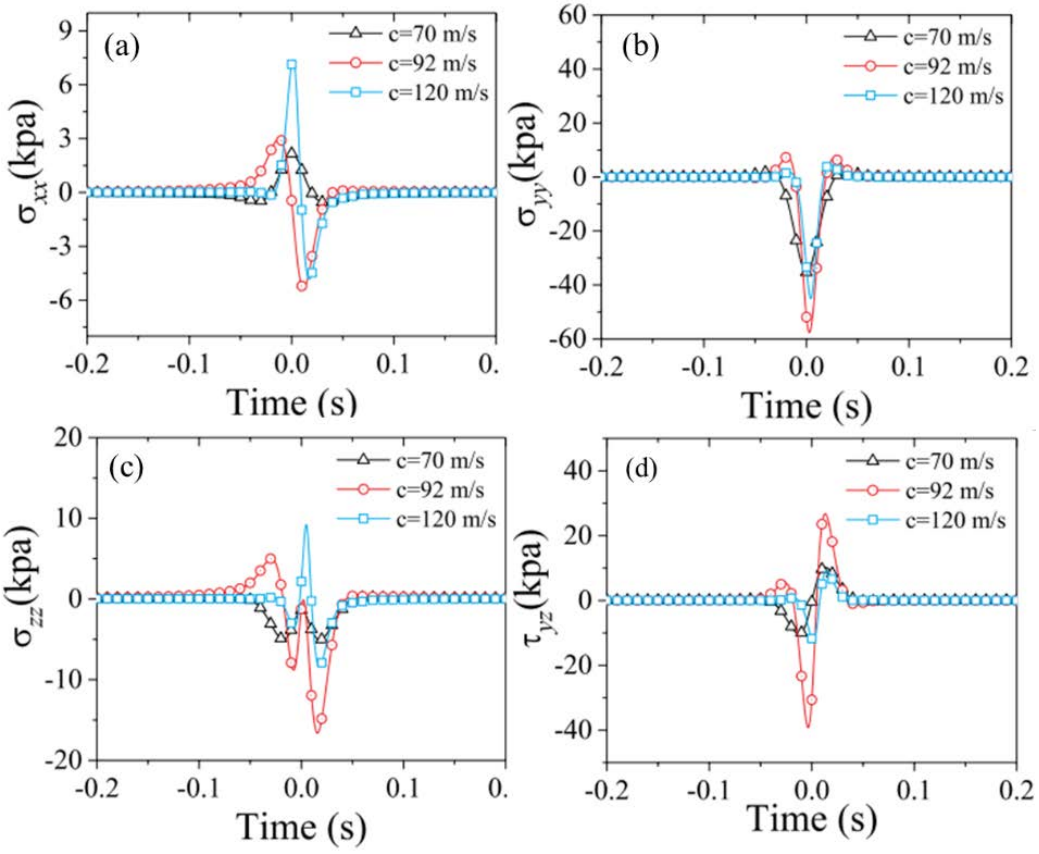

Figure 2.15 Effect of train speed on track stress based on 2.5D FE modelling (Yang et al., 2019)

It can also be noted from Figure 2.15 that the maximum shear stress is observed before the load. In contrast, the maximum lateral and longitudinal stress consistently trails behind the load at high speed. Hence, increasing train speed influences the dynamic stress path and the magnitude of stresses. Similarly, Dong et al. (2019) observed significant amplification of deviator stress in track subgrade using 2.5D semi-analytical models, as

shown in Figure 2.16. The result shows that the stress path is influenced by subgrade non-linearity and train speed, while high-speed response exhibits turbulent stress.

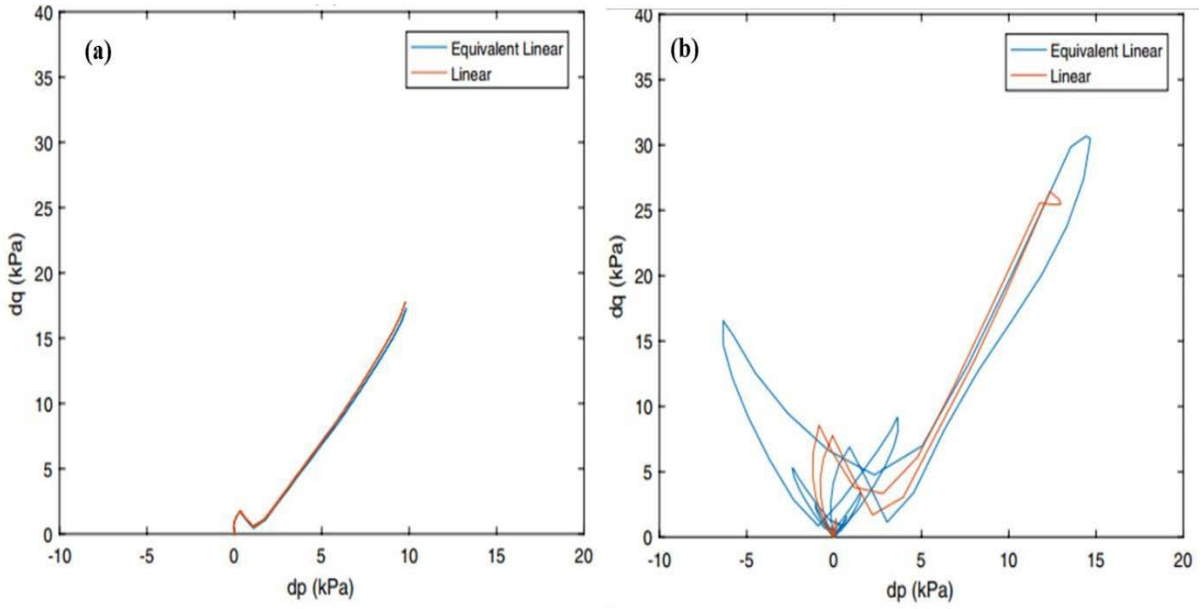

Figure 2.16 The stress path followed in followed by an element in the subgrade (a) low speed at 10m/s (b) critical speed at 90m/s (adopted from Dong et al. (2019))

2.4.2.3 Principal stress rotation

An additional geodynamic aspect associated with a moving train is the rotation of the principal stress axis. The stress state in an element in the track substructure continually changes as the traffic load is approaching and receding away, as shown in Figure 2.17 (Brown, 1996).

Figure 2.17(c) illustrates that the vertical stress increases when the load moves towards the soil element and peaks when the load is precisely above it. The vertical stress monotonically decreases to zero as the load departs. In contrast, shear stress increases before vertical stress and reduces to zero when the wheel load arrives above the element. As the load recedes, the shear stress peaks in the opposite direction before reducing back

to zero. Hence, the shear and vertical stress increments are out of phase resulting in a "cardioid" shaped stress path (Brown, 1996; Powrie et al., 2019).

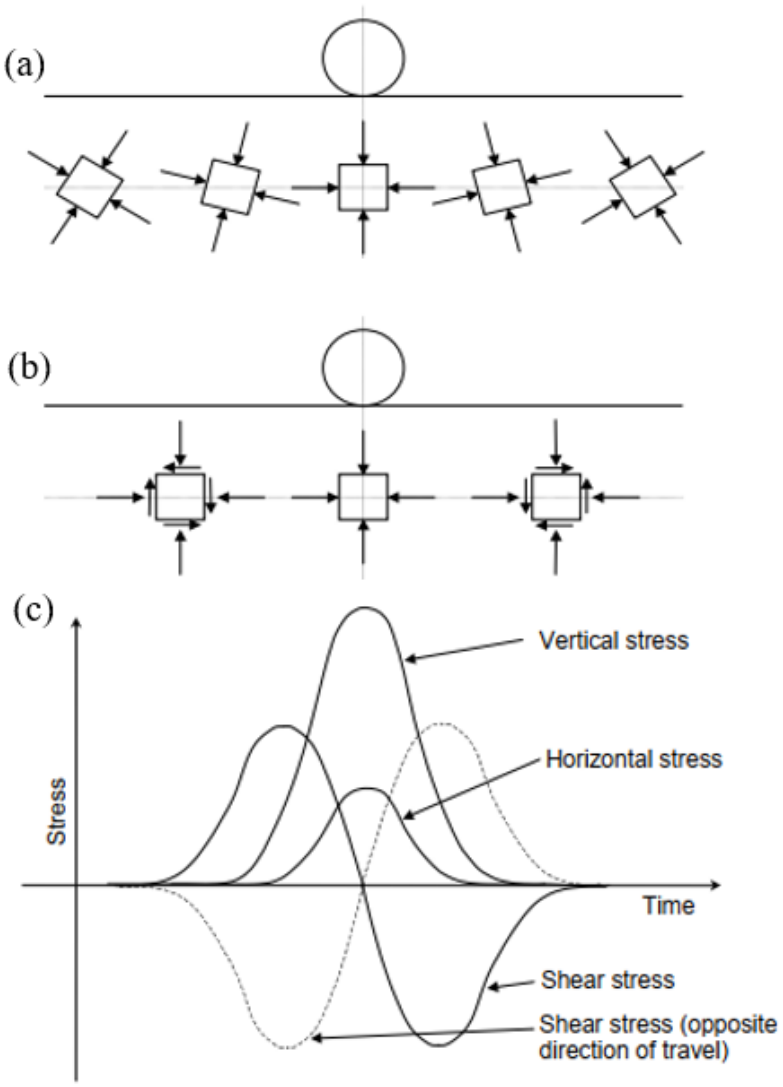

Figure 2.17 (a) PSR under moving load (b) stress condition under static load (c) stress condition under single moving load (modified after Brown (1996))

In literature, the "cardioid" stress path generated by moving loads is implemented in the laboratory using Hollow Cylindrical Apparatus (HCA) (Cai et al., 2018; Gräbe and Clayton, 2009; Ishihara and Towhata, 1983; Tong et al., 2010). It is reported that the rotational stress path accelerates the rate of plastic strain accumulation resulting in higher permanent deformation of soft clays (Gräbe and Clayton, 2009; Xiao et al., 2014) and

sands (Cai et al., 2018; Tong et al., 2010), as shown in Figure 2.18. A recent study by Malisetty et al. (2020), employing a multilaminate constitutive model, showed that the magnitude of ballast breakage and the associated axial and dilatant strains increase with PSR. Similarly, Bian et al. (2020) compared ballast response under a stationary cyclic load and moving train load using DEM. It was found that track degradation and settlement increased when PSR was considered, as shown in Figure 2.19.

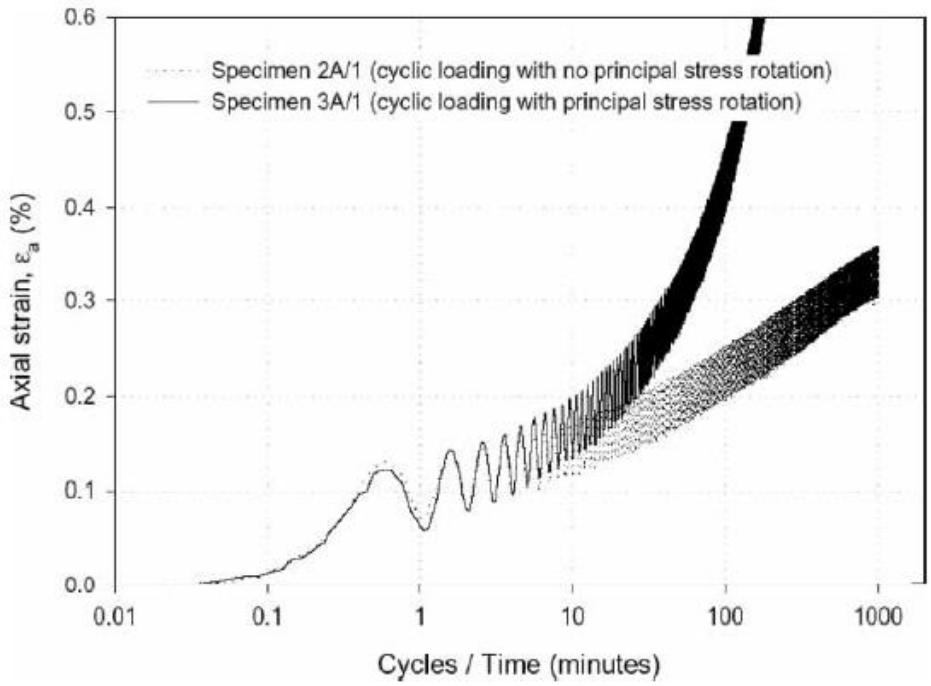

Figure 2.18 Effect of principal stress axis rotation soft subgrade (Gräbe and Clayton, 2009; Grabe et al., 2005)

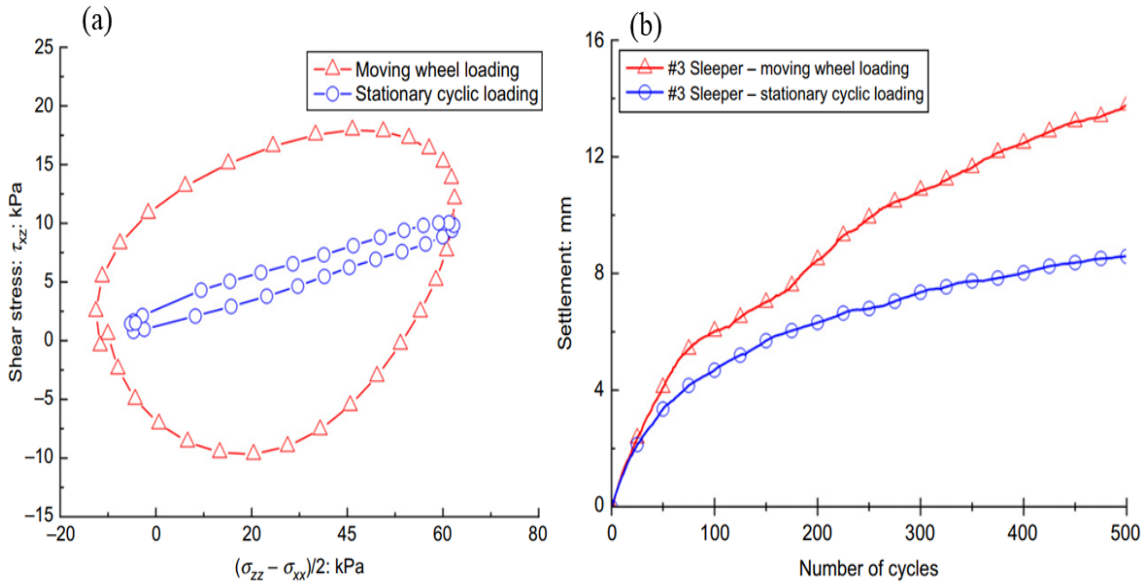

Figure 2.19 Comparison of stationary cyclic loading and moving load response (a) stress path (b) settlement (modified after Bian et al. (2020))

The accuracy of stress-deformation prediction of PSR models is influenced by the stress path considered and the spatial orientation of soil elements with respect to the moving load. Hence, the stress path induced by the moving train on the track substructure has to be quantified accurately. To this end, Powrie et al. (2007) studied the stress change in track substructure and associated angle of rotation using a 2D FE model under static load. It was reported that the angle of rotation is affected by the initial stress and depth in the track substructure. The static FE analysis results show that principal stress rotation is significant within the depth of 0.3 – 1.3m below the sleeper base (Powrie et al., 2019). However, previous studies show that surface wave propagation associated with elevated train speed could result in unequal amplification of stresses in the three-dimensional stress field, and they predominantly influence the surficial layer of the track substructure. Therefore, the "cardioid" stress path may not be adequate in capturing the stress field at medium to high speed. Recent 2D analytical (Malisetty, 2019) and FE-based (Varandas

et al., 2016; Xue, 2016) studies considering moving loads have shown the prevalence of stress rotations in shallow track layers such as ballast.

2.5 Ballast degradation

Ballast degradation is among the primary challenges in the railway track industry since it increases track settlement leading to an inflated track maintenance budget and reduced service life. During its operational period, the ballast layer is subjected to continual particle degradation caused by track loading and environmental influences such as weathering and maintenance tamping operations. The granular particles may break, rotate and slide, with crushed fragments occupying the void space between the ballast aggregates. During the passage of trains, the track buckles up just before the load reaches the location, but they bounce down as soon as the wheels roll over, creating an impact load, which leads to ballast grinding, wearing, splitting, and breakage over time.

The broken and disintegrated ballast particles are the primary sources of fouling (up to 76%), as per Selig and Waters (1994). Excessive accumulation of fine materials results in clogging the voids in the ballast matrix, reducing track drainage (Chrismer, 1994). Furthermore, the higher percentage of fine particles within the granular matrix also affects the mechanical response of the ballast layer, such as the shear strength and axial and volumetric strain (Budiono et al., 2004; Sussmann et al., 2012).

2.5.1 Factors affecting the breakage of particles

Various factors that affect the degradation of the ballast layer are summarised in Table 2.7. Australian ballast contains angular particles made from quarried basalt and is characterized by high crushing strength, compressive strength, and weathering resistance

(Indraratna et al., 2011). It is noteworthy that large angular particles of the ballast layer are more prone to disintegration under high confining stress than smaller aggregates (Lee and Farhoomand, 1967). Synthetic inclusions such as geogrids influence the particle breakage by providing additional track confinement, whereas rubber inclusions reduce the energy absorption of the ballast aggregates (Arachchige et al., 2021; Hussaini et al., 2015).

2.5.2 Methods for quantifying ballast breakage

Various studies have proposed simplified methods to quantify aggregate breakage considering the evolution of the particle size distribution (PSD) curve before and after load application. Marsal (1967) introduced the breakage model (B_g) to quantify the particle breakage of rockfill material under triaxial state. The Marsal's index (B_g) is expressed within a range of 0 and 100; where the lowest end corresponds to unavailability breakage while the upper limit represents the complete breakage of aggregates into small pieces. Lee and Farhoomand (1967) introduced an index to quantify the crushed particles in an earth dam, and they presented the index based on the change in particle size D_{15} from particle size distribution curve.

Alternatively, Hardin (1985) proposed the relative breakage index (B_r), which is the ratio of the breakage potential after loading to the initial breakage potential. In this approach, the breakage potential is calculated by considering the region that is bounded by the initial PSD curve and 0.074mm line, that represents the maximum possible breakage provided that the particles are crushed to the size of silt. Lade et al. (1996) presented the comparison between the breakage indices presented above, which is

shown in Figure 2.20.

Table 2.7 Factors affecting the ballast degradation (modified after Malisetty (2019))

Class	Factors	References
Nature of the parent material	Particle crushing strength, mineralogy, hardness, weathering resistance	Esmaeili et al. (2022); Lee and Farhoomand (1967); Qian et al. (2017)
Properties of individual particles	Size, shape, angularity, surface smoothness	Guo et al. (2018); Lee and Farhoomand (1967); Sun et al. (2017)
Parameters of the granular assembly	Packing density or initial void ratio, particle sizedistribution	Indraratna et al. (2016); Nålsund (2010); Qian et al. (2014); Sun et al. (2017)
Loading characteristics	Type of loading (static or cyclic, triaxial compression or pure compression), confining stress,stress levels	Lackenby (2006); Lackenby et al. (2007); Sun et al. (2014); Zhang et al. (2019)
Presence of inclusions	Geogrids, shock mats, rubber granules, geocomposites	Arachchige et al. (2021); Indraratna et al. (2013); (Navaratnarajah and Indraratna, 2017)

The methods shown in Figure 2.20 are developed for fine granular materials and may be inadequate for railway ballast. Hence, Indraratna and Salim (2005) introduced a ballast breakage index (BBI) to estimate particle breakage in railway ballast, as shown in Figure 2.21. This approach is based on PSD and can be calculated using Equation 2.11, as the ratio of the area bounded by the initial and final PSD to the area between the PSD curve and the boundary of maximum breakage.

$$BBI = \frac{A}{A + B} \tag{2.11}$$

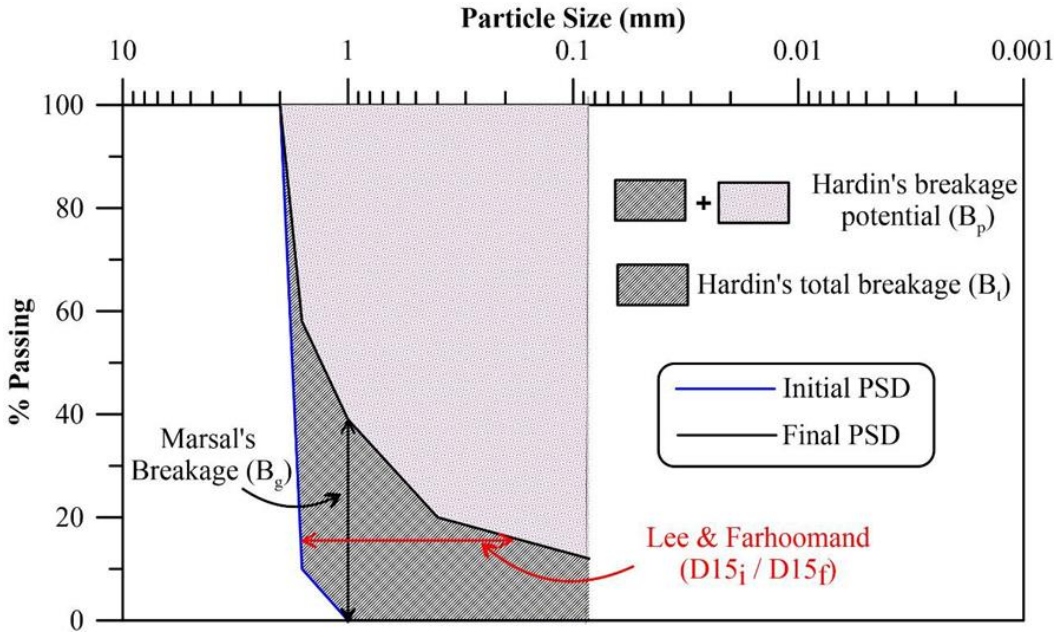

Figure 2.20 Graphical representation of various breakage models (modified after Lade et al. (1996))

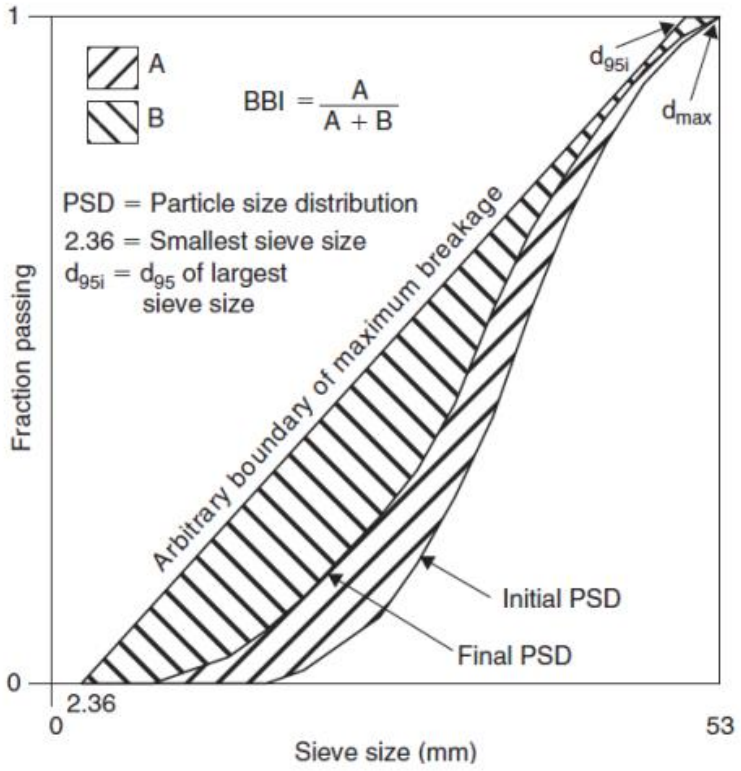

Figure 2.21 Ballast breakage index (BBI) (Lackenby et al., 2007)

2.6 Ballast response under monotonic and cyclic loading

The stress-deformation response of railway ballast are governed by its loading conditions, which are the magnitude of deviator stress, confining pressure, past stress history, and stress path of the applied load, among others (Indraratna and Salim, 2005; Malisetty, 2019; Sun, 2015). The experimental response of coarse granular material, including stress-strain behavior, volumetric change, and friction angle, under a range of confining and deviator stress are discussed in the upcoming sections.

2.6.1 Stress-strain response of ballast under monotonic loading

Numerous experimental studies of granular materials subjected to triaxial loading have been conducted to capture the effect of confining pressure on the volumetric and stress-strain responses (Anderson and Fair, 2008; Indraratna et al., 1998; Indraratna et al., 2015; Sevi et al., 2009; Suiker, 2004). The salient observations from pertinent literature can be summarised as:

1. The maximum deviator stress increases with the applied confining stress due to the limited horizontal movement of aggregates, as shown in Figure 2.22. Hence, the bearing capacity of the granular assembly and the required deviator stress corresponding to a particular strain increase with the applied confining stress.
2. At low confining pressure (<60kPa), the volumetric strain is compressive at low strain, but the response becomes dilative with increasing strain. In contrast, the volumetric response becomes compressive with increased confining stress.
3. The friction angle reduces with an increase in confining stress. The relationship between the effective mean and deviator stress becomes non-linear at high confining pressure because of restricted dilation and particle crushing.

4. The initial stiffness of the ballast increases with increasing confining pressure.
5. The breakage and degradation of ballast increase with confining stress, and the critical state stress ratio decreases is inversely related to breakage index and confining stress.

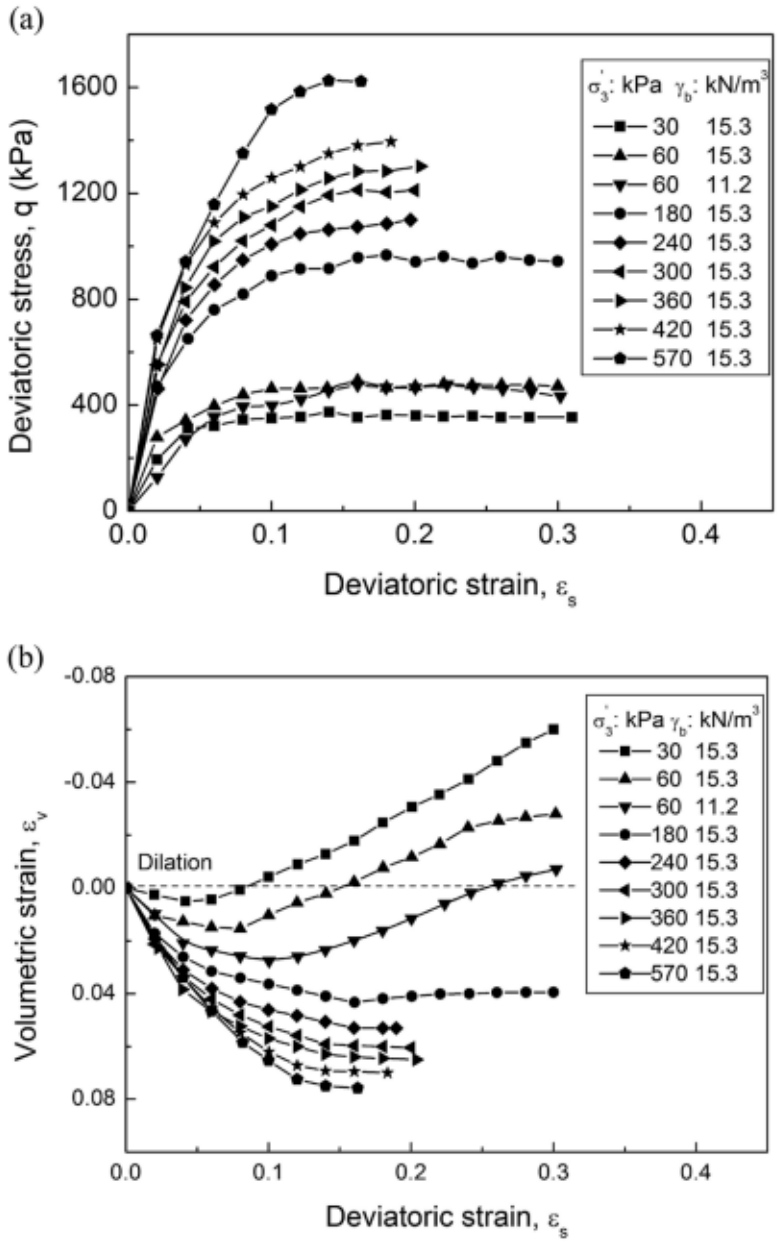

Figure 2.22 Typical stress-strain response of ballast during triaxial loading (a) variation of deviator stress (b) variation of volumetric strain at various confining stress (Indraratna et al., 2015)

2.6.2 The behaviour of ballast under cyclic loading

2.6.2.1 Confining pressure

Indraratna et al. (2005) and Lackenby et al. (2007) studied the influence of confining and deviator stress on particle breakage mechanisms. They identified three distinct zones depending on the magnitude of the applied confining pressure under cyclic triaxial loading, as given in Figure 2.23(b).

1. Zone I*:* The samples experienced overall volumetric dilation due to the rapid axial and expansive radial strains at low confining stress. The ballast in Zone-I demonstrated the highest degradation, with significant particle breakage occurring as the load was applied. Most of the degradation is attributed to the breakage of angular corners instead of splitting, caused by internal deformation responses such as rolling and sliding, which limits the formation of interparticle contact.
2. Zone-II: Lackenby et al. (2007) showed that a small increment in confining stress results in redistribution of contact stress amongst the ballast aggregates and, as a result, reduced breakage Thus, the tensile stress within the individual aggregates diminishes, reducing the axial strain and the risk of particle breakage.
3. Zone-III: here, the dilation and particle movement were limited due to considerable confinement. Compared to Zone-II, the movement of ballast particles is reduced, and the interparticle contact stress is significant in Zone-III. Although corner breakage is the predominant mode of breakage at high confining pressure, the level of particle splitting and fatigue are also significant (Indraratna et al., 2005).

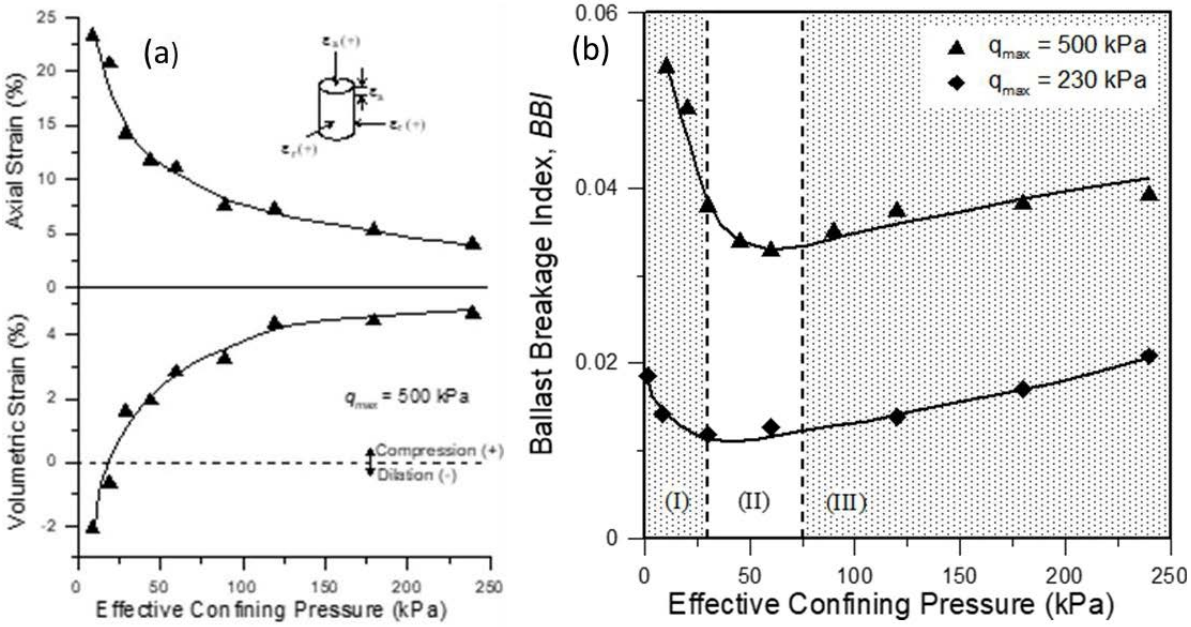

Figure 2.23 Effect of confining pressure (a) axial and volumetric strain (b) particle breakage and maximum deviator stress (Lackenby et al., 2007)

2.6.2.2 Resilient and permanent deformation of ballast

The deformation of ballast associated with densification, degradation, and distortion under repeated cyclic loading can be explained in two mechanisms: resilient deformation, which is recoverable, and permanent deformation, which accumulates with successive cycles, as shown in Figure 2.24. In track design and analysis, the stiffness of track geomaterials is generally expressed in terms of resilient modulus.

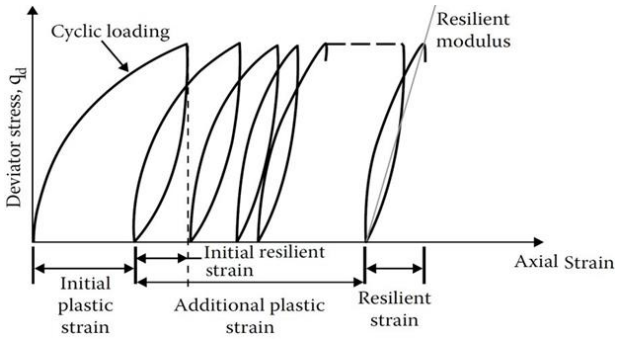

Figure 2.24 Resilient and permanent strain of railway ballast subjected to cyclic stress (Li et al., 2015)

The recoverable and permanent deformation of granular material depends on the magnitude of deviator cyclic stress, and it is described using the shakedown theory proposed by Werkmeister et al. (2001). Accordingly, the mechanical response of ballast can be divided into four zones based on stress level, the magnitude, and rate of deformation, as shown in Figure 2.25.

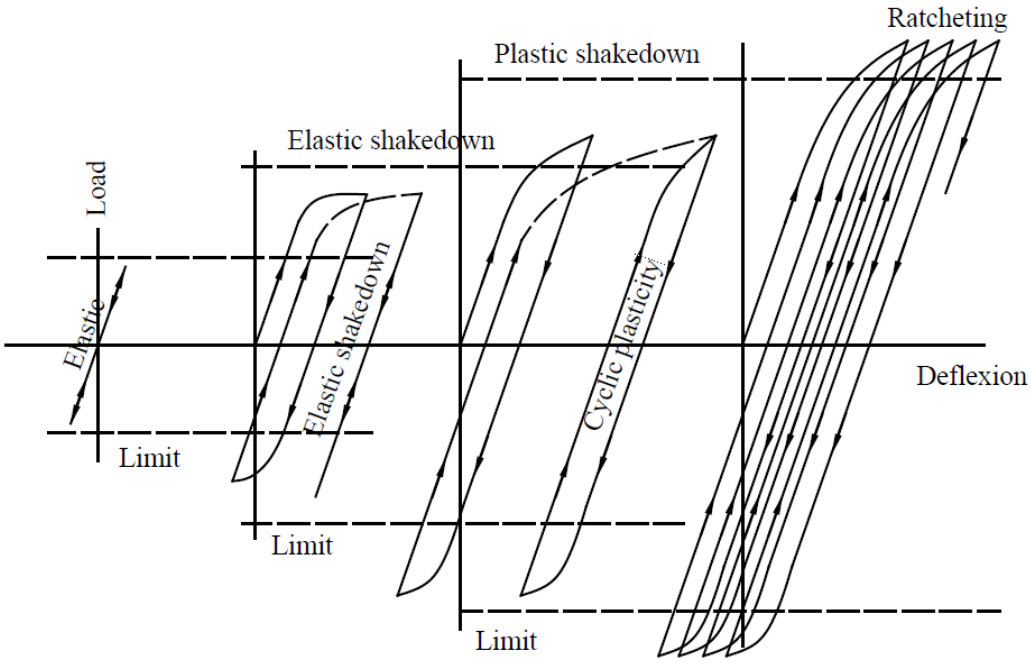

Figure 2.25 Principle of the shakedown response of granular material (Werkmeister et al., 2001)

(1) A Purely elastic zone where the cyclic stress level is very small as compared to the yield stress, and the material exhibit pure elastic response under successive loading cycles.

(2) An elastic shakedown zone in which the magnitude of cyclic stress is sufficient to produce plastic deformation during the first few cycles; the response eventually becomes elastic. The maximum stress at which the elastic response is achieved called the elastic shakedown limit.

(3) A Plastic shakedown zone, where the granular assembly approaches a densified state with successive loading cycles. In this region, the magnitude of stress is slightly below the failure stress of the material. The response of granular material reaching the plastic shakedown state is characterized by a rapid increment of permanent deformation in the first few cycles. However, as the number of cycles increases, the strain accumulation rate reduces, and the material becomes steady. After the strain attains a steady state, the plastic strain accumulation becomes insignificant, while the stress-strain behaviour under cyclic stress exhibits a hysteretic response.

(4) A Ratcheting zone, where the magnitude of cyclic stress amplitude in the granular assembly reaches its yield limit. The permanent strain accumulates at a higher rate leading to failure or collapse of the granular assembly.

2.6.2.3 Resilient modulus

The resilient modulus (M_R) of railroad ballast under repeated cyclic loading can be defined as the ratio of the cyclic deviator stress (σ'_{cyc}) to the axial recoverable (elastic) strain, as given in Equation 2.12 (Lekarp et al., 2000). Figure 2.26 shows how the resilient modulus is obtained from cyclic triaxial test results.

$$M_R = \frac{\sigma'_{cyc}}{\varepsilon_1^e} \qquad 2.12$$

The resilient modulus of railway ballast increases within the first few cycles and then stabilises when the elastic shakedown state is reached (Grabe, 2003; Lekarp et al., 2000).

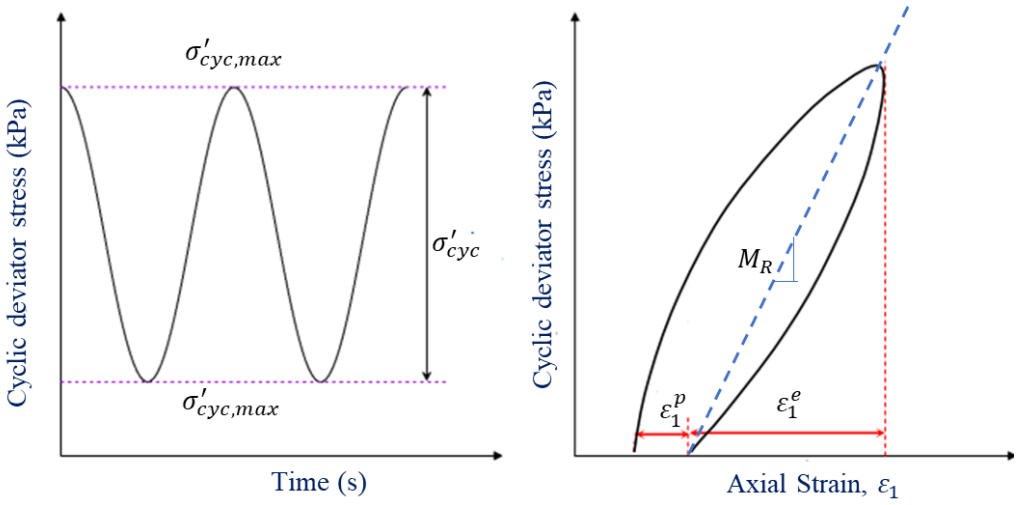

Figure 2.26 Determination of resilient modulus (modified after Jayasuriya et al. (2019))

Past studies show that resilient modulus depends on confining stress, stress history, the number of load cycles, duration, sequence and frequency of the applied load, among others (Brecciaroli and Kolisoja, 2006; Lackenby et al., 2007; Lekarp et al., 2000). Several researchers have recommended empirical modes to related resilient modulus (M_R) with the level of deviator and the magnitude of confining stress using power models (Lackenby et al., 2007; Lekarp et al., 2000; Uzan et al., 1992). For a latite basalt, the commonly used ballast material in Australia, the resilient modulus depends on ballast breakage, effective confining stress, and maximum deviator stress applied during repeated cyclic loading (Indraratna et al., 2005; Indraratna et al., 2009). Large-scale cyclic triaxial test conducted by Sun et al. (2016) shows that ballast breakage and associated densification leads to increased resilient modulus with the number of cycles. Accordingly, a mathematical model that relates the contribution of frequency (f) and bulk stress ($\theta = \sigma_1 + \sigma_2 + \sigma_3$) with M_R was proposed (Figure 2.27).

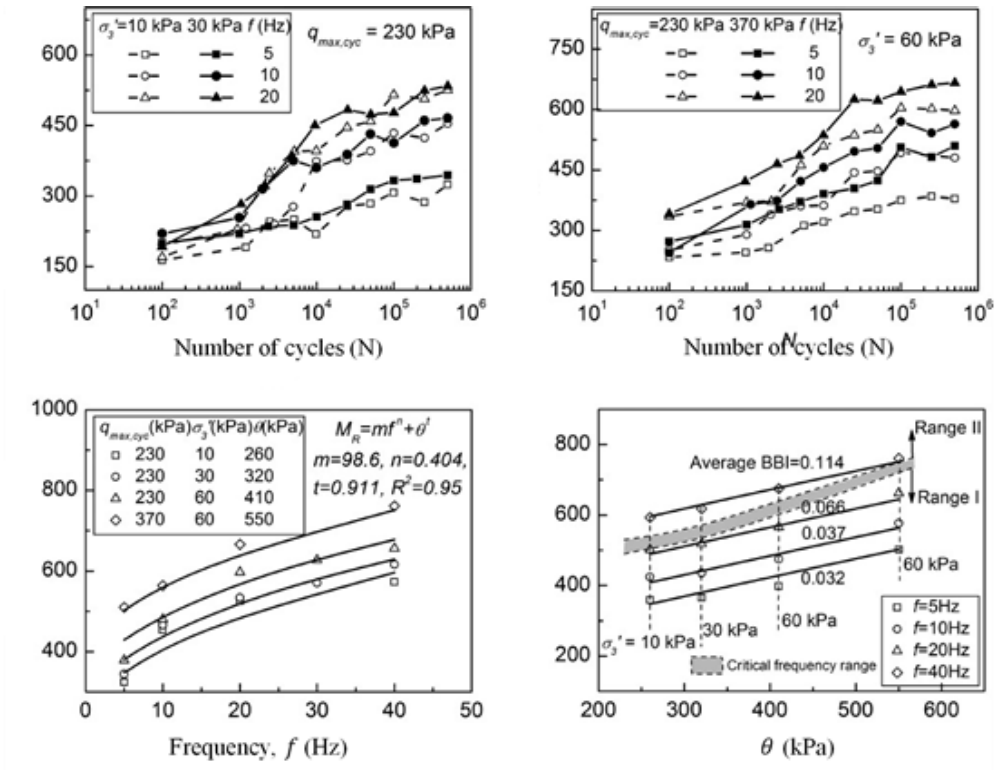

Figure 2.27 Effect of the number of loading cycles (N), frequency (f) and bulk stress (θ) on M_R (Sun et al., 2019; Sun et al., 2016)

2.6.2.4 Effect of frequency

Several field and numerical studies have shown that increasing train speed increases transient displacement, stress amplification, plastic settlement and degradation of granular materials (Indraratna et al., 2010; Nimbalkar and Indraratna, 2016; Yang et al., 2009). Railway tracks are subjected to several loading frequencies that depend on speed, axle loads configuration and track irregularities (Knothe and Grassie, 1993; Kouroussis et al., 2014). Furthermore, the frequency of loading in the track substructure is affected by the depth and stiffness of track layers, and it reduces with an increase in depth (Milne et al., 2017; Powrie et al., 2019). For the ballast layer, the speed of the train (V) is directly related to cyclic loading frequency (f), as $f = V/\lambda$, where λ represents a characteristics length corresponding to the smallest distance between train wheels. Sun et al. (2016)

observed through large scale triaxial test that load frequency has a profound effect on ballast deformation and breakage.

Figure 2.28 (a) and (b) illustrate the effect of the number of cycles and cyclic frequency on axial strain (ε_a) at for maximum cyclic deviator stress ($q_{max,cyc}$) of 230kPa and 370kPa representing conventional and heavy-haul train loading, respectively. The axial strain rapidly increases for initial cycles and reaches a stable state at a larger number of cycles, with an exception for 40Hz with $q_{max,cyc}$ of 460kPa. The result illustrated the existence of four zones of axial strains (Sun et al., 2019; Sun et al., 2016):

(i) Elastic shakedown regimen: where; a zone the ballast exhibits pure elastic response without accumulation of plastic strain,
(ii) Plastic shakedown and ratcheting: where the axial strain is initially steady-state, but as the number of cycles increases, the plastic strain accumulation that leads to ballast failure due to ratcheting.
(iii) Ratcheting region, where a continuous increase in plastic strain is observed with an increasing number of loading cycles,
(iv) Plastic collapse zone exhibits rapid accumulation of plastic strain leading to the collapse of the granular assembly in a relatively few loading cycles

Moreover, three distinct frequency ranges are identified considering the confining stress and maximum deviator stress applied, as shown in Figure 2.28(c). The critical frequency ranges between 20 and 40Hz depending on the confining stress. In Range, I, which is a plastic shakedown regimen, the critical frequency increases with BBI, and the breakage mechanism is predominantly corner breakage and attrition of asperities. Ratcheting failure with significant particle breakage is observed in Range II with increased level

attrition induced by vibration of the granular matrix. The form of breakage in Range III corresponding to high frequency (f ≥ 60 Hz) exhibits particle splitting due to a reduced coordination number.

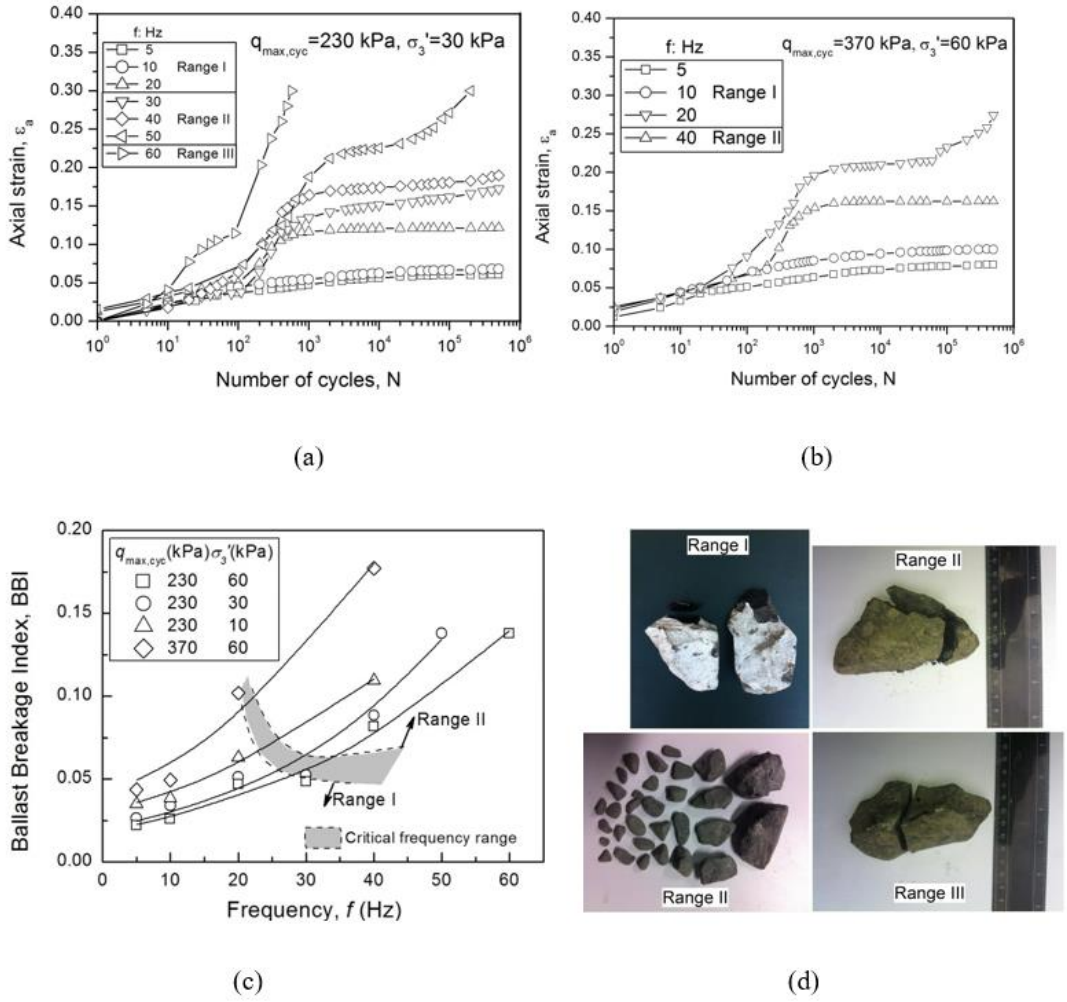

Figure 2.28 Evolution of axial strain ε_a with number of cycles (N) :(a) at $q_{max,cyc}$ = 230 kPa; (b) at $q_{max,cyc}$ = 370 kPa; (c) effect of frequency (f) on BBI; (d) illustrations of ballast breakage (Sun et al., 2016)

2.7 Influence of TDA on ballast response

2.7.1 General

Several studies have been conducted to explore the mechanical response of recycled rubber crumb mixed with ballast particles and recommend the optimal percentage of tire-

derived aggregate required to reduce ballast degradation while increasing damping and energy absorption. Sol-Sánchez et al. (2015) studied the behaviour of ballast-TDA mixes, at 5, 10, 20 and 30% by volume, under cyclic uniaxial compression and concluded that inclusion of TDA leads to a reduction in ballast stiffness and breakage as well as increased dissipation of energy. However, increased settlement is observed when the rubber quantity in the rubber-ballast matrix is more than 10%. Fathali et al. (2019) examined the mechanical response of TDA mixed with ballast aggregate and concluded that breakage and settlement of ballast are reduced by 47 and 6%, respectively. In addition to reducing particle breakage, rubber aggregate inclusions also reduced the degree of ballast abrasion, fragmentation and corner breakage (Arachchige et al., 2021; Fathali et al., 2017; Guo et al., 2019). Figure 2.29 shows the visual appearance of rubber granules, ballast and rubber-ballast mixture (RIBS) (Arachchige et al., 2021).

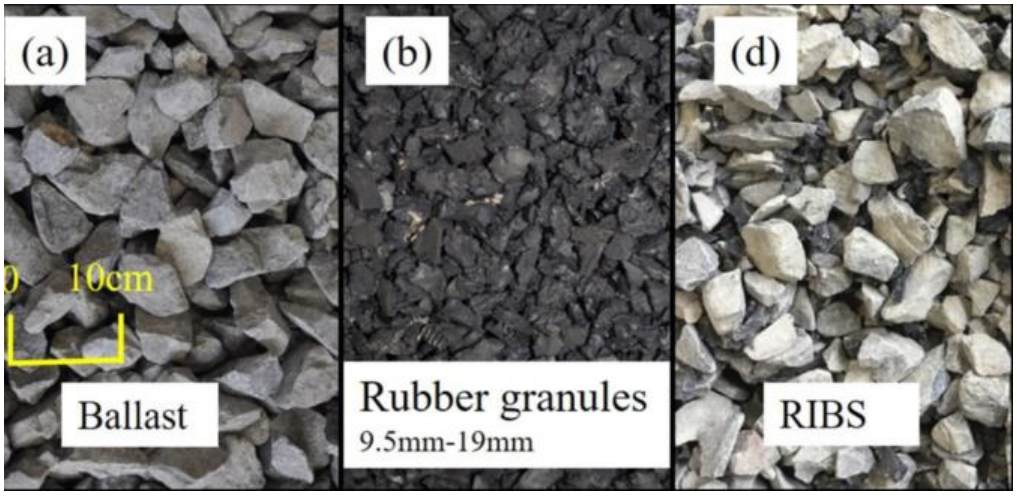

Figure 2.29 Visual appearance of (a) ballast ;(b) rubber granules; (c) RIBS (modified after Arachchige et al. (2021))

Studies conducted using direct shear tests under static and cyclic loading indicated that TDA increases the damping ratio and energy absorption, and decreases peak shear stress and dilation (Fathali et al., 2017; Gong et al., 2019; Song et al., 2019). In addition to the

reduction in an effective angle of internal friction and dilation, granulated rubber inclusion in the ballast layer resulted in a decreased rate of modulus degradation and increased ductility (Arachchige et al., 2021). Recently, Arachchige et al. (2022) studied the cyclic response of Rubber Intermixed Ballast System (RIBS) under cyclic loading using large-scale triaxial apparatus under varying confining stress. In line with previous studies, compared to conventional ballast stratum, RIBS reduces ballast breakage and volumetric strain (dilation) and increases energy dissipation and damping ratio. However, RIBS reduces ballast stiffness and resilient modulus, which in turn compromises its applicability as load bearing layer when a higher percentage of rubber (R_b>10%) is incorporated in the ballast matrix. The salient observation from pertinent literature on the application of tire-derived aggregate in the ballast layer are discussed in this section.

2.7.2 Stress-strain behavior

As discussed previously, the inclusion of rubber granules in the ballast matrix affects the shear strength, which is attributed to reduced interlocking amongst ballast particles and compressibility characteristics of rubber aggregates (Arachchige et al., 2021; Fathali et al., 2017; Song et al., 2019). Figure 2.30 shows a typical stress-strain curve retrieved from a large-scale triaxial test conducted for various percentages of rubber (R_b= 0%, 5%, 10%, 15%) in ballast aggregates and confining pressure (σ'_3) (Arachchige et al., 2021). The general trend peak deviator stress (q_{peak}), indicated by black dots on each curve, shows a reduction with an increase in R_b and increment with an increase in σ'_3. Compared to pure ballast, RIBS mixtures attain the peak stress at higher axial strain with an increase in rubber content, indicating the transformation of the rubber-ballast matrix from a brittle to a ductile state. Moreover, the sudden fluctuation is observed in deviator stress–axial

strain plots of low rubber content (R_b= 0% and 5%), which are attributed to the breakage of coarser ballast particles during triaxial shearing. In contrast, the stress-strain curves at higher rubber content representing a reduction of particle breakage due to increased interparticle contacts in the ballast-rubber matrix.

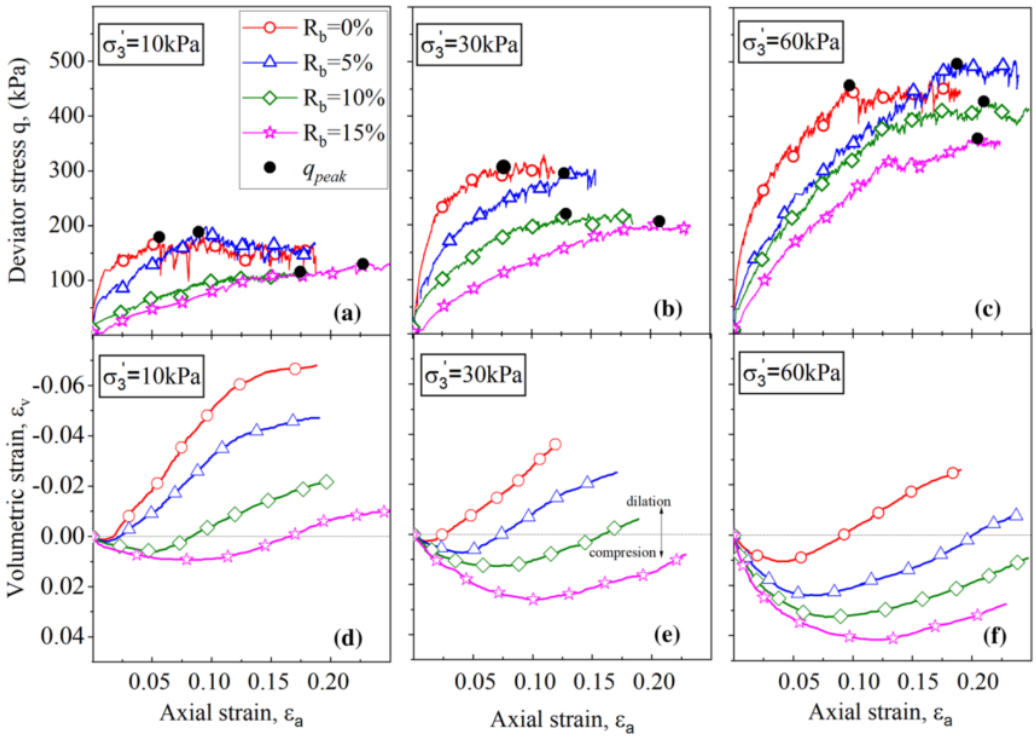

Figure 2.30 Influence of rubber on the stress-strain response at various confining stress (a-c) axial strain (d-f) volumetric strain (Arachchige et al., 2021)

The volumetric-axial strain, as shown in Figure 2.30(d-f), shows that the specimens with higher content of rubber (R_b> 5%) undergo initial compression followed by dilation at higher strains. Though reduced dilation reduces lateral track instability, the compressions observed at increased rubber content results in significant compression, which could lead to settlement in the ballast layer. Similar observations were made from laboratory tests conducted using direct shear box tests under various normal stresses and rubber content (R_b= 0%, 5%, 10%) (Gong et al., 2019; Song et al., 2019). Accordingly, the volumetric

response changes from dilation to compression with increased rubber content and normal stress.

2.7.3 Effect of rubber crumbs inclusions on ballast breakage

Breakage of ballast aggregates under repeated loading is one the primary factors that lead to track degradation, such as reduction in bearing capacity, increased settlement and fouling (Indraratna et al., 2011; Sussmann et al., 2012). The breakage of ballast aggregates mixed with TDA is quantified by the breakage indices such as the Ballast Breakage Index (BBI) and Marsal's breakage index (B_g) discussed in Section 2.5.2. BBI quantify the overall breakage of ballast-TDA mixture whereas Marsal's breakage (B_g) index can be utilised to identify the sizes of particles that are susceptible to breakage and subsequent improvement attained by incorporating recycled rubber aggregates (Arachchige et al., 2021; Fathali et al., 2017).

Arachchige et al. (2021) studied the influence of adding tire-derived aggregate with a size ranging from 9.5 to 19.5mm in the ballast layer under monotonic triaxial loading and observed that the addition of rubber crumbs reduces the degradation of ballast particles as shown in Figure 2.31. As compared to pure ballast, which exhibits considerable breakage (BBI > 0.15) for all confining pressure considered, the rubber ballast mixture exhibits negligible breakage (BBI <0.1) when the rubber percentage (R_b) exceeds 5%. Moreover, the change in B_g with the percentage of rubber shows more than 70% reduction in breakage of large particles (>38mm), for all rubber percentages considered. According to Arachchige et al. (2022), three distinct degradation zones are observed when rubber-intermixed-ballast systems under cyclic loading:

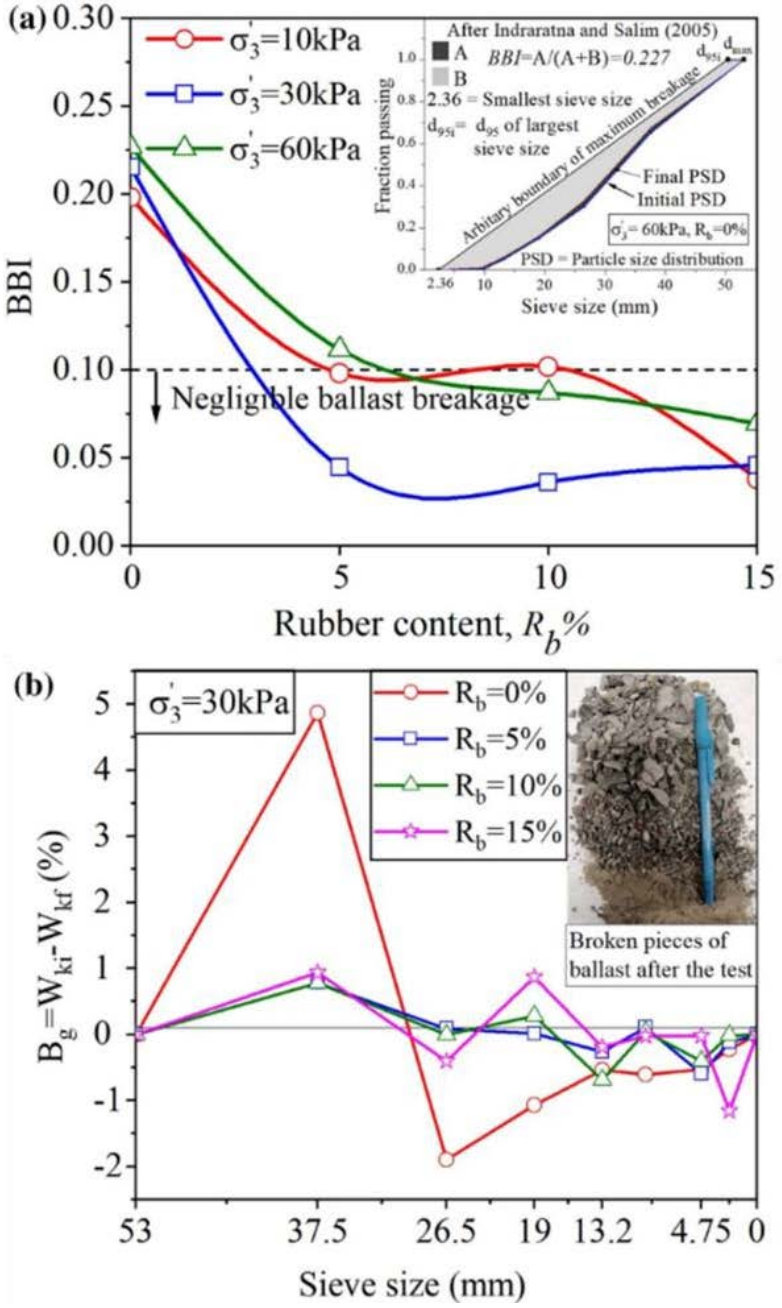

Figure 2.31 Influence of rubber content (R_b) on the (a) ballast breakage index (BBI) and Marsal's breakage index (B_g) (modified after Arachchige et al. (2021))

a) Zone-1 ($R_b \leq 5\%$), rubber granules primarily serve as void fillers; hence, they significantly reduce inter-particle abrasion and subsequent breakage.

b) Zone-2 ($5\% \leq R_b \leq 10\%$), where the particle breakage is less dependent on the amount of rubber mixed in with the ballast since the minimal amount of 5% had sufficiently filled the voids within the RIBS,

c) Zone-3 ($R_b \geq 15\%$), where the rubber granules substitute a significant amount of ballast particles, resulting in a lesser inter-particle contact force and hence reduced breakage.

In addition to the percentage of tired-derived aggregates incorporated in the ballast, the response of RIBS depends on the initial gradation of ballast aggregates and the size of rubber crumbs and subgrade conditions (Koohmishi and Azarhoosh, 2021; Zhang et al., 2022). Koohmishi and Azarhoosh (2021) conducted impact load testing on RIBS using a large-scale impact load test apparatus considering two distinct ballast gradations, AREMA No. 25 and AREMA No.3 pertinent to AREMA (2014) specifications, and crumb rubber sizes. AREMA No. 25 consists of a broad range of aggregates compared to the relatively uniform PSD of AREMA No. 3 aggregates, as shown in Figure 2.32(a).

Figure 2.32(b) & (c) show that breakage of aggregates comprising a uniform gradation (AREMA No.3) is reduced by incorporating coarser TDA. In contrast, finer-sized rubber crumbs are more effective for ballast with broader particle size ranges. Hence, the efficiency of crumb rubber in reducing particle breakage depends on the relative size of rubber granules and the volume of voids in the granular assembly. Large rubber crumbs can reduce the breakage of ballast aggregates by enhancing internal stress redistribution amongst the ballast aggregates. However, increasing the size of tire aggregates beyond 25mm led to reduced ballast shear strength and increased settlement (Guo et al., 2018). Furthermore, incorporating large percentages of smaller-sized crumb rubber reduces hydraulic conductivity, which can cause ballast fouling and track deterioration (Arachchige et al., 2021; Koohmishi and Azarhoosh, 2020).

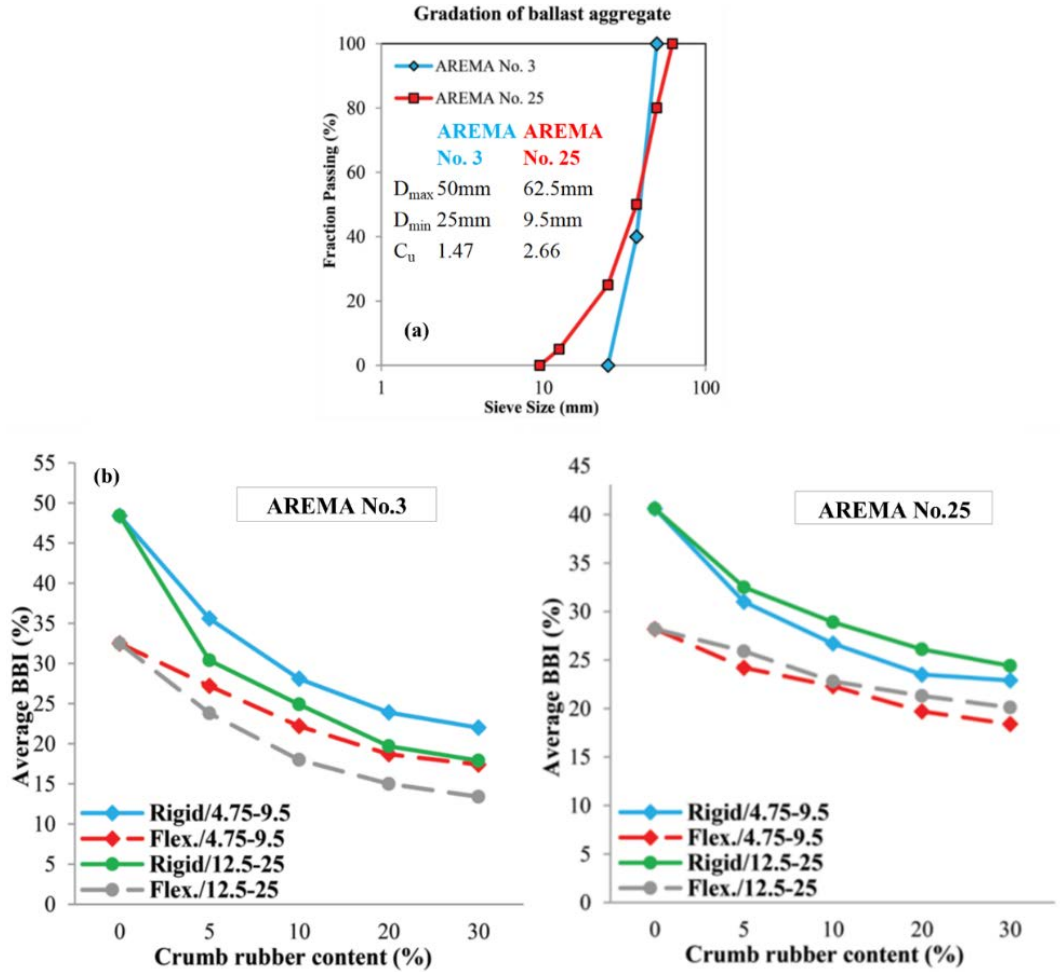

Figure 2.32 (a) Particle size distribution of ballast aggregate according to AREMA (2014)(b) effect of crumb rubber on particle breakage on AREMA No.3 graded ballast (c) effect of crumb rubber on particle breakage on AREMA No.25 graded ballast (modified after Koohmishi and Azarhoosh (2021))

The degradation of aggregates reduces with the crumb rubber percentage irrespective of the choice of ballast gradation and subgrade stiffness, which is attributed to the attenuation of dynamic loads by elastic elements and the associated lubrication attained by the CR inclusions in the granular matrix. The observed trend in Figure 2.32(b) and (c) reveals that the rate of decrement in ballast degradation is minimal for CR exceeding 10%, irrespective of the subgrade condition or choice of aggregate gradation. Higher particle breakage is observed when the ballast aggregates are placed on rigid subgrade for all CR percentages considered. Moreover, a comparison of the plots on rigid and flexible

subgrades reveals that the reduction in breakage achieved by incorporating CR in the ballast matrix is consistently higher when the underlying layer is rigid.

2.7.4 Stiffness and settlement of RIBS

Several laboratory studies reveal that the addition of TDA reduces ballast breakage but, it can compromise track performance parameters such as track stiffness, initial settlements and resilient modulus (Arachchige et al., 2022). Sol-Sánchez et al. (2015) compared ballast settlement at various by-volume percentages of crumb rubber ranging under cyclic loading and reported that RIBS with CR >10% demonstrates higher permanent settlement as compared to pure ballast and under ballast mats, as shown in Figure 2.33(a). Similarly, Fathali et al. (2017) observed that a lower amount of CR (i.e. 10% by weight) results in a reduction in magnitude and rate of permanent settlement compared to a specimen comprising only pure ballast. According to Koohmishi and Azarhoosh (2021), RIBS specimen with crumb rubber of 10% demonstrates the minimum axial strain under drop weight impact loading.

An optimal track vertical stiffness is essential to ensure vertical track stability hence an essential parameter in track design and maintenance planning (Tong et al., 2022). A very low vertical track stiffness results in higher deflection, which can cause an uneven operating surface for the train wheels and increased track deterioration. Esmaeili et al. (2016) evaluated the reduction in the stiffness of RIBS using the modal shaker test and observed the stiffness reduces with an increase in rubber content, which attributed to smaller Young's modulus and the higher Poisson's ratio of crumb rubbers. Sol-Sánchez et al. (2015) compared the vertical stiffness of RIBS with $R_b = 10\%$, which was found to be optimum in reducing breakage without inducing additional track settlement, with two

cases: pure ballast and under ballast mat, as shown in Figure 2.33(b). The result shows that using RIBS with 10% crumb rubber reduces stiffness by 23% compared to pure ballast. At optimum rubber content $R_b = 10\%$, RIBS can provide better vertical stiffness as compared to under ballast mats (Sol-Sánchez et al., 2015).

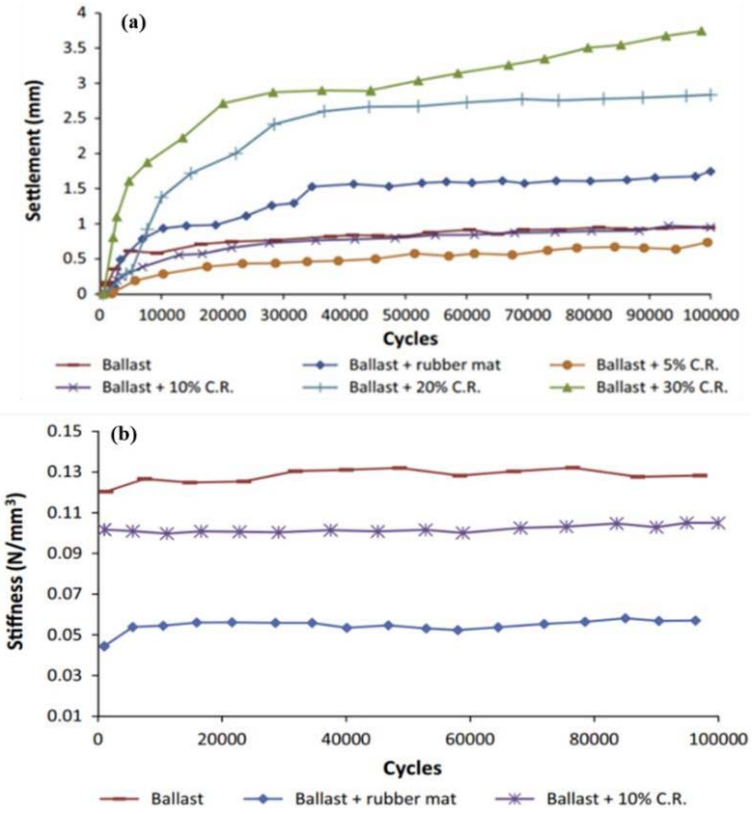

Figure 2.33 (a) Comparison of various percentage of crumb rubber with other reference systems (b) Comparison of vertical stiffness of RIBS with other elastic solutions (after Sol-Sánchez et al. (2015))

2.7.5 Shear strength of RIBS

The stability and performance of railway track is governed by the shear strength of the ballast layer (Indraratna et al., 2011). However, the shear strength of crumb rubber and ballast mixture decreases with increased rubber content (Fathali et al., 2017; Gong et al., 2019). Arachchige et al. (2021) conducted large-scale triaxial tests and observed that the friction angle (ϕ_p) at the peak stress ratio (η_{peak}) and effective friction angle (ϕ_{eff})

reduces with the rubber content irrespective of the confining stress, as shown in Figure 2.34. The peak stress ratio (η_{peak}) is the ratio of peak deviator stress (q) to mean effective stress (q') computed from the stress-strain data plotted in Figure 2.30. Similarly, tests conducted using large-scale ballast box indicated a significant reduction in friction angle (up to 24%) and cohesion (up to 13%) (Song et al., 2019). Moreover, the dilation angle (ψ) decreases as the percentage of rubber increases, and the effect of confining pressure on the dilatancy of RIBS becomes less significant at higher rubber content ($R_b > 5\%$), which is desirable in reducing and controlling the lateral misalignment of railway tracks (Arachchige et al., 2021).

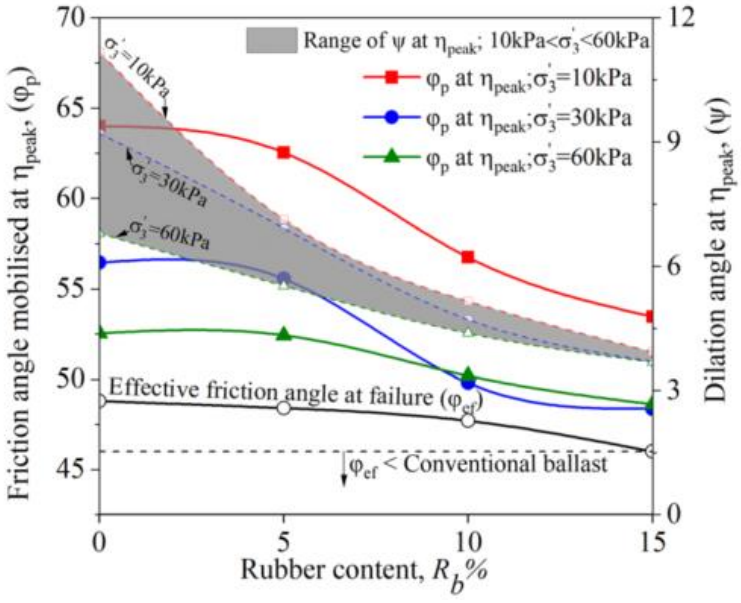

Figure 2.34 Effect of crumb rubber content on effective friction angle, dilation angle and mobilised friction angle (after Arachchige et al. (2021))

2.7.6 Damping and energy dissipation of RIBS

The energy generated by the moving train is distributed and dissipated through the railway track structure to the ballast layer. The ballast layer attenuates and distributes energy to the underlying substructure layers and ground (Esveld, 2001). The total energy

transferred to ballast and subgrade is primarily dissipated by plastic deformation, particle rearrangement, breakage, and other forms of energy, such as heat and sound. Under cyclic loading, ballast exhibits a hysteretic response depending on the amplitude of cyclic loading, and the corresponding energy dissipation is often expressed in terms of damping ratio (Song et al., 2019). The damping is defined as the ratio of energy dissipated and maximum elastic energy absorbed during a single loading-unloading cycle (Ashmawy et al., 1995). The damping ratio under hysteretic response can be calculated by (Madhusudhan et al., 2017):

$$D = \frac{A_L}{4\pi A_S} \tag{2.13}$$

where A_L is the energy dissipated per loading cycle as represented by the area bounded by the loading/unloading loop (A_L) in the stress-strain curve and A_S is the area of the triangle that represents the maximum elastic energy stored during the cycle, as shown in Figure 2.35(a).

The energy dissipation of RIBS increases with the rubber content due to the highly elastic nature of rubber and increased damping in ballast-rubber granule mixtures (Arachchige et al., 2022; Fathali et al., 2017). Song et al. (2019) tested RIBS under cyclic loading utilising large-scale direct shear apparatus and observed a significant increase in damping ratio (up to 72%) as compared to pure ballast, as shown in Fig 2.15(b). However, an increase in the normal and confining increases the friction while reducing the movement of particles in granular assembly; hence the damping reduces (Arachchige et al., 2022; Song et al., 2019). Arachchige et al. (2021) showed through large-scale triaxial testing that the damping ratio and energy dissipation do not show a significant increase when the

rubber content exceeds 10%. The reason can be attributed to the fact that adding a higher percentage of rubber crumb to the ballast granules transforms the response of RIBS to rubber-like material, resulting in a significant reduced shear strength and increased track settlement.

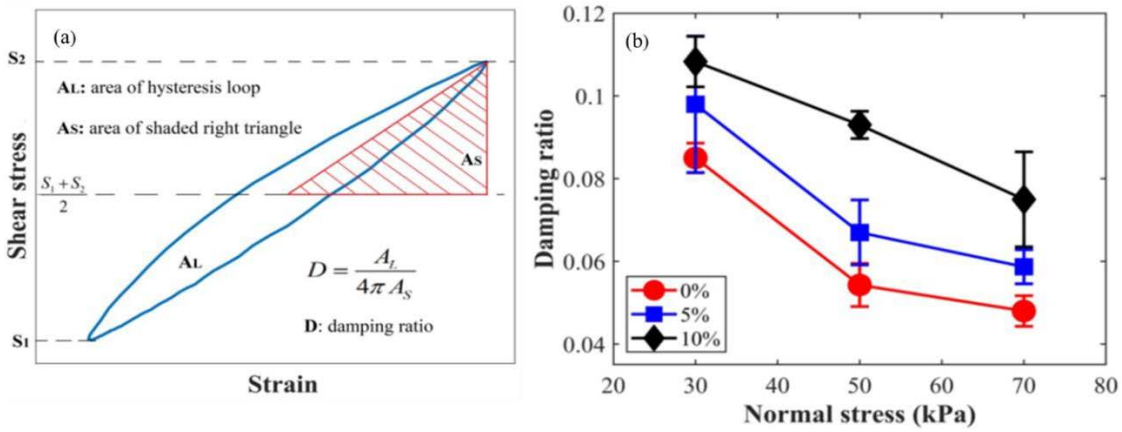

Figure 2.35 Computation of damping ratio from hysteretic stress-strain relationships (b) Variation of damping ratio with rubber content and normal stress (modified after Song et al. (2019))

2.8 Track dynamic analysis methods

2.8.1 Analytical and semi-analytical methods

Numerous analytical and semi-analytical methods have been used to predict the dynamic response of tracks. In this approach, the track and foundation are modelled as rheological variants of the beam theory, mass and spring-dashpot assemblies to represent steel rails, rail pads, sleepers, ballast, and the formation or subgrade layers (Kouroussis et al., 2011; Zhai et al., 2009). The most straightforward approach represents the track superstructure as a simple flexural beam with bending stiffness resting on continuous spring and dashpots, as shown in Figure 2.36. The general differential equation is given by:

$$E_r I_r \frac{\partial^4 w(x,t)}{\partial x^4} + m_r \frac{\partial^2 w(x,t)}{\partial x^4} + c_f \frac{\partial w(x,t)}{\partial x} + k_f w(x,t) = F\delta(x - Vt) \quad 2.14$$

where $E_r I_r$ is the flexural stiffness of the rail; $w(x,t)$ is the vertical displacement; m_r is the mass per unit length of the rail, F is the concentrated force of constant magnitude, $\delta(x-t)$ is Dirac function; whereas k_f and c_f represent the linear elastic spring and damping of the foundation, respectively.

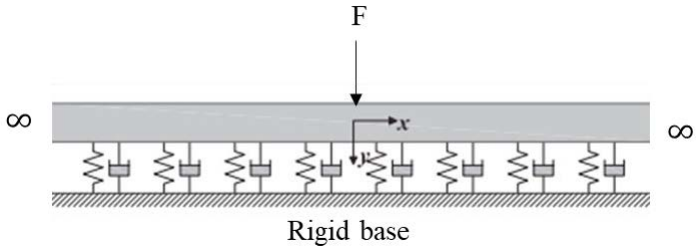

Figure 2.36 Beam on single layer visco-elastic foundation (modified after Lamprea-Pineda et al. (2021))

Ignoring the inertial and viscous damping of the foundation, the quasi-static deflection of the track is expressed in terms of space and time by, as given (Krylov et al., 2000):

$$w(x,t) = \frac{F\beta}{2k} e^{-C_e|x-Vt|}[\cos(C_e[x-Vt]) + \sin(C_e|x-Vt|)] \quad 2.15$$

where

$$C_e = \sqrt[4]{\frac{4E_r I_r}{k_f}} \quad 2.16$$

The characteristic length (C_e) is a measure of the inflection point measured from the load beyond which the effect of the load is negligible. The substructure layers are idealised with elastic springs, and each component of the track is accounted for via a combination

of their properties. For example, the stiffness of the foundation is calculated using a "springs-in-series approach" (Indraratna and Ngo, 2018; Lamprea-Pineda et al., 2021).

Figure 2.37 illustrates the influence of track modulus on the deflection profile when a typical train moves at 50m/s. The result shows that the deflection profile is highly affected by the track modulus, k_f. The deflection profile shows that the track response is confined to wheel load locations, while for the soft track, the deflection profile is controlled by bogie locations.

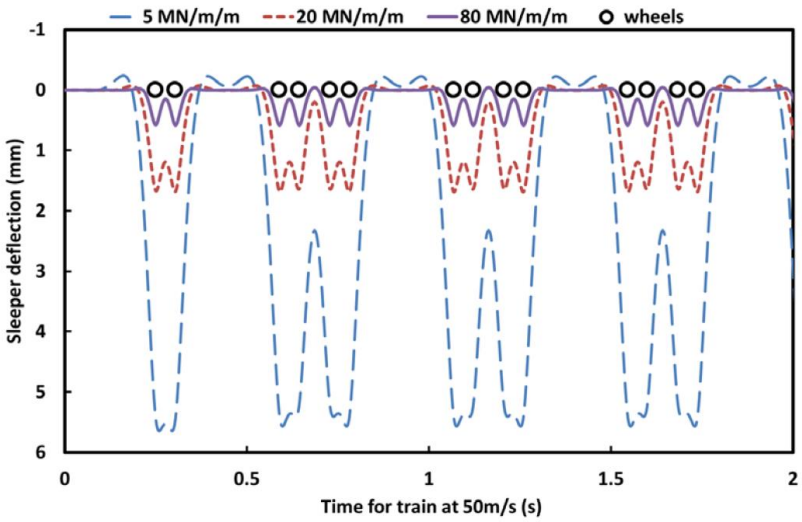

Figure 2.37 Effect of track modulus on deflection under moving train (Powrie and Le pen, 2016) .

Though the single-layer beam on the visco-elastic foundation model has been widely employed to estimate the track deflection, it is sufficient only to evaluate the vertical vibration of the track (Knothe and Grassie, 1993). In addition, it can not capture the variation in dynamic properties of track components since a single lumped parameter, track modulus, is used to represent the stiffness of the whole track substructure. To this end, two and three-layered have been developed as shown in Figure 2.38(a) and (b). In the two-layered model, the railpad and ballast are represented by spring and damper

assembly, whereas inertial properties are assigned to the sleeper. This model is appropriate when the track is built on rocks or bridges. In contrast, the three-layered model has additional spring-dashpot assemblies representing the subgrade. Irrespective of the number of layers considered, the continuous support models face difficulties in simulating the discrete nature of the sleeper, and they struggle to capture the "pin-pin" resonance frequency (Xie and Iwnicki, 2008).

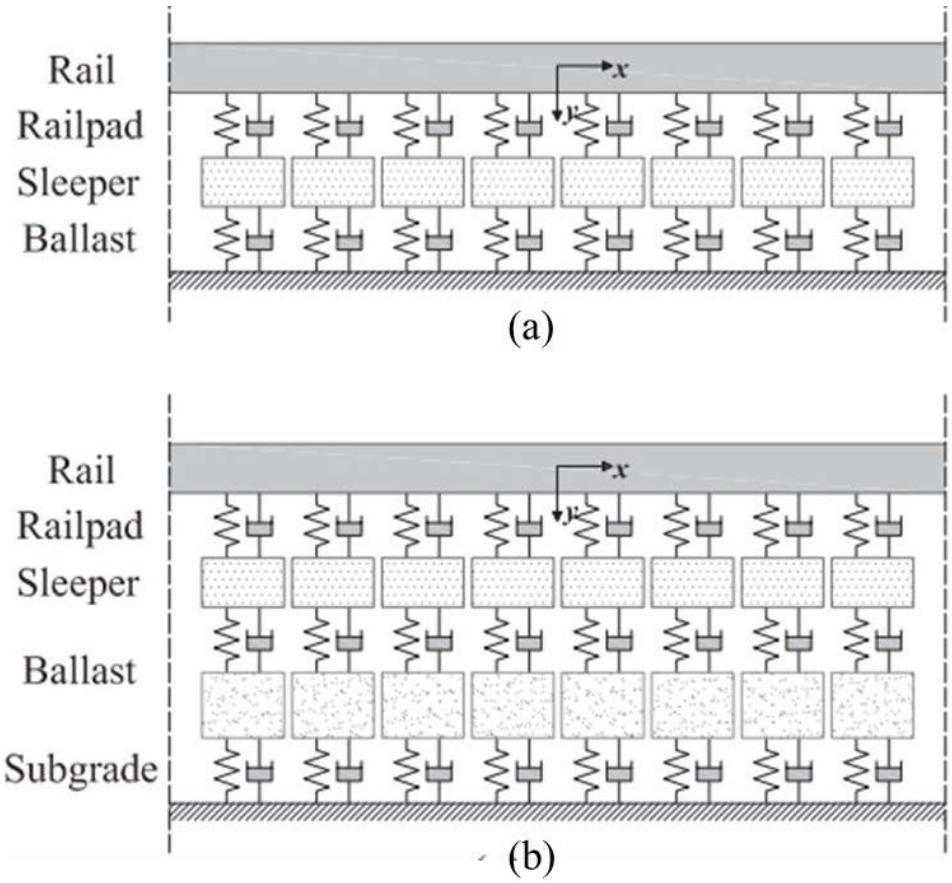

Figure 2.38 Continuous supported railway track model (a) Two-layered model (b) Three-layered model (Knothe and Grassie, 1993; Lamprea-Pineda et al., 2021)

The models based on variants of spring-damper assemblies discussed above are the most adapted method for vertical train-track analysis since they provide a representative response at the rail (Zhai et al., 2009). However, the foundation spring model is insufficient to represent the track substructure response involving wave propagation.

In order to overcome the limitations of one-dimensional analytical models discussed above, the Wrinker-type representation is replaced by half-space or layered half-space models. Krylov (1995) presented an analytical method to predict track vibration due to quasi-static loading. The model initially predicts the deflection of the track and forces transmitted to the sleeper, assuming the track is an Euler-Bernoulli beam resting on an elastic or viscoelastic foundation. In this approach, the transferred force and associated deflection bowl are applied to the elastic half-space to predict the ground vibration spectra at the track surface using frequency domain analysis (Krylov and Ferguson, 1994; Krylov, 1995). The classical solution proposed by Lamb (1904) was employed to represent the wave transmission on the ground using Fourier transform in the frequency-wave number domain.

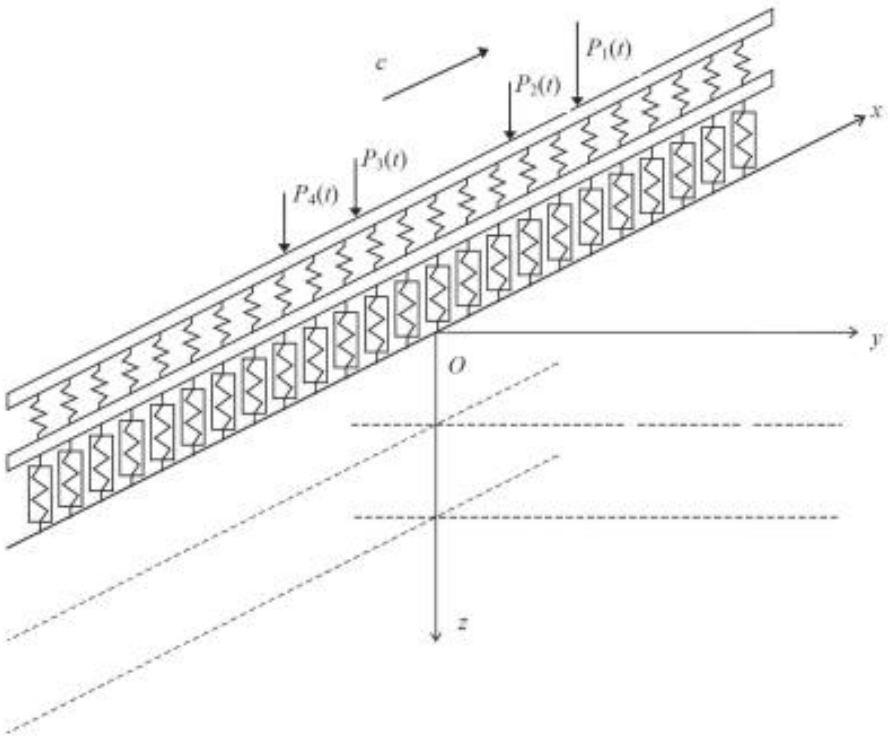

Figure 2.39 Model for a track on layered half-space proposed by Sheng et al. (1999)

In railway track application of the beam-on-ground models, the modelling technique employed is also found to influence model accuracy. Mostly, the beam is considered a characteristic equivalent of the whole track, considering the bending stiffness of the rail, pads, sleeper, and ballast (Dieterman and Metrikine, 1996; Madshus and Kaynia, 2001). Then beams and half-space representing the subgrade are coupled through equivalent stiffness to facilitate interface compliance. In contrast, Sheng et al. (1999) represent only the rail as a beam as per the Euler-Bernoulli framework in which rail pads are modelled by distributed stiffness; the sleepers are idealised as distributed stiffness, and the ballast as continuously distributed mass and stiffness resting over a multi-layered elastic ground ,as shown in Figure 2.39.

The analytical and semi-analytical methods have been extensively applied to estimate ground vibration and associated wave dispersion characteristic curves and critical speed (Madshus and Kaynia, 2001; Sheng et al., 1999; Sheng, 2004; Takemiya and Bian, 2005). Though these models have been used to study the vertical vibration response of a track under moving load, they are rarely applied in track analysis involving complex track geometry and the 3D stress-deformation response.

2.8.2 Numerical methods for rail track analysis

In order to overcome the limitation of analytical and semi-analytical, several railway track modelling techniques have been developed within the scope of moving load analysis. The widely adopted methods are the Finite Element Method (FEM), Boundary Element Method (BEM), Discrete Element Method (DEM), and hybrid methods. In the following section, the modelling strategies and application of those numerical approaches are discussed, focusing on their capabilities and limitation as they pertain to track analysis.

2.8.2.1 Finite Element Methods

The Finite Element Method (FEM) has been widely applied in the dynamic track response involving wave propagation problems. It allows the implementation of complex geometries and sophisticated material models for the track substructure. However, modelling unbounded soil domain with finite elements poses significant challenges, the wave energy generated by wheel load excitation will result in reflected waves rather than continuously propagating to outer regions. Hence, classical boundary conditions such as free and fixed must be cautiously used (Kouroussis et al., 2014).

The strategy to overcome this limitation is to make sure the models are sufficiently large than those used for static analysis and apply absorbing boundary conditions (Shih et al., 2016). In order to prevent these spurious waves from contaminating the solution, several approaches have been recommended. Kuhlemeyer and Lysmer (1973) dashpot absorbing boundaries have been introduced. This enables the incident waves to be absorbed at the boundary by introducing infinitesimal viscous dampers, orientated along the normal and tangential direction with respect to the boundary. Though the infinite elements provide good energy absorption for most practical modelling cases, they do not provide perfect energy transmission leading to residual reflection. An alternative approach to overcome wave reflection is introducing infinite elements with decay function or a perfectly matched layer (PML) (Zhang et al., 2019). This approach rapidly decays most waves irrespective of the angle of incidence by using a stretching function chosen to increase the attenuation of waves at the boundary.

The FEM models have applied different model dimensions (i.e. 2D, 3D and 2.5D) and the plane of symmetry to reduce computational time. Kece et al. (2019) used a 2D model

to study the wave propagation along the lateral direction in ballast and slab tracks. There are two types of 2D models: plain strain models in transversal and longitudinal directions. The transversal plane strain model (Figure 2.40) assumes the simplification assumption that the track is continuous in the longitudinal direction, which does not consider the effect of discrete sleeper support. Hence, the stress transfer from the sleeper to the ballast is not accurately considered. The additional shortcoming in the 2D plane strain model is related to wheel load distribution among neighbouring sleepers in the longitudinal direction. In this case, simplified expressions based on a beam on an elastic foundation or analytical expressions of load function are employed. In contrast, a moving load or full train model can be applied directly on the train.

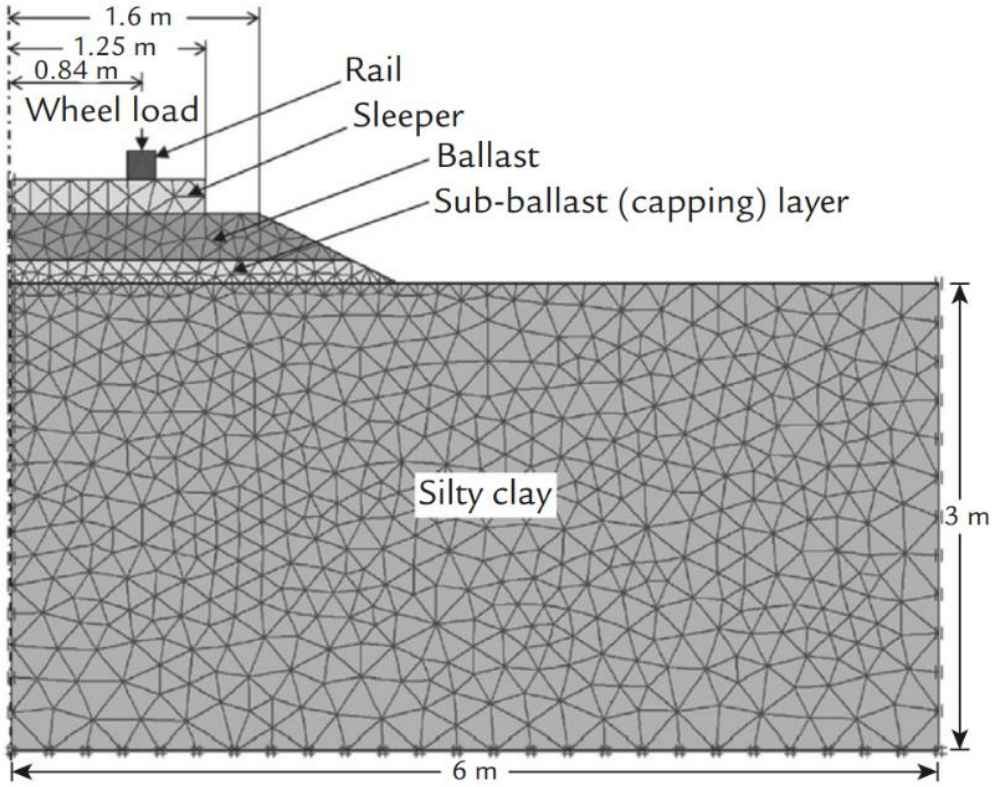

Figure 2.40 Example of a 2D FE model in plain strain (Indraratna et al., 2011)

Yang et al. (2009) studied the effect of speed and track imperfection, including a hanging sleeper on a subgrade stress path, using a 2D plane strain model along the direction of the moving train. Alves Ribeiro et al. (2015) applied a 2D model to study the effect of under sleeper pads at railway transitions by calibrating the material parameters to an equivalent 3D FE model. In this case, discrete sleeper support is considered, but the variability of track cross-section is not taken into account (Paixão, 2014)

Though computationally demanding, the 3D FE models do not necessitate simplifying assumptions related to model geometry and load distribution. Hence, the geometry characteristics of the track can be correctly represented, as given in Figure 2.41. This technique has been successfully employed to study railway vibrations (Banimahd et al., 2013; Connolly et al., 2013; El Kacimi et al., 2013; Hall, 2002; Sayeed and Shahin, 2016), complex geometries involving piled-embankment (Thach et al., 2013), track stiffness transitions (Chumyen et al., 2022; Ramos et al., 2022; Shan et al., 2013). In terms of ground modelling technique and infinite element representations, an elongated sphere domain with infinite elements, as shown in Figure 2.42, has been applied to increase the absorption capacity of the model edges (Connolly et al., 2013; Kouroussis et al., 2011).

The main advantage of time-domain 3D FEM is the ability to represent the complex response of track geomaterials through appropriate constitutive relationships. Several authors have used advanced models for numerical analysis of track under cyclic and moving load. For example, Ferreira (2013) and Banimahd et al. (2013) have implemented a non-linear elastic model for resilient modulus.

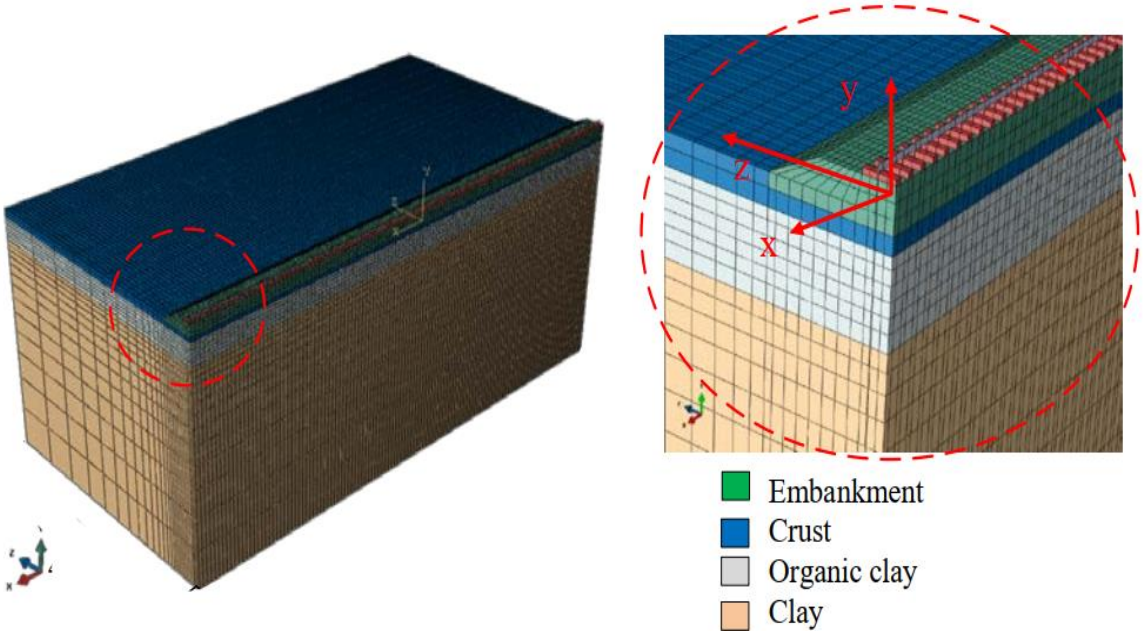

Figure 2.41 Cuboid Three-dimensional FE model (Shih et al., 2017)

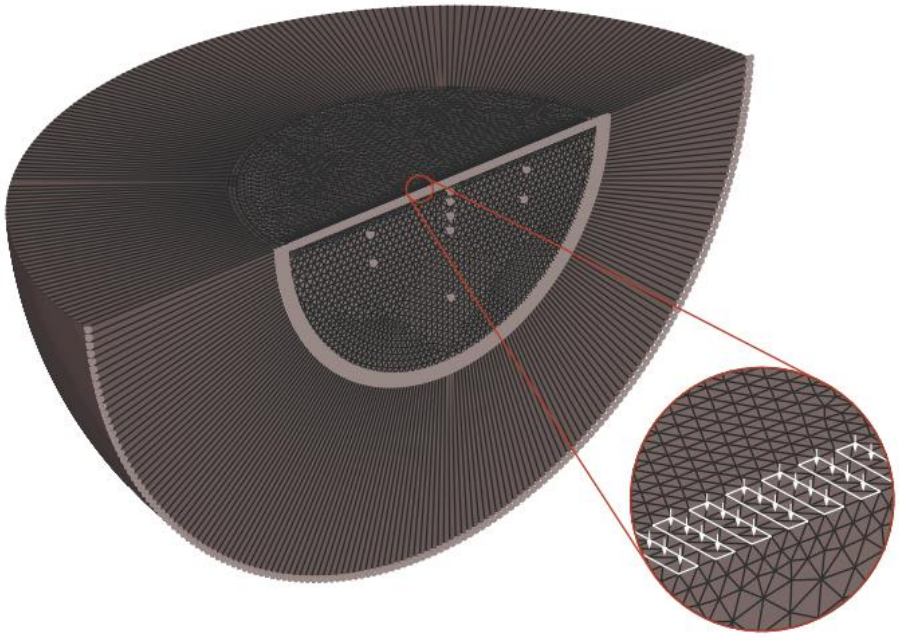

Figure 2.42 Finite element model with elongated sphere for track analysis (Kouroussis et al., 2011)

The 2.5D approach considers the railway track as invariant along the longitudinal direction, the FE equilibrium equations are solved in the frequency-wave number domain,

and the model is discretised only in the transversal direction, as shown in Figure 2.43. This approach is computationally efficient as compared to the 3D model while capturing the 3D track structure. Several studies have been conducted to better understand the effect of wave propagation by considering the track as a 2.5D model (Costa et al., 2012; Gao et al., 2019; Yang et al., 2019). Moreover, the longitudinal direction of the model is implemented in the frequency domain, restricting the approach to linear or equivalent linear analysis (Dong et al., 2019). This approach helps study the dynamic response and vibration of slab tracks with uniform geometry along the direction of train movement. However, this technique cannot capture the discretely spaced sleepers of the ballasted track and associated sleeper-ballast stress transfer. These computationally efficient methods are widely applied to predict ground vibration, but they are rarely considered to study dynamic track responses involving geometric and material complexities.

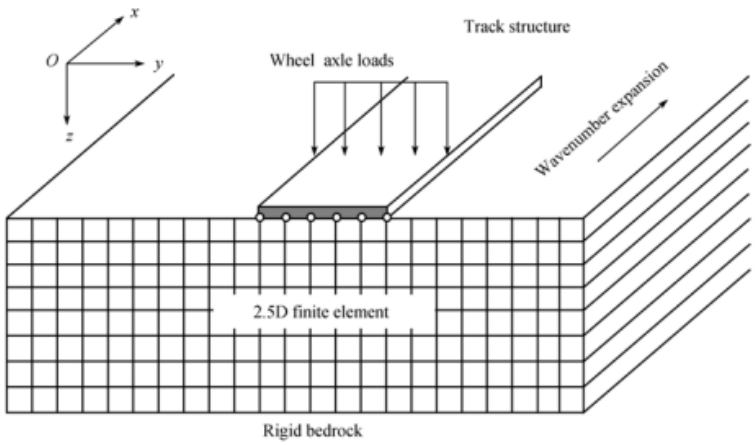

Figure 2.43 Representation of 2.5D FE model (Bian et al., 2008)

2.8.2.2 Coupled Finite – Boundary Element Method

The Boundary Element Method (BEM) is an efficient technique for predicting wave propagation and ground vibration generated by moving trains. In this approach, the track foundation or embankment is idealised as half-space or layered half-space, whereas the

track components above the subgrade are modelled using complex arrangements of spring and dampers (Lombaert et al., 2006). The model assumes continuous support along the longitudinal direction, and the boundary integral of the Green's function of the soil is solved in the frequency-wave number domain (Kausel and Roësset, 1981). Hence, it cannot be applied to complex track structures and non-linearities (Galvín et al., 2010; Kausel and Roësset, 1981). In order to account for complex geometries and non-linearities of the track, 2.5D Coupled Finite - Boundary Element methods are widely adapted to benefit from the benefits of each method. In this case, the rail, pads, sleeper, and ballast are discretised in FE framework, whereas the wave propagation and dissipation in the subgrade are modelled with BE method, as shown in Figure 2.44. The coupling at the model interface is performed in FE formulation by transforming the flexibility matrix of the BEM domain into a stiffness matrix (Costa et al., 2012; François et al., 2010).

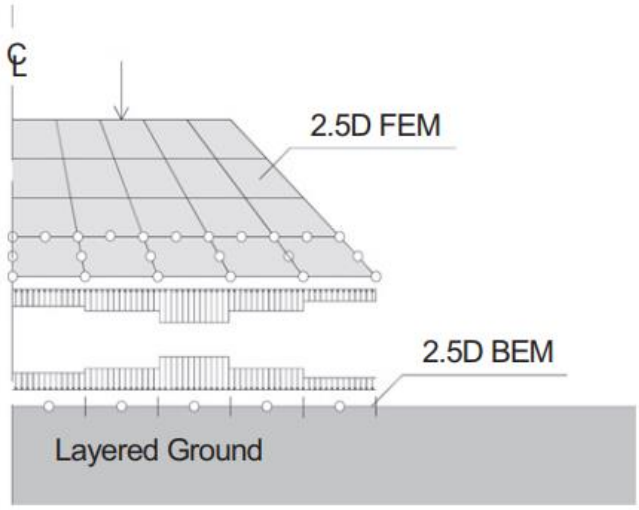

Figure 2.44 Coupled FE-BE model for track and ground (Costa et al., 2012)

Costa et al. (2012) developed a 2.5D FE-BE model to predict vertical track embankment vibration induced by moving trains and validated it against measured response. The

moving load is simulated based on coupled-track interaction to capture the dynamic excitation by train-track interaction. Other authors (François et al., 2010; Galvín et al., 2010; Sheng et al., 2006) have employed 2.5D FE-BE method to predict the free-field wave propagation under moving trains.

2.8.2.3 Discrete Element Method

Application of Discrete Element Method (DEM) shows an increasing trend in particular to the ballast layer. The discrete nature of ballast material results in a complex response under traffic loading that cannot be adequately represented by continuum methods (Cundall and Strack, 1979; Ngo et al., 2017). The DEM has been widely used to examine the dynamic response of ballasted tracks. It gives additional insight into micromechanical characteristics such as ballast breakage, contact force distribution, and fabric anisotropy (Ngo, 2012; Saussine et al., 2008). Hence, DEM codes simulate the complex interactions between a large number of particles to predict the macro-behaviour of the granular assembly. Recently, several authors have resorted to this method to simulate and reproduce experimental results from triaxial and shear box tests under monotonic and cyclic loading conditions (Indraratna et al., 2010; Lu and McDowell, 2010; Ngo et al., 2014; Tutumluer et al., 2012)

Conventionally, there are two components in DEM models: particles and walls. The walls provide constraints to the particle assemblies to restricted volume region. The DEM keeps track of particle motion, and the contact between particles is updated using constitutive contact law. The contact between the particles is constantly updated through Newton's second law of motion, whereas the force-displacement law is employed to update the contact interactions caused by the relative particle displacements at each contact point.

The integration of the law of motion gives an updated particle position. Then, a new contact force is calculated using the force-displacement law, which will be applied to the particles in the following times (Itasca, 2020; Ngo, 2012).

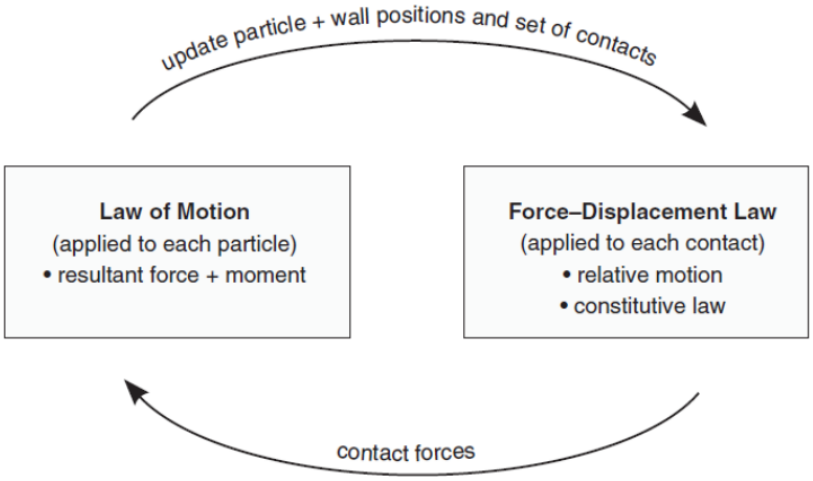

Figure 2.45 Calculation cycle in DEM (Itasca, 2020)

Due to the substantial computational cost of DEM, it is rarely applied for dynamic analysis of full track models. In most cases, the rail and rail pads are neglected; moving loads are directly applied to the sleeper through analytical expressions (Bian et al., 2020). Also, the length of the track model is truncated to a few sleepers (<10); and the contribution of the subgrade is neglected or replaced by a rigid bottom boundary, which is not a realistic representation of rail tracks (Bian et al., 2020; Zhang et al., 2017). Given the computational demand of DEM to accurately analyse a large-scale model involving different particle assemblies and additional track layers, a few authors have developed a coupled discrete-continuum approach (Ngo et al., 2017; Nishiura et al., 2018; Shi et al., 2020). In coupled discrete-continuum modelling, DEM is utilised to model track superstructure components (*i.e.,* rail, rail pads, sleepers) and the ballast layer, while capping and subgrade are simulated using continuum approaches. The coupling between the ballast (modelled with DEM) and capping (modelled with FEM/FDM) layers is

achieved using interface elements that satisfies the conditions of compatibility and equilibrium at the boundary. Hence, coupling DEM with FEM/FDM is a promising approach to capture the discrete nature of rail ballast and subgrade mechanical response under moving load with reasonable computational cost, as compared to DEM.

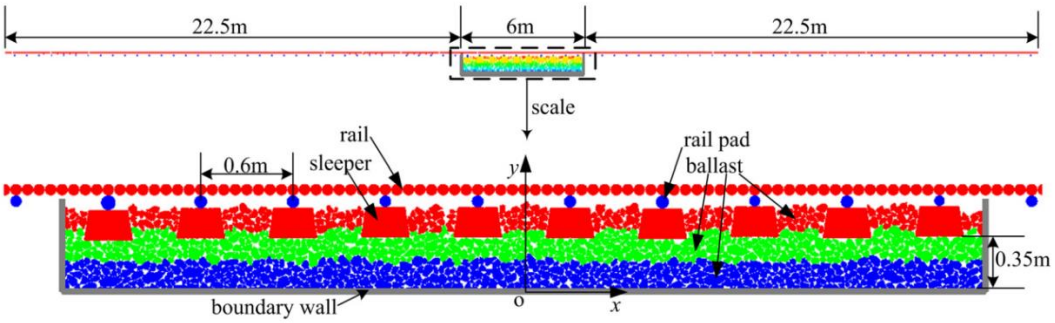

Figure 2.46 Discrete element modelling of moving load (Zhang et al., 2017)

2.9 Chapter summary

This chapter presented pertinent literature on dynamic analysis of ballasted railway tracks under increasing train speed. Heavier and faster train induces higher dynamic stresses in the track substructure, accelerating track deterioration and permanent settlement while increasing the risk of derailment. Several analytical, numerical, and field studies have shown that dynamic amplification of transient vertical stress and displacement increases with train speed. In conventional track analysis and design, dynamic track response is predicted by multiplying the quasi-static response by the dynamic amplification factor (DAF), which is the function of the train speed and superstructure characteristics. However, those amplification factors overlook the complex track response involving moving load and amplifications of stress associated with Rayleigh wave propagation. In addition, the same magnitude DAF has been recommended for all track substructure

components without capturing the influence of track subgrade and depth below the track surface.

The chapter then presented the application of rubber granules mixed with ballast particles to mitigate track deformation, ballast degradation and vibration reduction. Most studies conducted in the laboratory setting have proved the effectiveness of RIBS in reducing ballast breakage and increasing energy absorption. Still, there is a research gap on how the changes in the ballast layer properties would influence the track's global response, such as transient displacements and stress distribution.

Lastly, the chapter described several analytical and numerical analysis techniques employed in track dynamic analysis under moving wheel loading; highlighted their relative advantage and applicability in capturing both the vertical and lateral (dilatational) track response under moving train load. The review of pertinent literature indicated that 3D FEM could be effectively used to study the effect of increasing train speed on dynamic stress-displacement response under moving wheel loads. However, those studies analysed the critical speed, transient vertical displacement, and embankment vibration rather than the dynamic responses of the load-bearing layers.

CHAPTER 3 THREE-DIMENSIONAL FINITE ELEMENT MODELLING OF BALLASTED TRACK

3.1 Introduction

In order to capture the dynamic response of the train/track system under an increasing train, a three-dimensional (3D) FE model has been developed in this study. The numerical model included the rail, pads, sleeper, ballast, capping, and formation based on Australian train and track properties. In this study, 3D Finite element-based code ABAQUS V.20 has been employed based on successful studies on track vibration analysis (Connolly, 2013; Ramos et al., 2022; Shih et al., 2017; Tang et al., 2019). According to Kouroussis et al. (2014), time-domain analysis is required to capture elasto-plastic response since frequency domain analysis can deal with purely elastic analysis. This study aims to evaluate the dynamic response of ballasted railway track under increasing train speed and proposed design recommendations to protect against track instability. Therefore, it is imperative to ensure that the proposed FE model provides reliable track performance prediction. Therefore, the initial study is devoted to validation against analytical predictions and field measurements from well-documented literature. This chapter elucidates the different components of the developed numerical modes, including the FE model, material properties, contact modelling, boundary conditions, and the dynamic moving load simulation scheme adopted. Then, the result of validation studies will be presented.

3.2 Finite element model

3.2.1 Model geometry

The ballasted rail track employed in this study consists of steel rails, concrete sleepers, ballast (quarried aggregates), a capping layer (compacted sandy gravel beneath ballast),

and the subgrade (natural foundation). The 3D model with dimensions of 44m (length) x 12.65m (width) x 10.68m (depth) was implemented as illustrated in Figure 3.1. The model consists of 61 sleepers placed at a center-to-center spacing of 600mm spanning over the middle 36m of the track. The half-track is considered in the FEM analysis, exploiting symmetry along the longitudinal axis (y-z plane).

The rail is modeled as a solid rectangular section, i.e., equivalent cross-section to 60kg/m standard profile placed at 1.435m standard gauge. The reinforced concrete ties (sleepers) have dimensions of 2.5m (length) x 0.26m (width) x 0.23m (thickness), following the typical concrete sleepers dimensions used in Australia (Indraratna et al., 2010; Nimbalkar and Indraratna, 2016). The ballast and capping layers are 300mm and 150mm in thickness, respectively, resting over a subgrade of 10m in thickness, as shown in Figure 3.2.

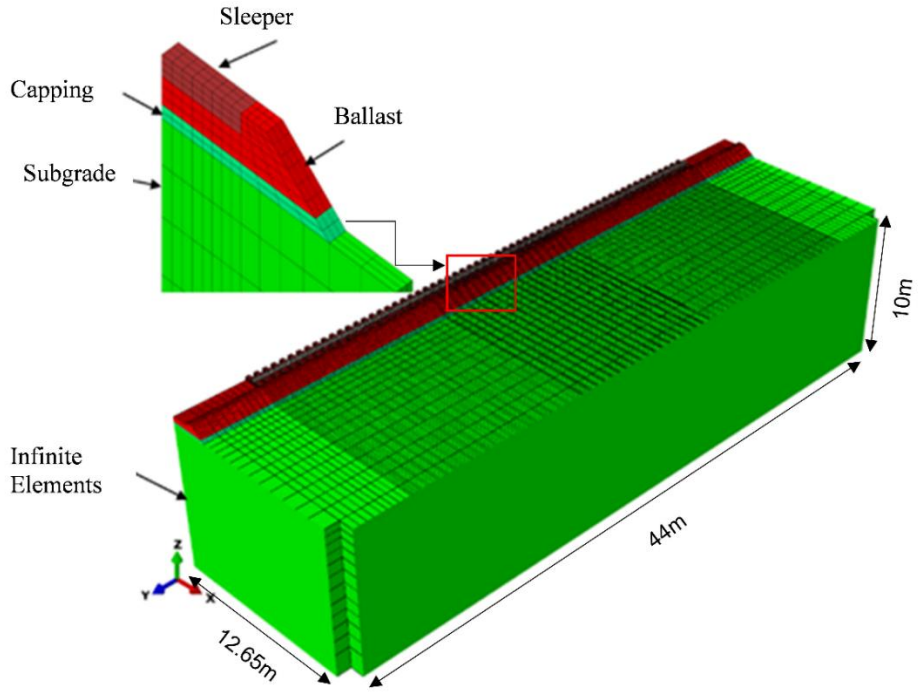

Figure 3.1 Finite model geometry for moving load analysis

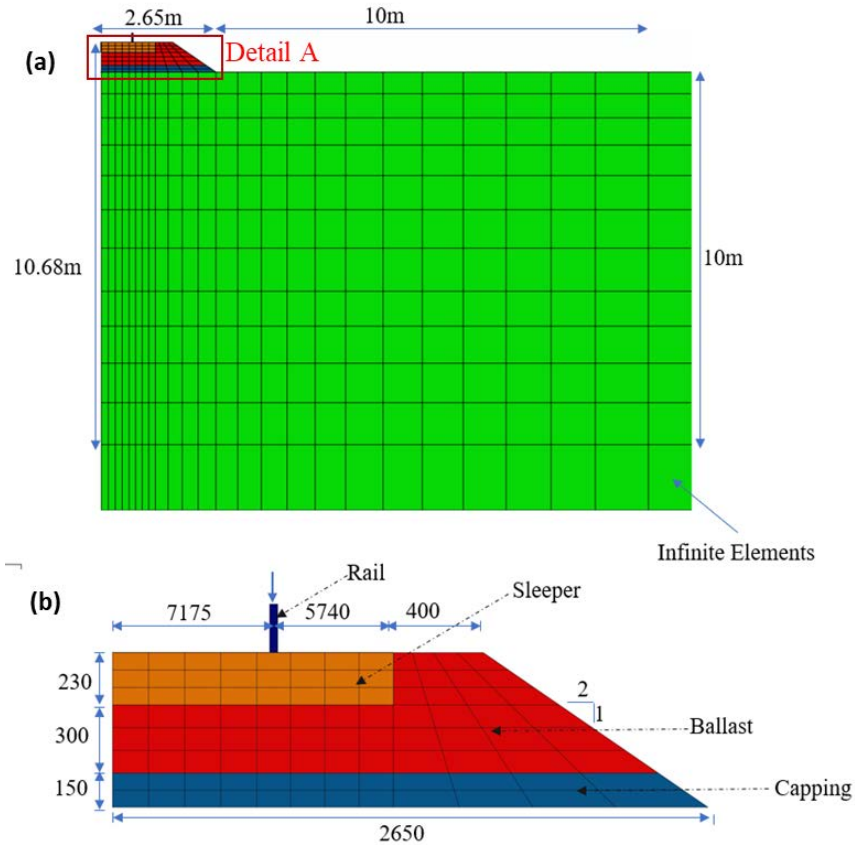

Figure 3.2 Cross-section of finite element model (a) full section (b) Detail A, dimension in mm

3.2.2 Material properties

The track superstructure components (steel rail and concrete sleeper) are modeled as linear-elastic materials since non-yielding behaviour is expected. For track substructure geomaterials, most studies have adopted an elastic model since the transient deformations are assumed to be very small when only a few wheel passes are simulated (Connolly et al., 2013; Costa et al., 2015; Hall, 2002; Nsabimana and Jung, 2015; Tang et al., 2019). In this regard, simulating an elastoplastic response coupled with the large-scale FE models required to capture wave propagation associated with moving load often necessitates considerable computational resources.

Table 3.1 Parameters used in the validation of 3D-FEM analysis (Connolly et al., 2013; Hall, 2002; Indraratna et al., 2010; Priest et al., 2010; Yang et al., 2009)

	Indraratna et al. (2010)	Priest et al. (2010)
Track Components	Value	Value
Rail[1]		
Density (kg/m^3)	7850	7850
Young's modulus (MPa)	210000	210000
Poisson's ratio, ν	0.3	0.3
Sleeper		
Density (kg/m^3)	2500	2400
Young's modulus (MPa)	30000	30000
Poisson's ratio, ν	0.25	0.2
Ballast		
Density (kg/m^3)	1530	1800
Young's modulus (MPa)	200	100
Poisson's ratio, ν	0.3	0.3
Cohesion (kPa)	1	
Friction angle, ϕ (degrees)	50	
Dilation angle, ψ (degrees)	20	
R-Wave velocity (km/h)	734	
Capping		
Density (kg/m^3)	1800	2300
Young's modulus (MPa)	150	321
Poisson's ratio, ν	0.3	0.3
Cohesion (kPa)	1	
Friction angle, ϕ (degrees)	35	
Dilation angle, ψ (degrees)	5	
R-Wave velocity (km/h)	586	
Thickness (m)	0.15	0.2
Structural Fill[a]		
Density (kg/m^3)	NR	2100/2100/2200[a]
Young's modulus (MPa)	NR	296/143/118[a]
Poisson's ratio, ν	NR	0.3
R-Wave velocity (km/h)	NR	
Thickness (m)	NR	0.6
Subgrade		
Density (kg/m^3)	1730	2300
Young's modulus (MPa)	50	27000
Poisson's ratio	0.35	0.25
Cohesion (kPa)	30	
Friction angle, ϕ (degrees)	24	
Thickness (m)	10	30

[a] Structural fill layer is not reported (NR) in the case of Indraratna et al. (2010)

Previous studies considering both non-linear and elastoplastic models have shown that advanced material models have a moderate effect on the critical speed and the associate

transient vertical displacement when few loading cycles are considered (Costa et al., 2010; Dong et al., 2019; Sayeed and Shahin, 2016; Shih et al., 2017). However, laboratory and field tests conducted on ballasted track have shown that the vertical and lateral deformations increase in the first few loading cycles, which finally stabilise as the resilient response is attained with a higher number of cycles (Ramos et al., 2020).

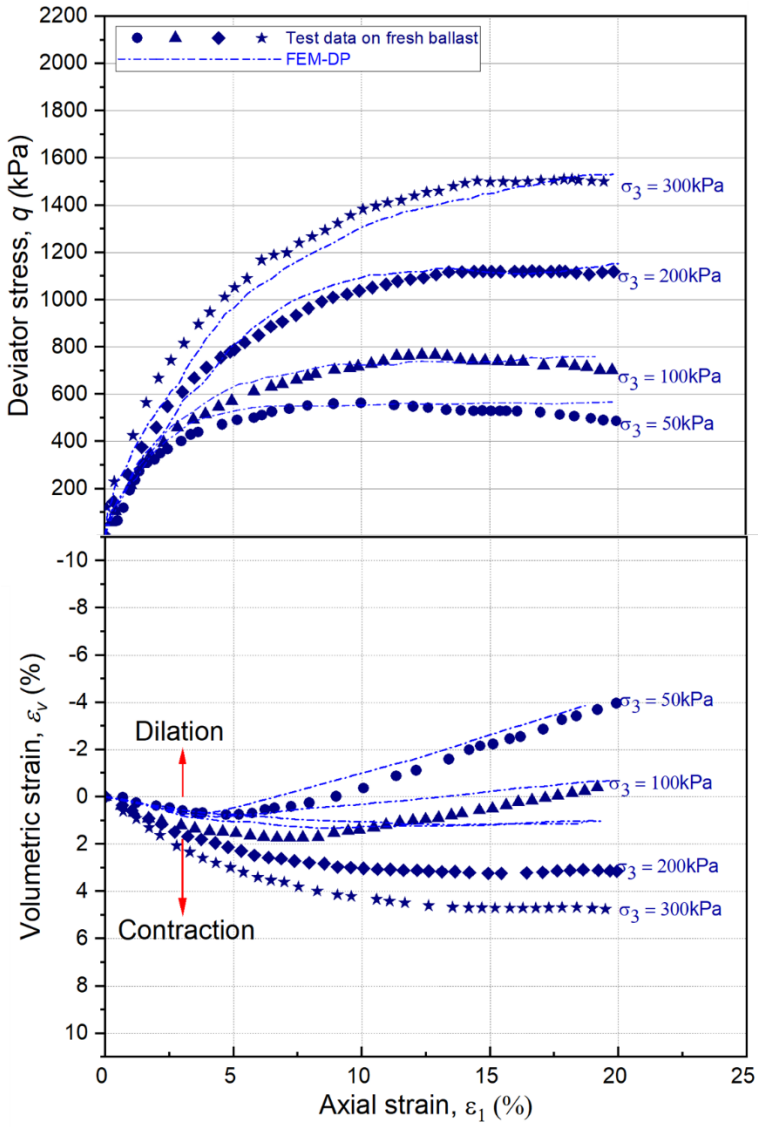

Figure 3.3 Comparison of experimental data and FE prediction for ballast using Drucker-Prager model (modified after Indraratna et al. (2007))

In the case of elastoplastic models, the non-associative Drucker-Prager (DP) model was selected to model the ballast stratum. The non-associative D-P model has been used in various numerical analyses of the granular geomaterials subjected to cyclic loading conditions because the strength and plastic response depends on the applied repeated stress level, the number of loading cycles and volumetric strain (Leshchinsky and Ling, 2013; Shih et al., 2019). The influence of confining stress level on the stress-strain response of ballast is shown in Figure 3.3 based on large-scale triaxial tests conducted on latite ballast in New South Wales, Australia (Indraratna et al., 2007).

At low confining pressure (<50kPa), the volumetric strain is compressive at low strain, but the ballast response exhibits significant volume expansion at high strain level. In contrast, the volumetric response shifts to a compressive state with an increased lateral stress level. Similarly, the deviator stress behaviour strongly depends on the applied confining stress with observable post-peak strain softening at low confining pressure. Indraratna et al. (2007) compared the predicted stress-strain behaviour of ballast using the extended Drucker-Prager (DP) model implemented in ABAQUS with experimental results, as shown in Figure 3.3. The DP model has been employed to simulate the frictional material, such as ballast, with confining pressure-dependent yield and plastic deformation. Accordingly, the extended DP models reasonably predict stress-strain behaviour at low confining pressure (<50kPa). However, as implemented in FE analysis,

the DP model could not capture the volumetric behaviour at a high confining stress level as the model does not capture volumetric contraction associated with particle breakage at high confining stress. Though the DP model underestimated volumetric contraction at high confining pressure (>.200kPa), it can provide a reasonable prediction of inelastic deformation for the range of confining stress commonly encountered in conventional ballasted tracks (<50kPa).

In the current FE analysis, the deformation and strength parameters for the ballast are obtained from large scale triaxial testing conducted on latite ballast in New South Wales, Australia (Indraratna et al., 2011; Indraratna et al., 2015); and computed using the approach illustrated in Appendix A. The mechanical properties of each component of the ballasted track considered in this study are summarised in Table 3.1, corresponding to the two validation case studies.

3.2.3 Governing equation

In order to simulate the transient dynamic response under moving train loading, the governing equation of dynamic equilibrium in matrix form is expressed as (Zienkiewicz et al., 2005):

$$[M]\{\ddot{U}\} + [C]\{\dot{U}\} + [K]\{U\} = [F] \tag{3.1}$$

where, $[M]$, $[C]$ and $[K]$ are mass matrix, the damping matrix and the stiffness matrix, respectively; while $[F]$ is the nodal force vector varying with the time and location of the

load the moving load. $\{\ddot{U}\}$, $\{\dot{U}\}$ and $\{U\}$ are the nodal vectors of acceleration, velocity and displacement, respectively; and solved using the central difference integration.

$$\dot{U}^N_{\left(i+\frac{1}{2}\right)} = \dot{U}^N_{\left(i-\frac{1}{2}\right)} + \frac{\Delta t_{(i+1)} + \Delta t_{(i)}}{2} \ddot{U}^N_{(i)} \qquad 3.2$$

$$U^N_{(i+1)} = U^N_{(i)} + \Delta t_{(i+1)} \dot{U}^N_{\left(i+\frac{1}{2}\right)}$$

$$\ddot{U}^N_{(i)} = (M^N)^{-1}(F^N_i - I^N_i)$$

where, U^N , $\dot{U}^N$ and $\ddot{U}^N$ are nodal displacement, velocity and acceleration for the increment i and node N. F^N_i and I^N_i is the applied load vector and the internal force vector, respectively. In this approach the mass matrix is lumped; hence; the matrix inversion is not required at each timestep of the integration (Δt) (Hibbitt et al., 2020).

The time increment in solving the governing equations of motion, as presented in Equation 3.1 and 3.2, has been considered based on the Courant-Friedrichs-Lewy (CFL) criteria to maintain numerical stability and accuracy (Courant et al., 1967). The range of stable time increment (dt) corresponding to the smallest element size in FE models based on CFL is computed using the following expression (Courant et al., 1967; Zerwer et al., 2002):

$$\frac{1}{10}\frac{h_e}{V_P} \leq dt \leq \frac{h_e}{V_p} \qquad 3.3$$

where, V_P is dilatational wave speed of track material. In all numerical simulations carried out in this study, the selected time step is less than 10^{-5} seconds to ensure the convergence of the FEM analysis (Zienkiewicz et al., 2005).

3.2.4 Finite element discretisation and element type

In order to ensure an acceptable accuracy of the track dynamic analysis, the track geometry, boundary conditions, element size and dynamic calculation time-step have to be properly established. To avoid numerical instability and reduce computational resources, the element size should be fine enough to capture high-frequency vibration generated by the moving load (Zerwer et al., 2002). In this study, an approximate characteristic element dimension (h_e) is determined by:

$$h_e \leq \frac{\lambda_{min}}{\chi} = \frac{V_s}{\chi f_{max}} \tag{3.4}$$

where, χ is taken to be 6–10, corresponding to the number of elements required per wavelength (Kuhlemeyer and Lysmer, 1973). The frequency response of ballast track to moving load is governed by several factors, including: the axle/wheel spacing, track irregularities, and sleeper spacing (Milne et al., 2017). It is seen that a critical resonant vibration commonly occurs in the range of frequency not exceeding 20 Hz (Shih et al., 2018). The maximum frequency occurs in the ballast layer and attenuates with radial distance from the point of excitation. Therefore, the location closer to the load (ballast and capping layers) were provided with finer mesh to capture the dynamic response with more computational accuracy. In contrast, for subgrade, the mesh coarseness could be increased from top to bottom provided that the largest mesh size would satisfy the criteria given in Equation 3.4. This modelling approach has also been adopted by previous studies (e.g. Hall (2002),Shih et al. (2017) and Connolly et al. (2013)).

For instance, based on the material properties stipulated in Table 3.1, the maximum element sizes for ballast, capping, and subgrade are 0.31m, 0.45m and 1.1m, respectively,

for a maximum sleeper passing frequency of f = 72Hz corresponding to the train speed of 450km/h at the top of the ballast layer. Hence, the maximum element size at the ballast layer is taken as 0.1m, 0.15m and 0.5-1m for the ballast, capping and subgrade, respectively. Overall, the discretised FE mesh grid consists of 152,685 nodes and 132,911 8-noded brick elements with reduced integration (element type: C3D8R). The reduced integration significantly reduces the computational time required for solving the integrals of large-scale FE models (Boulbes, 2020).

3.2.5 Boundary condition

The boundary condition at the plane of symmetry allows vertical displacement, while other model boundaries of the finite element domain were created by adopting one-way infinite elements (element type: CIN3D8) as shown in Figure 3.4. The infinite elements enable the incident waves to be absorbed in the model boundary by introducing viscous dampers, which are placed in parallel and perpendicular to the model boundary using (Hibbitt et al., 2020):

$$C_{Ni} = \rho V_P \qquad 3.5$$

$$C_{Ti} = \rho V_S$$

where C_{Ni} and C_{Ti} are coefficients of viscous damping along the normal and tangential directions, respectively, V_P and V_S are longitudinal and shear-wave velocity of the material, whereas ρ is density.

Though the infinite elements provide good energy absorption for most practical modelling cases, they do not provide perfect energy transmission leading to residual reflection (Kouroussis et al., 2014). Hence, the moving load was only applied at the

central portion of the track (at the middle, about 30m in the central portion) to provide an additional buffer zone. This will leave 10m on each side with an extra 2m where the infinite elements are placed. The entire analysis reported in this analysis focuses on the track substructure below the central sleeper, which is 22m away from the infinite element boundary along the direction of train movement, to reduce residual reflection from infinite elements further.

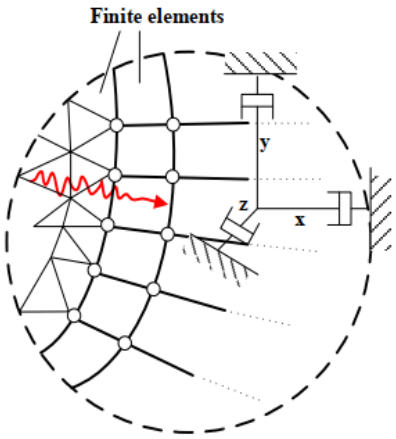

Figure 3.4 Viscous dashpot boundary condition (modified after ABAQUS,2020)

3.2.6 Damping formulation

Rayleigh viscous damping approach is adopted to solve Equation 3.1 in the current 3D-FEM analysis to capture the damping of railroad layers and geometric attenuation, which consists of a damping matrix $[C]$, as a linear combination of mass matrix $[M]$ and a stiffness matrix $[K]$, as follows (Zienkiewicz et al., 2005):

$$[C] = \alpha[M] + \beta[K] \qquad 3.5$$

where, the coefficients α and β are given by:

$$\begin{Bmatrix} \alpha \\ \beta \end{Bmatrix} = \frac{2D}{\omega_1 + \omega_2} \begin{Bmatrix} \omega_1 \omega_2 \\ 1 \end{Bmatrix} \quad 3.6$$

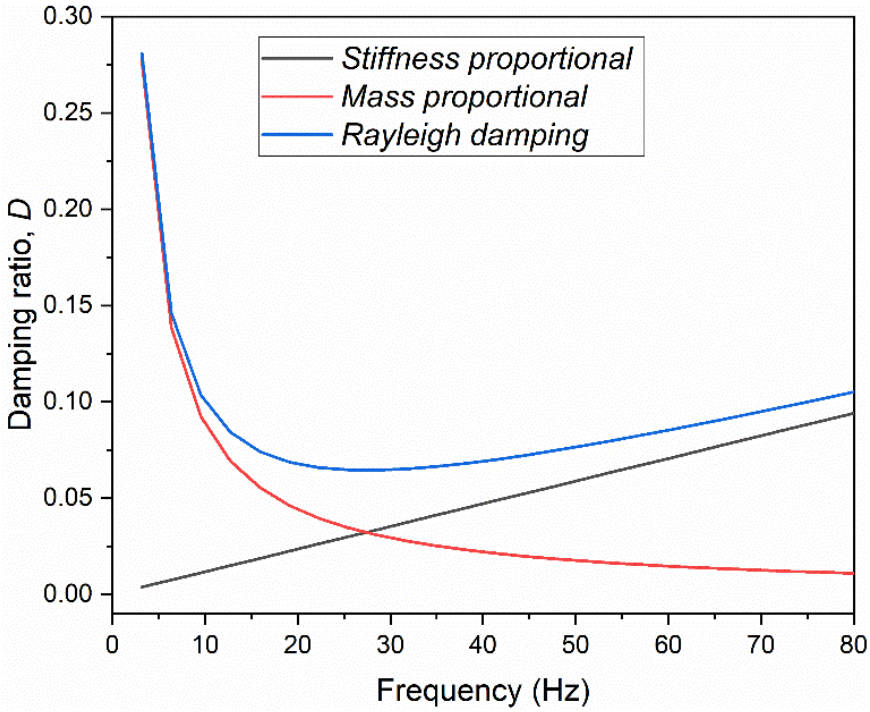

Figure 3.5 Typical Rayleigh damping determination for transient, moving load analysis (modified after Hibbitt et al. (2020))

where, D is the damping ratio, and ω_1 and ω_2 are the two frequencies defining the damping curves in rad/s. To ensure the wave energy associated with moving load is properly dissipated at the boundary and damping is adequately represented, an appropriate frequency range needs to be adopted. The first frequency (ω_1) is considered as a resonant cut-off of frequency of the subgrade, which is the frequency above which the stress waves start to propagate (El Kacimi et al., 2013). It can be approximated using Equation 3.7, where f_p is the cut-off frequency of the subgrade soil and H is the depth of track subgrade (El Kacimi et al., 2013). The second frequency is considered axle passage frequency or loading frequency, assuming higher frequency vibration associated with track and/or wheel-load irregularity is negligible.

$$\omega_1 = 2\pi f_p = 2\pi \frac{V_p}{4H} \quad 3.7$$

Error! Reference source not found. presents the Rayleigh damping formulations e mployed in this study. It can be seen that the low-frequency range attenuates with the mass proportional damping (α) whereas higher frequency range energy attenuates with the stiffness proportional (β).

3.2.7 Interaction modelling between track components

Because of the different characteristics between the track substructure and superstructure components, sliding and separation may occur at their interfaces under moving loads. Two aspects of contact formulations have to be established: contact discretization and contact enforcement (Hibbitt et al., 2020; Lu et al., 2020).

The choice of contact discretisation methods depends on the relative distance betweenpoints on the "slave" surface to the neighbouring points on the "master" surface (Boulbes, 2020). The slave surface is idealised as a group of discrete points not penetrating the master surface. The surfaces have to be defined initially; the surface with coarser mesh is considered as a master surface in this study, which means the stiffer track component with a coarser meshing is assigned to be the master surface (Connolly, 2013).

Figure 3.6 shows the difference between the node-to-surface and surface-to-surface discretisation. The efficiency of node-to-surface method is governed by the relative position of nodes on the slave surface and the adjoining elements on the master surface (Hibbitt et al., 2020; Shih, 2017). Hence, this technique is influenced by the choice of mesh size and type used in model discretisation. If the discretisation at the adjoining

surfaces is poor, then some nodes end up being excluded from the contact solution, as shown in Figure 3.6(a). In contrast, formulations of the surface-to-surface constraint consider the integral over the region around the slave node (Boulbes, 2020; Hibbitt et al., 2020), as shown in Figure 3.6(b). This formulation has been implemented for the sleeper-ballast interface since it improves the accuracy of contact stress and with better convergence. However, the contact between the rail and sleeper is modelled as a tie constraint of the "node to surface" type. This model is typically employed for the contact between complex surfaces due to the discontinuous nature of the sleepers, which reduces the effective contact area at the rail-sleeper interface.

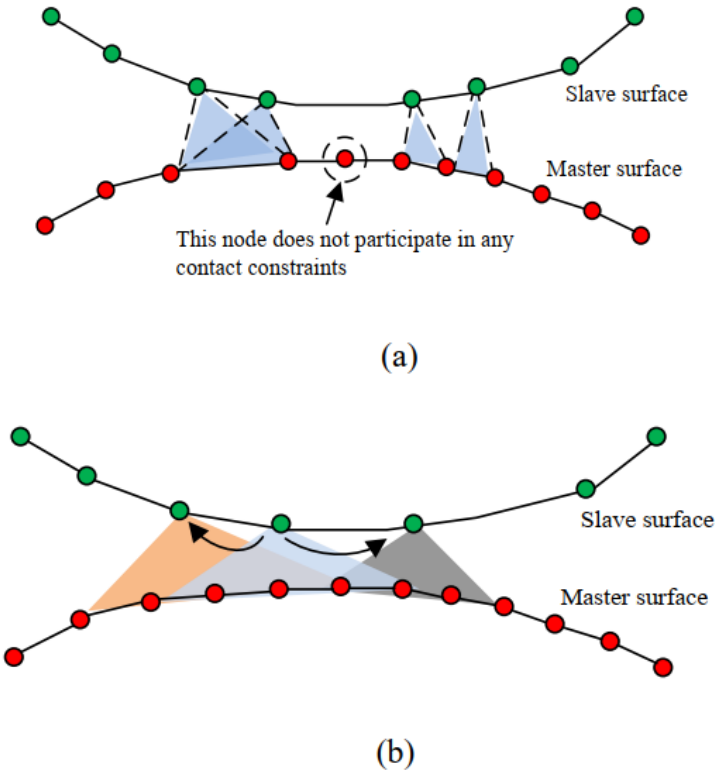

Figure 3.6 Contact modelling (a) Node-to-surface (b) surface-to-surface contact (modified after (Hibbitt et al., 2020; Shih, 2017))

In this study, the contact enforcement between the sleeper and ballast is modelled as surface-to-surface with "hard" normal contact and tangential interaction based on the penalty method with a friction coefficient equal to 2/3 of the tangent of ballast friction angle. This contact formulation allows the formation of a small gap and relative displacement between the sleeper and ballast when the rail cambers upwards under a moving wheel load. Node continuity between the sleeper and ballast is maintained to improve the accuracy of the FEM results at the interface. The tangential contact enforcement between the rigid body representing wheel loads and the rail was set as "frictionless" while the hard contact was implemented in the normal direction (Lu et al., 2020; Saleeb and Kumar, 2011) .

3.2.8 Modelling of moving train load

There are different ways to apply moving load within the scope of railway track analysis by the finite element method. Several authors have applied the triangular loading principle, where the triangular pulse travels from node to node (Araújo, 2011; Hall, 2003; Sayeed and Shahin, 2016). As schematically shown in Figure 3.7, the wheel load, *F*, at one specific *loading node*, n_i, increases once the wheel departs from node, n_{i-1}, reaching a maximum value when the wheel arrives at node n_i, then finally reduces to zero when the wheel arrives at the follwoing node n_{i+1} .

In this study, the numerical modelling of moving load is achieved by applying the vertical load to a rigid body representing a train wheel at the top of the rail; then, it slides horizontally at a constant speed. This approach does not require the application of triangular pulsed at the nodes since it transfers the load through contact interaction between the rigid body wheel and the rail. As the moving rigid body wheel travels over

the rail, the nodes participating in the contact event are continually updated because of the wheel movement and associated evolution in the contact mechanism. Hence, the adjoining nodes on the wheel surface are projected at each time step to the nodes on the rail surface (master surface), as shown in Figure 3.6. Then, the nodal displacements at the particular contact event are computed using inbuilt shape functions and Hermitian polynomials to ensure compatibility of deflection and slope among adjacent elements (Hibbitt et al., 2020). This technique has been implemented and validated for complex moving load analysis involving a coupled vehicle-bridge interaction, moving sprung mass models, and moving load analysis (Lu et al., 2020; Saleeb and Kumar, 2011).

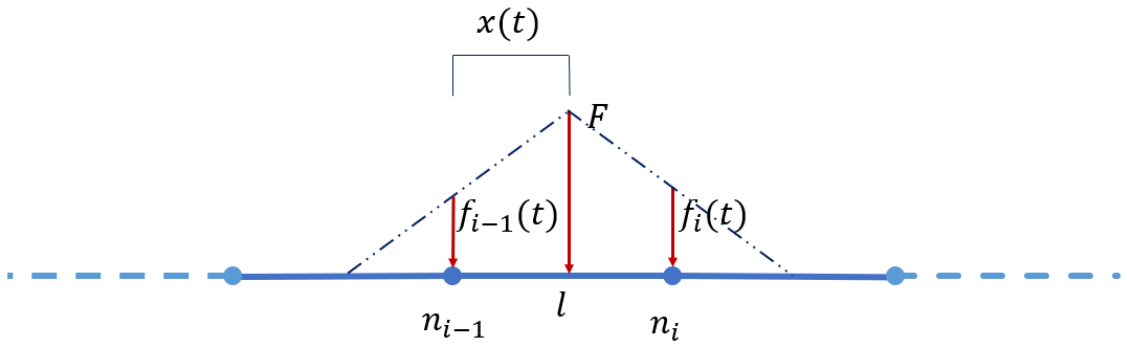

Figure 3.7 Simulation of moving load through triangular pules (Araújo, 2011; Cunha, 2013).

In this approach, the primary system is the track system (designated as a master surface), and the moving load is the secondary system (designated as the slave surface). The tangential contact enforcement between the rigid body representing wheel loads and the rail was “frictionless”. Since the load is translating beyond the typical element length along the longitudinal direction, the “finite slide” formulation was implemented at each time increment. Furthermore, the hard contact was implemented in the normal direction with penalty constraint enforcement. Figure 3.8 illustrates the geometry and axle load

configuration of a typical Australian and South African freight wagon (ARTC, 2011; Priest et al. 2010) considered in the model validation. Details of the train loading are shown in Figure 3.8 and companion Table 3.2.

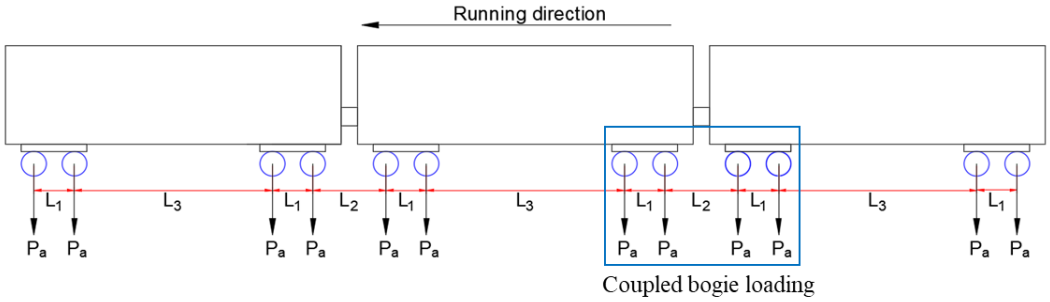

Figure 3.8 Schematic geometry and axle load configuration of a typical Australian freight train

Table 3.2 Geometry and axle load of the train loading considered in model validation

Validation cases	Train loading geometry (m)			Standard axle load, P_a (kN)
	L_1	L_2	L_3	
South African	1.83	1.93	8.31	260
Australian	1.72	3.1	8.4	250

In this study, the moving load is applied in two stages. Initially, the load is initialized from 0 to the maximum axle load (F_{max}) for a time t_o (t_o=0.2second) to reduce the signal disturbance. As purely static initialization is computationally incompatible with dynamic explicit analysis in ABAQUS FE modelling, the moving load is applied gradually at the beginning of the simulation to minimize a signal disturbance that occurs when a sudden constant amplitude impulse load is applied at the start of the simulation. Preliminary analysis showed that an initialization time (t_0) close to 0.2s provided insignificant

disturbance in the time history response of displacement and stresses, which is consistent with the previous literature (Araújo, 2011; Fernandes, 2014; Hall et al., 2022).

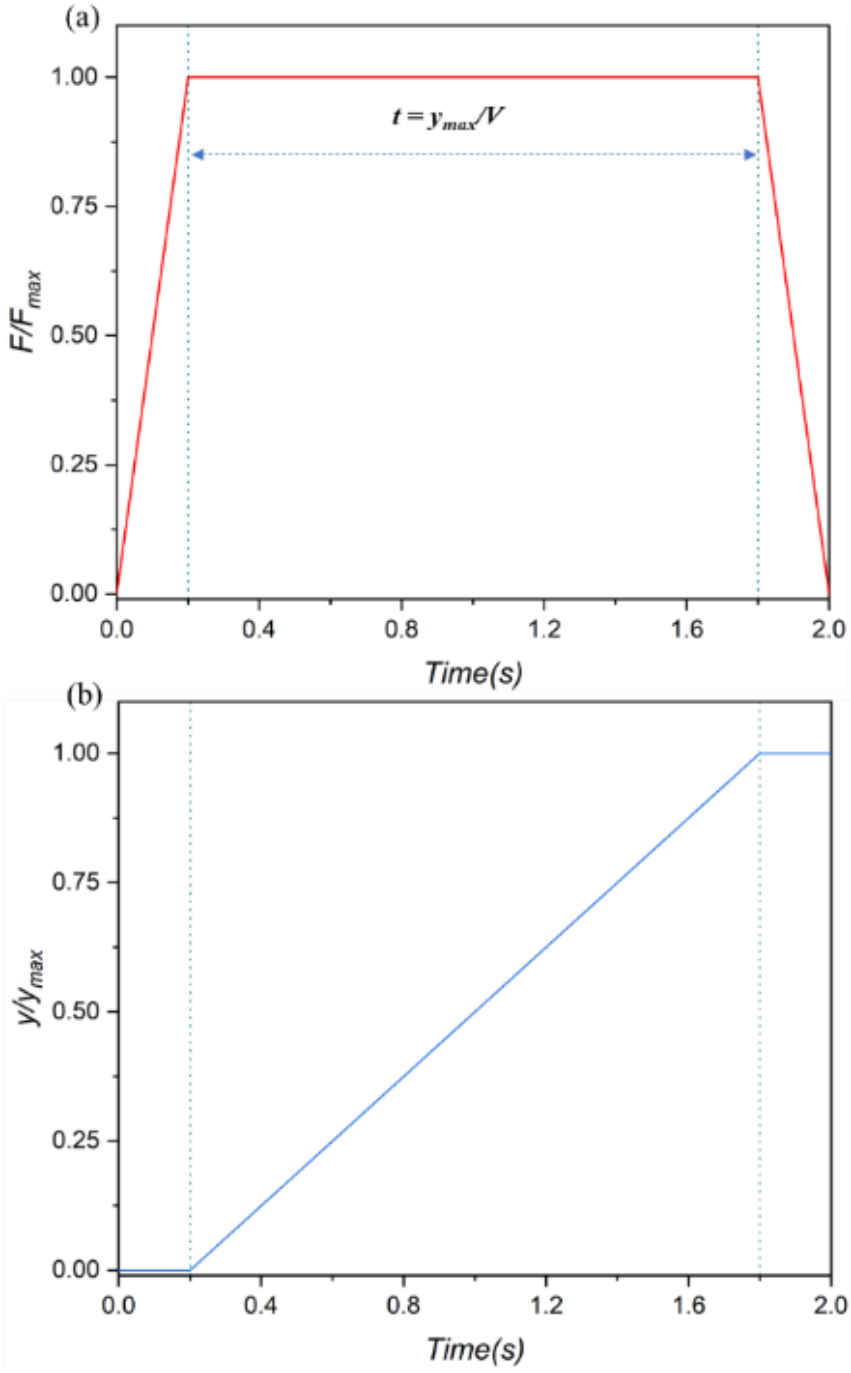

Figure 3.9 Load application methods (a) load initialization amplitude function (b) Speed initialization displacement function

In initialization stage, the wheel load is constrained in all directions except the vertical one to ensure the vertical load is transferred to the track. In the second phase, a constant velocity is applied to the load along the longitudinal direction, and here y_{max} is the distance covered by the moving load. For instance, the load and displacement amplitude function for the first load, for a speed of 60km/h moving over 30m portions of the track ($\Delta t = \frac{y_{max}}{V} = 1.8$s), is shown in Figure 3.9. These functions can be used for the multiple load sequence by considering the time lag of subsequent loads.

3.3 Model validations

3.3.1 Validation of Vryheid track

Priest et al. (2010) presented the results of ground deformations and transient vertical stress that occur during the passage of 26 tonnes axle load train traveling at 13.2m/s (47.52 km/h) measured at the Vryheid track. The instrumentation consists of particle image velocimetry to measure track transient deflection and a geophone arrangement to measure vertical vibrations at various depths. Figure 3.10 compares predicted transient vertical displacement taken at the sleeper and the middle of the structural fill (at a depth of 0.78m) with the field data.

An acceptable agreement is observed between the FEM prediction and field data, while the slight difference could be attributed to the minimal difference on the depth at which the data is retrieved in FE model and field measurement. The apparently low displacement can be attributed to the large stiffness of the natural ground, which is considered as the subgrade in the current FE model; in fact, it is a weathered tillite that is still substantially stiffer than a typical overconsolidated coastal clay. Moreover, it was reported that four

layers of compacted structural fills, each 200mm, had been placed below the ballast layer, as indicated in Table 3.2.

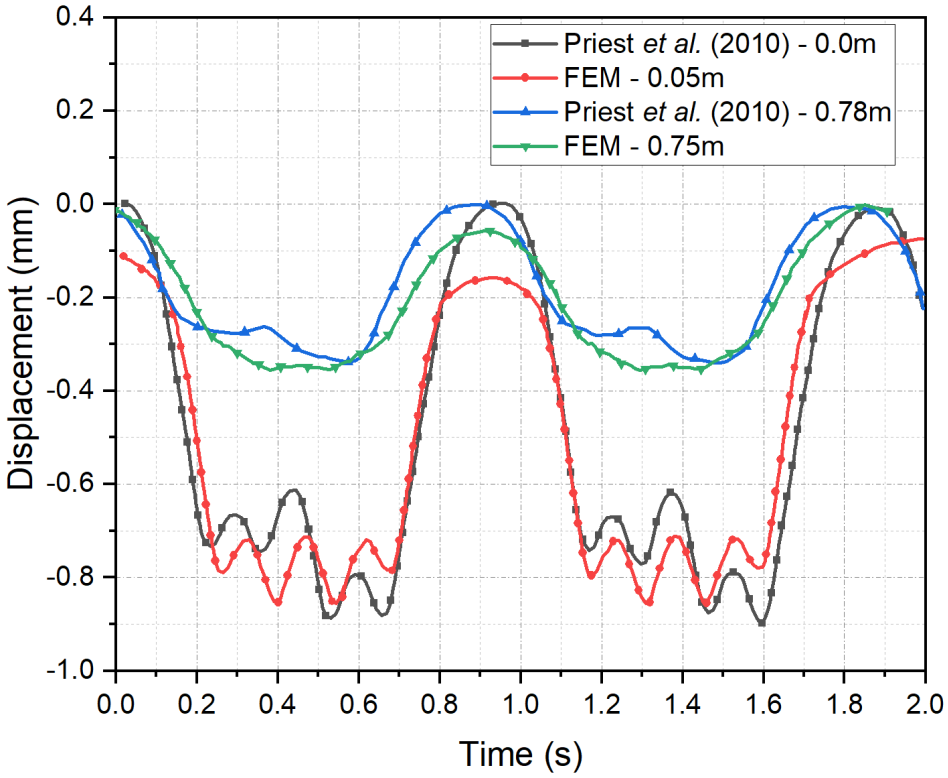

Figure 3.10 Comparison of measured and predicted transient displacement for the Vryheid track

3.3.2 Validation of Bulli track

In the town of Bulli (75 km South of Sydney, Australia), Indraratna et al. (2010) carried out an extensive track monitoring program with field data recorded over 18 months under a few millions train loading cycles. The track was built over a stiff subgrade consisting of over-consolidated silty clay (estuarine) intermixed with shale cobbles and gravels with adequate strength to sustain heavy haul trains (Indraratna et al., 2010). The monitoring scheme consisted of 20 pressure cells, settlement pegs and horizontal displacement transducers as shown in Figure 3.11.

To validate the FE modelling of this Bulli track model, the time history response of vertical stress was calculated at various depths and then compared with the field measurements. Figure 3.12(a) presents the vertical stress attenuation in the track substructure from the FE analysis for a freight train of a 25-tonne axle load. The stress at the top of the ballast layer was retrieved from the corresponding peak nodal output, while at all other depths, the stresses were computed at the integration point of elements. The vertical stresses agree with those measured from the case study for a train running at 60km/h. The magnitude of vertical stress at the sleeper-ballast interface from another instrumented track (town of Singleton, North of Sydney) was also validated within reasonable accuracy (Nimbalkar and Indraratna 2016) for 25-tonne axle loading.

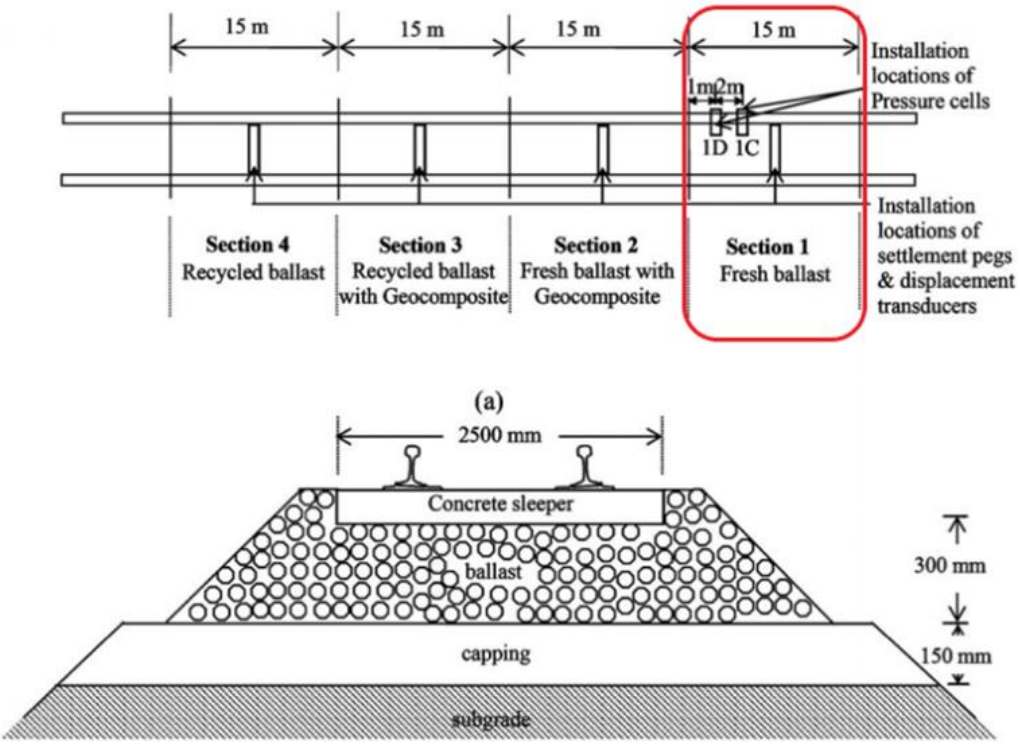

Figure 3.11 Schematic of ballasted track at Bulli, NSW (adopted from Indraratna et al. (2010))

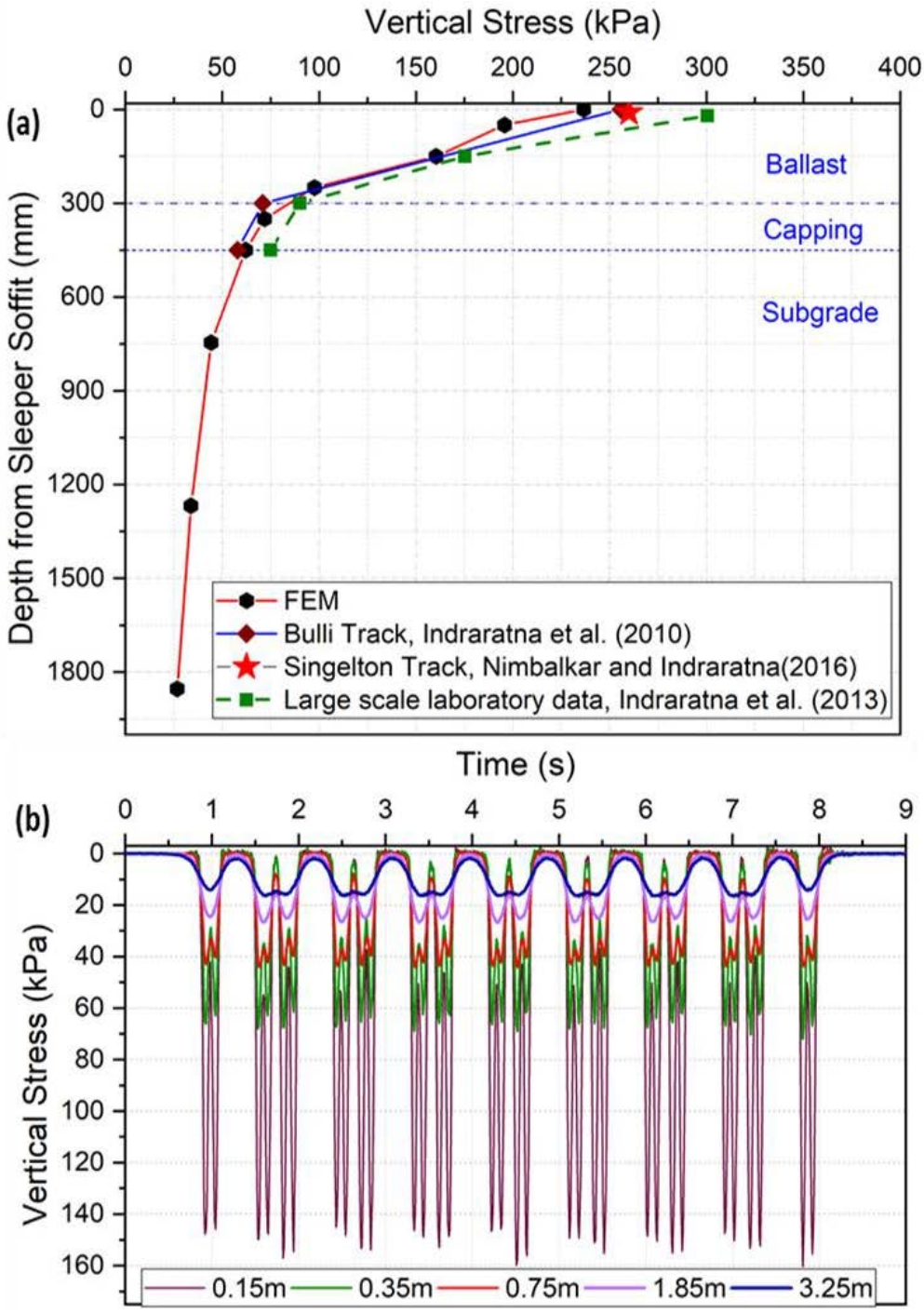

Figure 3.12 (a) Validation of vertical stress with depth and comparison with field studies; (b) Time history of vertical at various depths measured from sleeper bottom, peaks plotted in (a)

In addition, vertical stresses based on the laboratory test results conducted by Indraratna et al. (2013) are plotted in Figure 3.12(a), and they show slightly higher than the FE

results. This is because the laboratory equipment has a rigid boundary at a limited depth, which inevitably increases the vertical stress at the base of the ballast layer. Figure 3.12(b) shows the time history response of vertical stress at various depths from the bottom of the sleeper. The data indicate that the peaks of 'M' shape vertical stress pulses flatten out as the stress from the nearby axle starts to overlap at about 0.75m. The vertical stress time history peaks correspond to predicted stress attenuation from the FE simulation, as indicated in **Error! Reference source not found.**Figure 3.12(a). Hence, the model can adequately represent the vertical stress response of Australian track and loading conditions.

3.3.3 Moving load on the half-space model

The accuracy of the proposed FE model relies on the accuracy of the stress-deformation response across all speeds simulated. In section 3.3.2, the attenuation of vertical stresses from FE prediction is validated against field measurement conducted for 60km/h train speed at Bulli, NSW, Australia (Indraratna et al., 2010). Hence, model validation is required at the high-speed range to ensure the proposed model can capture stress-displacement response at speeds approaching the critical velocity. The most widely used field measurement for validation of transient vibration analysis for high-speed trains using FE analysis is Lesdsgaard, Sweden (Dong et al., 2019; Hall et al., 2022; Madshus and Kaynia, 2000; Shih et al., 2017). However, the stress variation and associated attenuation of stress waves in the track substructure was not reported. In light of the limited availability of field measurement capturing the stress response at high speed, the proposed model is validated against the analytical model proposed by Eason (1965).

Eason (1965) developed a solution for vertical pressure (P) distributed on rectangular area which moves with a velocity (V) on the surface of half-space along a straight line as shown in Figure 3.13.

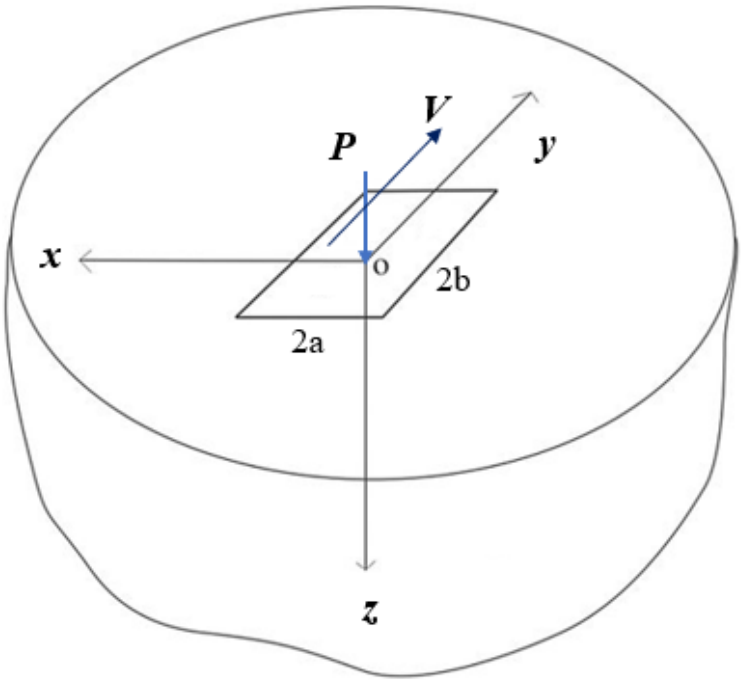

Figure 3.13 Schematics of semi-infinite space subjected to a surface rectangular moving load (modified based on Eason (1965))

$$\sigma_x = -\frac{P}{\pi^2}\int_0^{\frac{\pi}{2}} \frac{1}{H\sin\phi\cos\phi}\left[\left(1-\frac{1}{2}\alpha_2^2 cos^2\phi\right)\left[sin^2\phi + \left(\frac{1}{2}\alpha_2^2-\alpha_1^2\right)cos^2\phi\right]\nu_1 - \gamma_1\gamma_2\upsilon_2 sin^2\phi\right]d\phi \quad 3.8$$

$$\sigma_y = -\frac{P}{\pi^2}\int_0^{\frac{\pi}{2}} \frac{\cot\phi}{H}\left[\left(1-\frac{1}{2}\alpha_2^2 cos^2\phi\right)\left(1+\frac{1}{2}\alpha_2^2-\alpha_1^2\right)\nu_1 - \gamma_1\gamma_2\upsilon_1\right]d\phi \quad 3.9$$

$$\sigma_z = -\frac{P}{\pi^2}\int_0^{\frac{\pi}{2}} \frac{1}{H\sin\phi\cos\phi}\left[\left(1-\frac{1}{2}\alpha_2^2 cos^2\phi\right)^2\nu_1 - \gamma_1\gamma_2\upsilon_2\right]d\phi \quad 3.10$$

$$H = \gamma_3^2 - \gamma_1\gamma_2 \quad 3.11$$

$$\gamma_1 = \sqrt{1-\alpha_p^2 cos^2\phi} \quad 3.12$$

$$\gamma_2 = \sqrt{1-\alpha_s^2 cos^2\phi} \quad 3.13$$

$$\gamma_3 = 1 - 0.5\alpha_s^2 cos^2\phi \quad 3.14$$

$$\nu_{1,2} = \log\left[\frac{(a\cos\phi - b\sin\phi)^2 + \gamma_{1,2}^2 z^2}{(a\cos\phi + b\sin\phi)^2 + \gamma_{1,2}^2 z^2}\right] \quad 3.15$$

where ϕ is an auxiliary variable introduced during integral transform and integrated from 0 to π; $\alpha_p = V/V_P$ and $\alpha_p = V/V_s$ are speed ratio where V_P and V_s are compression and shear wave velocity. This solution is applicable only when the speed is less than the Rayleigh wave speed of the half-space since the function H, which is the denominator of the integrands, becomes 0 when $\phi = \pi/2$ (Eason, 1965; Wei et al., 2017).

In this study, the results of semi-analytical solutions shown above are employed to evaluate whether the model boundaries are adequate and justifiable due to the lack of field stress measurements to validate the model at high speeds It is noted that the solution is applied for sub-critical speed range and is only applicable for homogeneous soil. Hence, a moving square load with 50kPa rectangular vertical stress at the top of subgrade corresponds to the stress measurement by Indraratna et al. (2010), using VDLOAD user subroutine shown in Appendix B.

Figure 3.14(a-c) shows a comparison between the semi-analytical and FE model for lateral, horizontal, and vertical normal stresses. It can be observed that the FE model gives a reasonable prediction of stresses until the speed corresponding to 70% of $\frac{V}{V_s}$. The difference observed beyond 70% can be attributed to the inherent limitation of the semi-analytical model in around Rayleigh wave speed of the subgrade and the damping effect considered in the FE simulations.

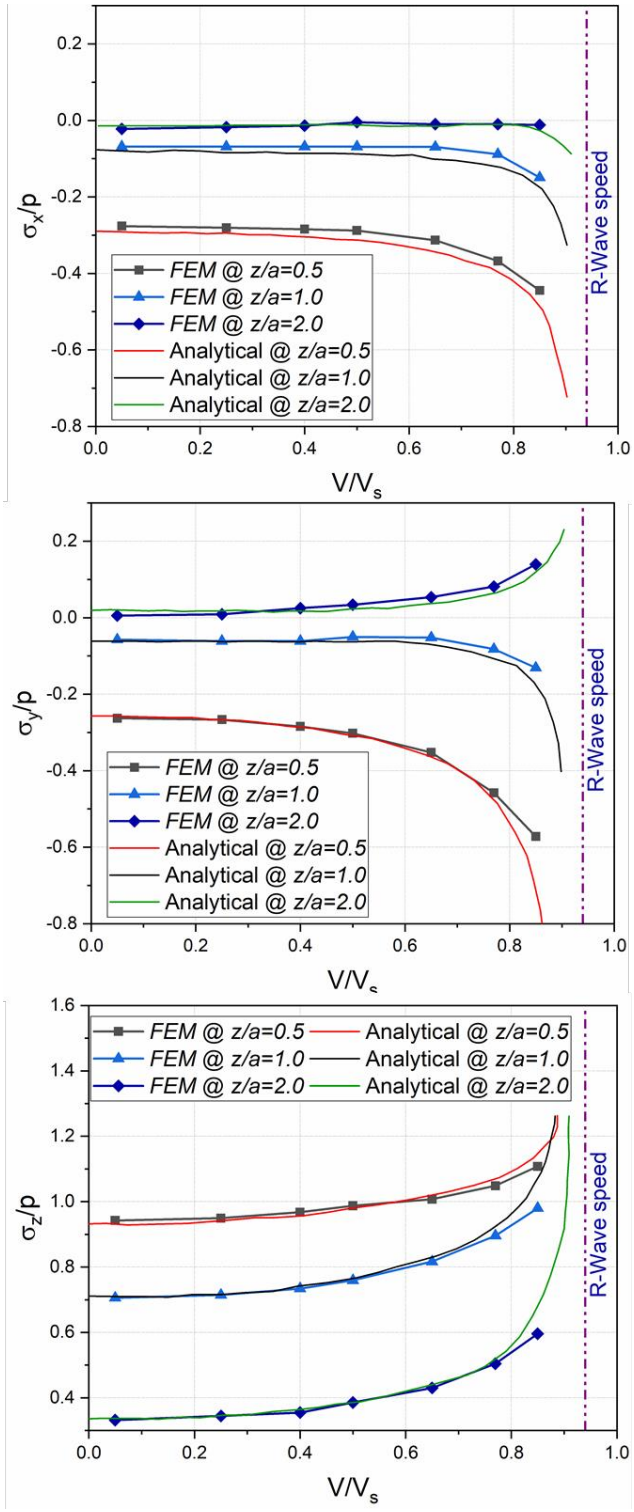

Figure 3.14 Model validation for moving load on half space against analytical method proposed by Eason (1965): (a)lateral stress (σ_x) (longitudinal stress (σ_y) and (c vertical stress (σ_z)

3.4 Chapter summary

In this chapter, a three-dimensional finite element model is developed to study the effect of moving load on the dynamic responses of tracks. The track substructure is modelled using elasto-plastic models to capture the stress-displacement response under increasing trains speed and axle loads and associated shear failure of track geomaterial under instantaneous train loading. The penalty contact is implemented to account for the sliding and separation at sleeper-ballast interface as train wheel traverse. During the dynamic analysis of moving loads, the infinite elements are successfully integrated at the model boundaries to impede reflection of outward propagating waves back into the model.

The implementation technique described in this chapter was successfully validated against two distinct and well-documented field measurements available in the published literature. Furthermore, the model prediction is compared with semi-analytical solution for various speeds approaching the critical speed showing an acceptable agreement in terms of transient displacement response. This developed 3D FEM model will be implemented in Chapter 4 to study the critical speed and associated vibration responses of ballasted tracks under increasing train speed.

CHAPTER 4 CRITICAL SPEED AND DISPLACEMENT RESPONSE OF BALLASTED TRACK

4.1 Introduction

This chapter investigates the critical speed of ballasted track with a special focus on Australian loading and track conditions. The effect of train speed on vertical and lateral displacement is presented by varying subgrade properties. The developed FE in Chapter 3 is further extended for the predictions of critical speed.

Previous studies on the relationship between track transient response and Rayleigh wave speed have confirmed that the high vibration at train speed close to critical speed results in track deterioration and risk of train derailment. Hence, examining the track response at speed closer to critical speed is essential to understanding the mechanism of dynamic amplification which is one of the main focuses of this chapter. The main content of this chapter has been published in the Transportation Geotechnics (Tucho et al. (2022)).

4.2 Critical speed of a ballasted track

In order to study the effect of increasing train speed, a train loading configuration simulating the Australian standard wagon (RAS 210) equivalent to 20.5 ton axle load could be considered (Indraratna et al. 2010). The ballast and capping material parameters were adopted from the triaxial test results reported by Indraratna et al. (2011). The subgrade was assumed to have a resilient modulus(E_s) of 50 MPa corresponding to material parameters (Table 3.1).

Figure 4.1(a-c) shows the variations in deformation contours when the moving load speed increases from 60 km/h to 360 km/h as captured by the 3D-FEM analysis. At a relatively low speed, the vertical deformation contours are almost quasi-symmetric. In contrast,

asymmetrical and cone-shaped transient displacements are observed at a higher speed, a phenomenon similar to the condition when an airplane travels through a sound barrier (Krylov et al., 2000; Madshus and Kaynia, 2001). It can be seen from Figure 4.1(b) that when the train speed further increases and approaches a high speed of 300 km/h, the deformation contour shows a noticeable development of the Match cone that results in the amplification of the dynamic track deformation.

Figure 4.2 presents the predicted vertical dynamic displacement of the track at various speeds when subjected to a moving coupled bogie load. The simulations were carried out based on elastic and elasto-plastic analysis. It is noted that the predicted dynamic displacement data are plotted versus normalised coupled bogies using the relationship $\frac{Vt}{L_b}$ (where V is the train's speed, t is the time required for the coupled bogies to travel across the FE mesh, and L_b is the total length of coupled bogie). This normalisation is selected to combine and present all the speed variations on a common scale, which would otherwise be six distinct plots for each speed.

The critical speed is defined as the speed that results in the peak transient displacement. For both cases of adopted material models, the changes in vertical displacement patterns correspond to the increased speed change from the range of sub-critical (60km/h), critical (300km/h) and super-critical (360 & 450 km/h) can be observed. For a given rail-formation condition considered herein, the vertical displacement time histories for the case of 60km/h and 120km/h are very similar, consistently plunging following the footprint of the bogies, both at the front and rear ends of the loads; in fact, this is a quasi-static stress/deformation response. In contrast, at higher speeds, the displacement is amplified, and the peak displacement is located towards the rear end of the load,

indicating a lag between the time of arrival of the axle load and the R-waves propagating at the track surface.

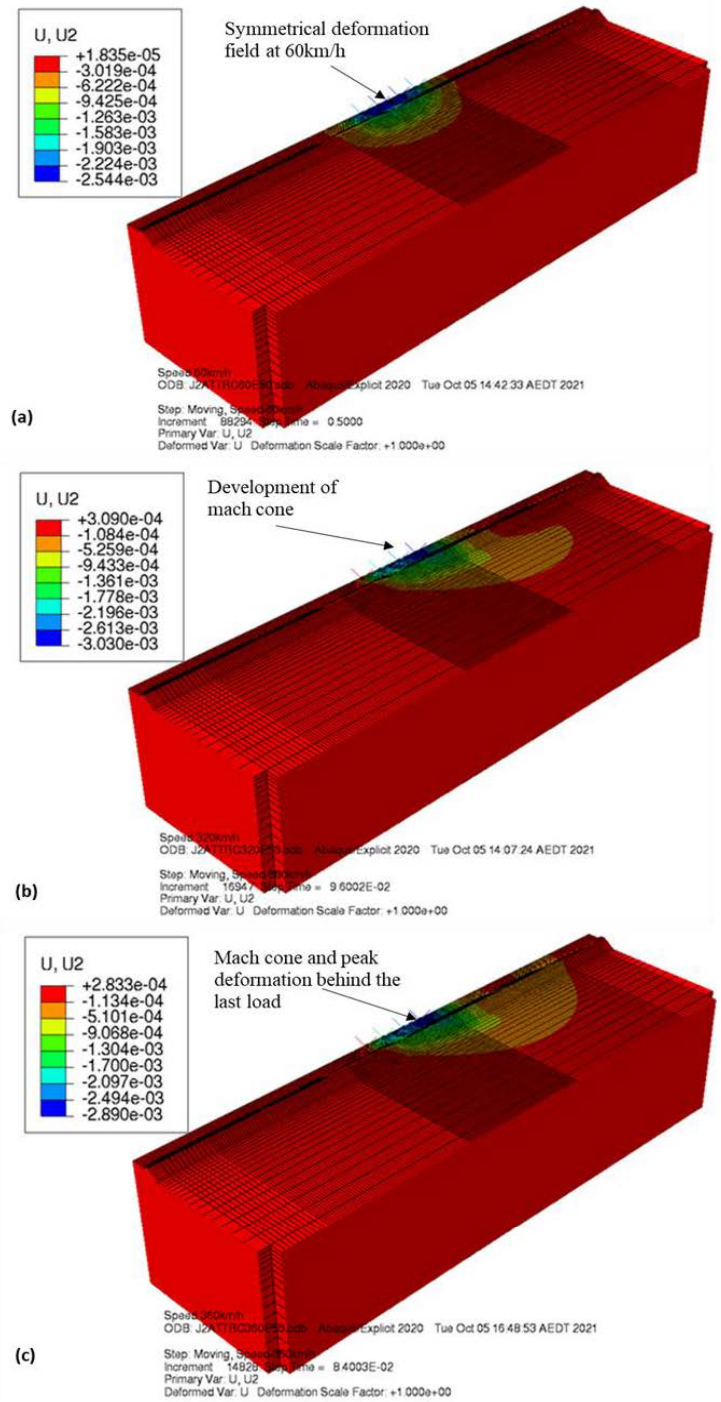

Figure 4.1 Predicted transient deformation contours captured from FEM simulations for: (a) Train speed: 60km/h; (b) Train speed: 300km/h; and (c) Train speed: 360km/h

Figure 4.3 shows the variation of downward vertical transient deflection (δ_{dvp}) and the distance at which the peak displacement shift (δ_{dvs}) from the center line of the coupled-bogie towards the rear end of the moving load. The 3D FE analysis shows the amplitude of the δ_{dvp} measured at the middle of ballast layer increases with the train speed, reaching a maximum value at 300 km/h and 240 km/h for elastic and elasto-plastic analysis, respectively. Subsequently, the value of δ_{dvp} decreases with further increased train speed, exceeding the Rayleigh wave speed of the subgrade.

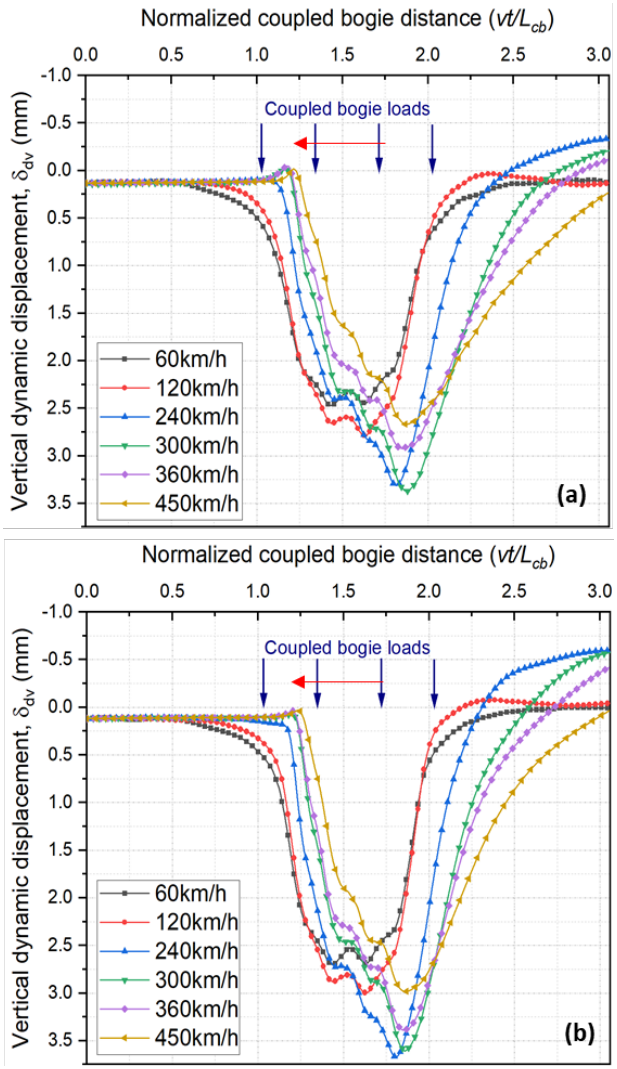

Figure 4.2 Predicted dynamic displacement with increasing speed for different substructure models: (a) Elastic analysis; and (b) Elasto-plastic Drucker-Prager (D-P)

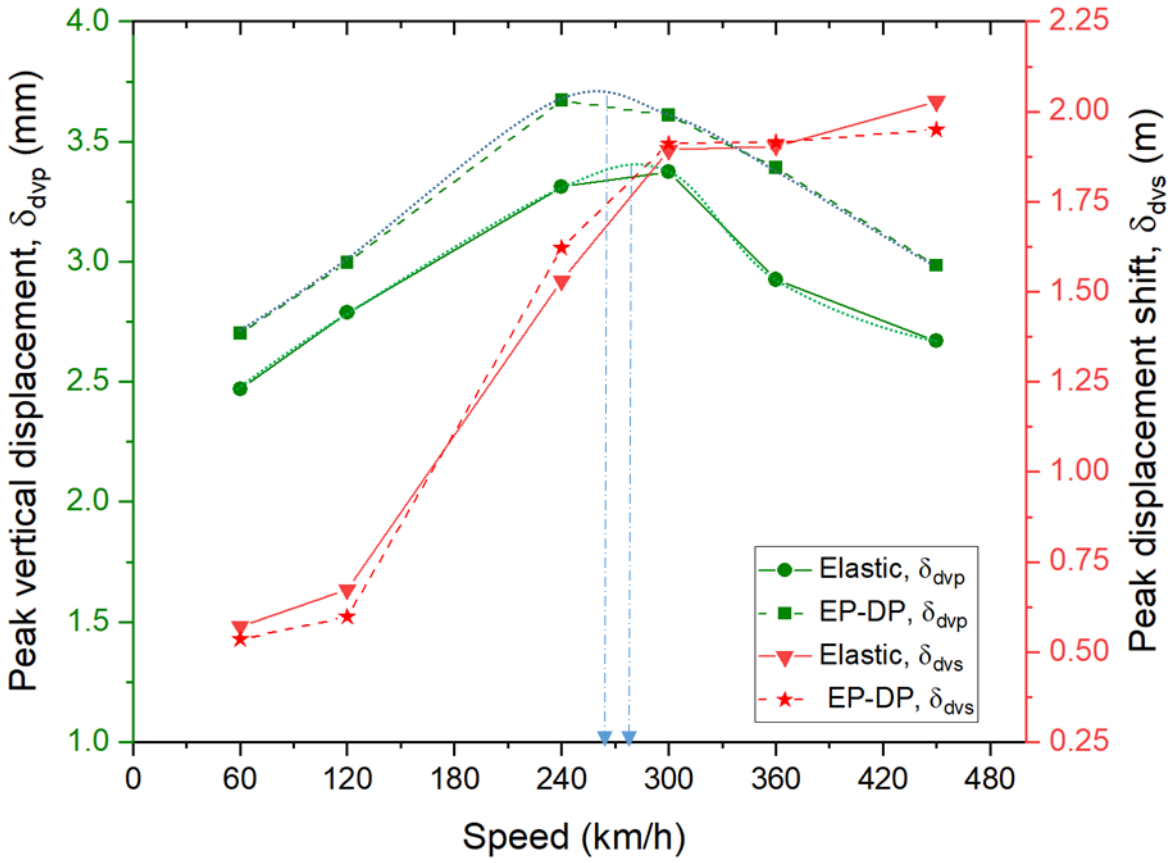

Figure 4.3 Comparison of dynamic displacement and peak displacement shift with increasing speed between elastic and elasto-plastic analysis (EP-DP)

It can be noted that vertical deflections observed at 240km/h and 300km/h do not show a significant difference, indicating the possibility that the response peaks between those speeds. Hence, the choice of the constitutive model adopted for the track substructure does not significantly affect the critical speed, with the critical speed predicted from the elastic response being 265km/h while the elastoplastic is 280km, which is about a 6% discrepancy. This could be attributed to the fact that this analysis considered a limited number of cycles (i.e., only coupled bogies are simulated in the current analysis), which makes the associated plastic response from elasto-plastic analysis minimal.

However, the vertical displacement from elasto-plastic analysis using the Drucker-Prager yield criterion (EP-DP) results in a higher transient deflection throughout the simulated speed range. It is observed from Figure 4.3 that at the critical speed (V_R), the difference in dynamic vertical displacement between the elastic and elastoplastic model is about 11%.

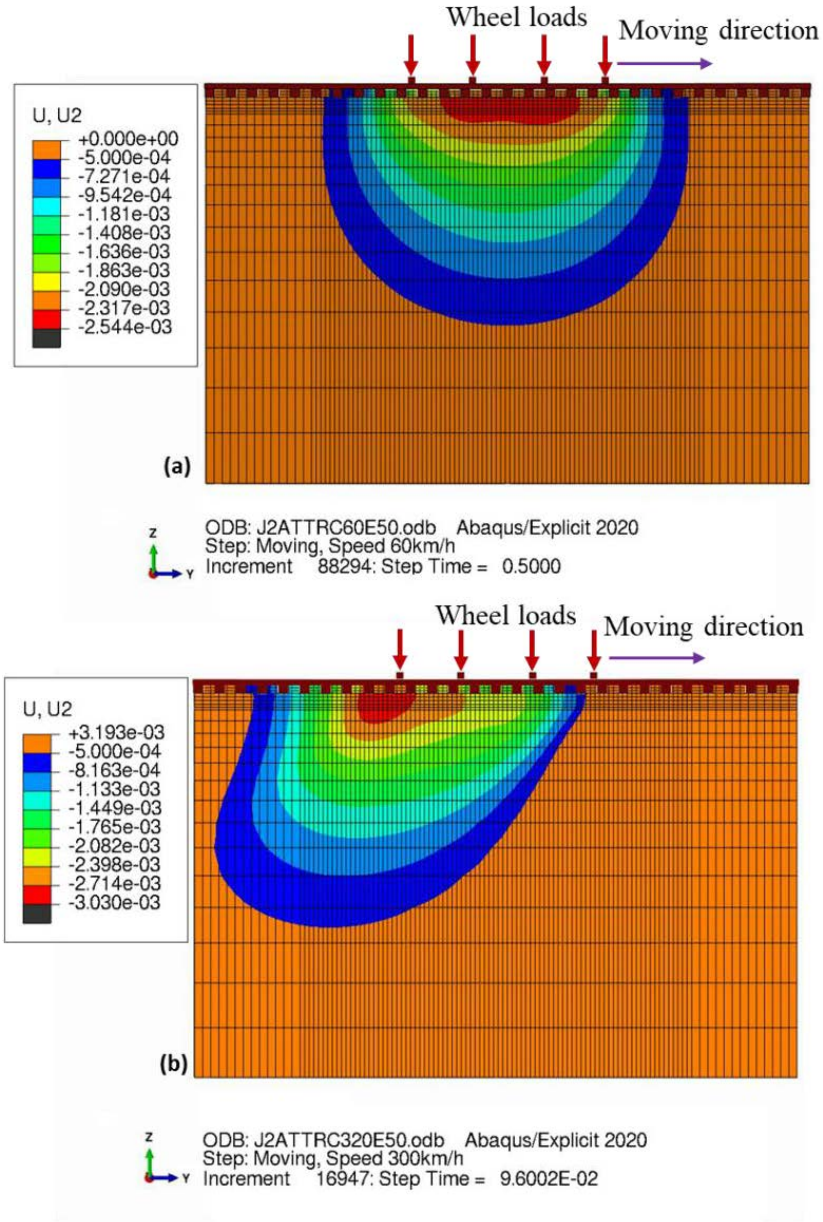

Figure 4.4 Vertical displacement contour at the speed of (a) 60km/h and (b) 300km/h

However, the general trend of the predicted amplification of vertical displacement remains almost identical, irrespective of the material model. For instance, the DAF at the critical speed is 1.37 and 1.36 for elastic and elastoplastic models, respectively, based on vertical displacements under moving train loading. This is evidently lower than the amplification of dynamic deflection as reported for very soft to soft subgrade (i.e. shear wave velocity less than 40m/s), in which case, a critical amplification factor exceeding 200% (DAF ~3) is recorded (Kaynia et al., 2000; Sayeed and Shahin, 2016).

Figure 4.3 also shows a phase-shift between the loads and the displacement field whereas Figure 4.4 indicates the trailing vertical displacement contour at quasi-static and dynamic states, when the train speed increases from a low speed (i.e., quasi-static at 60km/h) to a higher speed of 450 km/h. When the speed increases from 60km/h to 120km/h, the displacement shift is almost constant; hence the displacement peak coincides with the location of the middle axles of the coupled bogies considered. The phase lag increases from about 0.6m at 120km/h to about 1.95m at high-speed exceeding 300km/h, for both elastic and elasto-plastic models. It is noticeable in Figure 4.3 that once the speed exceeds 300km/h, the phase lag (δ_{dvs}) in the peak displacement remains almost constant with speed while vertical displacement (δ_{dvp}) decreases.

In addition to increased vertical displacement, the CPU time required to solve the moving load problem increased in track models simulated with elastoplastic constitutive models, compared to elastic domain analysis, as shown in Table 4.1. The simulations were conducted using iHPC shared computational facility at the University Technology of Sydney using 16 parallel processing cores from the available 56 cores on the workstation computer (Intel® Xeon® Gold 6238R Processor 38.5M Cache, 2.20 GHz). The run time

of FE analysis depends on several factors, such as model size, degrees of freedom, mesh refinement, material models, available physical and/or virtual memory, and the number of output variables computed.

Table 4.1 Run time comparison between elastic and elastoplastic simulation

Speed (km/h)	Elastic model (hr)	Elasto-plastic model (hr)
60	6.71	10.67
120	3.90	6.32
240	2.39	4.30
300	2.06	3.45
360	1.86	2.72
450	1.71	2.41

4.3 Lateral displacement

Figure 4.5 presents the distribution of peak lateral displacements that are measured at the shoulder ballast (Section A-A) in the ballast and capping layer subjected to different train speeds based on elastic and elastoplastic analysis. For both material models, the lateral displacement increases with the train speed until it reaches the critical speed of 300km/h and reduces towards the supercritical speed range. Although the critical speed predicted with respect to the vertical displacement (*i.e.,* 300km/h as shown in Figure 4.3) and lateral displacement (Figure 4.5(a) and (b)) remains the same, the magnitude of lateral deformation is significantly higher by about 260% when elastoplastic model capturing the dilation of ballast is used for predicting track response. Hence, a ballasted track designed with pure elastic theory cannot capture the lateral spreading of the ballast stratum; and hence runs the risk of lateral instability.

At low speed (<120km/h), the peak lateral displacement exhibits a slight increment with depth around the bottom ballast layer, then gradually reduces in the capping layer. This is because the top of the ballast layer is subjected to a lower lateral (confining) stress than

the bottom ballast layer, since the moving wheel load is applied away from the end of sleeper (at 0.5325m for standard gauge track). This result is consistent with previous large-scale laboratory tests and numerical studies (Indraratna and Nimbalkar, 2013; Navaratnarajah et al., 2018). In contrast, at high speed (>240km/h) the lateral displacement is maximum at the ballast top and reduces with track depth since the stress wave propagation significantly alters the response at the surficial layers.

It can be seen that the peak lateral displacement increases with the increased speed, and it decreases when the speed exceeds beyond the critical velocity of the moving load (Figure 4.5(b)). The lateral displacement response at speeds of 60km/h and 120km/h (i.e., corresponds to the quasi-static condition) shows insignificant amplification. However, a significant amplification of lateral displacement is observed for the high speeds of 240km/h, 300km/h and 360km/h. The effect of speed is more pronounced in the ballast layer, where the maximum increase over 300% is observed in the ballast top and reduces with the depth of the trackbed.

Figure 4.5(b) and (c) show plots of lateral displacement contours predicted by the FEM analysis indicating any critical zones in terms of excessive lateral displacement that is situated beneath the edge of the sleeper and towards the track shoulder. It is predicted that the edge of the track towards the shoulder becomes more critical to be stabilised against excessive lateral spreading (dilation) and associated track instability and loss of track alignment than the middle of the track, hence the need for enhanced confinement required from the sides of the track. In other words, the loading applied by moving trains will always generate transverse lateral forces (in the direction parallel to the sleepers), causing

ballast and capping materials to move laterally in the absence of sufficient confining pressure from the track shoulder regions.

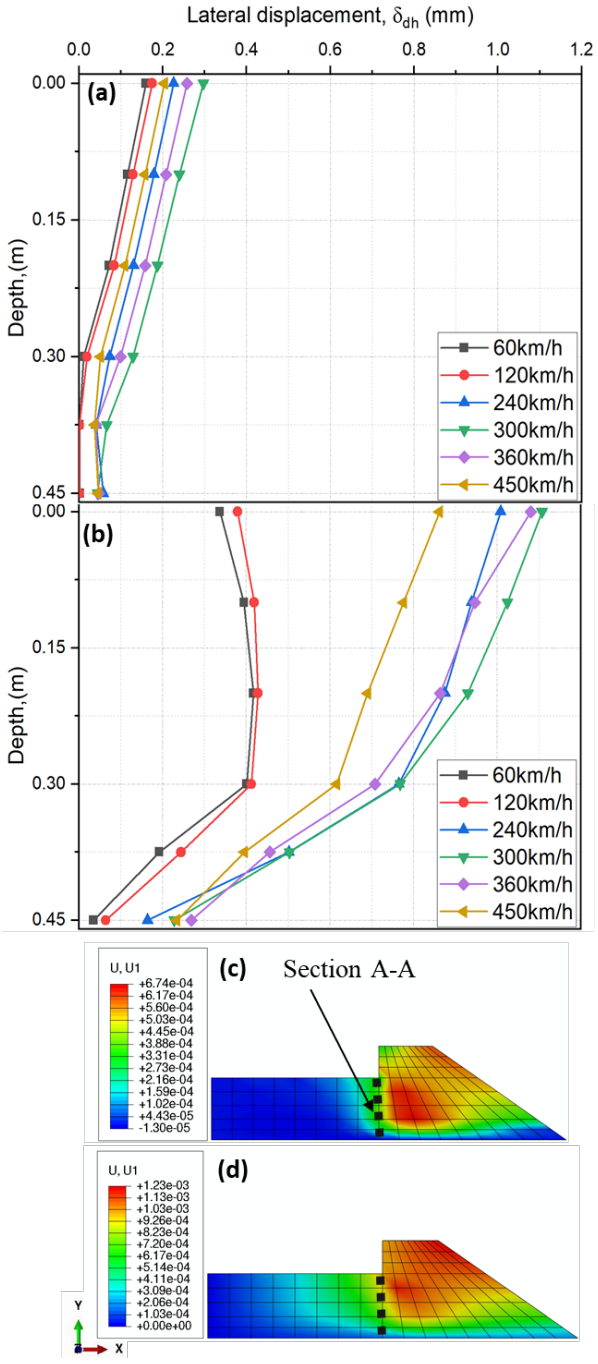

Figure 4.5 Dynamic lateral displacement in railroad at sleeper edge measured from ballast top: Effect of speed on dynamic lateral displacement at sleeper edge (a) elastic response (b) elastoplastic response (c) typical lateral displacement contour at 60km/h; and (c) typical lateral displacement contour at 240km/h

4.4 Effect of subgrade stiffness on vertical and lateral displacements

The influence of subgrade on vertical and lateral displacement is studied by varying subgrade modulus, considering elastoplastic geomaterials. The selected subgrade modulus (E_S) are 25, 50 and 100 MPa corresponding to theoretical Rayleigh wave velocities of about 240, 340 and 480km/h. The lowest subgrade modulus is assumed to be E_S = 25MPa to represent rail tracks built on deep estuarine deposits and soft clays, which could result in excessive settlement and vibration under moving train loading. For instance, ballasted track built on mud and soft clay subgrade with E_s= 7-25kPa (or V_s= 44-75m/s) at Ledsgaard, Sweden, showed excessive vibration exceeding 400% (Hall, 2002; Madshus and Kaynia, 2000). It is not unusual to encounter challenging subgrade conditions in countries like Australia, where many rail tracks are located along coastal areas. For instance, a ballasted track constructed on a deep estuarine deposit in Sandgate, Australia, showed significant compression with train speed limited to 40km/h (Indraratna et al., 2010).

It is observed from Figure 4.6 that, for the subgrade modulus of 25 and 50MPa, the vertical displacement increases with the train speed which peaks in the vicinity of the Rayleigh wave speed of the subgrade, and then decreases. However, a clear decreasing trend is not achieved for the stiffer ground (E_S = 100MPa) since the speed range considered in this study is less than the Rayleigh wave speed of the subgrade.

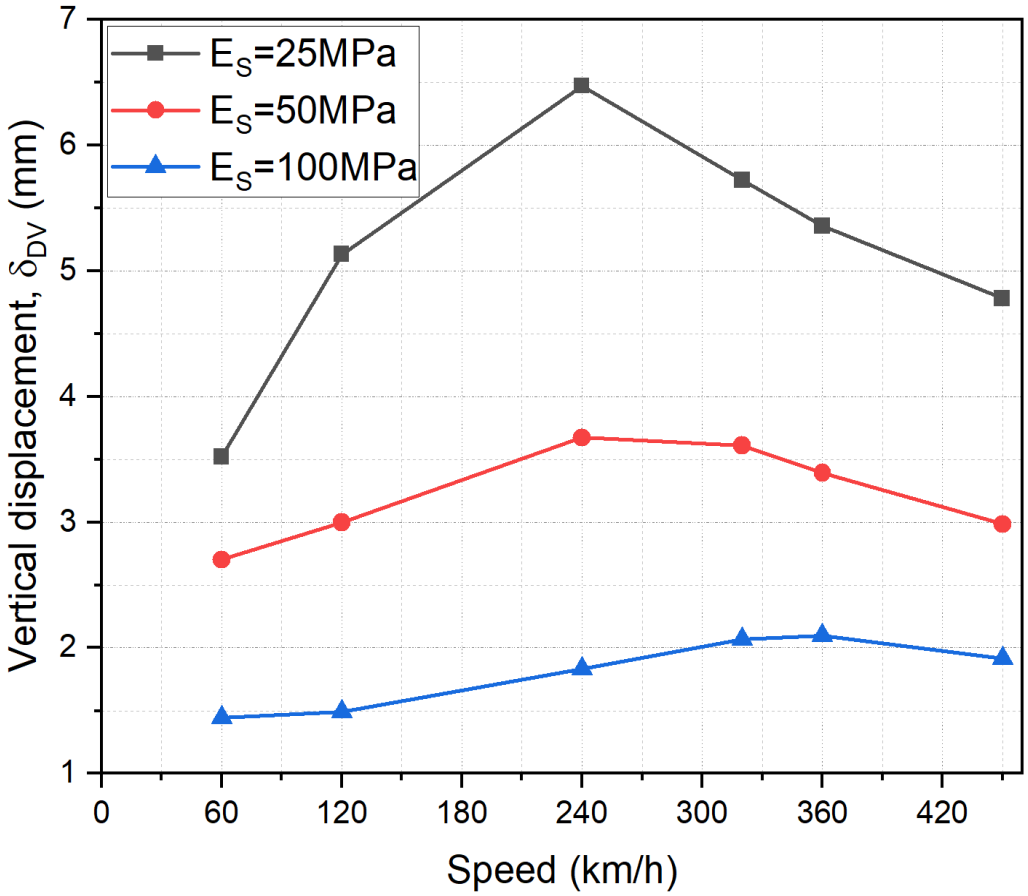

Figure 4.6 Effect of subgrade stiffness on critical speed and vertical displacements

Comparison of the vertical displacement (δ_{DV}) from the three subgrade moduli considered shows that peak response shifts to a higher speed as the subgrade modulus increases while the magnitude of peak δ_{DV} decreases by about 37% for E_s = 50MPa and about 64% for E_s = 100MPa, as compared to the lowest modulus considered. Figure 4.6 also shows the variation of δ_{DV} with increasing speed decreases with an increase in ground modulus. For instance, the amplification factor at 240km/h ($\delta_{DV@240}/\delta_{DV@60}$) is about 1.84, 1.35 and 1.26 for E_s = 25, 50 and 100MPa, respectively.

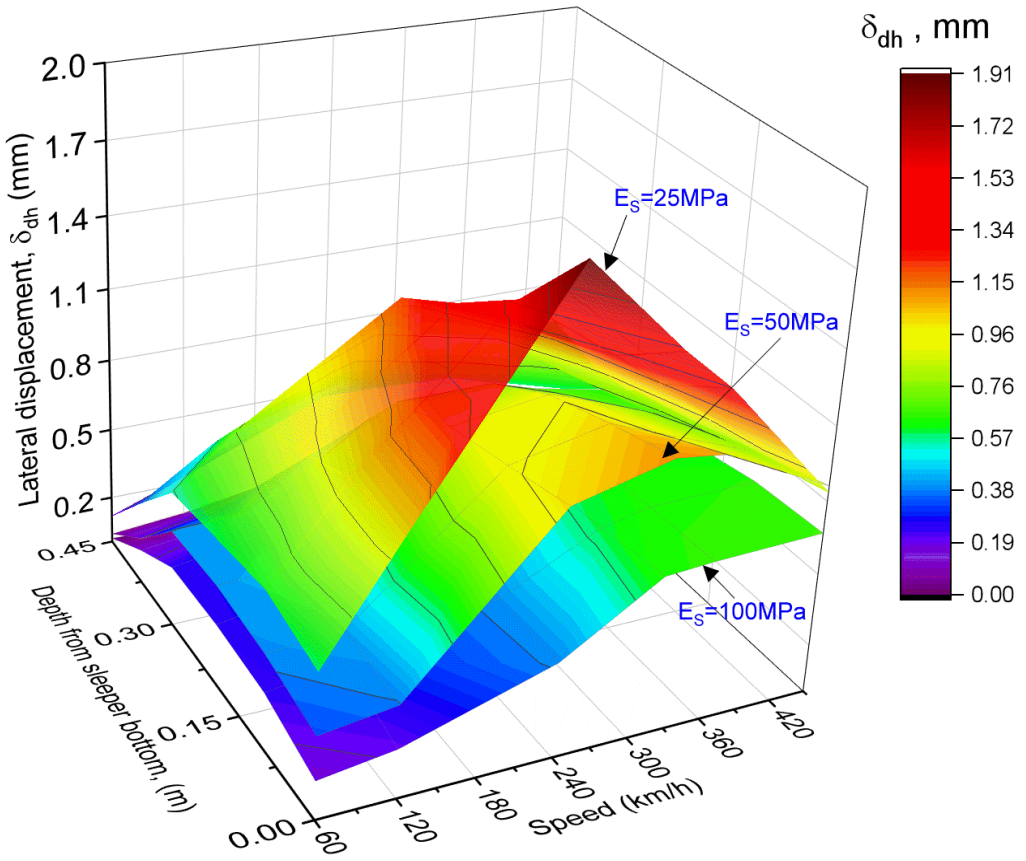

Figure 4.7 Effect of subgrade stiffness on critical speed and vertical displacement

Figure 4.7 shows the cross-influence of speed and subgrade moduli on lateral displacement at various depths from sleeper bottom (along the section in Figure 4.5(b)). The lateral displacement shows a distinct peak at around 240km/h and 360km/h for E_s=25MPa & 50MPa, respectively. The ratio of the maximum lateral displacement to the lateral displacement at a lower speed ($\delta_{DV@60}$) computed at the top of the ballast layer is 3.23, 3, and 2.47 for E_s= 25, 50 and 100MPa, respectively. Therefore, increasing train speed exhibits a significant effect on lateral displacement amplification at the shoulder ballast.

4.5 Chapter summary

This chapter presented how increasing train speed results in large track displacements, with the maximum vertical and lateral deformations observed at the critical speed. The development of the Mach cone was observed at high-speed ranges approaching the Rayleigh wave speed of the subgrade. From the evolution of the peak vertical displacement shift (δ_{dvp}), the dynamic effect and associated change in displacement field were affected when the train speed exceeded 120km/h ($V/V_C \sim 0.36$), for the subgrade modulus of E_s = 50MPa.

The result from transient vertical displacement responses shows that the choice of the constitutive model adopted for the track substructure does not significantly affect the critical speed, which is limited to 5%. However, the track lateral deformation increased by 260% compared to the elastic model. Further, the analysis showed that the amplification of lateral deformation in the shoulder ballast could exceed 300% at the critical speed, which was significantly higher than the vertical amplification of 135%. Therefore, the edge of the track in the vicinity of the track shoulder is more prone to lateral spreading in the absence of adequate confining pressure from the track shoulder regions at the resonating speed of the track. Often linear analysis is employed to predict a track substructure response overlooking the effect of the lateral spreading of the ballast stratum; in this case, the track may be at risk of instability associated with an elevated dynamic response if the design is solely based on elastic approximations. A further parametric study was conducted to investigate the vertical and lateral response by varying the subgrade modulus. The critical speed increases with the subgrade modulus while the peak vertical and lateral displacements reduce. The results indicated that more

maintenance interventions would be required to reduce vibration induces track deterioration for tracks built on a relatively soft subgrade.

CHAPTER 5 STRESS PATH AND AMPLIFICATION IN BALLASTED TRACK UNDER MOVING LOAD

5.1 Introduction

The state of stress in a railroad subjected to moving train loading exhibits a complex stress path as the load approaches and passes a given point in the track. As axle loading moves towards a given observation point, the shear stress gradually increases, then decreases to pass through zero when the load is precisely above the observation point, while the vertical stress peaks at that time. As the axle load moves away from the observation point, the shear stress changes its sign and increases before gradually returning to zero again once the axle loading is beyond a certain distance from the point. Not surprisingly, this makes the shear stress to be 90^o out of phase with the normal stress, which in turn results in a continuous rotation of the principal stress axes (Momoya et al., 2005; Powrie et al., 2019). Based on two-dimensional FE models, Yang et al. (2009) have shown that the vertical and longitudinal shear stresses increase with the train speed. Their results show that the vertical and shear stresses at the critical speed are about 20% and 80% higher than the statically calculated values, respectively. Moreover, when the speed approaches 50% of the critical speed (V_R), the shear stress and vertical stress are underestimated by about 30% and 15%, respectively. Therefore, these results confirm that the stress path corresponding to a higher speed would be affected by the propagation of R-waves, and thus inducing a retrograde motion of particles at the track (ballast) surface. This chapter analyses and presents the influence of train speed on the 3D stress responses, stress path, and principal stress rotation. Then, the cross-influence of train speed and subgrade stiffness on ballast response is presented. It is noted that the main content of this chapter has been published in the Transportation Geotechnics (Tucho et al. (2022)).

In this study, two different material models are considered for the track substructure, elastic and elastoplastic, to study the effect of the type of material model on stress response and path of the ballast layer subjected to moving loads. In the case of elastoplastic models, the ballast is modelled following the Drucker-Prager (DP) yield criteria while capping and subgrade (assumed fully drained) are simulated using an elastic-perfectly plastic model according to the Mohr-Coulomb failure theory. The 3D stress, stress paths, rotation of principal stresses, and associated redistribution observed in elastoplastic response are presented and compared against prediction from elastic models. Further, the predicted elastic stress response is compared against the failure criterion deduced from large-scale monotonic and cyclic tests conducted on the ballast material to delineate the stress state and associated train speed that induces instantaneous instability in the ballast layer.

5.2 Stress response in the ballast layer

Figure 5.1 shows the corresponding stress changes in the middle of the ballast stratum at a relatively low speed of around 60 km/h ($0.2V_R$) and close to the critical speed (V_R = 300 km/h) of the current track-ground model. At the critical speed, the vertical stress (σ_{zz}) increases about 40% while the shear stress along the longitudinal direction (τ_{yz}) increases almost 200% in the opposite direction.

As shown in Figure 5.1(a), at 60 km/h, all the stress curves are generally symmetrical. In contrast, at a much higher speed of 300 km/h, the peak stress values are considerably higher, confirming the role of stress amplification. The general symmetry of the stress response is no longer observed, except for the vertical stress (σ_{zz}) that still retains some consistency of its variation with time, albeit variation in magnitude as expected, as shown

in the contour plot given in Figure 5.2. It can be noted that the transient vertical stress at a higher speed of 300km/h is slightly lower than the predicted stress at 60km/h. This can be attributed to the fact that the peak stress amplification occurred at a lower speed of 240km/h, hence supercritical response is prevalent at 300km/h, consistent with dynamic vertical displacement (Section 4.2, Figure 4.3).

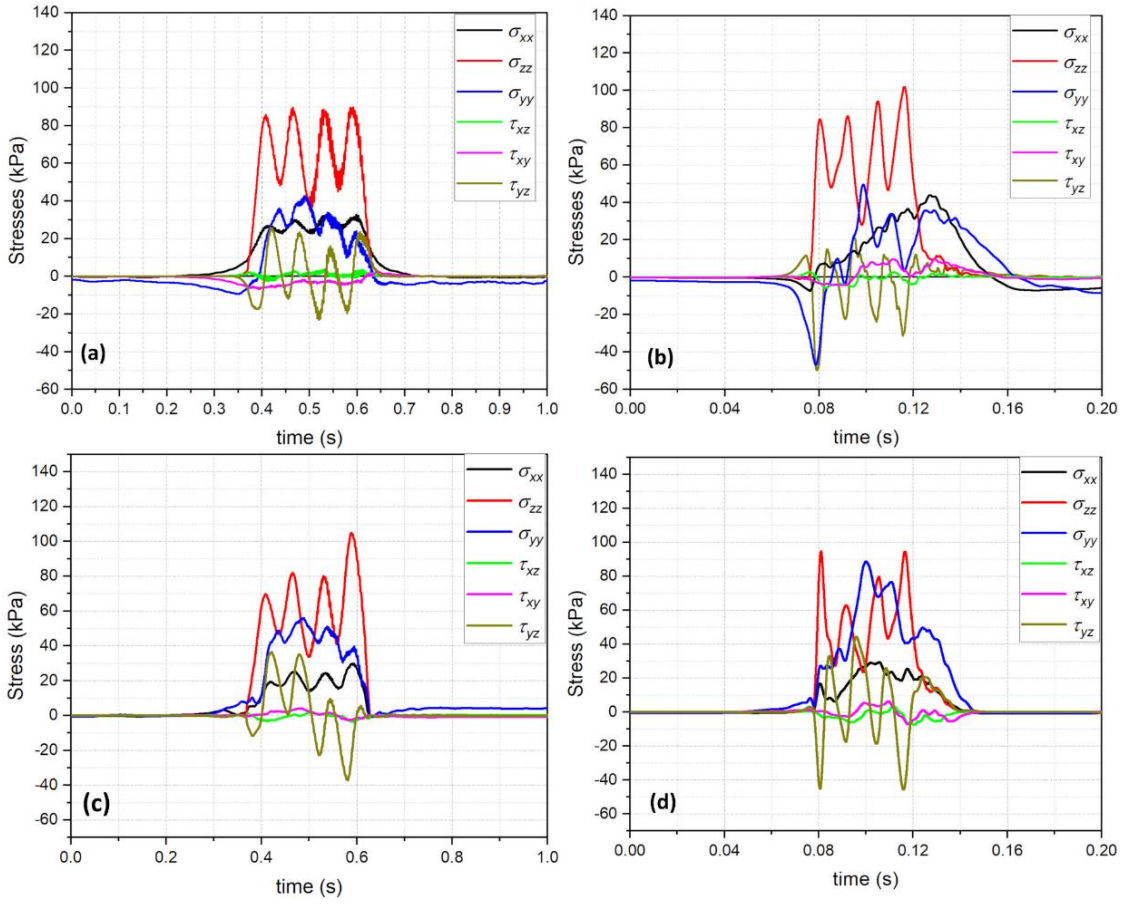

Figure 5.1 Stress response under moving load at in the ballast layer (a) 60km/h - elastic response, (b) 300km/h - elastic response, (c) 60km/h - elastoplastic response (d) 300km/h - elastoplastic response

5.3 Stress path and angle of rotation

It is known that a moving train results in a continuous rotation of the principal stress axes in the track. The magnitude and direction of the principal stress angle depend on the axle load, train speed, geometric parameters of the train such as the distance between wheels,

and the location of the point of interest in the track substructure (Powrie et al. 2007; Varandas et al. 2016). Figure 5.3 illustrates the effect of loading location on the orientation of the principal planes and the typical cardioid-shaped stress path associated with moving load.

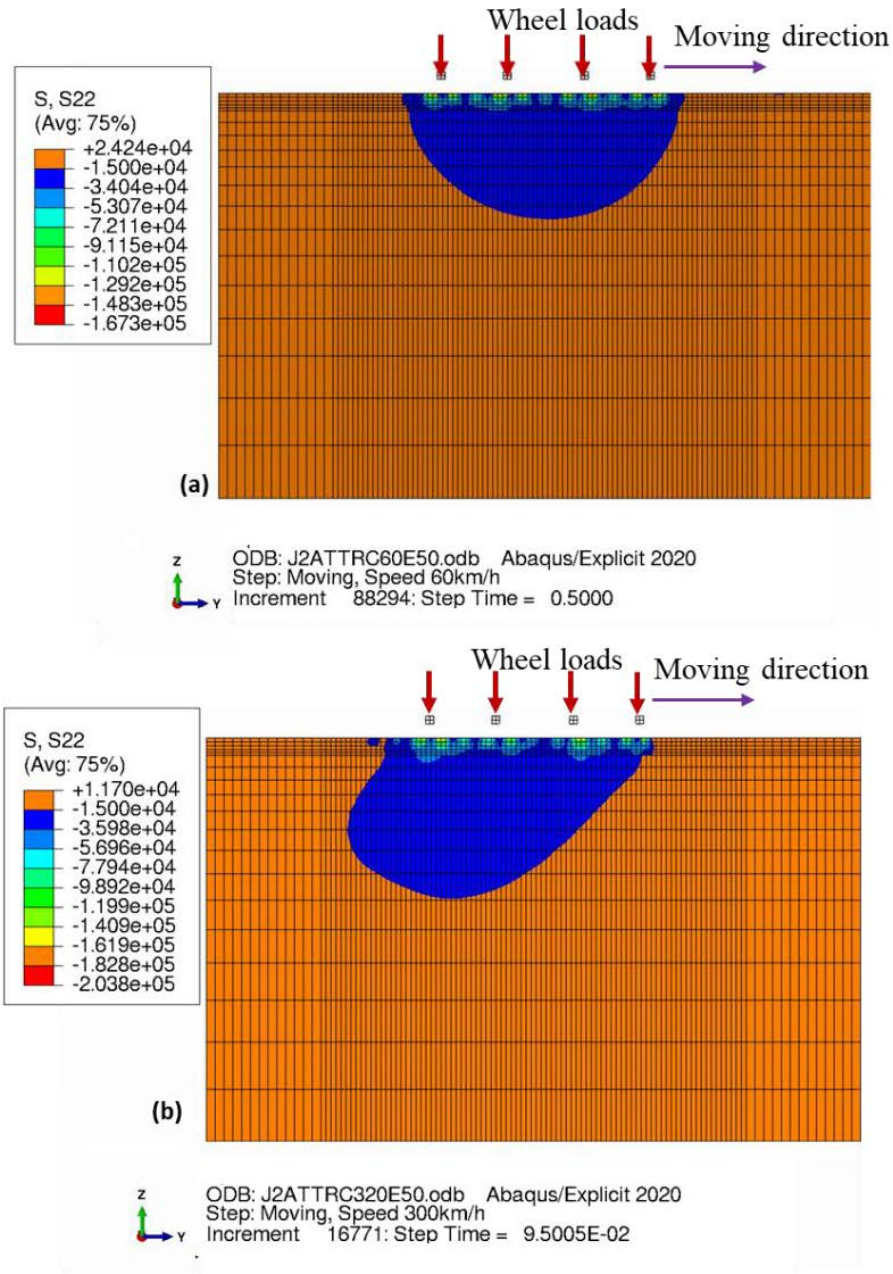

Figure 5.2 Typical track response contour plots for E_S = 50MPa: (a) vertical stress field at 60km/h (b) vertical stress field at 300km/h

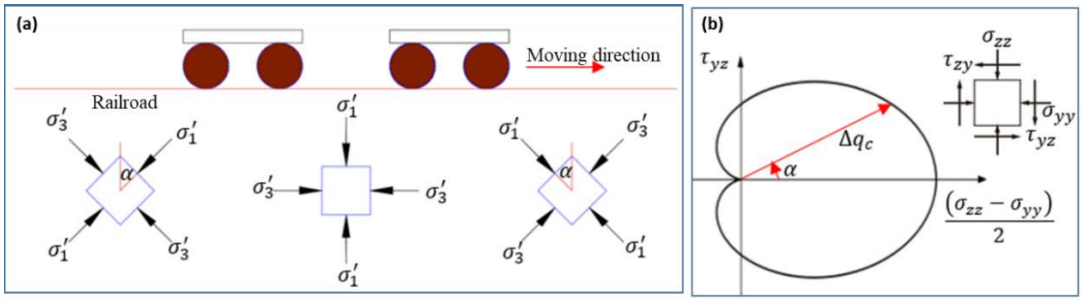

Figure 5.3 (a) Schematics of PSR under moving wheel loads; and (b) Typical stress path under moving load.

Several past studies have shown that principal stress rotation caused by moving load could exacerbate the permanent deformations compared to a single point (non-moving) cyclic loading (Bian et al., 2020; Momoya et al., 2005). Other studies have also shown that the accumulation of the axial permanent strain is dependent on the width and height of the heart-shaped stress path as well as angle of stress rotation (Cai et al., 2018; Qian et al., 2016; Wei et al., 2017).

The rotation angle of principal stress planes (α_{yz}) can be defined as a function of the shear stress along the direction of train passage (τ_{yz}) and the difference between the horizontal normal stress (σ_{yy}) and the vertical normal stress (σ_{zz}), where this rotation is determined by (Zhao et al., 2021):

$$\alpha_{yz} = \frac{1}{2}\tan^{-1}\left(\frac{2\tau_{yz}}{\sigma_{zz} - \sigma_{yy}}\right) \qquad 5.1$$

Figure 5.4(a) and (b) show the variation of the angle of principal stress rotation (α) for an element located at the mid-depth of the ballast layer predicted at varying speeds. The results indicate that the principal stress plane continuously rotates when the wheel load approaches and leaves the point of observation in the ballast layer. At a relatively low

speed, the rotation of the principal stress plane is mainly due to the change of location of the load as a function of time. It is clearly evident that the cycles of stress reversal increase with increasing speed. However, the predicted values of α at relatively low speeds < 120km/h (i.e., quasi-static response) and at much higher speeds > 240km/h (i.e., true dynamic response) is significantly different, accompanied by loss of symmetry at high speeds.

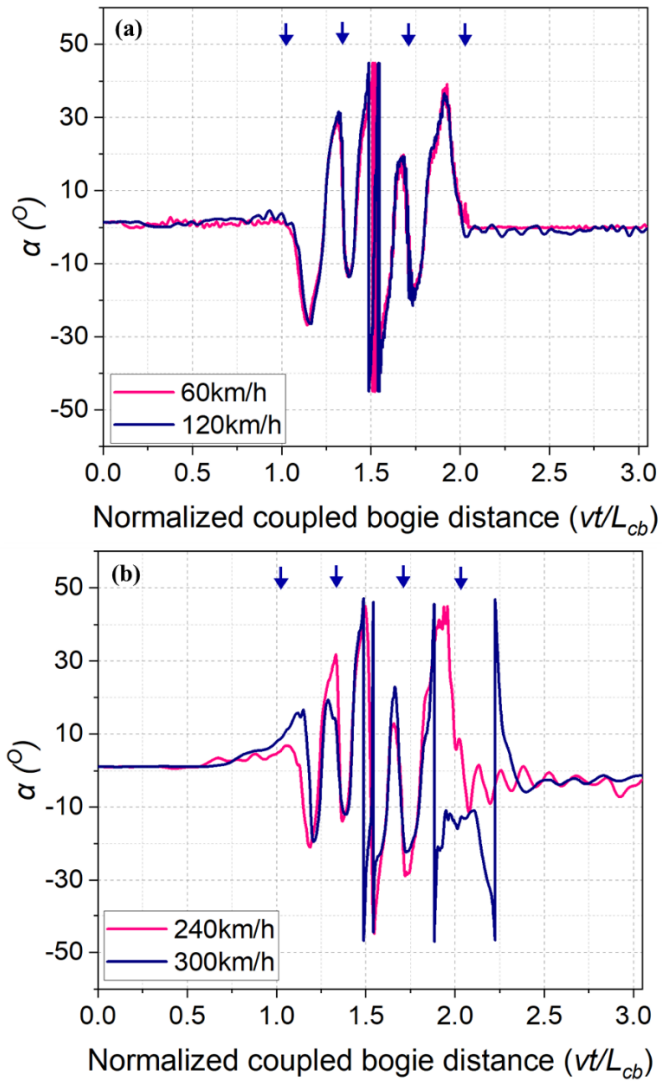

Figure 5.4 Typical angle of stress rotation at: (a) 60km/h and 120km/h; and (b) 240km/h and 300km/h

Figure 5.5 shows the changes in the predicted dynamic stress path in the middle of the ballast layer at train speed of 60 km/h and 300 km/h, for both elastic and elastoplastic analysis. For the train speeds of 60 km/h (Figure 5.5(a) & (c)), the predicted dynamic stress paths show a symmetry shape as similarly observed for the stress field. At the speed increases to 300 km/h, it is observed that the dynamic stress paths become asymmetric, and the stresses significantly increase with the increased train speed, for both elastic and elastoplastic material models. The stress path is near-symmetrical at a quasi-static response and becomes totally oblique when the train travels at a much higher speed.

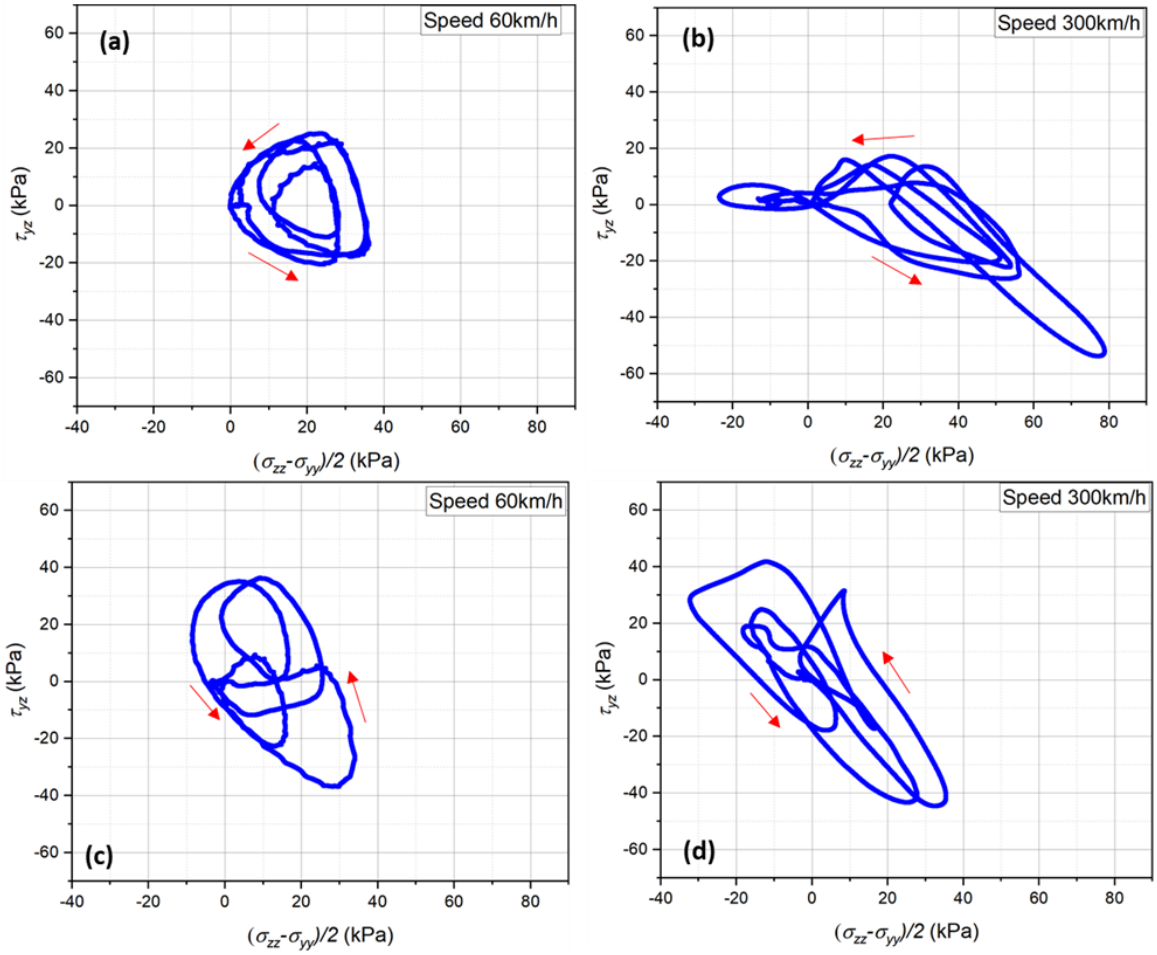

Figure 5.5 Stress path at the center of ballast: (a) 60km/h- elastic analysis (b) 300km/h-elastic analysis (c) 60km/h-elasto-plastic analysis; and (d) 300km/h elasto-plastic analysis

This observation is consistent with the dynamic displacement and stress fields discussed earlier. Therefore, the conventional 'heart-shape" stress path is valid to the speed range characterised by quasi-static range; hence, this stress path falls short in capturing track response for the high-speed track. Ling et al. (2018) studied the effect of a single moving aircraft loading on the stress path in subgrade soil, observed the change stress path from "cardioid shape" to the elongated "egg-shape" with increasing speed. Likewise, unsymmetrical stress paths are attributed to the additional wave effect associated with dynamic loading and/or moving load (Cai et al., 2015; Ling et al., 2018).

Despite the magnitude difference, the stress path evolution based on elastic and inelastic constitutive models shows stress redistribution at both low-speed and high-speed simulations. The deviator stress (τ_{yz}) remains symmetrical at low speed (60km/h) at both elastic (Figure 5.5(a)) and inelastic (Figure 5.5(c)) simulation as the load travels in the direction of the y-axis. The elastic simulation at a low-speed range resulted in fairly repeatable circular stress patterns since each successive axle load does not induce an additional stress field. However, the stress path based on inelastic simulation is slightly skewed, accounting for increased vertical stress in each successive wheel passage. However, the stress path response predicted using both elastic and inelastic simulation exhibits significant stress distribution at high speed, as shown in Figures 5.5(b) and 5.5(d). The peak deviator stress (τ_{yz}) from inelastic simulations is less than elastic by about 37% showing the ballast layer yields well before the stress state from the elastic simulation is achieved, which results in more significant vertical and lateral displacement, as discussed in Chapter 4.

5.4 Dynamic stress amplification factor (SAF)

As the train speed increases, the dynamic loading due to acceleration from the vehicle components becomes more significant. Irregularities at the wheel-rail interface amplify the acceleration of the unsprung masses (i.e., wheels and axles). Acceleration of both sprung and unsprung masses also occurs due to more prolonged wavelength irregularities such as track support stiffness and unsupported sleepers (Esveld, 2001; Milne et al., 2019; Shi et al., 2021). These dynamic loads are commonly considered in the track design by adopting the Dynamic Amplification Factor (DAF) which is the ratio of dynamic to the static response in relation to deflection and vertical stress. In the conventional DAF calculations, the track substructure is considered with a single parameter, namely, the track modulus. Field trials and full-scale laboratory testing have shown that the dynamic amplification is primarily influenced by the R-wave propagation speed, stiffness variation, and the type of track (Costa et al., 2015; Ramos et al., 2022; Ramos et al., 2021)

In this study, a dynamic stress amplification factor (SAF) is introduced, and that can be computed according to the ratio of dynamic to the pseudo-static stress response. Figure 5.6 shows the comparison of the SAF for an element located in the mid-depth of the ballast layer, i.e., deviatoric stress (q), mean stress (p) and vertical stress (σ_{zz}). The additional mean normal stress (Δp) and deviatoric stress (Δq) induced by the moving train is given by (Dong et al., 2019):

$$\Delta p' = \frac{\Delta\sigma_x + \Delta\sigma_y + \Delta\sigma_z}{3} \tag{5.2}$$

$$\Delta q = \sqrt{\frac{1}{2}\left(\left(\Delta\sigma_x - \Delta\sigma_y\right)^2 + \left(\Delta\sigma_y - \Delta\sigma_z\right)^2 + \left(\Delta\sigma_z - \Delta\sigma_x\right)^2\right) + 3\left(\Delta\tau_{xy}^2 + \Delta\tau_{yz}^2 + \Delta\tau_{zx}^2\right)} \tag{5.3}$$

It is observed from Figure 5.6 that the peak vertical stress amplification (σ_{zz}) and deviatoric stress amplification (q) show 35% and 40% increase, respectively, in the critical speed range. This can be attributed to the fact that the subgrade considered in this study exhibits a moderate stiffness (E_s =50 MPa) and the range of amplification factors obtained from FEA analysis falls within the range of responses reported by others, including Costa et al. (2015); Sayeed and Shahin (2016). However, the deviatoric stress amplification (q) is significantly higher than the vertical stress amplification (σ_{zz}) factor due to the increased shear stress, as the train speed approaches the R-wave speed.

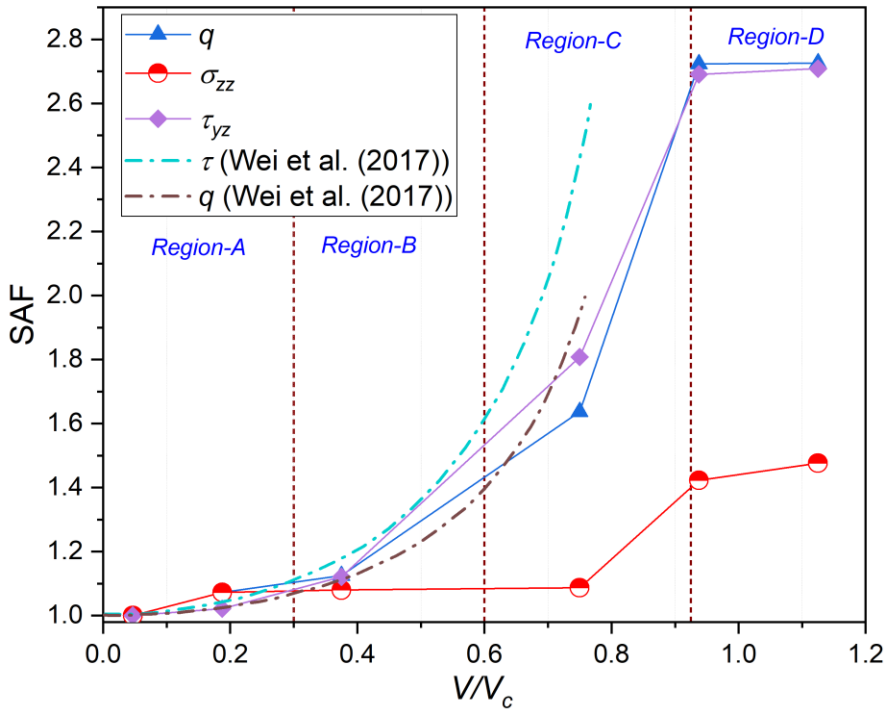

Figure 5.6 Variation of stress amplification factor (SAF) with speed ratio (V/V_R) predicted for a medium-stiff subgrade (E_S = 50MPa)

To validate the significant amplification observed in the distortional stress field, the results are compared to the closed-form solution developed by Eason (1965) and Wei et

al. (2017), and plotted as a function of V/V_R. This closed-form solution has been developed for a moving surface load on the half-space and the solutions are available for the case when the velocity of the axle load is less than the critical R-wave speed of homogeneous ground. The parameters q and τ are the deviatoric stress and horizontal shear stress amplification, respectively, along the direction of train passage. It is noteworthy that the amplification factors obtained from the FE solution are in close agreement with the closed-form solution for the range of velocities plotted herein.

Based on the deviator stress amplification attributed to Rayleigh or R-wave propagation, four regions can be identified as follows: (i) Region A: where the response is predominantly quasi-static corresponding to speeds less than 120km/h; (ii) Region B: moderately dynamic response up to 60% of the critical speed; (iii) Region C: dynamic response approaching a critical zone where significant deviator stress amplification occurs, and (iv) Region D: the zone beyond which SAF ceases to increase further.

Comparison of deviator and vertical stress amplification proves that a design based on vertical stress amplification may only be sufficient within the quasi-static region, and certainly not valid for high speeds causing principal stress rotations and considerably higher shear stresses being generated.

5.5 Effect of subgrade stiffness

5.5.1 Effect of subgrade stiffness on attenuation of vertical stress

Figure 5.7 presents attenuation of the maximum vertical stress with the depth of track substructure simulated at different train speeds and subgrade modulus (E_s). It is seen that the shape and distribution of vertical stress are affected by the increasing speed, except at

60km/h and 120km/h, which fall into quasi-static speed range. The influence of speed on vertical stress increment decreases with an increase in the subgrade modulus. The vertical stress distribution exhibits higher scatter with speed for E_S = 25MPa, as compared to the higher modulus (Figure 5.7a-c). For instance, as the speed increases from 60km/h to 360km/h, the vertical stress at the center of the ballast layer increases by about 78%, 33% and 10% for E_S= 25MPa, E_S= 50Mpa and E_S= 100Mpa; respectively.

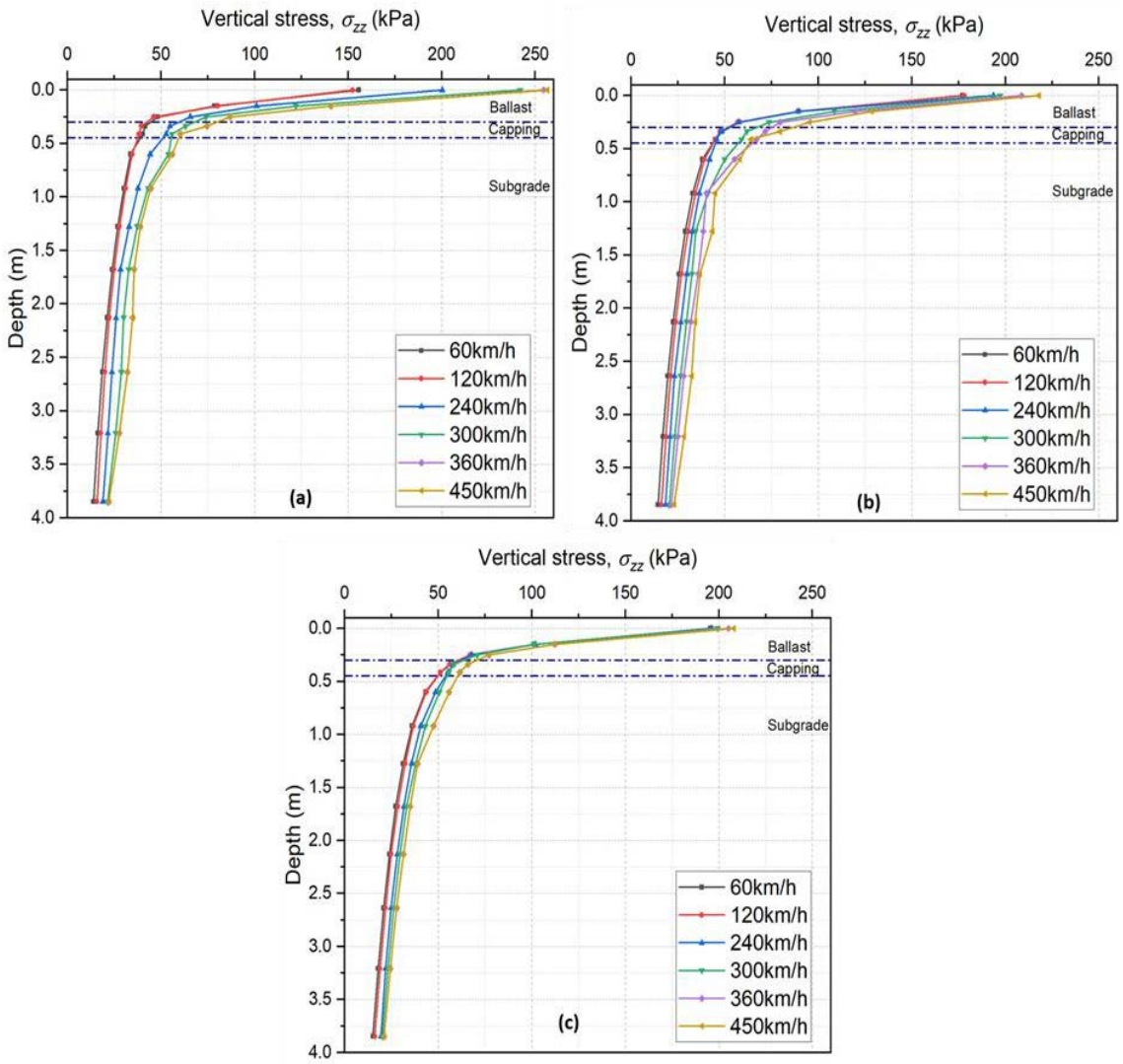

Figure 5.7 Attenuation of vertical stress with depth and subgrade stiffness: (a) Soft subgrade, E_S = 25MPa (b) Medium stiff subgrade, E_S = 50MPa (c) Stiff subgrade, E_S = 100MPa

Figure 5.8 summarises the vertical stress results measured at the middle of the ballast and capping layers. The vertical stress exhibits a slight variation for the train speed of less than $0.5V_R$, where higher vertical stress is observed in both ballast and capping layers with increasing subgrade moduli. Previous field measurements conducted on a conventional ballasted track built on soft alluvial deposits, concrete bridge and hard rock indicate without doubt that the stiffer foundations resulted in higher vertical stress in the ballast layer as compared to those built on a soft alluvial deposit (Nimbalkar and Indraratna, 2016). However, this trend changes when the effect of stress wave propagation begins to affect the response, which corresponds to 120km/h ($\sim 0.5V_R$ for E_s= 25MPa), 240km/h ($\sim 0.7V_R$ for E_s= 50MPa) and 300km/h ($\sim 0.6V_R$ for E_s= 100MPa).

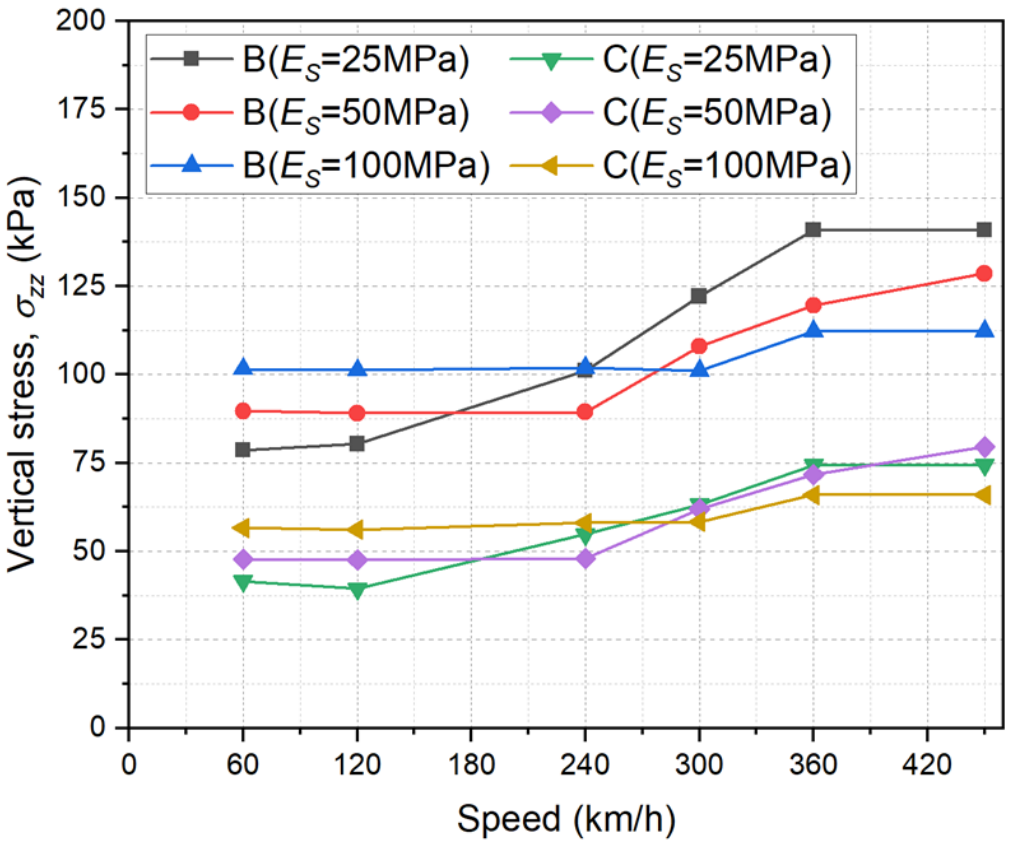

Figure 5.8 Vertical stress variation with speed at the centre of Ballast (B) and Capping (C)

5.5.2 Variation of SAF with depth and speed

Figure 5.9 to Figure 5.12 show the variation of deviator stress amplification factor (SAF) as a function of the train speed and depth of trackbed, measured from sleeper soffit for three subgrade scenarios. The SAF is defined as the ratio of deviator stress computed at various speeds to the deviator stress induced by the quasi-static train loading. In the current FEM analysis, the stress response at 60km/h is considered as a control provided that the speed is significantly lower than the Rayleigh wave speed of the subgrade considered, which is approximately $0.25V_R$, $0.18V_R$ and $0.12V_R$ for E_s= 25MPa, E_s= 50MPa and E_s= 100MPa; respectively.

At a given subgrade modulus (E_s), a higher amplification of deviator stress is observed at shallow depth having the peak SAF situated in the middle of the ballast layer. However, for stiffer subgrade scenario (E_s= 100MPa), the maximum amplification occurs in the subgrade as shown in Figure 5.11. With increasing depth, the SAF tends to be constant with minor fluctuations, especially in deeper subgrade layers located within the zone of influence of the moving train.

Figure 5.12 shows the summary of the SAF values at the centre of ballast (B) and capping (C) layer as a function of train speed, and here, the SAF is higher in the ballast layer as compared to the capping layer, except for E_s= 100MPa. The general trend indicates that the peak SAF decreases with an increase in subgrade moduli (E_s). The peak SAF values are predicted as 2.98, 2.43 and 1.7 for E_s= 25MPa, E_s= 50MPa and E_s= 100MPa; respectively.

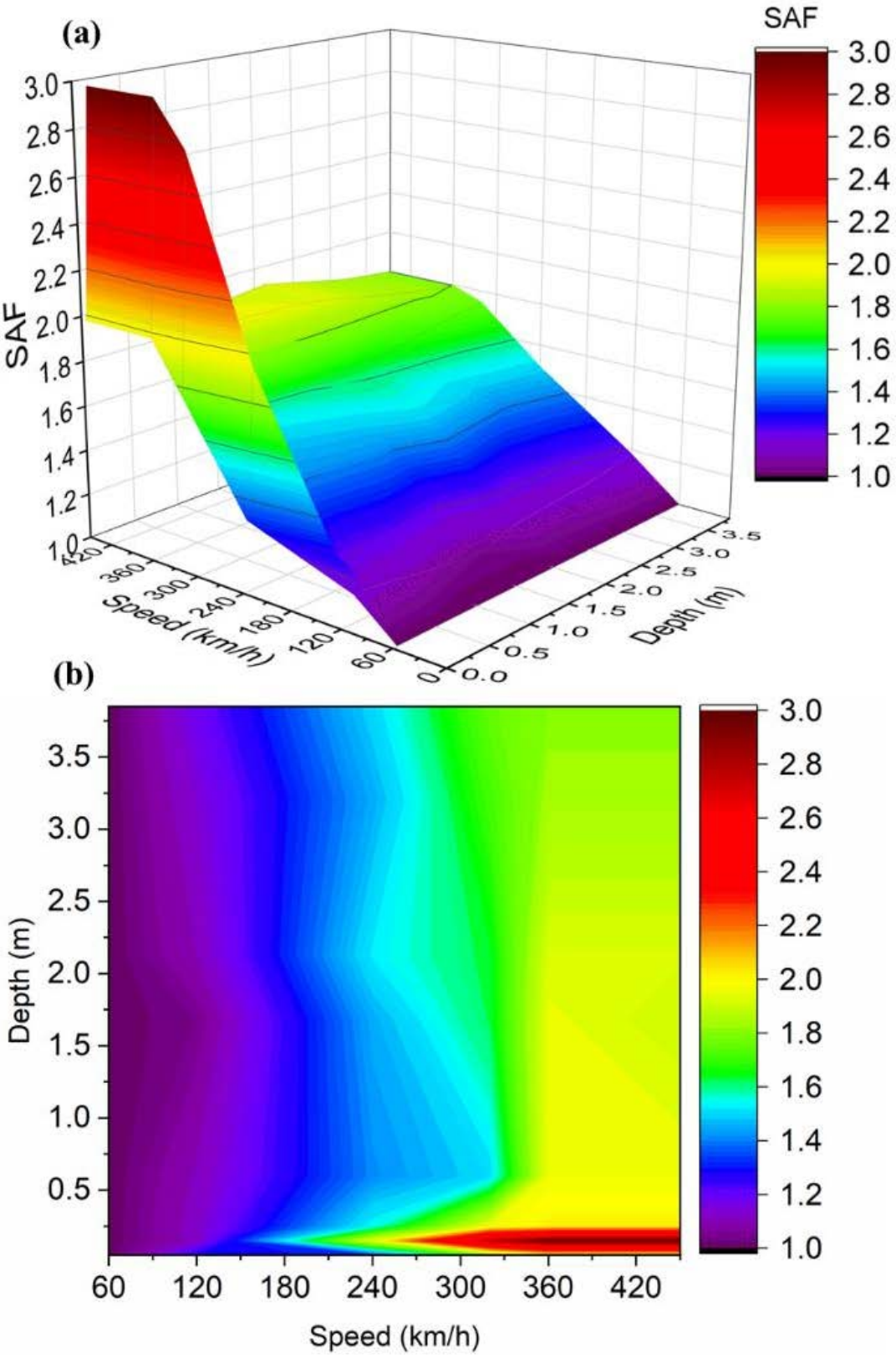

Figure 5.9. Stress amplification factor with speed and depth measured from sleeper bottom E_s = 25MPa (a) 3D plot (b) Contour poat in plan view

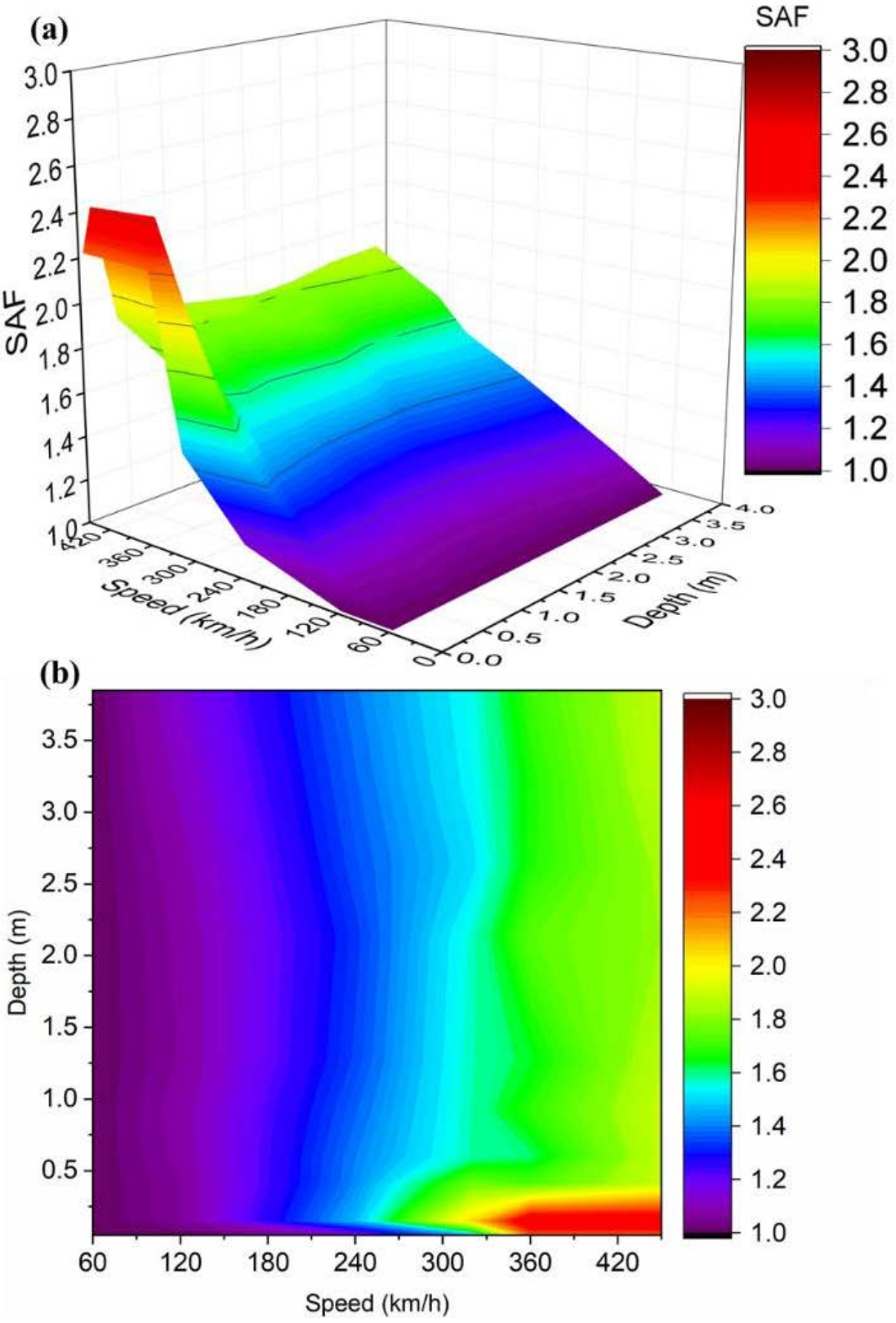

Figure 5.10. Stress amplification factor with speed and depth measured from sleeper bottom E_s = 50MPa (a) 3D plot (b) Contour plat in plan view

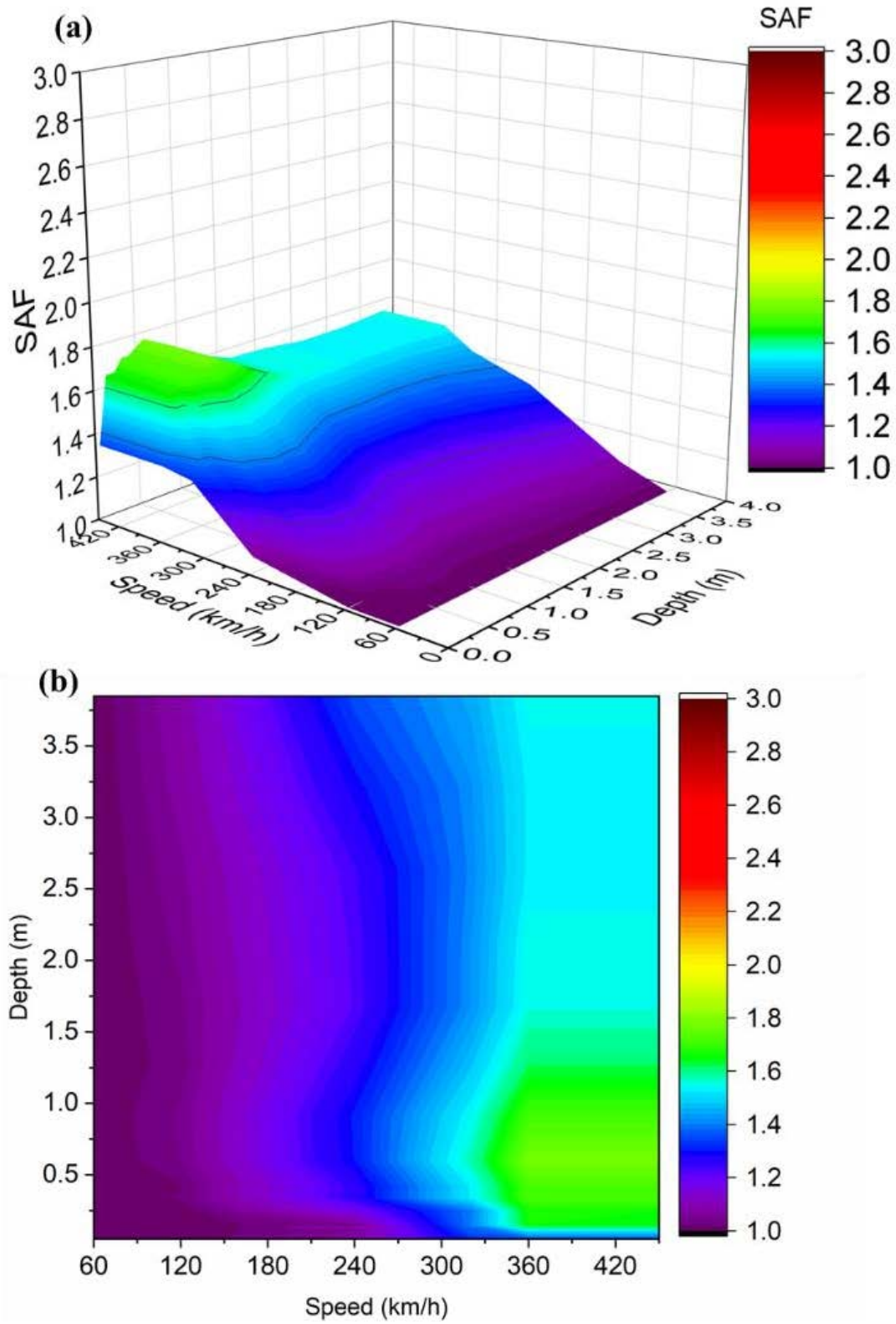

Figure 5.11 Stress amplification factor with speed and depth measured from sleeper bottom E_s = 100MPa (a) 3D plot (b) Contour plot in plan view

For a low to medium speed range (<120km/h), the SAF is less dependent on the subgrade moduli where the maximum SAF is less than 1.3 for all subgrade properties considered. Similarly, the SAF shows less variation with the depth of track substructure for the relatively low speed. When the speed is greater than 120km/h, the rate of SAF increment is significantly affected by the depth in the track substructure, speed, and subgrade moduli.

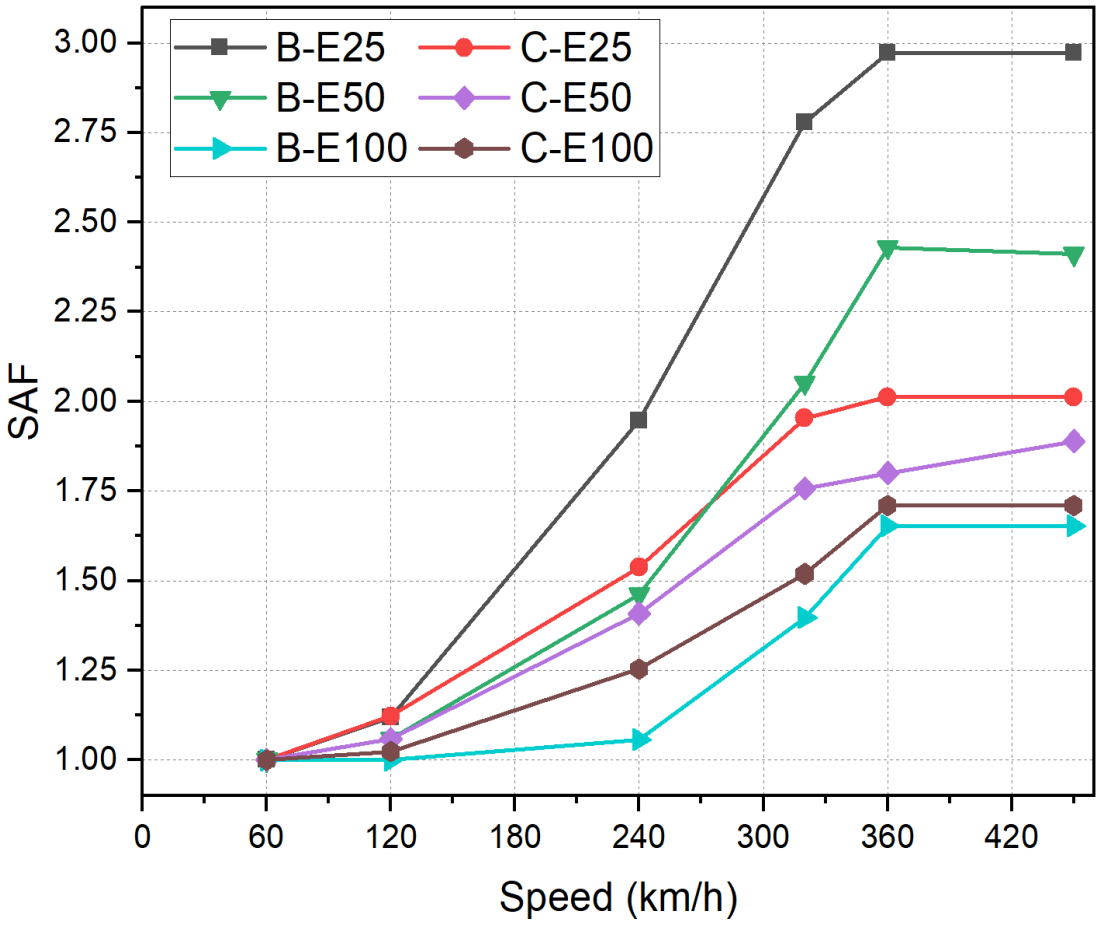

Figure 5.12 Variation of amplification factor with subgrade stiffness

For all subgrade cases considered, the SAF peaks at the ballast centre reduce through the capping layer and keep almost a constant value at the subgrade (Figure 5.9-Figure 5.11). The SAF exceeds two-fold at about 220km and 300km/h for subgrade modulus of E_s=

25MPa and E_s= 50MPa, implying that stiffening the track subgrade by 25MPa can significantly reduce the SAF and increase the allowable train speed. In the high-speed range exceeding 240km/h, a significant deviator stress amplification is observed in the ballast and capping layer for both types of subgrades. In contrast, the variation of SAF with depth at a higher speed exceeding 360km/h is less pronounced, having a peak SAF of 1.75 and then remains at a relatively constant for the rest of the subgrade depth.

5.6 Railroad limiting speed and practical implication

5.6.1 Limiting speed

The conventional track design aims at limiting predominant track failure modes by preventing excessive plastic deformation of railroad track substructure (Li and Selig, 1998). Upon repeated train loading, the accumulation of plastic deformation of ballast is significantly influenced by the confining stress provided by the track shoulder and the deviator stress induced by the moving train, in addition to the mechanical properties of ballast (Indraratna et al., 2015; Xiao et al., 2017). Indraratna et al. (2015) conducted a series of large-scale triaxial tests on latite ballast (commonly used in New South Wales, Australia), under increasing confining and deviator stress. They observed that the critical state stress ratio ($M_c = q/p'$) of ballast shows non-linear behaviour as a function of confining pressure. They found that the ballast reaches a critical state at M_c = 2.33 for confining stress of 30kPa. Previous field studies have shown that the confining pressures provided by the track shoulder to the ballast layers very relatively small (<30kPa) (Indraratna et al., 2010; Nimbalkar and Indraratna, 2016).

Other studies have shown that the plastic deformation and associated failure of railway ballast is significantly influenced by frequency (*f*) of the cyclic loading, confining stress

and stress ratio, q/p' (Sun et al., 2019; Zhang et al., 2019). Accordingly, the accumulated axial and volumetric plastic strain under cyclic loading shows three distinct states: plastic shakedown, ratcheting and plastic collapse. The plastic shakedown exhibits a small accumulation of plastic strain marked by the steady-state response, while the ratcheting shows a constant accumulation of strain. The extreme response is plastic collapse which is characterized by rapid accumulation of plastic strains leading to failure under a small number of cycles. Sun et al. (2019) conducted cyclic triaxial tests on ballast and found that the frictional failure at $(q/p')_{max}$ were of 2.58 and 2.43 for f = 5Hz and 30Hz, respectively.

Critical speed (V_C) corresponds to the speed at which maximum dynamic deflection is observed, based on the conventional definition. The peak vertical displacement (δ_{DV}) is determined to be around 240km/h, 300km/h and 360km/h for E_s= 25MPa E_s= 50MPa and E_s= 100MPa, respectively. However, interpretation of large-scale laboratory test results shows that granular materials would undergo significant plastic strain and experience plastic collapse well below the conventional critical speed (Sun et al., 2016; Xiao et al., 2017). Hence, it is important to compare the dynamic response obtained from FE analysis in relation to ballast behaviour observed in the laboratory through monotonic and cyclic tests. Therefore, the speed at which the stress induced by the moving load reaches the critical stress ratio defined by monotonic loading (q/p' = 2.33) and cyclic loading (q/p' = 2.43) can be taken as a limiting speed (V_L) against track instability.

Figure 5.13 shows limiting speeds (V_L) for the track against track instability for a given subgrade modulus (E_s). The limiting speeds are shown through two vertical line pairs corresponding to monotonic and cyclic failure conditions (the higher line for cyclic

condition – Sun et al. 2019). When the speed is less than 120km/h, the stress ratio $(q/p')_{max}$) for E_s = 50MPa and 100MPa is almost similar, while the softer subgrade (E_s = 25MPa) shows an immediate amplification in the stress ratio. The stress ratio increases with speed and remains almost unchanged at super-critical speed. The stable stress ratio for cyclic load is higher than that of monotonic condition, showing that tracks can sustain a higher deviator stress under cyclic loading conditions. The limiting speed is close to 170km/h, 220km/h and 270km/h, which is significantly reduced from the conventional critical speed of 240km/h, 300km/h and 360km/h for E_s= 25MPa, E_s= 50MPa and E_s= 100MPa; respectively. It is seen that ballast fails in shear well ahead of V_R at about 60% of the peak response speed. This value falls at the upper bound of Region B, confirming that this track will become unstable in shear.

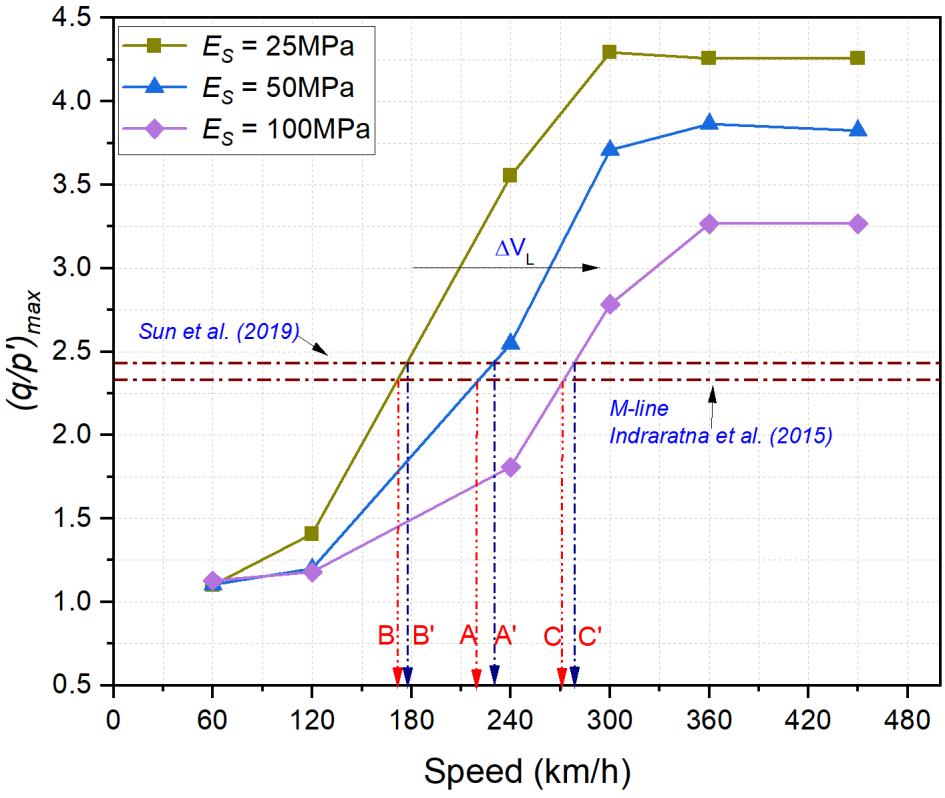

Figure 5.13 Limiting speed based on shear failure observed from monotonic and cyclic triaxial tests on ballast

Overall, when the subgrade modulus is increased, the curves shift to the right towards a higher speed. Hence, by stiffening the soil, the safe or allowable speed can be increased. In a practical sense, this implies that some form of localised ground improvement may be beneficial for the soft soil subgrade, such as dynamic compaction or chemical treatment (deep mixing etc.).

5.6.2 Comparison of SAF

Figure 5.14 illustrates the variation of deviator stress and SAF as a function trains speed and subgrade moduli (E_s) together with calculated amplification factors from relevant studies (Esveld (2001); Li and Selig (1998); Sun et al. (2016)).

Based on the FEM analysis, the deviator stress response mechanisms can be divided into three speed ranges: (i) Range-I: ($V \leq 120$ km/h), (ii) Range-II: (120 km/h $\leq V \leq 360$ km/h) and (iii) Range-III: ($V \geq 360$km/h). In Range-I, increasing the train speed seems to have a minimal effect on the change of deviator stress (Δq) and a higher subgrade modulus (E_s) results at a higher deviator stress. However, the dynamic mechanism associated with stress wave propagation becomes evident at a lower speed for smaller subgrade moduli. Hence, the response is reversed and the rate of SAF increment decreases with an increasing subgrade modulus in Range-II. Likewise, increasing the subgrade modulus reduces the SAF in Range-III except for the fact that SAF ceases to increase with the train speed when considering the high-speed range.

Sun et al. (2016) introduced a stress amplification factor as the ratio of the dynamic stress measured from cyclic tests to the applied deviator stress subjected to varying loading frequencies. They proposed a non-linear exponential function to calculate the stress

amplification responses for a train speed of less than 260km/h. Li and Selig (1998) method overestimates the dynamic response, with the exception of train speed exceeding 300km/h for a relatively low subgrade modulus. In contrast, Esveld (2001) approach overpredicts the dynamic response for all speed ranges until 240km/h, while underpredicting the amplification factor at higher speeds for E_s = 50MPa and 100MPa.

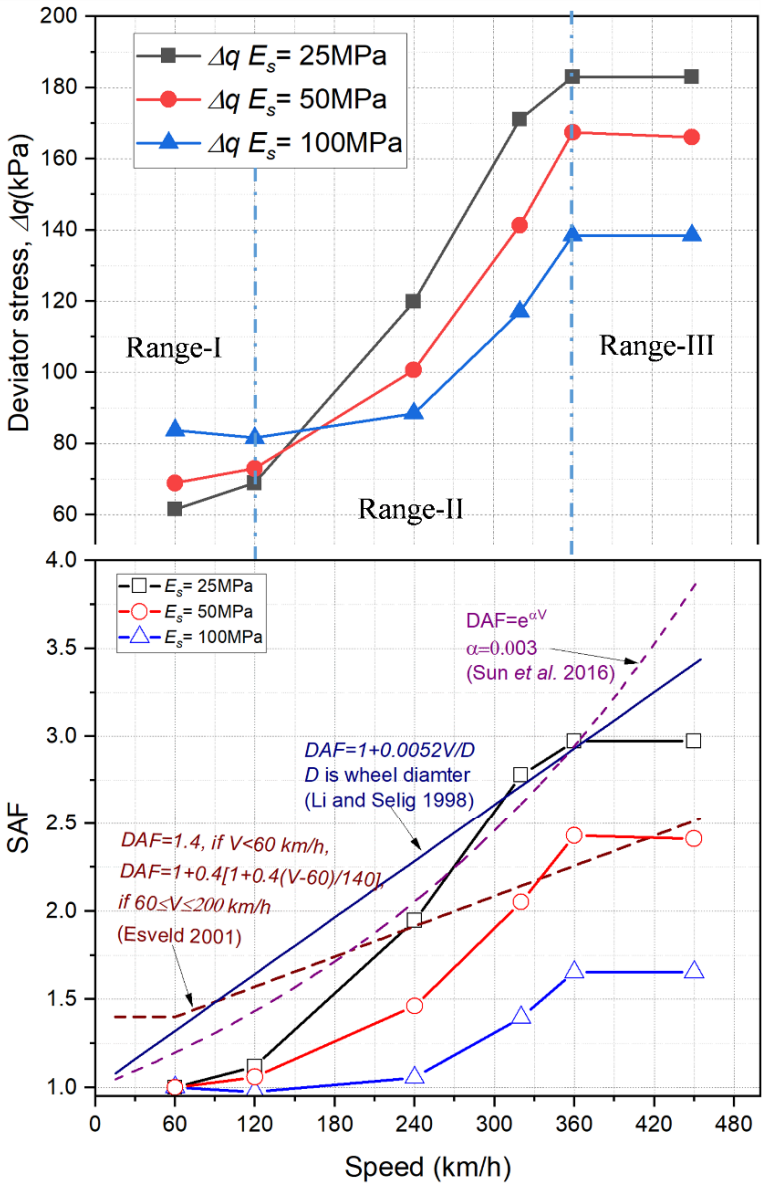

Figure 5.14 Deviator stress response of at the center of ballast and comparison of computed amplification factors against previous studies

These simulation results demonstrate that the aforementioned amplification factors are independent of subgrade conditions and provide an upper bound or conservative prediction of the stress responses. It is noted that the Li and Selig (1998) and Esveld (2001) amplification factors capture the effect of dynamic response associated with wheel-rail irregularities and localised impact loads, as these relationships have been developed based on actual field measurements (Van Dyk et al. 2017). However, overlooking the effect of subgrade stiffness and associated amplification has serious consequences for a track built on a soft to medium stiff soil subjected to a moving train at a moderate speed in the range of 120 – 200km/h.

5.7 Chapter summary

This chapter presented the three-dimensional stress response of ballasted track subjected to increased train speeds in view of stress amplification, the evolution of stress paths and stress attenuations. Based on simulation results, it was found that the effect of train speed is more significant on deviator stress than the normal vertical stresses. The increase in deviator stress is related to the stress wave propagations in the top layers of the track substructure. Based on the amplification of deviator stress, four distinct regions are recommended for track design, considering the ratio of train speed and R-wave velocity of the track.

The rotation of principal stress axes takes place when subjected to moving wheel loads. At low-speed ranges, the rotation of the principal stress occurs due to a change in the location of the train wheel traversing the track. However, the shear stress amplification coupled with the time lag between the shear and vertical stress at high-speed altered the shape of the stress path from the conventional “cardioid” to an “elongated egg”.

In addition to the train speed, the stress amplication factor (SAF) is significantly influenced by the subgrade stiffness and the depth of an element in the track substructure. The SAF decreases with subgrade stiffness, while the maximum amplification is observed in the ballast and capping layers. Hence, applying a single amplification factor for all track components would not be economical at high speeds. However, the amplification factors are less sensitive to the depth and location in the track substructure as well as the variation of subgrade stiffness. The comparison of DAF and SAF proposed in this work shows that the existing empirical equations can not accurately capture the effect of subgrade stiffness at high-speed. However, the empirical methods provide a conservative prediction of amplification at a low-to-moderate speed for all subgrade cases considered.

Finally, limiting speed is recommended based on shear stability criteria and avoiding a plastic collapse of the ballast layer. From the model response, the ballast layers will become unstable when the speed approaches 60% of the Rayleigh wave speed of the subgrade.

CHAPTER 6 FINITE ELEMENT ANALYSIS FOR RUBBER INTERMIXED BALLAST SYSTEM

6.1 Introduction

In recent years, researchers have proposed the use of rubber granules mixed with ballast as an innovative way of recycling end-of-life tyres. The rubber granules intermixed within ballast system (RIBS) can increase energy absorption and damping, reducing track degradation and vibrations (Fathali et al., 2019; Fathali et al., 2017; Qi and Indraratna, 2022). However, it can reduce the stiffness, shear strength and resilient modulus, which in turn may compromise its applicability as a load-bearing layer when a significant percentage of tire-derived aggregates is incorporated in the ballast material. A moderate percentage of rubber crumbs, not exceeding 10% by weight, is recommended as an optimum rubber content resulting in an acceptable performance in shear strength, stiffness, resilient modulus and ballast settlement (Arachchige et al., 2021; Arachchige et al., 2022; Sol-Sánchez et al., 2015).

Though the application of shredded rubber as a mitigation against ballast breakage and track vibration was established through extensive laboratory investigations, the reduction in stiffness can lead to excessive transient deformation under moving train loading. In contrast, the increase in energy absorption and damping can attenuate vibrations, while reducing track displacement and associated stresses in the track substructure. Hence, the 3D FE model developed in the previous chapters will be used to study how the crumb rubber inclusions in the ballast would affect the stress-deformation response of ballasted track under moving train loads.

6.2 Finite element model

6.2.1 Model geometry and train loading

The dimensions of the 3D FEM discretization developed to capture the track dynamic with RIBS subjected to moving wheel loading is shown in Figure 6.1(a). This model consists of steel rails, concrete sleepers, RIBS as the main load-bearing layer (i.e. traditional quarried ballast mixed with rubber aggregates), and a compacted capping layer (sandy gravel) placed above the natural subgrade (predominantly upper holocene sandy clay). For optimising the computational time, the double symmetry of the track could be exploited, hence it was adequate to analyse half of the track considering the moving wheel load along a single rail (i.e., transverse y-z plane). The rail is idealised as a solid section corresponding to the 60kg/m standard profile placed at 1.435m spacing along the longitudinal direction (i.e. in the direction of train passage). The sleepers have dimensions of 2.5m (length) x 0.26m (width) x 0.23m (thickness), following the typical concrete sleepers dimensions commonly employed in Australian tracks (Indraratna et al., 2010; Nimbalkar and Indraratna, 2016). The thickness of RIBS, capping, and subgrade are 0.3m, 0.15m and 10m; respectively, as shown in Figure 6.1 (b).

The boundary condition at the plane of symmetry restricts the lateral (transverse) displacement parallel to the sleeper, while other domain edges are modelled as one-way infinite elements to reduce model disturbance from residual wave reflection at the boundaries (Connolly et al., 2013; Kouroussis et al., 2014), as described in detail in Section 3.2.5. Overall, the discretised FE mesh consists of 152,685 nodes and 132,911 hexahedral elements (element type: C3D8R).

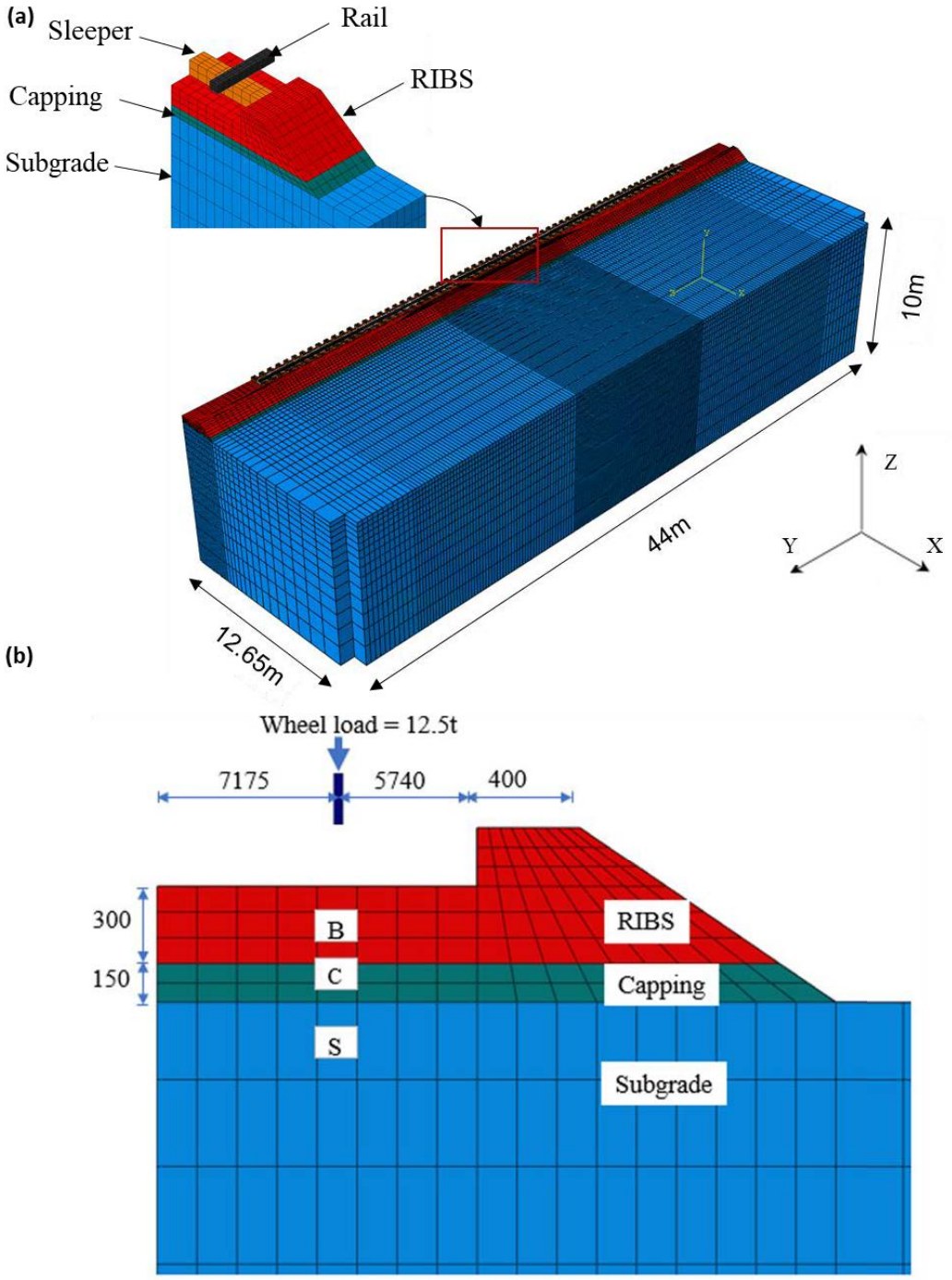

Figure 6.1 Finite element model geometry of RIBS track for moving load analysis

In order to study the influence of RIBS on the dynamic response of ballasted tracks, the Australian standard wagon RAS210(M210) was considered, as shown in Figure 6.2. According to ARTC (2018), the maximum allowable axle load on RAS 210 (M210)

standard wagon configuration shown in Figure 6.2 is 25t. Hence, this analysis considers the maximum allowable load to capture the critical loading condition for the train configuration selected, consistent with previous studies on Australia ballasted tracks (Indraratna et al., 2010; Sun et al., 2016). The moving wheel was idealised as a rigid body (element type: R3D4) located on top of the rail, which slides horizontally (along y-axis) at a constant speed.

The analysis is conducted at three different speeds to capture the track response at three distinct response regimes considering the R-wave speed of the subgrade: (a) pseudo-static (60km/h or $0.18V_R$), sub-critical (240km/h or $0.7V_R$) and resonating speed (300km/h or $0.9V_R$) for the subgrade property shown in Table 6.1.

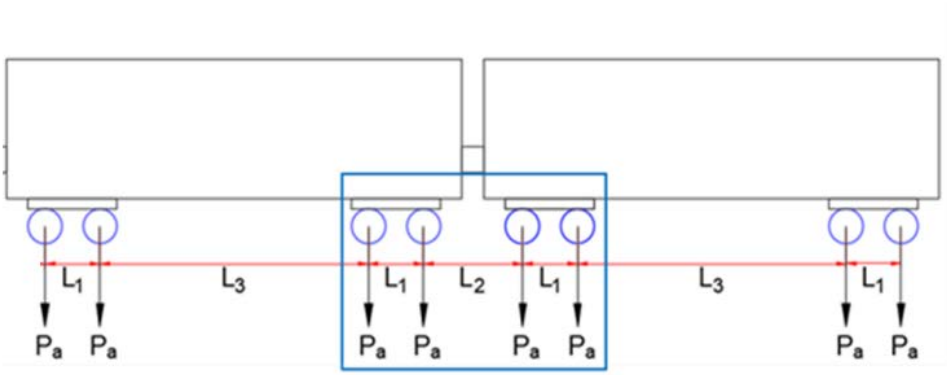

Coupled bogie loading

P_a	125kN
L_1	1.72m
L_2	3.1m
L_3	8.4m

Figure 6.2 Australian standard freight wagon load and dimensions (based on(ARTC, 2018))

6.2.2 Material models and train loading

The rail and concrete sleeper elements are modelled as small-strain linear-elastic material .The capping and subgrade layers are idealised using an elasto-plastic model following

the Mohr-Coulomb yield criterion. The subgrade is assumed to represent a dry, and over-consolidated silty clay. The mechanical properties of track material considered in this study are selected based on published literature (Arachchige et al., 2021; Arachchige et al., 2022; Hall, 2002; Indraratna and Nimbalkar, 2013; Nimbalkar and Indraratna, 2016)

The experimental studies on RIBS have shown that rubber inclusion improves the energy absorption and damping of a granular assembly, while the presence of rubber particles reduces shear strength, stiffness, and resilient modulus (Arachchige et al., 2021; Arachchige et al., 2022; Sol-Sánchez et al., 2015). The rubber aggregates generally dissipate energy since their stress-strain response exhibits viscoelastic behavior associated with a higher energy dissipation and recoverable deformation upon each loading-unloading cycle (Gent, 2012). This viscoelastic behavior of rubber aggregates increases the energy dissipation of the granular medium and enhances particle rearrangement and mobility under train loading (Gong et al., 2019). However, the rubber percentage (R_b) exceeding 10% significantly reduced shear strength, stiffness, and resilient modulus as higher rubber content shifted the response towards a rubber-like medium compared to conventional ballast (Arachchige et al., 2021). Similar to the conventional ballast, the stress-strain response of RIBS depends on the magnitude of confining and deviator stress as well as the number of loading cycles and volumetric strain (Arachchige et al., 2021; Arachchige et al., 2022; Gong et al., 2019), among others. The increase in the axial and volumetric strain response of compacted RIBS and standard ballast at very low loading cycles exhibit insignificant variation (Arachchige et al., 2022). Hence, the numerical implementation of RIBS should take into account the predicted response of RIBS under anticipated field stress and strain condition.

Esmaeili et al. (2017) recently modeled the ballast-TDA stratum as a linear elastic material to study the effect of TDA in reducing track vibration and associated attenuation speed. However, the strength and deformability of RIBS and the associated dependency of the response on confining pressure cannot be captured in linear elastic models (Arachchige et al., 2021; Badinier and Maiolino, 2018). Amongst the limited number of studies on RIBS, recently, Gong et al. (2019) and Arachchige (2022) have proposed the Mohr-Coulomb (MC) failure theory to predict the stress-strain response of RIBS. It was observed that the axial and volumetric behavior of RIBS could reasonably be predicted using the MC failure criterion with a non-associative flow rule for the range of confining stress observed in conventional ballasted tracks ($\sigma_3' < 30kPa$) (Arachchige, 2022). In this study, DP model was employed by computing the equivalent model parameters from the reported MC parameters (Arachchige, 2022; Arachchige et al., 2021) due to the computation efficiency of the circular yield surface in DP compared to MC that exhibits sharp corners in the stress space. Furthermore, the DP model is preferred since the effect of the reduced shear strength and dilation attributed to RIBS and the associated dependency of the response on confining pressure cannot be captured in linear elastic models and MC models (Arachchige et al., 2021; Badinier and Maiolino, 2018).

The strength, deformation and damping parameters were obtained from large-scale monotonic and cyclic triaxial testing on RIBS (Arachchige et al., 2021; Arachchige et al., 2022) Based on the experimental evaluation, RIBS with R_b =10% provides an improved ballast performance by reducing degradation and volumetric strain, albeit an acceptable compromise on a slight reduction in the stiffness and resilient modulus (Arachchige et al., 2022). Hence, RIBS with R_b =10% is appropriately considered for this numerical analysis.

Table 6.1 Material parameters used 3D FEM Analysis for the standard and RIBS track (Arachchige et al., 2021; Arachchige et al., 2022; Hall, 2002; Indraratna and Nimbalkar, 2013)

	Rail Track Components					
	Rail	Concrete Sleeper	Ballast[1]	RIBS[1]	Capping[2]	Subgrade [2]
Material Model	LE	LE	DP	DP	MC	MC
Material Type	Non-porous	Non-porous	Drained	Drained	Drained	Drained
Density (kg/m^3)	7800	2500	1535	1342	1667	2140
Modulus of Elasticity, E (MPa)	210,000	30,000	205	140	140	60
Poisson's ratio, ν	0.25	0.2	0.3	0.35	0.35	0.33
Friction angle, ϕ (^{O})			48.8	47.7	35	20
Cohesion, C'(kPa)			1	1	5	10
Dilation angle, ψ (^{O})			11	4.0		
Damping ratio (D)			0.2	0.47	0.04[3]	0.04[3]
R-wave velocity, V_R (Km/h)						337

[1] (Arachchige et al., 2021; Arachchige et al., 2022)
[2] (Indraratna and Nimbalkar, 2013)
[3] (Hall, 2002)

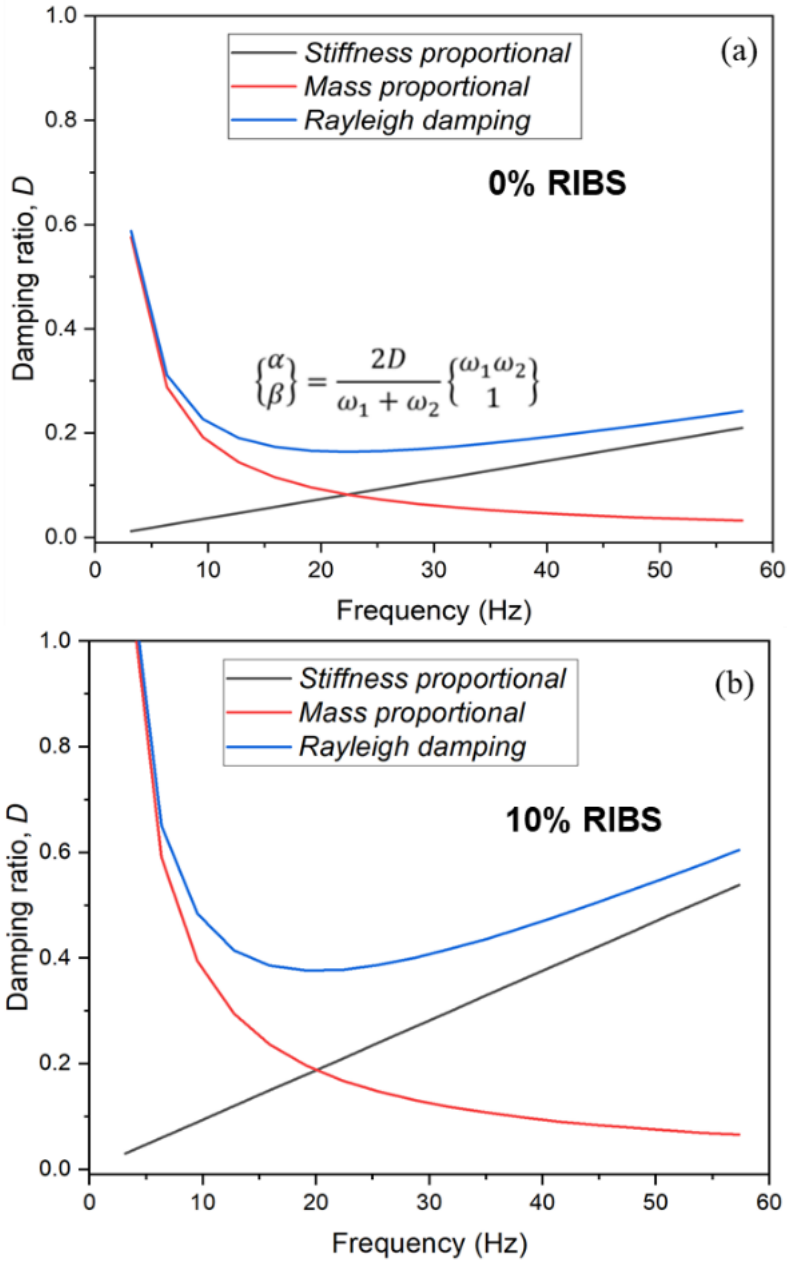

Figure 6.3 Rayleigh damping model for Pure Ballast and RIBS with 10% rubber

The rubber granules intermixed within ballast system (RIBS) can increase energy absorption and damping while reducing the ballast resilient modulus (Arachchige et al., 2022; Esmaeili et al., 2016). At R_b =10% , the damping ratio of RIBS increased by 135% as compared to conventional ballast (i.e., damping ratio D increased from 0.2 to 0.47) while the resilient modulus reduces by about 32% (Arachchige et al., 2022). The effect

of damping associated with the inclusion of TDA can be captured through implementation of Rayleigh damping models in FE analysis (Esmaeili and Siahkouhi, 2019; Fernández-Ruiz et al., 2020). Hence, Rayleigh damping model is adopted to capture the influence of damping and associated energy absorption in the time domain analysis employed in this study. Following the approach discussed in Section 3.2.6, the mass-proportional (α) and stiffness-proportional damping (β) coefficients of each layer have been incorporated in the FEM analysis. Figure 6.3 illustrates the effect that TDA mixed with ballast aggregates has on Rayleigh damping coefficients as implemented in this FE analysis.

6.3 Results and discussion

6.3.1 Vertical displacement of RIBS under moving wheel load

Figure 6.4 (a-c) shows the dynamic vertical deflection predicted at the centre of the RIBS/ballast layer subjected to various train speeds. At a relatively low speed of 60km/h, downward vertical transient deflection (δ_{dvp}) is consistently higher in the RIBS track (R_b =10%) compared to the standard track. However, at a much higher speed (i.e., exceeding 240km/h) the analysis of RIBS track shows a reduced δ_{dvp} as compared to the standard track model with conventional ballast. This implies that the increased damping in RIBS increases the attenuation of stress waves at higher train speeds approaching a resonant response as also explained in earlier studies (Athanasopoulos et al., 2000; Yang et al., 2019). Hence, any adverse effects of the reduction in the stiffness and the resilient modulus of ballast are counter-balanced by the extent of damping and ductility that represents the energy dissipation in RIBS track. However, the difference in transient deflection between the standard and RIBS track is not substantial (<11%) for all speeds considered. The profile of transient deflection shows that the upward deflection behind

the moving wheels reduces with the inclusion of RIBS tracks, which reduces the peak-to-peak vertical displacement. At lower speeds, the two distinct peaks corresponding to each bogie load, which means at the middle of the ballast layer, the response is dominated by the interaction of axles (*i.e.,* the stress-displacement response from the individual axles under a single bogie overlap). However, the displacement profiles at high speed exhibit a single peak, located towards the rear of the couple-bogies, which does not align with the location of individual axles but is influenced by an overlap of displacement field created by the adjoining four axles creating a cone-shaped displacement field.

Figure 6.5(a-b) and Figure 6.6(a-b) present the deformation contours at 60km/h and 300km/h, respectively. At a lower speed of 60km/h, the vertical displacement contours are quasi- symmetrical consistently following the wheel loads in both RIBS and standard tracks, albeit the difference in magnitude. In contrast, at higher speeds, the peak displacement is amplified and shifted towards the ends of the bogies, which indicate the development of Mach cones, i.e., a cone-shaped displacement field formed when the train speed approaches or exceeds the R-wave velocity. However, the shape of vertical displacement curves presented in Figure 6.4(a-c) are similar irrespective of the type of track, which indicates that the critical speed would remain the same. The maximum downward displacement at 60km/h (Figure 6.5) increases from 2.97mm to 3.26mm due to the inclusion of RIBS (i.e., rubber granules in the ballast layer). However, the contour in Figure 6.6 illustrates a reduction in peak displacement (from 4.1mm to 3.94mm) at 300km/h (or $0.9V_R$).

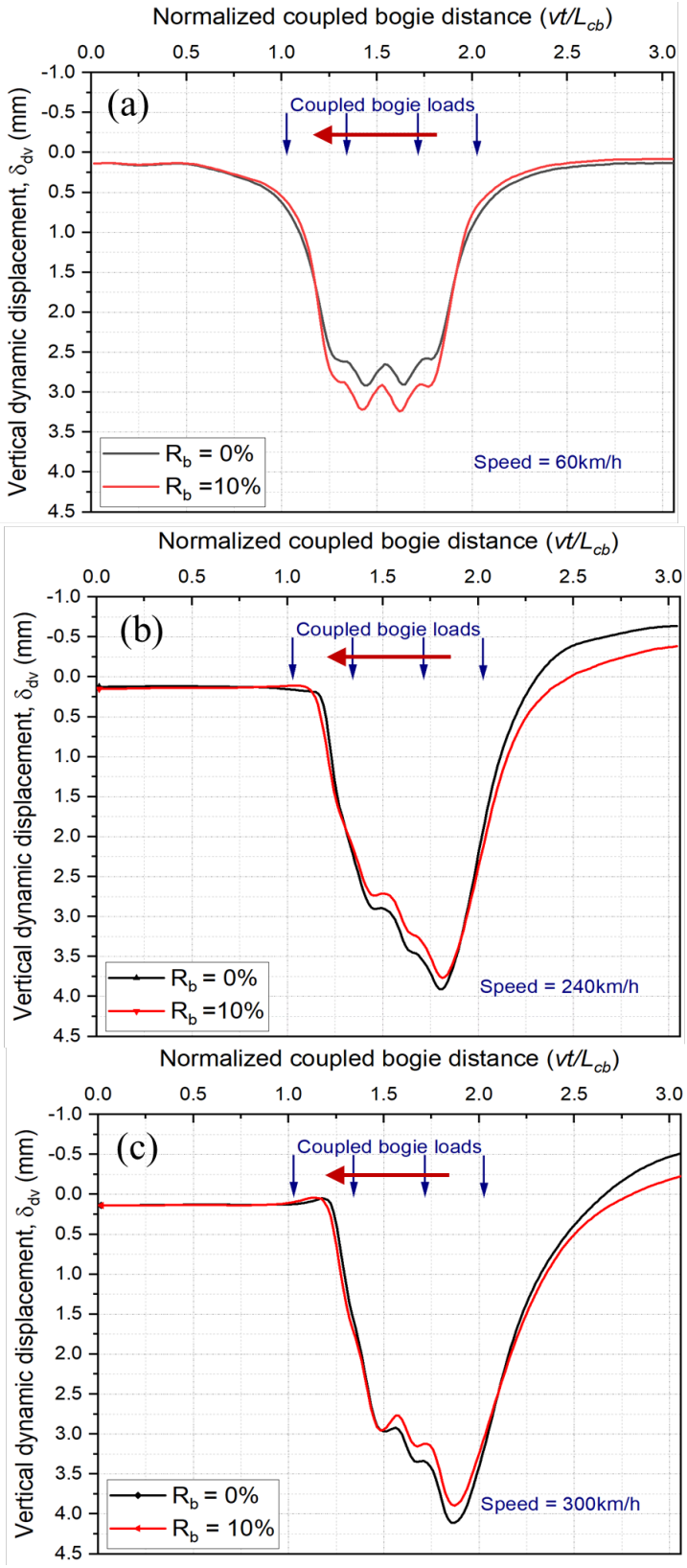

Figure 6.4 Comparison of ballast vertical displacements using standard and RIBS track: (a) 60km/h, (b) 240km/h and (c) 300km/h

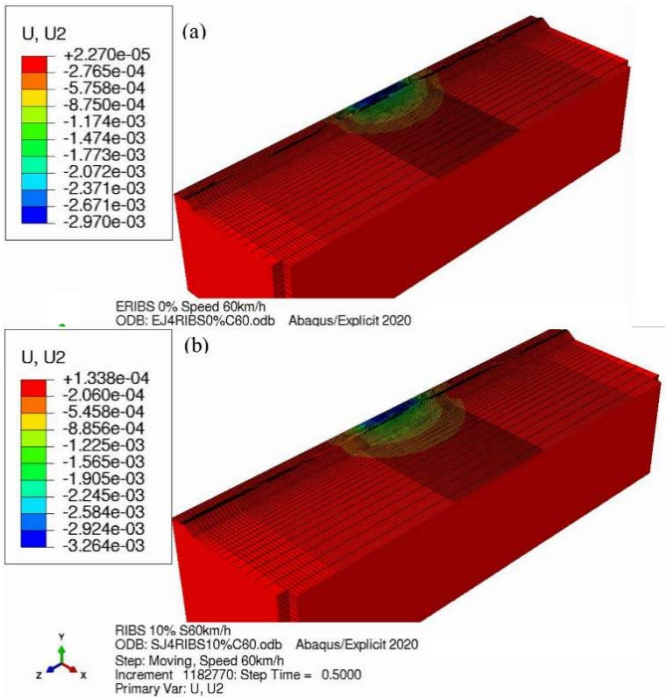

Figure 6.5 Contour plots of vertical deformation under moving load at 60km/h: (a) pure ballast ($R_b = 0\%$) (b) RIBS with $R_b = 10\%$

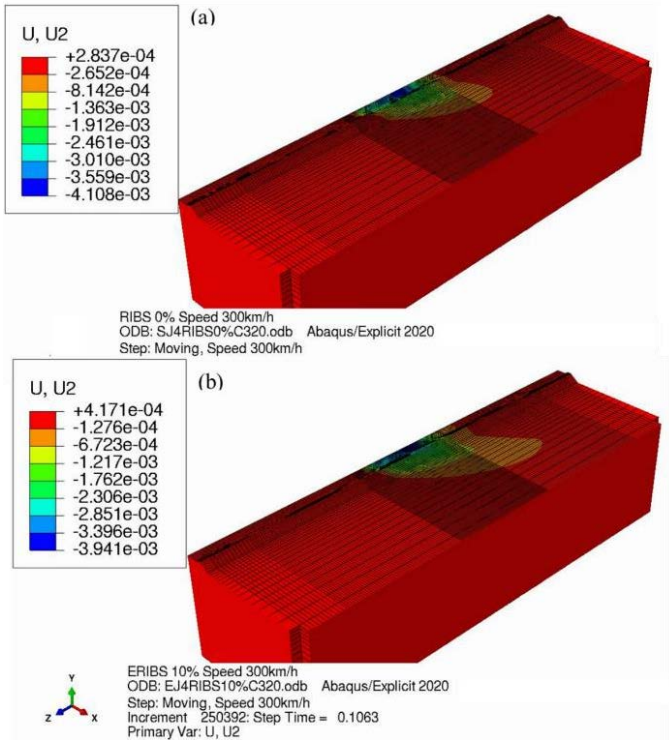

Figure 6.6 Contour plots of vertical deformation under moving load at 300km/h: (a) pure ballast ($R_b = 0\%$) (b) RIBS with $R_b = 10\%$

6.3.2 Lateral displacement of RIBS under moving wheel load

Figure 6.7 shows the maximum lateral displacement in the ballast and capping layers measured along the shoulder ballast, considering the inclusion of RIBS and the train speed. At all the speeds considered, the lateral displacement predicted in RIBS track is lower than the standard track due to reduced dilation in the RIBS (i.e., 63% reduction in dilation as indicated in Table 6.1). Further reduction in lateral displacement is observed at high speed due to increased damping, hence the energy retention/dissipation capacity of RIBS.

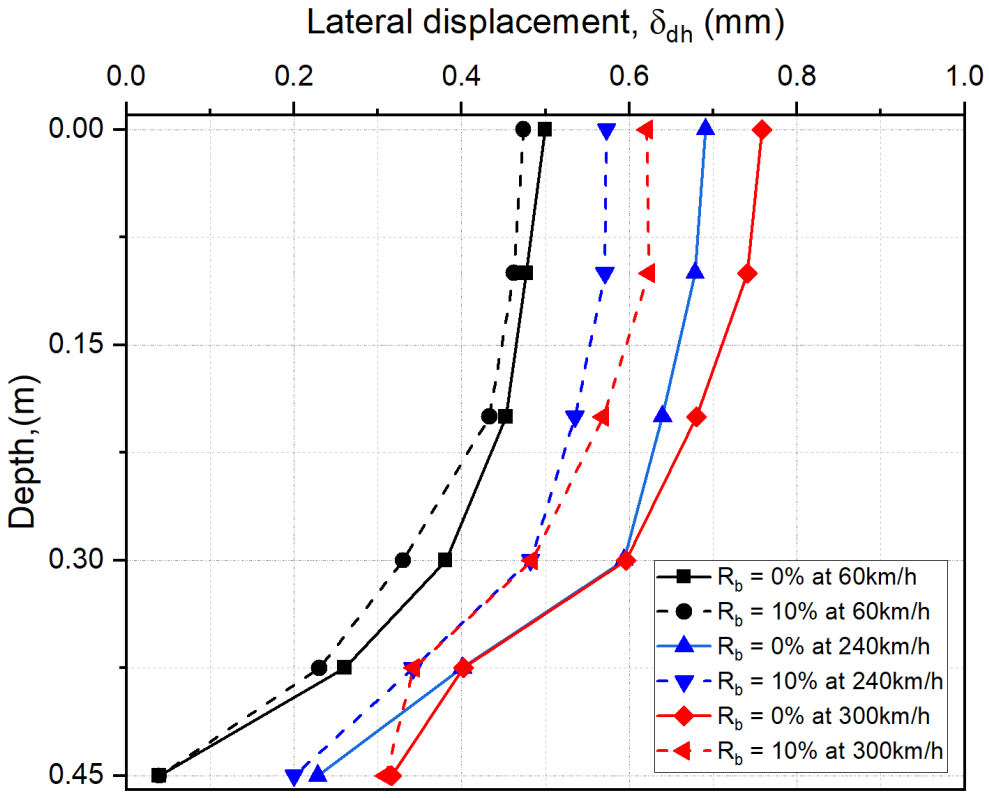

Figure 6.7 Comparison of predicted lateral displacement for the standard track (R_b = 0%) and RIBS track (R_b = 10%)

From Figure 6.7, it can be seen that the lateral displacement is maximum at the ballast top, and it decreases with depth in the ballast and capping layers. Similarly, the extent of

reduction in lateral displacement at the ballast surface (about 18%) attained by rubber aggregates is also maximum at the ballast surface and becomes insignificant at the capping bottom. The reduction in the lateral displacement decreases with depth since damping-induced attenuation of stress waves achieved through rubber inclusions are confined at the top 0.3m. That means, the vibrations generated by the stress wave propagation associated with R-waves, whose propagations are confined to surficial layers of the rail track substructure, are reduced due to increased damping in RIBS (Athanasopoulos et al., 2000; Richart et al., 1970).

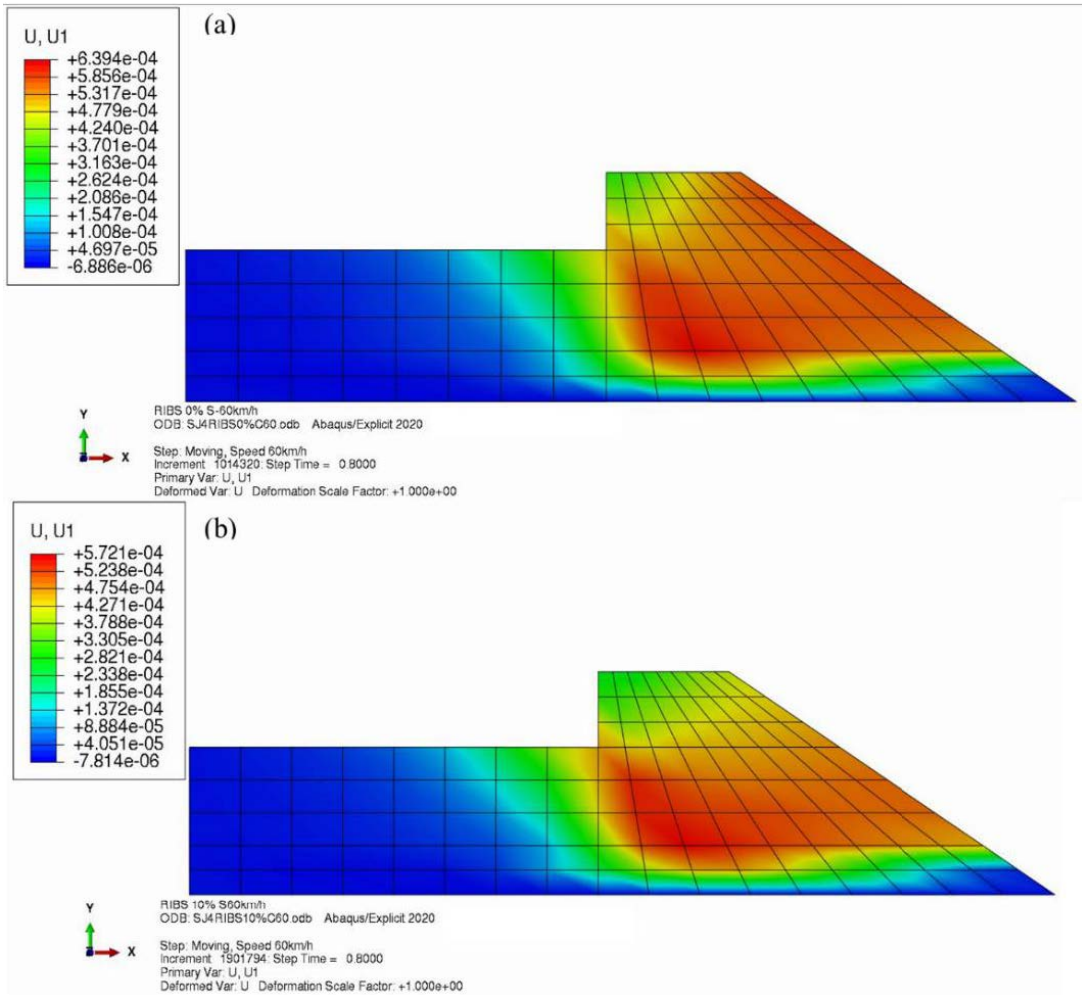

Figure 6.8 Contour plots of lateral displacement under moving wheel load at 60km/h: (a) pure ballast (R_b = 0%) (b) RIBS with R_b = 10%

Figure 6.8 and Figure 6.9 present the lateral displacement contours showing critical regions in the vicinity of the shoulder ballast. The regions close to the shoulder ballast are generally prone to significant lateral displacement, which can contribute to track instability and misalignment. Although significant amplification of lateral displacement is evident in standard ballasted tracks at relatively high speeds, the reduction in the dilatative response of RIBS associated with a high damping coefficient certainly improves the performance of the track in terms of lateral stability. In summary, it is noteworthy that at relatively high speed, the lateral and vertical track displacement in the RIBS track is lower than that of the standard track.

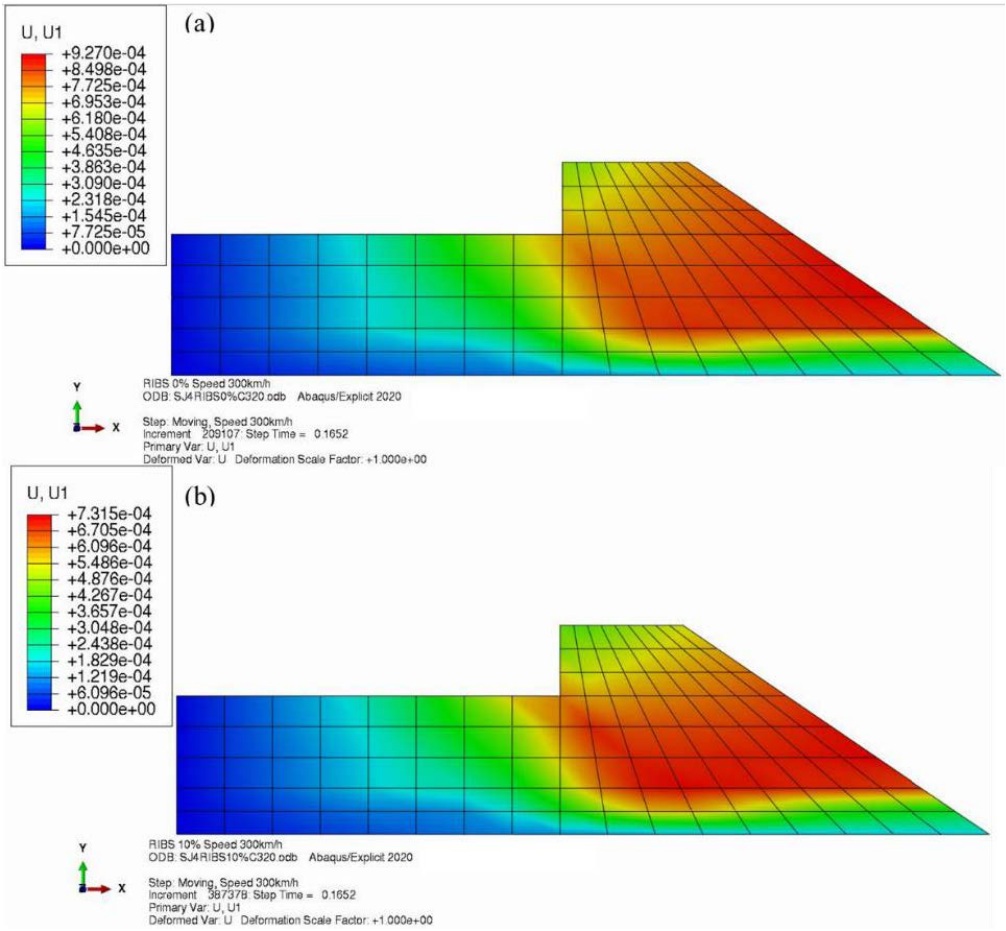

Figure 6.9 Contour plots of lateral displacement under moving wheel load at 300km/h: (a) pure ballast ($R_b = 0\%$) (b) RIBS with $R_b = 10\%$

6.3.3 Vertical stress distribution of RIBS track under moving wheel load

Figure 6.10(a-c) summarises the transient vertical stress at the center of the ballast layer (0.15m from the sleeper bottom) located along the axis of the rail.

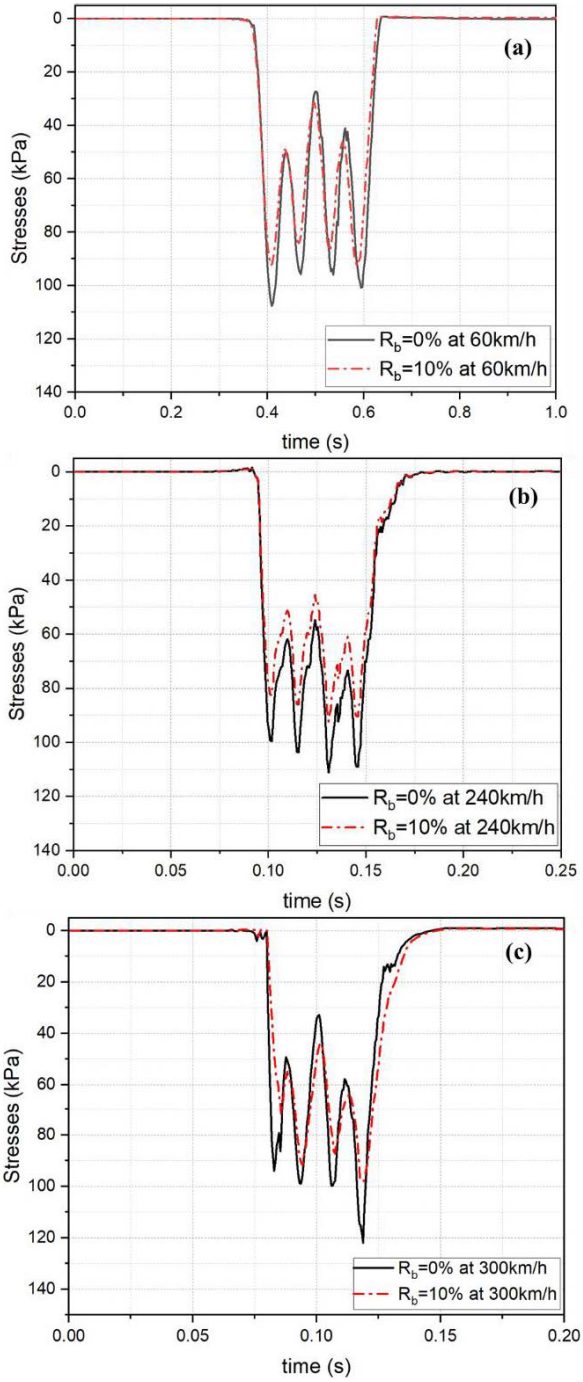

Figure 6.10 Vertical stress predicted at the center of RIBS and standard ballast layers at various train speeds: (a) 60km/h (b) 240km/h, and (c) 300km/h

For all speeds, the plots indicate that the ballast stress reduces when the RIBS material is introduced as a load-bearing layer. However, these plots also show that during wheel-load passing at a specific speed, the shape of the vertical stress curves remains generally similar for both RIBS and standard tracks albeit having different magnitudes. The amplitude of the maximum vertical stress is reduced by 14%, 17%, and 25% for the train speed of 60km/h, 240km/h, and 300km/h when the ballast layer is replaced by the RIBS track. An increase in the percentage reduction of vertical stresses at a higher speed range (240km/h and 300km/h) can be attributed to the increased damping property of the RIBS layer.

Figure 6.11 shows the maximum vertical stress distribution with depth predicted for the RIBS compared to the standard track. The magnitude of sleeper-ballast contact stress and depth-wise attenuation of vertical stress is affected by train speed and the inclusion of rubber in the ballast stratum. It can be seen that the reduction in the vertical stress is maximum at the ballast top and decreases with depth in the ballast and capping layers. However, an increase in vertical stress caused by the increasing train speed is apparent in all track substructure layers for both RIBS and standard tracks, with a maximum amplification of 1.3 (R_b = 0%) and 1.2 (R_b = 10%) in the ballast and RIBS layers, respectively.

Figure 6.12(a-c) presents the peak vertical stress attenuation in the topmost layers of the track substructure (0.6m), where the influence of rubber granules is significant. The peak ballast-sleeper interface stress was retrieved from the peak nodal output at the top of the ballast layer, while at substructure depths, the stresses were computed at the elemental integration points in the finite element mesh.

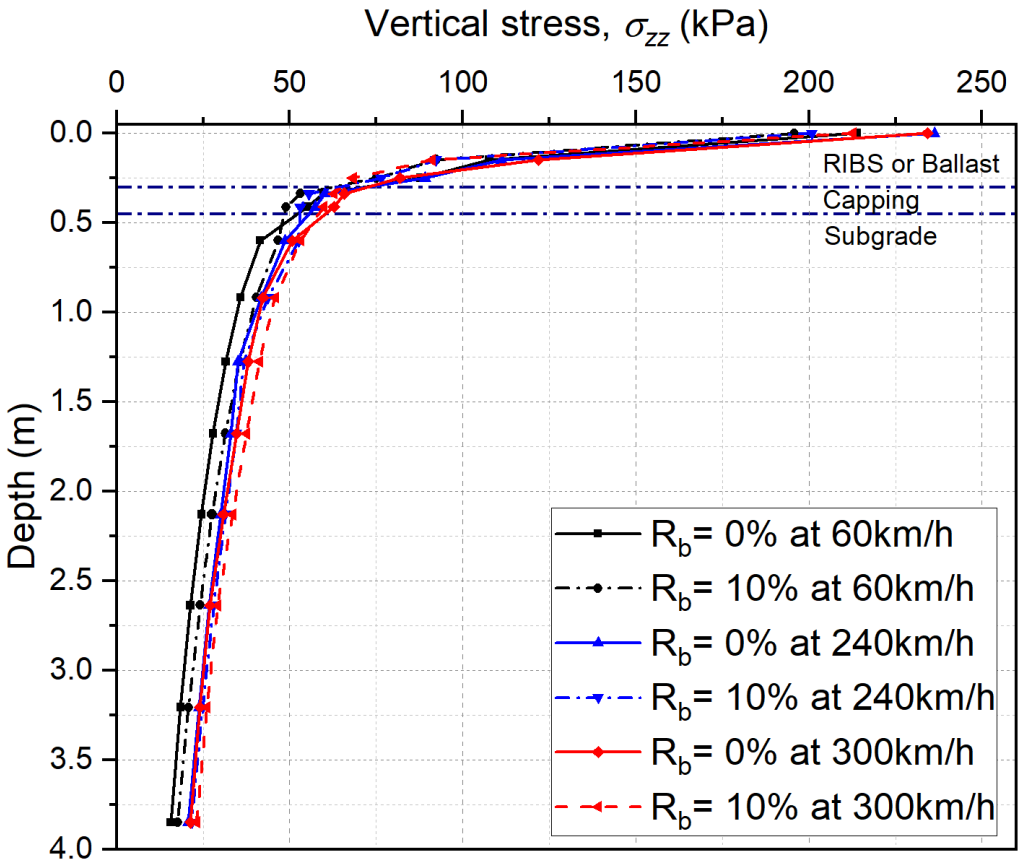

Figure 6.11 Comparison of predicted vertical stress with depth for the standard track (R_b = 0%) and RIBS track (R_b = 10%) at various speeds

The peak vertical stress, predicted at 0.15m from the sleeper bottom in the RIBS track is lower than the standard track by 14%, 17%, and 25% for the train speeds of 60km/h, 240km/h, and 300km/h, respectively. However, the maximum vertical stress attenuation achieved by the inclusion of RIBS contributes to a stress reduction of about 11% (at 60km/h), 8% (at 240km/h), and 5% (at 300km/h) at the capping-subgrade interface. Therefore, the reduction in vertical stress due to RIBS is maximum in the ballast layer, when the train load travels at 300km/h. This may be attributed to the attenuation of stresses as a result of increased damping within the zone R-wave propagation depth.

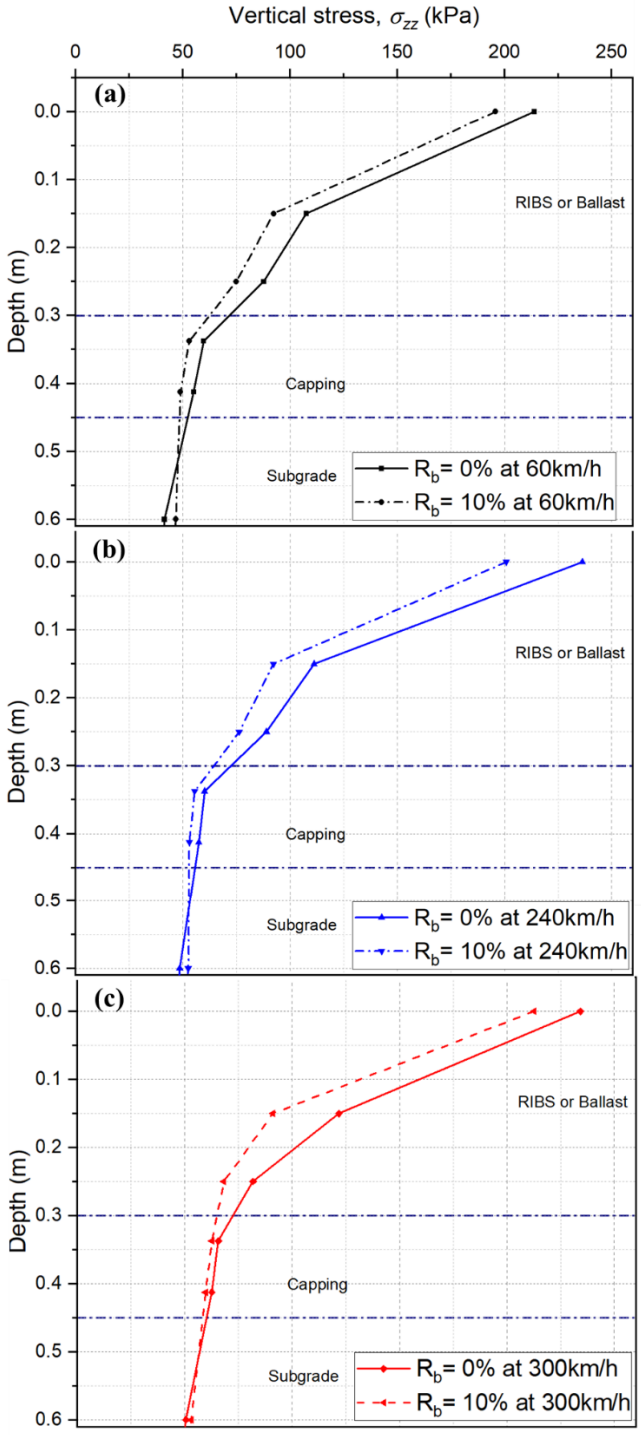

Figure 6.12 Detailed comparison of vertical stresses at the top 0.6m for the standard track (R_b = 0%) and RIBS track (R_b = 10%) at various speeds

6.4 Chapter summary

This chapter presented the findings of a 3D finite element analysis of a simulated rail track considering the effect of RIBS under moving wheel load. FEM analysis was conducted at various simulated train speeds (60km/h, 240km/h and 300km/h) considering the passage of a heavy haul train having an axle load of 25t.

The instantaneous track response was analysed using an optimum rubber percentage of 10% (by weight) in RIBS. Naturally, mixing rubber granules with ballast reduced the resilient modulus by about 47% from conventional fresh ballast, resulting in a slightly increased vertical displacement especially at the initial loading stage when compared to the displacement t of conventional track without rubber aggregates.

The RIBS track showed reduced lateral displacement at all train speeds caused by high damping ratio and reduced dilation of the RIBS material as compared to traditional ballast. As expected, the vertical displacement response varied depending on the train speed. A higher vertical displacement was predicted at lower speed, and this is in conformity with the apparent decrease in the resilient modulus of RIBS. In contrast, the prescribed damping in the model associated with RIBS contributed to the reduction in lateral displacement at relatively high speed. Similarly, the peak vertical stress in the RIBS track was lower than that of the standard track; in fact, the percentage reduction increased with the train speed, reaching 25% at 300km/h (or $0.9V_R$).

CHAPTER 7 CONCLUSION AND RECOMMENDATIONS

7.1 Introduction

This study focused on the dynamic stress-deformation analysis of ballasted track substructure under moving train wheel loading and establishing the limiting train speed against apparent track instability. The 3D FEM model was developed and successfully validated with two independent field measurements taken from the literature. Furthermore, the model prediction was compared with semi-analytical solutions for various speeds approaching the critical speed showing an acceptable agreement in terms of 3D stress response in the half-space. Dynamic responses in terms of vertical and lateral displacements, critical speed, the evolution of stress paths and the corresponding angle of principal stress rotation, and stress amplification attributed to moving load were analysed for both the ballast and subgrade layers. The influence of subgrade stiffness on critical speed, dynamic amplifications, lateral and vertical displacement was analysed for different train speeds. The model was further extended to compare the stress-deformation response of Rubber-Intermixed-Ballast (RIBS) against conventional ballast under moving train loading. The following sections provide the salient outcomes from the current study. Recommendations for future research are also provided following the conclusions.

7.2 Critical speed and deformation response of ballasted track at high speeds

a) The vertical and lateral displacement of track substructure subjected to varied train speeds of 60km/h to 450km/h were captured and analysed. At a low speed (< 120 km/h), the deformation contours were quasi-symmetric for all subgrade

cases considered. In contrast, asymmetrical deformation and cone-shaped transient displacement contours were observed at greater speeds due to the time lag between moving load and stress waves propagation.

~~b)~~ The 3D FE analysis showed that the amplitude of vertical deformation at the middle of ballast layer increased with the train speed, reaching a maximum value at the critical speed. The transient vertical displacement response predicted using elastoplastic constitutive models results in higher deflection under moving load compared to the linear elastic models by 11%.

c) Increasing the train speed had significantly influenced the transient lateral deformation of shoulder ballast as compared to the vertical deformation. At the critical speed close to 300 km/h, the lateral displacement increased to 3.3mm from 1.1mm predicted at 60km/h, i.e., about 200% increase, in contrast to about 37% increase in vertical displacements (from 2.7 mm to 3.7 mm), for the case of subgrade modulus E_s= 50MPa. Hence, design based on vertical displacement alone is totally insufficient at high speeds, where track design modifications are imperative to account for the excessive lateral movement. In a practical sense, track region at the edge of sleepers (i.e., in the vicinity of the track shoulder is prone instability at high speeds due to lateral spreading of ballast in the absence of adequate confining pressure. Therefore, to alleviate instability of shoulder ballast at high trains speeds, end restrains may be necessary to be installed beyond the track shoulder boundary (Lackenby et al., 2007)

d) The amplification of both lateral and vertical deformations decreased with an increase in subgrade resilient modulus. In contrast, the critical speed increased

with an increase in subgrade modulus. The deformation responses predicted from the numerical analysis implied that increasing the subgrade modulus through localised ground improvement could increase the critical speed while reducing the dynamic track displacement.

7.3 Stress path and amplification under moving load

a) Consistent with vertical and horizontal deformation response, this study verified that the peak vertical stress and shear stresses generally amplify with the increasing train speed. However, the peak vertical stress (σ_{zz}) amplifications were moderate as compared to deviator stress amplifications. Hence, maximum dynamic stress amplification factor (SAF) was analysed based on deviator stress. The (SAF) from the FEM analysis was found to be consistent with analytical predictions.

b) Based on SAF, three specific regions could be identified, namely, Range-I ($\leq 30\%V_R$): quasi-static response, Range-II ($30\% - 60\%V_R$): moderate amplification ($30\% - 60\%V_R$) and Range-III ($60\% - 100\%V_R$): significant amplification that can lead to shear failure. Therefore, the effect of moving load and associated R-wave propagation should be considered for tracks design with dimensionless speed ratio (V/V_R) exceeding 0.3.

c) In addition to amplifying the vertical stress, the 3D stress state inside the track substructure changed with the moving wheel load. Hence, the principal stress plane continuously rotated thus generating a complex stress path. The cycles of stress reversal also significantly increased at high speed. The generally adopted

'cardioid shaped' stress path was observed at quasi-static speed ranges (V/V_R<0.3); however, this cardioid shape did not adequately capture the response associated with Rayleigh wave propagation at an elevated speed.

d) In addition to the train speed, SAF is significantly influenced by the subgrade stiffness and the depth in the track substructure. Based on this study, SAF decreased with subgrade stiffness, while the maximum amplification was observed in the ballast and capping layers. The predicted maximum amplification factors in the ballast layer were 2.98 and 2.43 for E_s= 25MPa and E_s= 50MPa; respectively. However, the maximum SAF in the case of stiff subgrade (E_s= 100MPa) was observed in the capping layer (SAF = 1.7). For all subgrade scenarios considered herein, the amplification factors seem to be less sensitive to the depth and location in the track substructure when the train speed is less than 120km/h. In contrast, at high speeds exceeding 30% V_R, SAF is significantly influenced by the substructure depth as measured from the ballast surface. In essence, applying a single maximum SAF computed at the ballast layer for all track components would not lead to an economical design prediction at high speeds.

7.4 Stress-deformation response of RIBS

The instantaneous response of the track was analysed considering RIBS at an optimum crumb rubber percentage of 10% and compared against the standard track. The material parameters of RIBS and standard ballast were selected from an earlier PhD study

(Arachchige (2022)) to predict the track response subjected to various speeds. Based on 3D FE analysis, the following conclusion can be made:

(a) For all train speeds, the RIBS track showed reduced lateral displacement (up to 18%), which was caused by the relatively high damping coefficient of D = 0.47, in comparison with D = 0.2 for standard ballast, as well as the reduced dilation of RIBS ($\psi = 3^{O}$) when compared to pure ballast ($\psi = 11^{O}$).

(b) The vertical displacement response varied by up to 11% depending on the train speed. For RIBS track, a higher vertical displacement of 3.26mm (compared to 2.9mm for standard track) was predicted at low speed (60 km/h) due to the reduced resilient modulus of RIBS (140MPa) by about 30% from the fresh ballast (205MPa). In contrast, the vertical displacement at high-speed (240km/h and 300km/h) showed insignificant variations. Therefore, the response at a relatively low speed can be idealised as being governed predominantly by the magnitude of initial small-stain stiffness and the resilient modulus, whereas the damping coefficient plays a significant role in reducing track deformation at a higher speed approaching its resonant threshold.

(c) The peak vertical stress in the RIBS track is smaller than that of the standard track, and a percentage reduction of 25% in vertical stress was associated with a train speed of 300km/h (or $0.9V_R$). At low speed of 60 km/h (i.e., pseudo-static response), the reduction in vertical stress was about 14% in the RIBS stratum, which could be related to the reduction in the initial (small strain) stiffness of RIBS. However, the vertical stress reduction observed at high-speed could be

caused by the combined effect of increased damping property and reduced resilient modulus of RIBS having 10% rubber content.

7.5 Limitations and recommendations for further study

The stress-deformation response of ballasted tracks under a moving train loading was investigated in this study using 3D-FEM analysis. The developed 3D-FEM model was utilised to investigate the application of RIBS in railway track applications. However, numerous assumptions and associated limitations required further investigation. Hence, some recommendations are proposed for future research to further understand the dynamic response of ballasted tracks.

(a) The moving train is usually modelled as moving discrete point load pulses or sliding rigid bodies representing train wheels traversing on the top of the rail (Araújo, 2011; Hall, 2003; Sayeed and Shahin, 2016). Hence, the dynamic loads generated at wheel-rail interfaces due to track irregularities and track stiffness variations are often ignored. Those dynamic loads associated with track geometry irregularities could influence the stress-deformation response of ballasted track. The magnitude of dynamic amplification associated with train-track irregularities could be higher than the stress-deformation predictions from numerical modelling for smooth tracks at high speeds. This study modelled the wheel as a rigid body sliding on the top of the rail. Therefore, the numerical model could be extended by coupling train and track models, which would be of interest when considering heavy axle loads moving at high speeds.

(b) Permanent deformation of the track substructure is a critical design criterion for ballasted tracks. However, many loading cycles must be simulated to capture accumulations of permanent vertical and lateral deformations track substructure. In this study, the transient stress-deformation response of the ballasted track was simulated only for a limited wheel load cycle, and this was due to the significantly high computational resources and convergence times required for large-scale FE models capturing wave propagation associated with moving loads. Therefore, this study can be ideally extended to capture the accumulation of permanent deformations with a large number of moving wheel loads, which also requires large-strain elastoplastic constitutive models for track geomaterials such as ballast.

(c) The breakage of ballast particles with the number of loading cycles significantly influences the lateral deformation and settlement of ballasted track. The effect of particle breakage and the associated accumulation of permanent strain with many moving loads could not be considered in the numerical simulations. A better understanding of safe operating speed could be achieved by capturing the effect of moving load on ballast breakage and permanent strains. Hence, a constitutive model capturing ballast breakage should be developed using user-defined material models to predict the stress-strain response of ballasted tracks accurately. It is recommended that Indraratna and Salim (2005) type ballast breakage model be extended and captured in large strain 3D FEM analysis.

(d) The analysis of the RIBS track under moving wheel loading was conducted based continuum-approach, specifically FE analysis. Hence, dynamic response RIBS, such

as rubber-ballast interaction and ballast breakage were not considered. Those aspects can be studied by extending this study through coupled DEM-FEM analysis to capture particulate nature RIBS through DEM while the remaining track substructure can be modelled with FEM.

(e) In this study, the track substructure was assumed to be fully drained, hence the effect of any pore pressure build-up was not considered. However, the fouling of ballast by fine particles over time can lead to sustained excess pore water pressure. Moreover, under prolonged cyclic loading by long and heavy trains, the development of excess pore pressure in soft subgrade can lead to fluidization and subsequent mud pumping to contaminate ballasted tracks, which in turn can cause differential settlement and instability. Therefore, any numerical analysis for railway tracks especially built on saturated soft subgrade should be able to capture the development of excess pore pressures and plastic strains under moving wheel loading. Under these circumstances, further numerical advancement needs to be undertaken to capture the appropriate stress-strain amplification under increasing train speed and axle loads.

(f) At the time of this study, field data with vibration and stress-deformation measurement for a track constructed with RIBS was not available for validation purposes. Therefore, an appropriate real-life case study with vibration, stress-strain and deformation measurements is certainly recommended to capture the performance of RIBS under realistic loading and track conditions for a range of train axle loads and speeds.

(g) This study captured a single moving train cycle for both standard and RIBS tracks. The deformation and degradation of RIBS and associated energy absorption achieved through granulated rubber inclusions is significantly affected by the number of loading cycles. To study the long-term response of RIBS in greater rigour a more comprehensive constitutive model incorporating particle breakage and time-dependent damping (energy absorbing capacity) over a large number of loading cycles need to be developed and implemented in finite element modelling via a user-defined material model.

REFERENCES

Adam, D., Vogel, A. and Zimmermann, A. 2007. "Ground improvement techniques beneath existing rail tracks." Proceedings of the Institution of Civil Engineers-Ground Improvement 11(4): 229-235.

AECOM.2011. High Speed Rail Study - Phase 1. Australia, Department of Infrastructure and Transport.

Alves Ribeiro, C., Paixão, A., Fortunato, E. and Calçada, R. 2015. "Under sleeper pads in transition zones at railway underpasses: numerical modelling and experimental validation." Structure and Infrastructure Engineering 11(11): 1432-1449.

Andersen, L. (2002). Wave propagation in infinite structures and media. PhD Thesis, Aalborg Universitet, Denmark.

Anderson, W. F. and Fair, P. 2008. "Behavior of railroad ballast under monotonic and cyclic loading." Journal of Geotechnical and Geoenvironmental Engineering 134(3): 316-327.

Arachchige, C. (2022). Experimental and Numerical Study of Rubber Intermixed Ballast System Subjected to Monotonic and Cyclic Loading. PhD Thesis, University of Technology Sydney, Australia.

Arachchige, C. M. (2022). Experimental and Numerical Study of Rubber Intermixed Ballast System Subjected to Monotonic and Cyclic Loading.

Arachchige, C. M., Indraratna, B., Qi, Y., Vinod, J. S. and Rujikiatkamjorn, C. 2021. "Geotechnical characteristics of a Rubber Intermixed Ballast System." Acta Geotechnica: 1-12.

Arachchige, C. M., Indraratna, B., Qi, Y., Vinod, J. S. and Rujikiatkamjorn, C. 2022. "Deformation and degradation behaviour of Rubber Intermixed Ballast System under cyclic loading." Engineering Geology: 106786.

Araújo, N. M. F. (2011). High-speed trains on ballasted railway track: dynamic stress field analysis PhD thesis, Universidade do Minho, Portugal.

AREMA.2014. Manual for Railway Engineering, Volume 1: Track, Chapter 1: Roadway and Ballast. American Railway Engineering and Maintenance of Way

Association. Washington, DC: AREMA, American Railway Engineering and Maintenance of Way Association. 1.

AREMA. 2015. Manual for Railway Engineering. Lanham, MD.: American Railway Engineering and Maintenance of Way Association.

ARTC. 2018. Route Access Standard General Information: Australian Rail Track Corporation Limited.

Arulrajah, A., Abdullah, A., Bo, M. W. and Bouazza, A. 2009. "Ground improvement techniques for railway embankments." Proceedings of the Institution of Civil Engineers-Ground Improvement 162(1): 3-14.

AS2758.7. 2015. Aggregates and rock for engineering purposes, Part 7: Railway ballast. Sydney, New South Wales, Australia: Standard Australia.

Ashmawy, A., Salgado, R., Guha, S. and Drnevich, V. 1995. "Soil damping and its use in dynamic analyses." International conferences on recent advances in geotechnical earthquake engineering and soil dynamics.

Atalar, C. 2001. "Settlement of geogrid-reinforced railroad bed due to cyclic load." Proc. 15th Int. Conf. on Soil Mech. and Geothch. Engrg., Istanbul, Turkey.

Athanasopoulos, G., Pelekis, P. and Anagnostopoulos, G. 2000. "Effect of soil stiffness in the attenuation of Rayleigh-wave motions from field measurements." Soil Dynamics and Earthquake Engineering 19(4): 277-288.

Badinier, T. and Maiolino, S. 2018. "Limiting discrepancies when substituting Mohr-Coulomb with fast computation smooth criteria: application to ballast layers." International Journal of Railway Technology 7(2): pp. 41-66.

Banimahd, M., Woodward, P., Kennedy, J. and Medero, G. 2013. "Three-dimensional modelling of high speed ballasted railway tracks." Proceedings of the Institution of Civil Engineers-Transport, Thomas Telford Ltd.

Bergmann, L. 1938. Ultrasonics and their scientific and technical applications. New York: Wiley.

Bergmann, L. 1948. Ultrasonics and their scientific and technical applications. New York: Wiley.

Bian, X., Chen, Y. and Hu, T. 2008. "Numerical simulation of high-speed train induced ground vibrations using 2.5 D finite element approach." Science in China Series G: Physics, Mechanics and Astronomy 51(6): 632-650.

Bian, X., Jiang, H., Cheng, C., Chen, Y., Chen, R. and Jiang, J. 2014. "Full-scale model testing on a ballastless high-speed railway under simulated train moving loads." Soil Dynamics and Earthquake Engineering 66: 368-384.

Bian, X., Li, W., Qian, Y. and Tutumluer, E. 2020. "Analysing the effect of principal stress rotation on railway track settlement by discrete element method." Géotechnique 70(9): 803-821.

BITRE.2019. Multimodal Australian Aggregate Freight Forecast. Canberra, Australia, Department of Infrastructure, Transport, Cities and Regional Development.

Boulbes, R. J. 2020. Troubleshooting Finite-Element Modeling with Abaqus: Springer.

Brecciaroli, F. and Kolisoja, P. 2006. "Deformation behaviour of railway embankment materials under repeated loading." Literature review. Helsinki.

Briggs, A., Briggs, G. and Kolosov, O. 2010. Acoustic microscopy: Oxford University Press.

Brown, S. 1996. "Soil mechanics in pavement engineering." Géotechnique 46(3): 383-426.

Budiono, D., Mcsweeney, T., Gurung, N. and Dhanasekar, M. 2004. "The effect of coal dust fouling on the cyclic behaviour of railway ballast." Cyclic behaviour of soils and liquefaction phenomena: proceedings of the 2004 International Conference on Cyclic Behaviour of Soils and Liquefaction Phenomena, AA Balkema.

Burrow, M., Evdorides, H., Ghataora, G. and Gunn, D. 2006. "A comparative analysis of railway foundation design principles: A case study." Proceedings of First International Conference on Railway Foundations.

Cai, Y., Chen, Y., Cao, Z., Sun, H. and Guo, L. 2015. "Dynamic responses of a saturated poroelastic half-space generated by a moving truck on the uneven pavement." Soil Dynamics and Earthquake Engineering 69: 172-181.

Cai, Y., Wu, T., Guo, L. and Wang, J. 2018. "Stiffness degradation and plastic strain accumulation of clay under cyclic load with principal stress rotation and deviatoric stress variation." Journal of Geotechnical and Geoenvironmental Engineering 144(5): 04018021.

Chrismer, S. M. (1994). Mechanics-based model to predict ballast-related maintenance timing and costs, University of Massachusetts Amherst.

Chumyen, P., Connolly, D., Woodward, P. and Markine, V. 2022. "The effect of soil improvement and auxiliary rails at railway track transition zones." Soil Dynamics and Earthquake Engineering 155: 107200.

Connolly, D. (2013). Ground borne vibrations from high speed trains PhD Thesis, The University of Edinburgh, UK.

Connolly, D., Giannopoulos, A. and Forde, M. 2013. "Numerical modelling of ground borne vibrations from high speed rail lines on embankments." Soil Dynamics and Earthquake Engineering 46: 13-19.

Connolly, D. P. and Costa, P. A. 2020. "Geodynamics of very high speed transport systems." Soil Dynamics and Earthquake Engineering 130: 105982.

Connolly, D. P., Kouroussis, G., Laghrouche, O., Ho, C. and Forde, M. 2015. "Benchmarking railway vibrations–Track, vehicle, ground and building effects." Construction and Building Materials 92: 64-81.

Correia, A. G. and Cunha, J. 2014. "Analysis of nonlinear soil modelling in the subgrade and rail track responses under HST." Transportation Geotechnics 1(4): 147-156.

Costa, P. A., Calçada, R. and Cardoso, A. S. 2012. "Track–ground vibrations induced by railway traffic: In-situ measurements and validation of a 2.5 D FEM-BEM model." Soil Dynamics and Earthquake Engineering 32(1): 111-128.

Costa, P. A., Calçada, R., Cardoso, A. S. and Bodare, A. 2010. "Influence of soil non-linearity on the dynamic response of high-speed railway tracks." Soil Dynamics and Earthquake Engineering 30(4): 221-235.

Costa, P. A., Colaço, A., Calçada, R. and Cardoso, A. S. 2015. "Critical speed of railway tracks. Detailed and simplified approaches." Transportation Geotechnics 2: 30-46.

Courant, R., Friedrichs, K. and Lewy, H. 1967. "On the partial difference equations of mathematical physics." IBM journal of Research and Development 11(2): 215-234.

Cowie, T. (2018). "Is it real? Photo of railway track bent by the heat looks fake but isn't." The Age https://www.theage.com.au/national/victoria/is-it-real-photo-of-railway-track-bent-by-the-heat-looks-fake-but-isn-t-20180214-p4z0c2.html Accessed on 14 June 2022.

Cundall, P. A. and Strack, O. D. 1979. "A discrete numerical model for granular assemblies." geotechnique 29(1): 47-65.

Cunha, J. (2013). Modelling of ballasted railway tracks for high-speed trains PhD Thesis, Universidade do Minho.

Dieterman, H. and Metrikine, A. 1996. "The equivalent stiffness of a half-space interacting with a beam. Critical velocities of a moving load along the beam." European Journal of Mechanics Series A Solids 15: 67-90.

Dong, K., Connolly, D., Laghrouche, O., Woodward, P. and Costa, P. A. 2019. "Non-linear soil behaviour on high speed rail lines." Computers and Geotechnics 112: 302-318.

Doyle, N. F. 1980. "Railway track design: a review of current practice."

Eason, G. 1965. "The stresses produced in a semi-infinite solid by a moving surface force." International Journal of Engineering Science 2(6): 581-609.

El Kacimi, A., Woodward, P. K., Laghrouche, O. and Medero, G. 2013. "Time domain 3D finite element modelling of train-induced vibration at high speed." Computers & Structures 118: 66-73.

Esmaeili, M., Farsi, S. and Shamohammadi, A. 2022. "Effect of rock strength on the degradation of ballast equipped with under sleeper pad." Construction and Building Materials 321: 126413.

Esmaeili, M. and Siahkouhi, M. 2019. "Tire-derived aggregate layer performance in railway bridges as a novel impact absorber: Numerical and field study." Structural Control and Health Monitoring 26(10): e2444.

Esmaeili, M., Zakeri, J. A., Ebrahimi, H. and Khadem Sameni, M. 2016. "Experimental study on dynamic properties of railway ballast mixed with tire derived aggregate by modal shaker test." Advances in Mechanical Engineering 8(5): 1687814016640245.

Esveld, C. 2001. Modern railway track: MRT-productions Zaltbommel, Netherlands.

Fatahi, B., Khabbaz, H. and Indraratna, B. 2010. "Bioengineering ground improvement considering root water uptake model." Ecological Engineering 36(2): 222-229.

Fathali, M., Esmaeili, M. and Moghadas Nejad, F. 2019. "Influence of tire-derived aggregates mixed with ballast on ground-borne vibrations." Journal of Modern Transportation 27(4): 355-363.

Fathali, M., Nejad, F. M. and Esmaeili, M. 2017. "Influence of tire-derived aggregates on the properties of railway ballast material." Journal of materials in civil engineering 29(1): 04016177.

Fernandes, V. A. (2014). Numerical analysis of nonlinear soil behavior and heterogeneity effects on railway track response.

Fernández-Ruiz, J., Medina Rodríguez, L. E. and Costa, P. A. 2020. "Use of Tyre-Derived Aggregate as Backfill Material for Wave Barriers to Mitigate Railway-Induced Ground Vibrations." International Journal of Environmental Research and Public Health 17(24): 9191.

Ferreira, J. N. V. d. S. (2013). Long-term behaviour of railway transitions under dynamic loading application to soft soil sites PhD Thesis, Universidade Nova De Lisboa, Portugal.

François, S., Schevenels, M., Galvín, P., Lombaert, G. and Degrande, G. 2010. "A 2.5 D coupled FE–BE methodology for the dynamic interaction between longitudinally invariant structures and a layered halfspace." Computer methods in applied mechanics and engineering 199(23-24): 1536-1548.

Frýba, L. 2013. Vibration of solids and structures under moving loads: Springer Science & Business Media.

Galvín, P., François, S., Schevenels, M., Bongini, E., Degrande, G. and Lombaert, G. 2010. "A 2.5 D coupled FE-BE model for the prediction of railway induced vibrations." Soil Dynamics and Earthquake Engineering 30(12): 1500-1512.

Gao, G., Yao, S., Yang, J. and Chen, J. 2019. "Investigating ground vibration induced by moving train loads on unsaturated ground using 2.5 D FEM." Soil Dynamics and Earthquake Engineering 124: 72-85.

Gaskin, P. N. and Raymond, G. 1976. "Contribution to selection of railroad ballast." Transportation Engineering Journal of ASCE 102(2): 377-394.

Genever, M., O'Farrell, K., Randell, P. and Rebbechi, J. (2017). "National market development strategy for used tyres." Sep 10, 2022, from https://www.tyrestewardship.org.au/wp-content/uploads/2020/04/national-market-devt-strategy.pdf.

Gent, A. N. 2012. Engineering with rubber: how to design rubber components: Carl Hanser Verlag GmbH Co KG.

Gong, H., Song, W., Huang, B., Shu, X., Han, B., Wu, H. and Zou, J. 2019. "Direct shear properties of railway ballast mixed with tire derived aggregates: Experimental and numerical investigations." Construction and Building Materials 200: 465-473.

Gräbe, P. and Clayton, C. 2009. "Effects of principal stress rotation on permanent deformation in rail track foundations." Journal of Geotechnical and Geoenvironmental Engineering 135(4): 555-565.

Grabe, P., Clayton, C. and Shaw, F.2005. Deformation measurement on a heavy haul track formation. 8th International Heavy Haul Conference. Rio de Janeiro, Brazil.

Grabe, P. J. (2003). Resilient and permanent deformation of railway foundations under principal stress rotation PhD Thesis, University of Southampton, UK.

Gunn, D., Williams, G., Kessler, H. and Thorpe, S. 2015. "Rayleigh wave propagation assessment for transport corridors." Proceedings of the Institution of Civil Engineers-Transport, Thomas Telford Ltd.

Guo, Y., Markine, V., Qiang, W., Zhang, H. and Jing, G. 2019. "Effects of crumb rubber size and percentage on degradation reduction of railway ballast." Construction and Building Materials 212: 210-224.

Guo, Y., Markine, V., Song, J. and Jing, G. 2018. "Ballast degradation: Effect of particle size and shape using Los Angeles Abrasion test and image analysis." Construction and Building Materials 169: 414-424.

Guo, Y., Xie, J., Fan, Z., Markine, V., Connolly, D. P. and Jing, G. 2022. "Railway ballast material selection and evaluation: A review." Construction and Building Materials 344: 128218.

Hall, L. (2002). Simulations and analyses of train-induced ground vibrations: A comparative study of two-and three-dimensional calculations with actual measurements.

Hall, L. 2003. "Simulations and analyses of train-induced ground vibrations in finite element models." Soil Dynamics and Earthquake Engineering 23(5): 403-413.

Hall, L., Shih, J.-Y., Barros, J. A., Zangeneh, A., Pacoste, C., Johansson, J. and Kaynia, A. M.2022. Design of foundations for high-speed railway embankments - A methodology for setting-up and performing numerical calculations of ground vibrations, The Swedish Construction Industry Development Fund.

Hardin, B. O. 1985. "Crushing of soil particles." Journal of geotechnical engineering 111(10): 1177-1192.

Hay, W. W. 1991. Railroad engineering: John Wiley & Sons.

Heelis, M. E., Collop, A. C., Dawson, A. R., Chapman, D. N. and Krylov, V. V.2000. TheBow-Wave'Effect in Soft Subgrade Beneath High Speed Rail Lines. Performance Confirmation of Constructed Geotechnical Facilities**:** 338-349.

Hibbitt, Karlsson, Sorenson, a. and Inc. 2020. *ABAQUS User's Manual*.

Hunt, G. 1994. "Analysis of requirements for railway construction on soft ground." British Railway.

Hussaini, S. K. K., Indraratna, B. and Vinod, J. S. 2015. "Performance assessment of geogrid-reinforced railroad ballast during cyclic loading." Transportation Geotechnics 2: 99-107.

Indraratna, B., Ionescu, D. and Christie, H. 1998. "Shear behavior of railway ballast based on large-scale triaxial tests." Journal of geotechnical and geoenvironmental Engineering 124(5): 439-449.

Indraratna, B., Lackenby, J. and Christie, D. 2005. "Effect of confining pressure on the degradation of ballast under cyclic loading." Geotechnique 55(4): 325-328.

Indraratna, B., Ngo, N. T. and Rujikiatkamjorn, C. 2013. "Deformation of coal fouled ballast stabilized with geogrid under cyclic load." Journal of Geotechnical and Geoenvironmental Engineering 139(8): 1275-1289.

Indraratna, B. and Ngo, T. 2018. Ballast railroad design: smart-uow approach: CRC Press.

Indraratna, B. and Nimbalkar, S. 2013. "Stress-strain degradation response of railway ballast stabilized with geosynthetics." Journal of geotechnical and geoenvironmental engineering 139(5): 684-700.

Indraratna, B., Nimbalkar, S., Christie, D., Rujikiatkamjorn, C. and Vinod, J. 2010. "Field assessment of the performance of a ballasted rail track with and without geosynthetics." Journal of Geotechnical and Geoenvironmental Engineering 136(7): 907-917.

Indraratna, B., Nimbalkar, S. and Rujikiatkamjorn, C. 2011. "Stabilisation of ballast and subgrade with geosynthetic grids and drains for rail infrastructure."

Indraratna, B., Rujikiatkamjorn, C., Ewers, B. and Adams, M. 2010. "Class A prediction of the behavior of soft estuarine soil foundation stabilized by short vertical drains beneath a rail track." Journal of geotechnical and geoenvironmental engineering 136(5): 686-696.

Indraratna, B. and Salim, W. 2005. Mechanics of ballasted rail tracks: a geotechnical perspective: CRC Press.

Indraratna, B., Salim, W. and Rujikiatkamjorn, C. 2007. "Development and application of constitutive model for railway ballast."

Indraratna, B., Salim, W. and Rujikiatkamjorn, C. 2011. Advanced rail geotechnology-ballasted track: CRC press.

Indraratna, B., Shahin, M. A., Rujikiatkamjorn, C. and Christie, D., Eds. (2006). Stabilisation of ballasted rail tracks and underlying soft formation soils with geosynthetic grids and drains. Ground modification and seismic mitigation

Indraratna, B., Singh, M., Nguyen, T. T., Leroueil, S., Abeywickrama, A., Kelly, R. and Neville, T. 2020. "Laboratory study on subgrade fluidization under undrained cyclic triaxial loading." Canadian Geotechnical Journal 57(11): 1767-1779.

Indraratna, B., Sun, Q. D. and Nimbalkar, S. 2015. "Observed and predicted behaviour of rail ballast under monotonic loading capturing particle breakage." Canadian Geotechnical Journal 52(1): 73-86.

Indraratna, B., Sun, Y. and Nimbalkar, S. 2016. "Laboratory assessment of the role of particle size distribution on the deformation and degradation of ballast under cyclic loading." Journal of Geotechnical and Geoenvironmental Engineering 142(7): 04016016.

Indraratna, B., Thakur, P. K. and Vinod, J. S. 2010. "Experimental and numerical study of railway ballast behavior under cyclic loading." International Journal of Geomechanics 10(4): 136-144.

Indraratna, B., Vinod, J. and Lackenby, J. 2009. "Influence of particle breakage on the resilient modulus of railway ballast." Géotechnique 59(7): 643-646.

Ishihara, K. and Towhata, I. 1983. "Sand response to cyclic rotation of principal stress directions as induced by wave loads." Soils and foundations 23(4): 11-26.

Itasca, C. 2020. "PFC3D (Particle Flow Code in Three Dimensions), Version 7· 0." Minneapolis: Itasca.

Iwnicki, S. 2006. Handbook of railway vehicle dynamics: CRC press.

Jayasuriya, C., Indraratna, B. and Ngo, T. N. 2019. "Experimental study to examine the role of under sleeper pads for improved performance of ballast under cyclic loading." Transportation Geotechnics 19: 61-73.

Jeffs, T. and Tew, G. 1991. "A review of track design procedures: Sleepers and ballast." Railways of Australia, Melbourne, Australia.

Jiang, H. 2015. "Failure criteria for cohesive-frictional materials based on Mohr–Coulomb failure function." International Journal for Numerical and Analytical Methods in Geomechanics 39(13): 1471-1482.

Jiang, H. and Xie, Y. 2011. "A note on the Mohr–Coulomb and Drucker–Prager strength criteria." Mechanics Research Communications 38(4): 309-314.

Kausel, E. 2006. Fundamental solutions in elastodynamics: a compendium: Cambridge University Press.

Kausel, E., Estaire, J. and Crespo-Chacón, I. 2020. "Proof of critical speed of high-speed rail underlain by stratified media." Proceedings of the Royal Society A 476(2240): 20200083.

Kausel, E. and Roësset, J. M. 1981. "Stiffness matrices for layered soils." Bulletin of the seismological Society of America 71(6): 1743-1761.

Kaynia, A. M., Madshus, C. and Zackrisson, P. 2000. "Ground vibration from high-speed trains: prediction and countermeasure." Journal of Geotechnical and Geoenvironmental Engineering 126(6): 531-537.

Kece, E., Reikalas, V., DeBold, R., Ho, C. L., Robertson, I. and Forde, M. C. 2019. "Evaluating ground vibrations induced by high-speed trains." Transportation Geotechnics 20: 100236.

Knothe, K. and Grassie, S. 1993. "Modelling of railway track and vehicle/track interaction at high frequencies." Vehicle system dynamics 22(3-4): 209-262.

Koohmishi, M. and Azarhoosh, A. 2020. "Hydraulic conductivity of fresh railway ballast mixed with crumb rubber considering size and percentage of crumb rubber as well as aggregate gradation." Construction and Building Materials 241: 118133.

Koohmishi, M. and Azarhoosh, A. 2021. "Degradation of crumb rubber modified railway ballast under impact loading considering aggregate gradation and rubber size." Canadian Geotechnical Journal 58(3): 398-410.

Kouroussis, G., Connolly, D. P. and Verlinden, O. 2014. "Railway-induced ground vibrations–a review of vehicle effects." International Journal of Rail Transportation 2(2): 69-110.

Kouroussis, G., Van Parys, L., Conti, C. and Verlinden, O. 2014. "Using three-dimensional finite element analysis in time domain to model railway-induced ground vibrations." Advances in Engineering Software 70: 63-76.

Kouroussis, G. and Verlinden, O. 2015. "Prediction of railway ground vibrations: accuracy of a coupled lumped mass model for representing the track/soil interaction." Soil Dynamics and Earthquake Engineering 69: 220-226.

Kouroussis, G., Verlinden, O. and Conti, C. 2011. "Free field vibrations caused by high-speed lines: measurement and time domain simulation." Soil Dynamics and Earthquake Engineering 31(4): 692-707.

Krylov, V. and Ferguson, C. 1994. "Calculation of low-frequency ground vibrations from railway trains." Applied Acoustics 42(3): 199-213.

Krylov, V. V. 1994. "On the theory of railway-induced ground vibrations." Le Journal de Physique IV 4(C5): C5-769-C765-772.

Krylov, V. V. 1995. "Generation of ground vibrations by superfast trains." Applied Acoustics 44(2): 149-164.

Krylov, V. V. 1999. "Ground vibration boom from high-speed trains." Journal of Low Frequency Noise, Vibration and Active Control 18(4): 207-218.

Krylov, V. V., Dawson, A., Heelis, M. and Collop, A. 2000. "Rail movement and ground waves caused by high-speed trains approaching track-soil critical velocities." Proceedings of the Institution of Mechanical Engineers, Part F: Journal of Rail and Rapid Transit 214(2): 107-116.

Kuhlemeyer, R. L. and Lysmer, J. 1973. "Finite element method accuracy for wave propagation problems." Journal of the Soil Mechanics and Foundations Division 99(5): 421-427.

Lackenby, J. (2006). Triaxial behaviour of ballast and the role of confining pressure under cyclic loading PhD Thesis, University of Wollongong, Asutralia.

Lackenby, J., Indraratna, B., McDowell, G. and Christie, D. 2007. "Effect of confining pressure on ballast degradation and deformation under cyclic triaxial loading." Géotechnique 57(6): 527-536.

Lade, P. V., Yamamuro, J. A. and Bopp, P. A. 1996. "Significance of particle crushing in granular materials." Journal of geotechnical engineering 122(4).

Lamas-Lopez, F., Cui, Y.-J., Calon, N., D'Aguiar, S. C., De Oliveira, M. P. and Zhang, T. 2016. "Track-bed mechanical behaviour under the impact of train at different speeds." Soils and Foundations 56(4): 627-639.

Lamprea-Pineda, A. C., Connolly, D. P. and Hussein, M. F. 2021. "Beams on elastic foundations–a review of railway applications and solutions." Transportation Geotechnics: 100696.

Lee, K. L. and Farhoomand, I. 1967. "Compressibility and crushing of granular soil in anisotropic triaxial compression." Canadian geotechnical journal 4(1): 68-86.

Lekarp, F., Isacsson, U. and Dawson, A. 2000. "State of the art. I: Resilient response of unbound aggregates." Journal of transportation engineering 126(1): 66-75.

Leshchinsky, B. and Ling, H. I. 2013. "Numerical modeling of behavior of railway ballasted structure with geocell confinement." Geotextiles and Geomembranes 36: 33-43.

Li, D., Hyslip, J., Sussmann, T. and Chrismer, S. 2015. Railway geotechnics: CRC Press.

Li, D. and Selig, E. T. 1998. "Method for railroad track foundation design. I: Development." Journal of geotechnical and geoenvironmental engineering 124(4): 316-322.

Li, D. and Selig, E. T. 1998. "Method for railroad track foundation design. II: Applications." Journal of geotechnical and geoenvironmental engineering 124(4): 323-329.

Li, K., Brough, M., Sharley, P., Thomas, B., Sharpe, P. and Thom, N. 2007. "Alternative to sand blanket: anti-pumping geocomposite in maintenance & track renewal." 9th International Conference, Railway Engineering, University of Westminster, London.

Li, L., Nimbalkar, S. and Zhong, R. 2018. "Finite element model of ballasted railway with infinite boundaries considering effects of moving train loads and Rayleigh waves." Soil Dynamics and Earthquake Engineering 114: 147-153.

Li, X., Ekh, M. and Nielsen, J. C. 2016. "Three-dimensional modelling of differential railway track settlement using a cycle domain constitutive model." International Journal for Numerical and Analytical Methods in Geomechanics 40(12): 1758-1770.

Lim, W. L. (2004). Mechanics of railway ballast behaviour PhD Thesis, University of Nottingham Nottingham, UK.

Ling, D.-s., Zhao, Y., Huang, B., Zhang, F. and Zhou, Y. 2018. "Analysis of dynamic stress path in inhomogenous subgrade under moving aircraft load." Soil Dynamics and Earthquake Engineering 111: 65-76.

Lombaert, G., Degrande, G., Kogut, J. and François, S. 2006. "The experimental validation of a numerical model for the prediction of railway induced vibrations." Journal of sound and vibration 297(3-5): 512-535.

Lu, M. and McDowell, G. 2010. "Discrete element modelling of railway ballast under monotonic and cyclic triaxial loading." Géotechnique 60(6): 459-467.

Lu, X., Kim, C.-W. and Chang, K.-C. 2020. "Finite element analysis framework for dynamic vehicle-bridge interaction system based on ABAQUS." International Journal of Structural Stability and Dynamics 20(03): 2050034.

Madhusudhan, B., Boominathan, A. and Banerjee, S. 2017. "Static and large-strain dynamic properties of sand–rubber tire shred mixtures." Journal of Materials in Civil Engineering 29(10): 04017165.

Madshus, C. and Kaynia, A.2001. High-speed trains on soft ground: track–embankment–soil response and vibration generation. Noise and vibration from high-speed trains, Thomas Telford Publishing**:** 315-346.

Madshus, C., Lacasse, S., Kaynia, A. and Hårvik, L.2004. Geodynamic challenges in high speed railway projects. Geotechnical Engineering for Transportation Projects**:** 192-215.

Madshus, C. c. and Kaynia, A. 2000. "High-speed railway lines on soft ground: dynamic behaviour at critical train speed." Journal of Sound and Vibration 231(3): 689-701.

Malischewsky, P. G. 2005. "Comparison of approximated solutions for the phase velocity of Rayleigh waves (Comment on ‘Characterization of surface damage via surface acoustic waves’)." Nanotechnology 16(6): 995.

Malisetty, R. S. (2019). A multi-laminate framework for analysing the deformation and degradation of ballast PhD Thesis, University of Wollongong, Australia.

Malisetty, R. S., Indraratna, B., Ngo, T. and Tucho, A. 2022. "Dynamic stress response of track layers under high speed trains." 20th Internation Conference on Soil Mechanics and Geotechnical Engineering, Australian Geomechanics Society.

Malisetty, R. S., Indraratna, B. and Vinod, J. 2020. "Behaviour of ballast under principal stress rotation: Multi-laminate approach for moving loads." Computers and Geotechnics 125: 103655.

Marsal, R. J. 1967. "Large scale testing of rockfill materials." Journal of the Soil Mechanics and Foundations Division 93(2): 27-43.

Milne, D., Harkness, J., Le Pen, L. and Powrie, W. 2019. "The influence of variation in track level and support system stiffness over longer lengths of track for track performance and vehicle track interaction." Vehicle System Dynamics: 1-24.

Milne, D., Le Pen, L., Thompson, D. and Powrie, W. 2017. "Properties of train load frequencies and their applications." Journal of sound and vibration 397: 123-140.

Momoya, Y., Sekine, E. and Tatsuoka, F. 2005. "Deformation characteristics of railway roadbed and subgrade under moving-wheel load." Soils and Foundations 45(4): 99-118.

Momoya, Y., Watanabe, K., Sekine, E., Tateyama, M., Shinoda, M. and Tatsuoka, F. 2007. "Effects of continuous principal stress axis rotation on the deformation characteristics of sand under traffic loads." Proceedings of the international workshop on design and construction of pavements and rail tracks–Geotechnical aspects and processed materials.

Nålsund, R. 2010. "Effect of grading on degradation of crushed-rock railway ballast and on permanent axial deformation." Transportation Research Record 2154(1): 149-155.

Navaratnarajah, S. K. and Indraratna, B. 2017. "Use of rubber mats to improve the deformation and degradation behavior of rail ballast under cyclic loading." Journal of geotechnical and geoenvironmental engineering 143(6): 04017015.

Navaratnarajah, S. K., Indraratna, B. and Ngo, N. T. 2018. "Influence of under sleeper pads on ballast behavior under cyclic loading: experimental and numerical studies." Journal of Geotechnical and Geoenvironmental Engineering 144(9): 04018068.

Ngo, N. T. (2012). Performance of geogrids stabilised fouled ballast in rail tracks PhD Thesis, University of Wollongong, Australia.

Ngo, N. T., Indraratna, B. and Rujikiatkamjorn, C. 2014. "DEM simulation of the behaviour of geogrid stabilised ballast fouled with coal." Computers and Geotechnics 55: 224-231.

Ngo, N. T., Indraratna, B. and Rujikiatkamjorn, C. 2017. "Coupled DEM-FEM analysis for simulating ballasted rail tracks."

Ngo, N. T., Indraratna, B. and Rujikiatkamjorn, C. 2017. "Simulation ballasted track behavior: numerical treatment and field application." International Journal of Geomechanics 17(6): 04016130.

Nguyen, T. T., Indraratna, B., Kelly, R., Phan, N. M. and Haryono, F. 2019. "Mud pumping under railtracks: mechanisms, assessments and solutions." Aust Geomech J 54(4): 59-80.

Nimbalkar, S. and Indraratna, B. 2016. "Improved performance of ballasted rail track using geosynthetics and rubber shockmat." Journal of Geotechnical and Geoenvironmental Engineering 142(8): 04016031.

Nishiura, D., Sakai, H., Aikawa, A., Tsuzuki, S. and Sakaguchi, H. 2018. "Novel discrete element modeling coupled with finite element method for investigating ballasted railway track dynamics." Computers and Geotechnics 96: 40-54.

Nsabimana, E. and Jung, Y.-H. 2015. "Dynamic subsoil responses of a stiff concrete slab track subjected to various train speeds: a critical velocity perspective." Computers and Geotechnics 69: 7-21.

O'Rourke, M. 1978. Critique of conventional track design procedures as applied to heavy axle load conditions: BHP Melbourne Research Laboratories.

ORE. 1987. The dynamic effects due to increasing axle loads from 20 to 22.5 ton. Utrecht, Netherlands: Office of Research and Experiments (ORE), International Union of Railways.

Paixão, A. (2014). Transition zones in railway tracks: An experimental and numerical study on the structural behaviour PhD Thesis.

Paul de Vos, S.2017. Railway Induced Vibration-State of the art report. International Union of Railways: Paris, France.

Powrie, W. and Le pen, L.2016. A Guide to Track Stiffness. UK, University of Southampton

Powrie, W., Le Pen, L., Milne, D. and Thompson, D. 2019. "Train loading effects in railway geotechnical engineering: Ground response, analysis, measurement and interpretation." Transportation Geotechnics 21: 100261.

Powrie, W., Yang, L. and Clayton, C. R. 2007. "Stress changes in the ground below ballasted railway track during train passage." Proceedings of the Institution of Mechanical Engineers, Part F: Journal of Rail and Rapid Transit 221(2): 247-262.

Priest, J., Powrie, W., Yang, L., Grabe, P. and Clayton, C. 2010. "Measurements of transient ground movements below a ballasted railway line." Géotechnique 60(9): 667-677.

Profillidis, V. A. 2006. Railway management and engineering: Ashgate Publishing, Ltd.

Qi, Y. and Indraratna, B. 2022. "Influence of Rubber Inclusion on the Dynamic Response of Rail Track." Journal of Materials in Civil Engineering 34(2): 04021432.

Qian, J.-G., Wang, Y.-G., Yin, Z.-Y. and Huang, M.-S. 2016. "Experimental identification of plastic shakedown behavior of saturated clay subjected to traffic loading with principal stress rotation." Engineering Geology 214: 29-42.

Qian, Y., Boler, H., Moaveni, M., Tutumluer, E., Hashash, Y. M. and Ghaboussi, J. 2017. "Degradation-related changes in ballast gradation and aggregate particle morphology." Journal of Geotechnical and Geoenvironmental Engineering 143(8): 04017032.

Qian, Y., Tutumluer, E., Hashash, Y. M. and Ghaboussi, J. 2014. "Effects of ballast degradation on permanent deformation behavior from large-scale triaxial tests." ASME/IEEE Joint Rail Conference, American Society of Mechanical Engineers.

Rahman, M. and Barber, J. 1995. "Exact expressions for the roots of the secular equation for Rayleigh waves." Journal of applied mechanics 62: 150-252.

Rahman, M. and Michelitsch, T. 2006. "A note on the formula for the Rayleigh wave speed." Wave motion 43(3): 272-276.

Ramos, A., Correia, A. G., Calçada, R. and Connolly, D. 2022. "Ballastless railway track transition zones: an embankment to tunnel analysis." Transportation Geotechnics: 100728.

Ramos, A., Correia, A. G., Indraratna, B., Ngo, T., Calçada, R. and Costa, P. A. 2020. "Mechanistic-empirical permanent deformation models: Laboratory testing, modelling and ranking." Transportation Geotechnics 23: 100326.

Ramos, A., Gomes Correia, A., Calçada, R. and Alves Costa, P. 2021. "Stress and permanent deformation amplification factors in subgrade induced by dynamic mechanisms in track structures." International Journal of Rail Transportation: 1-33.

Randell, P., Baker, B. and O'Farrell, K.2020. Used tyres supply chain and fate analysis report. Victoria, Australia,

, Randell Environmental Consulting Pty Ltd**:** 1-60.

Raymond, G. P. 1985. "Research on railroad ballast specification and evaluation." Transportation Research Record 1006: 1-8.

Richart, F. E., Hall, J. R. and Woods, R. D. 1970. "Vibrations of soils and foundations."

Ruge, P. and Birk, C. 2007. "Longitudinal forces in continuously welded rails on bridgedecks due to nonlinear track–bridge interaction." Computers & structures 85(7-8): 458-475.

Sadeghi, J. 2005. "Investigation on the accuracy of the current practices in analysis of railway track concrete sleepers." International Journal of Civil Engineering 3(1): 31-45.

Sadeghi, J. and Barati, P. 2010. "Evaluation of conventional methods in Analysis and Design of Railway Track System." International Journal of Civil Engineering 8(1): 44-56.

Saleeb, A. F. and Kumar, A. 2011. "Automated finite element analysis of complex dynamics of primary system traversed by oscillatory subsystem." International Journal for Computational Methods in Engineering Science and Mechanics 12(4): 184-202.

Saussine, G., Azéma, E., Gautier, P., Peyroux, R. and Radjai, F. 2008. "Numerical modeling of the tamping operation by Discrete Element Approach." World Congress Rail Research.

Sayeed, M. (2016). Design of ballasted railway track foundations using numerical modelling with special reference to high speed trains PhD Thesis, Curtin University, Australia.

Sayeed, M. A. and Shahin, M. A. 2016. "Three-dimensional numerical modelling of ballasted railway track foundations for high-speed trains with special reference to critical speed." Transportation Geotechnics 6: 55-65.

Schramm, G. 1961. Permanent way technique and permanent way economy: with 23 tables: Elsner.

Selig, E. T. and Waters, J. M. 1994. Track geotechnology and substructure management: Thomas Telford.

Sevi, A. F., Ge, L. and Take, W. A. 2009. "A large-scale triaxial apparatus for prototype railroad ballast testing." Geotechnical testing journal 32(4): 297-304.

Shan, Y., Albers, B. and Savidis, S. A. 2013. "Influence of different transition zones on the dynamic response of track–subgrade systems." Computers and Geotechnics 48: 21-28.

Sheng, X.-z., Jones, C. and Petyt, M. 1999. "Ground vibration generated by a load moving along a railway track." Journal of sound and vibration 228(1): 129-156.

Sheng, X. (2004). Ground vibrations generated from trains PhD Thesis, University of Southampton, UK.

Sheng, X., Jones, C. and Thompson, D. 2004. "A theoretical study on the influence of the track on train-induced ground vibration." Journal of Sound and Vibration 272(3-5): 909-936.

Sheng, X., Jones, C. and Thompson, D. 2006. "Prediction of ground vibration from trains using the wavenumber finite and boundary element methods." Journal of Sound and Vibration 293(3-5): 575-586.

Shenton, M. 1985. "Ballast deformation and track deterioration." Track technology: 253-265.

Shi, C., Zhao, C., Yang, Y., Guo, Y. and Zhang, X. 2021. "Analysis of Railway Ballasted Track Stiffness and Behavior with a Hybrid Discrete–Continuum Approach." International Journal of Geomechanics 21(3): 04020268.

Shi, C., Zhao, C., Zhang, X. and Guo, Y. 2020. "Coupled discrete-continuum approach for railway ballast track and subgrade macro-meso analysis." International Journal of Pavement Engineering: 1-16.

Shih, J.-Y. (2017). Models for vehicle/track/ground interaction in the time domain PhD Thesis, University of Southamptony, UK.

Shih, J.-Y., Grossoni, I. and Bezin, Y. 2019. "Settlement analysis using a generic ballasted track simulation package." Transportation Geotechnics 20: 100249.

Shih, J.-Y., Thompson, D. and Ntotsios, E. 2018. "Analysis of resonance effect for a railway track on a layered ground." Transportation Geotechnics 16: 51-62.

Shih, J.-Y., Thompson, D. and Zervos, A. 2016. "The effect of boundary conditions, model size and damping models in the finite element modelling of a moving load

on a track/ground system." Soil Dynamics and Earthquake Engineering 89: 12-27.

Shih, J.-Y., Thompson, D. J. and Zervos, A. 2017. "The influence of soil nonlinear properties on the track/ground vibration induced by trains running on soft ground." Transportation Geotechnics 11: 1-16.

Sidhu, K., Keeslar, F. and Warner, P. 2006. "Potential health risks related to tire fire smoke." Toxicology International 13(1): 1-17.

Sol-Sánchez, M., Moreno-Navarro, F. and Rubio-Gámez, M. C. 2015. "The use of elastic elements in railway tracks: A state of the art review." Construction and building materials 75: 293-305.

Sol-Sánchez, M., Thom, N., Moreno-Navarro, F., Rubio-Gámez, M. and Airey, G. 2015. "A study into the use of crumb rubber in railway ballast." Construction and Building Materials 75: 19-24.

Song, W., Huang, B., Shu, X., Wu, H., Gong, H., Han, B. and Zou, J. 2019. "Improving damping properties of railway ballast by addition of tire-derived aggregate." Transportation research record 2673(5): 299-307.

Srinivasan, M. 1969. Modern permanent way. India: Somaiya Publications PVT Limited.

Suiker, A. S. J. (2004). The mechanical behaviour of ballasted railway tracks PhD Thesis, Delft University, The Netherlands.

Sun, Q. (2015). An elasto-plastic strain-based approach for analysing the behaviour of ballasted rail track PhD Thesis, University of Wollongong, Australia.

Sun, Q., Indraratna, B. and Ngo, N. T. 2019. "Effect of increase in load and frequency on the resilience of railway ballast." Géotechnique 69(9): 833-840.

Sun, Q., Indraratna, B. and Nimbalkar, S. 2014. "Effect of cyclic loading frequency on the permanent deformation and degradation of railway ballast." Géotechnique 64(9): 746-751.

Sun, Q. D., Indraratna, B. and Nimbalkar, S. 2016. "Deformation and degradation mechanisms of railway ballast under high frequency cyclic loading." Journal of Geotechnical and Geoenvironmental Engineering 142(1): 04015056.

Sun, Y., Chen, C. and Nimbalkar, S. 2017. "Identification of ballast grading for rail track." Journal of Rock Mechanics and Geotechnical Engineering 9(5): 945-954.

Sussmann, T. R., Ruel, M. and Chrismer, S. M. 2012. "Source of ballast fouling and influence considerations for condition assessment criteria." Transportation Research Record 2289(1): 87-94.

Takemiya, H. and Bian, X. 2005. "Substructure simulation of inhomogeneous track and layered ground dynamic interaction under train passage." Journal of Engineering Mechanics 131(7): 699-711.

Tang, Y., Xiao, S. and Yang, Q. 2019. "Numerical study of dynamic stress developed in the high speed rail foundation under train loads." Soil Dynamics and Earthquake Engineering 123: 36-47.

Tang, Y., Yang, Q., Ren, X. and Xiao, S. 2019. "Dynamic response of soft soils in high-speed rail foundation: in situ measurements and time domain finite element method model." Canadian Geotechnical Journal 56(12): 1832-1848.

Tasalloti, A., Chiaro, G., Banasiak, L. and Palermo, A. 2021. "Experimental investigation of the mechanical behaviour of gravel-granulated tyre rubber mixtures." Construction and Building Materials 273: 121749.

Thach, P.-N., Liu, H.-L. and Kong, G.-Q. 2013. "Vibration analysis of pile-supported embankments under high-speed train passage." Soil Dynamics and Earthquake Engineering 55: 92-99.

Thompson, D. 2008. Railway noise and vibration: mechanisms, modelling and means of control: Elsevier.

Tokimatsu, K., Tamura, S. and Kojima, H. 1992. "Effects of multiple modes on Rayleigh wave dispersion characteristics." Journal of geotechnical engineering 118(10): 1529-1543.

Tong, Y., Liu, G., Yousefian, K. and Jing, G. 2022. "Track Vertical Stiffness–Value, Measurement Methods, Effective Parameters and Challenges: A review." Transportation Geotechnics: 100833.

Tong, Z.-X., Zhang, J.-M., Yu, Y.-L. and Zhang, G. 2010. "Drained deformation behavior of anisotropic sands during cyclic rotation of principal stress axes." Journal of Geotechnical and Geoenvironmental Engineering 136(11): 1509-1518.

Torretta, V., Rada, E. C., Ragazzi, M., Trulli, E., Istrate, I. A. and Cioca, L. I. 2015. "Treatment and disposal of tyres: Two EU approaches. A review." Waste management 45: 152-160.

Trani, L. D. O. and Indraratna, B. 2010. "Assessment of subballast filtration under cyclic loading." Journal of Geotechnical and Geoenvironmental Engineering 136(11): 1519-1528.

TS3402. 2001. Specification for Supply of Aggregate for Ballast. Sydney, Australia: Rail Infrastructure Corporation (RIC) of New South Wales.

Tucho, A., Indraratna, B. and Ngo, T. 2022. "Stress-deformation analysis of rail substructure under moving wheel load." Transportation Geotechnics: 100805.

Tutumluer, E., Huang, H. and Bian, X. 2012. "Geogrid-aggregate interlock mechanism investigated through aggregate imaging-based discrete element modeling approach." International Journal of Geomechanics 12(4): 391-398.

UIC.2021. Atlas High-Speed Rail 2021, International Union of Railways, Paris.

Uzan, J., Witczak, M., Scullion, T. and Lytton, R. 1992. "Development and validation of realistic pavement response models." International Conference on Asphalt Pavements, 7th, 1992, Nottingham, United Kingdom.

Van Dyk, B. J., Edwards, J. R., Dersch, M. S., Ruppert Jr, C. J. and Barkan, C. P. 2017. "Evaluation of dynamic and impact wheel load factors and their application in design processes." Proceedings of the Institution of Mechanical Engineers, Part F: Journal of Rail and Rapid Transit 231(1): 33-43.

Varandas, J., Paixão, A., Fortunato, E., Coelho, B. Z. and Hölscher, P. 2020. "Long-term deformation of railway tracks considering train-track interaction and non-linear resilient behaviour of aggregates–a 3D FEM implementation." Computers and Geotechnics 126: 103712.

Varandas, J. N., Paixão, A., Fortunato, E. and Hölscher, P. 2016. "A numerical study on the stress changes in the ballast due to train passages." Procedia engineering 143: 1169-1176.

Walker, R. T. and Indraratna, B. 2018. "Moving loads on a viscoelastic foundation with special reference to railway transition zones." International Journal of Geomechanics 18(11): 04018145.

Wei, X., Wang, G. and Wu, R. 2017. "Prediction of traffic loading–induced settlement of low-embankment road on soft subsoil." International Journal of Geomechanics 17(2): 06016016.

Werkmeister, S., Dawson, A. R. and Wellner, F. 2001. "Permanent deformation behavior of granular materials and the shakedown concept." Transportation Research Record 1757(1): 75-81.

Wojciechowski, M. 2018. "A note on the differences between Drucker-Prager and Mohr-Coulomb shear strength criteria." Studia Geotechnica et Mechanica 40(3): 163-169.

Woldright, B. and New, B. 1999. "Embankment design for high speed trains on soft Grounds." Proc XIIth ECSMGE, Amsterdam, Balkema.

Woods, R. D. 1968. "Screening of surface wave in soils." Journal of the soil mechanics and foundations division 94(4): 951-979.

Woodward, P., Laghrouche, O. and El-Kacimi, A. 2013. "The development and mitigation of ground mach cones for high speed railways." ICOVP 2013-International Conference on Vibration Problems.

Xiao, J., Juang, C. H., Wei, K. and Xu, S. 2014. "Effects of principal stress rotation on the cumulative deformation of normally consolidated soft clay under subway traffic loading." Journal of Geotechnical and Geoenvironmental Engineering 140(4): 04013046.

Xiao, J., Zhang, D., Wei, K. and Luo, Z. 2017. "Shakedown behaviors of railway ballast under cyclic loading." Construction and building materials 155: 1206-1214.

Xie, G. and Iwnicki, S. D. 2008. "Simulation of wear on a rough rail using a time-domain wheel–track interaction model." Wear 265(11-12): 1572-1583.

Xue, F. 2016. "Spatial Rotations of Principal Stress Axes in Infrastructures on High-Speed Railway." International Symposium on Environmental Vibration and Transportation Geodynamics, Springer.

Yang, L., Powrie, W. and Priest, J. 2009. "Dynamic stress analysis of a ballasted railway track bed during train passage." Journal of Geotechnical and Geoenvironmental Engineering 135(5): 680-689.

Yang, Y. B., Liu, S. J., Li, Q. M. and Ge, P. B. 2019. "Stress waves in half-space due to moving train loads by 2.5D finite/infinite element approach." Soil Dynamics and Earthquake Engineering 125: 105714.

Zakeri, J. A. and Sadeghi, J. 2007. "Field investigation on load distribution and deflections of railway track sleepers." Journal of Mechanical Science and Technology 21(12): 1948-1956.

Zerwer, A., Cascante, G. and Hutchinson, J. 2002. "Parameter estimation in finite element simulations of Rayleigh waves." Journal of geotechnical and geoenvironmental engineering 128(3): 250-261.

Zhai, W., He, Z. and Song, X. 2010. "Prediction of high-speed train induced ground vibration based on train-track-ground system model." Earthquake Engineering and Engineering Vibration 9: 545-554.

Zhai, W., Wang, K. and Cai, C. 2009. "Fundamentals of vehicle–track coupled dynamics." Vehicle System Dynamics 47(11): 1349-1376.

Zhang, F., Chang, J. and Feng, H. 2022. "Laboratory study on degradation of ballast mixed with crumb rubber under impact loads." International Journal of Rail Transportation: 1-23.

Zhang, W., Seylabi, E. E. and Taciroglu, E. 2019. "An ABAQUS toolbox for soil-structure interaction analysis." Computers and Geotechnics 114: 103143.

Zhang, X., Zhao, C. and Zhai, W. 2017. "Dynamic behavior analysis of high-speed railway ballast under moving vehicle loads using discrete element method." International Journal of Geomechanics 17(7): 04016157.

Zhang, X., Zhao, C. and Zhai, W. 2019. "Importance of load frequency in applying cyclic loads to investigate ballast deformation under high-speed train loads." Soil Dynamics and Earthquake Engineering 120: 28-38.

Zhang, Y., Bernhardt, M., Biscontin, G., Luo, R. and Lytton, R. L. 2015. "A generalized Drucker–Prager viscoplastic yield surface model for asphalt concrete." Materials and Structures 48(11): 3585-3601.

Zhao, H., Indraratna, B. and Ngo, T. 2021. "Numerical simulation of the effect of moving loads on saturated subgrade soil." Computers and Geotechnics 131: 103930.

Zienkiewicz, O. C., Taylor, R. L. and Zhu, J. Z. 2005. The finite element method: its basis and fundamentals: Elsevier.

APPENDIX A DRUCKER-PRAGER MODEL

The extended Drucker-Prager (D-P) yield function is represented in equation A-1 (Wojciechowski, 2018; Zhang et al., 2015):

$$F = \sqrt{J'_2}\eta(K,\theta) - \mathrm{A}I'_1 - B = 0 \tag{A-1}$$

where, A and B are material constants corresponding to friction angle and cohesion of the material. The parameters I'_1 the first invariant of the effective stress tensor (σ'_{ij}) while J'_2 and J'_3 correspond to the second and third invariant of deviator stress tensor (S'_{ij}), respectively, and can be represented by the following equations:

$$I'_1 = \sigma'_{kk} \tag{A-2}$$

$$J'_2 = \frac{1}{2}S'_{ij}S'_{ji} \tag{A-3}$$

$$J'_3 = det\left(S'_{ij}\right) \tag{A-4}$$

where, $S_{ij} = \sigma'_{ij} - \frac{1}{3}\delta_{ij}I'_1$; and δ_{ij} is Kronecker delta.

The function $\eta(K,\theta)$ determines the shape of the yield surface in the deviatoric plane. The parameter K, which controls the effect of intermediate principal stress on the yield stress, is the ratio yield strength in triaxial tension to compression. Figure A-1a shows that D-P has smooth curves, that varies as a function of K, as compared to the irregular hexagon of Mohr-Coulumb (M-C) criterion. The sharp corners of M-C impair convergence during numerical simulations (Jiang, 2015).

$$\eta(K,\theta) = \frac{1}{2}\left[1 + \frac{1}{K} + \left(1 - \frac{1}{K}\right)\cos(3\theta)\right] \tag{A-5}$$

$$= \frac{1}{2}\left[1 + \frac{1}{K} + \left(1 - \frac{1}{K}\right)\left[\frac{3\sqrt{3}}{2}\frac{J'_3}{(J'_2)^{3/2}}\right]\right]$$

where, θ represents the Lode angle.

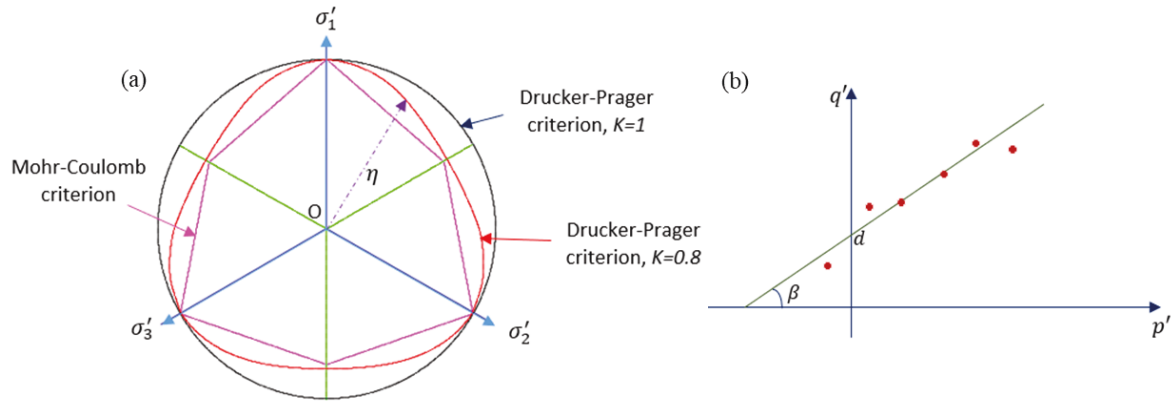

Figure A-1. (a) Representation of yield surfaces of Extended Drucker-Prager and Mohr-Coulomb octahedral plane; and (b) Drucker-Prager yield surface representation in p'-q' space

For the triaxial stress state expressed in effective principal stresses $\sigma'_1 \geq \sigma'_2 = \sigma'_3$, the stress invariants described in equations A-2 to A-4 are:

$$I'_1 = \sigma'_1 + 2\sigma'_3 \tag{A-6}$$

$$J'_2 = \frac{1}{3}(\sigma'_1 - \sigma'_3)^2 \tag{A-7}$$

$$J'_3 = \frac{2}{27}(\sigma'_1 - \sigma'_3)^3 \tag{A-8}$$

Hence, for triaxial stress state, the Extended Drucker-Prager model in equation A-1 becomes circular in deviatoric plane ($\eta(K,\theta)=1$) with a form:

$$F=\sqrt{J'_2}-\mathrm{A}I'_1-B=0 \tag{A-9}$$

The coefficients A and B can be determined by matching to the Mohr-Coulomb parameters, friction angle (ϕ') and cohesion (c') (Jiang and Xie, 2011; Zhang et al., 2015).

Alternatively, D-P yield function in p'-q'stress plane can be described (Hibbitt et al., 2020):

$$F=q'-p'tan\beta-d=0 \tag{A-10}$$

where

$$p'=\frac{1}{3}(\sigma'_1+\sigma'_2+\sigma'_3)=\frac{1}{3}I'_1 \tag{A-11}$$

$$q'=\left[\frac{1}{2}[(\sigma'_1-\sigma'_2)^2+(\sigma'_2-\sigma'_3)^2+(\sigma'_3-\sigma'_1)^2]\right]^{1/2}=\sqrt{3J'_2} \tag{A-12}$$

The coefficients β and d are the angle of yield surface and q-intercept of the yield surface in *p*-*q* stress, respectively, as illustrated in Fig. A-1b.

APPENDIX B USER DEFINED SUBROUTINE FOR MOVING LOAD

```
!=== VDLOAD subroutine For Moving Pressure Load
!Validation of Eason (1965) mathematical model for moving load
!@AmeyuT Supervisors: D/Prof Buddhima & Dr Trung
      subroutine vdload (
     1 nblock, ndim, stepTime, totalTime,
     2 amplitude, curCoords, velocity, dirCos, jltyp, sname,
     1 value )
!
      include 'vaba_param.inc'
!
      dimension curCoords(nblock,ndim), velocity(nblock,ndim),
     1  dirCos(nblock,ndim,ndim), value(nblock)
      character*80 sname
      !----------------------------------------------------------------72--------

      ! user parameters
         parameter (Pressure = 5e4, zi=0.5d0, zvel=16.6d0, zlen=1.0d0)
                     ! zi= Initial location(m),
                     ! zvel= velocity in of the load x(m/s)
                     ! zlen= length in in the moving direction
                     ! zpressure= Vertical pressure on subgrade

      ! index
      parameter(iX    = 1, ! x-coord for coords array
     *          iY    = 2, ! y-coord for coords array
     *          iZ    = 3) ! z-coord for coords array
```

```
!*          iTotTime  = 2) ! total time
!*          iStepTime = 1, ! step time


  ! Load current position (zc=zi+zdi)
          zdi=zvel*totalTime !Distance travelled
          zc=zi+zdi
          zmax=zc
          zmin=zmax-zlen
          ! Pressure dimensions = xmax - xmin (m)
            xmin=0.0d0
            xmax=1.0d0


   ! loop over points
  do i = 1, nblock
    ! Loop for finding points under vehicle's position
    ! if (curCoords(x,y) under area(xmin-xmax, ymin-ymax) then
      if(curCoords(i,iZ).lt.zmax.and.curCoords(i,iZ).ge.zmin) then
                  if(curCoords(i,iX).lt.xmax.and.curCoords(i,iX).ge.xmin) then
      value(i) = Pressure ! apply moving pressure
    else
      value(i) = 0.d0 ! apply zero pressure
    endif
          endif


  end do


  !----------------------------------------------------------------72--------
```

```
      return

      end


!-----------------------------------EOF---------------------------------------
```